Crack Propagation Life of Detail Fractures in Rails

US Department
of Transportation

**Federal Railroad
Administration**

Office of Research and
Development
Washington, DC 20590

O. Orringer
Y.H. Tang
J.E. Gordon
D.Y. Jeong
J.M. Morris
A.B. Perlman

U.S. Department of Transportation
Research and Special Programs Administration
Volpe National Transportation Systems Center
Cambridge, Massachusetts 02142

DOT/FRA/ORD-88/13
DOT-TSC-FRA-88-1

October 1988
Final Report

Technical Report Documentation Page

1. Report No.	2. Government Accession No.	3. Recipient's Catalog No.
DOT/FRA/ORD-88/13		

4. Title and Subtitle	5. Report Date
Crack Propagation Life of Detail Fractures in Rails	October 1988
	6. Performing Organization Code: DTS-76

7. Author(s)	8. Performing Organization Report No.
O. Orringer, Y.H. Tang, J.E. Gordon, D.Y. Jeong, J.M. Morris, and A.B. Perlman	DOT-TSC-FRA-88-1

9. Performing Organization Name and Address	10. Work Unit No. (TRAIS)
U.S. Department of Transportation Research and Special Programs Administration Transportation Systems Center Cambridge, MA 02142	RR819/R8001
	11. Contract or Grant No.
	13. Type of Report and Period Covered: Final Report, April 1978 - April 1988
12. Sponsoring Agency Name and Address U.S. Department of Transportation Federal Railroad Adminstration Office of Research and Development Washington, DC 20590	14. Sponsoring Agency Code: RRS-30

15. Supplementary Notes

16. Abstract

The results of a comprehensive study of the crack propagation behavior of detail fractures in railroad rails are presented. The study includes full-scale crack growth experiments in a test track under simulated heavy freight train service, similar field tests and observations on revenue tracks, and static tests to determine the breaking strengths of rails containing detail fractures. A fracture mechanics model of the detail fracture is presented, and the results of laboratory tests to determine the basic crack growth rate properties of rail steel are reviewed. Correlation of most of the experimental results by the model is demonstrated. The model is used to illustrate the sensitivity of safe crack growth life to nine railroad environmental factors. The most influential factors are found to be thermal stress in continuous welded rail, the curve high rail position (relative to tangent track), and residual stress in the rail head. The experimental and analytical results indicate that further investigation is required into the influence on residual stress of: track curvature, rail steel tensile strength, roller-straightening of rails, and increases in axle loads above the maximum currently permitted by U.S. freight railroad interchange rules.

17. Key Words	18. Distribution Statement
Crack Growth, Detail Fracture, Fracture Mechanics, Rail Integrity, Safe Crack Growth Life	DOCUMENT IS AVAILABLE TO THE PUBLIC THROUGH THE NATIONAL TECHNICAL INFORMATION SERVICE, SPRINGFIELD, VIRGINIA 22161

19. Security Classif. (of this report)	20. Security Classif. (of this page)	21. No. of Pages	22. Price
Unclassified	Unclassified	198	

Form DOT F 1700.7 (8-72) Reproduction of completed page authorized

PREFACE

This report brings together the results of ten years of research on the behavior of propagating fatigue cracks in railroad rails. The research is sponsored by the Office of Research and Development of the Federal Railroad Administration (FRA) as a part of the FRA Track Safety Research Program. The program objective is to develop technical information which can be used to support rational criteria for the preservation of safe operations on railroad tracks. The research is managed and in part performed by the DOT Transportation Systems Center (TSC) as the FRA/TSC Rail Integrity Project.

The Rail Integrity Project has benefitted from useful contributions by many railroad industry organizations, independent research laboratories, and universities. The American Railway Engineering Association (AREA) provides the experience of active railroad chief engineers to steer the project under the auspices of the AREA Ad Hoc Committee on Track Performance Standards. The Atchison, Topeka, & Santa Fe, Bessemer & Lake Erie, Boston & Maine, Burlington Northern, Chessie System, Kansas City Southern, Norfolk Southern, Southern Pacific, and Union Pacific railroads have donated test rails, provided revenue track test sites, and shared rail defect report records to support the project. The Association of American Railroads (AAR) has made major contributions through its management of rail integrity experiments at the Transportation Test Center and with laboratory tests and analytical work at the AAR's Chicago Technical Center. The project has also benefitted from exchanges of technical information with the Office of Research and Experiments of the International Union of Railways.

The Battelle Columbus Laboratories have made numerous laboratory research contributions, most notably in the advancement of experimental techniques for measuring rail residual stress. Arthur D. Little, Inc., has developed preliminary fracture mechanics models of bolt hold crack and vertical split head defects. Other independent laboratories which have contributed to the project include: Ensco, Inc.; Foster-Miller, Inc.; the IIT Research Institute; the Oregon Graduate Center; the Southwest Research Institute; and The Analytic Sciences Corporation.

The Massachusetts Institute of Technology has made key contributions toward the understanding of load-interaction effects on crack growth in the rail head and in fracture stability analysis of roller straightened rails. Poland's Krakow Technical University has developed a novel computational mechanics method for calculating the residual stresses which repeated wheel contacts create in the rail head. Other academic institutions which have contributed to the project through either FRA or AAR sponsorship include Lehigh University, Northwestern University, Tufts University, the University of California at Los Angeles, and Vanderbilt University.

METRIC CONVERSION FACTORS

Approximate Conversions to Metric Measures

Symbol	When You Know	Multiply by	To Find	Symbol
LENGTH				
in	inches	*2.5	centimeters	cm
ft	feet	30	centimeters	cm
yd	yards	0.9	meters	m
mi	miles	1.6	kilometers	km
AREA				
in^2	square inches	6.6	square centimeters	cm^2
ft^2	square feet	0.09	square meters	m^2
yd^2	square yards	0.8	square meters	m^2
mi^2	square miles	2.6	square kilometers	km^2
	acres	0.4	hectares	ha
MASS (weight)				
oz	ounces	28	grams	g
lb	pounds	0.45	kilograms	kg
	short tons (2000 lb)	0.9	tonnes	t
VOLUME				
tsp	teaspoons	5	milliliters	ml
Tbsp	tablespoons	15	milliliters	ml
fl oz	fluid ounces	30	milliliters	ml
c	cups	0.24	liters	l
pt	pints	0.47	liters	l
qt	quarts	0.95	liters	l
gal	gallons	3.8	liters	l
ft^3	cubic feet	0.03	cubic meters	m^3
yd^3	cubic yards	0.76	cubic meters	m^3
TEMPERATURE (exact)				
°F	Fahrenheit temperature	5/9 (after subtracting 32)	Celsius temperature	°C

*1 in. = 2.54 cm (exactly). For other exact conversions and more detail tables see NBS Misc. Publ. 286, Units of Weight and Measures. Price $2.25 SD Catalog No. C13 10 286

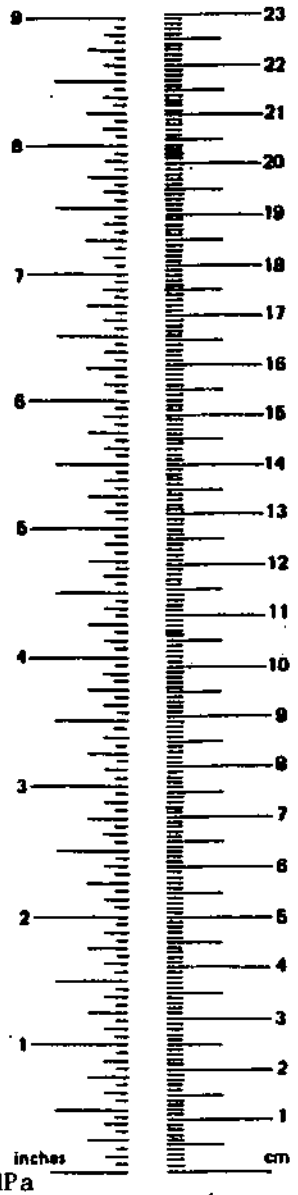

Approximate Conversions from Metric Measures

Symbol	When You Know	Multiply by	To Find	Symbol
LENGTH				
mm	millimeters	0.04	inches	in
cm	centimeters	0.4	inches	in
m	meters	3.3	feet	ft
m	meters	1.1	yards	yd
km	kilometers	0.6	miles	mi
AREA				
cm^2	square centimeters	0.16	square inches	in^2
m^2	square meters	1.2	square yards	yd^2
km^2	square kilometers	0.4	square miles	mi^2
ha	hectares (10,000 m^2)	2.5	acres	
MASS (weight)				
g	grams	0.035	ounces	oz
kg	kilograms	2.2	pounds	lb
t	tonnes (1000 kg)	1.1	short tons	
VOLUME				
ml	milliliters	0.03	fluid ounces	fl oz
l	liters	2.1	pints	pt
l	liters	1.06	quarts	qt
l	liters	0.26	gallons	gal
m^3	cubic meters	36	cubic feet	ft^3
m^3	cubic meters	1.3	cubic yards	yd^3
TEMPERATURE (exact)				
°C	Celsius temperature	9/5 (then add 32)	Fahrenheit temperature	°F

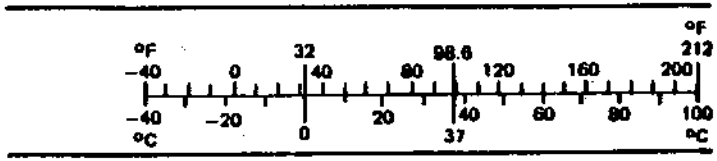

ksi 10^3 lb./in.^{2} 6.895 Megapascals MPa

ksi $\sqrt{in.}$ 1.1 MPa $\sqrt{m}$

TABLE OF CONTENTS

LIST OF ILLUSTRATIONS

LIST OF ILLUSTRATIONS (Continued)

LIST OF TABLES

LIST OF ABBREVIATIONS AND SYMBOLS

A - Projected area of detail fracture; penny crack area; axle center spacing; empirical constant
A' - Corner crack area
A_H - Rail head area
A_R - Rail section area
a - Ellipse semi-major or semi-minor axis; area enclosed by flaw boundary and stress contour
B - Truck center spacing; compact tension specimen thickness; empirical constant
BJR - Bolted-joint rail
B&LE - Bessemer & Lake Erie Railroad
b - Ellipse semi-minor axis
C - Carbon; length over couplers; empirical constant
CTS - Compact tension specimen
C.V. - Coefficient of variation
CWR - Continuous welded rail
c - Ellipse semi-minor axis
c_v - Coefficient of variation
D - Bending stiffness; empirical constant
DMS - Decreasing maximum stress sequence
E - Young's modulus; empirical constant
E_I, E_{II} Complete elliptic integrals of the first and second kind
e - Lateral distance from rail center plane to center of wheel-rail contact
F - Load in compact tension test; empirical constant
FAST - Facility for Accelerated Service Testing
F_T - Thermal force
f - Longitudinal resistance force per tie per rail
f_ℓ - Lateral resistance force per tie per rail
G - Shear modulus; crack geometry and stress distribution function for penny crack or detail fracture model
H - Crack geometry and stress distribution function for CTS
HA - Rail head area
h - Rail height
h_C - Height of rail neutral axis above rail base
h_{CB} - Height of rail base neutral axis above rail base
h_{CH} - Height of rail head neutral axis above rail base
h_S - Height of rail shear center above rail base
h_w - Rail web height
I - Second area moment of rail section or part of section
J - Rail section torsion constant
K - Stress intensity factor
K_C - Fast crack growth stress intensity factor
KCS - Kansas City Southern Railroad
K_{IC} - Fracture toughness
K_{Id} - Fracture toughness under dynamic loading conditions
K_{th} - Threshold stress intensity factor for crack growth
k - Foundation modulus
L - Lateral wheel-rail load; crack growth life
L.F. - Load factor
ℓ - Center spacing between anchored ties; crack length in compact tension specimen or finite-width plate
M - Magnification factor; moment; crack growth life
MGT - Million gross tons (English short tons)
Mn - Manganese
m - Magnification factor; service life fraction
N - Number of stress cycles; exceedance rate

NA - Number of axles per vehicle
n - Number of ties; number of stress cycles; occurrence frequency
P - Probability; cumulative probability; load in four-point bending test; empirical constant
p - Probability density; peak contact pressure
Q - Empirical constant
R - Load ratio; stress ratio; radius of curved track; rail crown radius
RSO - Real sequence order
r - Penny crack radius
r' - Corner crack radius
S - Stress
Si - Silicon
S_R - Average relieved residual stress
S_T - Thermal stress
T - Rail service temperature
T_n - Rail neutral temperature
TTC - Transportation Test Center
t_w - Rail web thickness
UT - Ultrasonic test
V - Vertical wheel-rail load
v - Rail lateral deflection
W - Weight; compact tension specimen width from notch tip to back face
w - Width; rail vertical deflection
x - Longitudinal coordinate axis
Y - Yield strength; flow stress
y - Lateral distance from rail center plane to center of detail fracture; lateral coordinate axis
z - Vertical distance from rail neutral axis to center of detail fracture; vertical coordinate axis
z^* - Vertical distance from unworn rail crown to center of detail fracture

Greek symbols

α - Coefficient of thermal expansion; ratio of longitudinal to vertical stress
β - Inverse of rail bending wavelength; ratio of lateral to vertical stress
γ - Scale factor for vertical stress as a function of depth
Δ - Increment; difference
$\Delta\ell$ - Rail end gap due to thermal contraction
ε - Strain
θ - Angle
κ - Argument of complete elliptic integral function
λ - Dimensionless ratio of rail section properties
ρ - Radius from geometric center to perimeter of ellipse
σ - Standard deviation
ϕ - Angle; angular deflection of rail about rail shear center; Mises-Hencky yield condition

EXECUTIVE SUMMARY

This report brings together the results of ten years of rail integrity research. The objective is to establish estimates for the safe lives of various types of fatigue cracks which form and grow in railroad rails. The results reported herein apply to a type of crack called a "detail fracture." Detail fractures predominate in the crack populations found in modern mainline freight railroad tracks, which are increasingly equipped with continuous welded rail and subjected to the heavy-weight high-density train traffic.

Fatigue is the term used to refer to the action of wheel loads exerted on the rail by passing trains. These loads repeatedly work the rail metal and eventually cause minute imperfections (which are present in any metal) to coalesce into microscopic cracks. Subsequent loads will cause such cracks to enlarge, first slowly but at a rate that increases as the crack is enlarged. If fatigue crack propagation is allowed to continue unchecked, the crack will eventually reach a "critical" size at which the next wheel load will cause the crack to extend rapidly, fracturing the rail into two or more pieces.

A critical crack puts the rail in an unsafe condition because of the risk of derailment associated with rail failure. However, cracks smaller than the critical size can be tolerated as long as they are monitored by means of periodic inspection. The railroads perform such inspections (called rail tests in the industry) with equipment which uses nondestructive ultrasound and/or magnetic induction to search the rail for cracks and other types of defects. Defects reveal their presence by reflecting ultrasound, blocking the transmission of ultrasound, or distorting an otherwise uniform induced magnetic field.

Federal safety regulations require annual testing of rail in tracks carrying freight traffic at speeds faster than 40 mph and/or passenger traffic at speeds exceeding 30 mph. On their own initiative, the railroads test additional trackage and perform two or more tests per year on some lines having high traffic densities. The existing arrangements have developed empirically from past experience but may not properly allocate rail test resources in the now rapidly changing railroad operating environment.

The goal of the rail integrity research project is to provide guidelines for rail test frequencies based on the safe crack growth life concept. For each type of crack and method of rail testing there exists a "detectable" size at which the crack begins to become visible to the test equipment. In most cases the detectable size is smaller than the critical size, and the crack can be said to have a safe life, i.e., the number of wheel passages or train passages required to make the crack grow from detectable to critical size. In order to facilitate comparison of different types of traffic (loaded versus empty, passenger versus freight, etc.), crack growth life is usually expressed in terms of gross tons.

Rail testing achieves its safety objective by providing the means to detect fatigue cracks during their safe life, so that repair or removal can be effected before the rail fails. In general, two or more rail tests per fatigue crack safe life should be performed in order to compensate for the irreducible uncertainties associated with the detection of cracks close to the detectable size and with the estimation of safe life by means of an approximate model using imprecise environmental data.

The behavior of detail fractures in rails was studied by means of field experiments and observations, laboratory tests, and mathematical analyses. These three elements of research were organized as a coordinated program, in which the experimental results were used to validate mathematical models which were in turn used to fill in the gaps between experimental results.

In field experiments and observations at the Transportation Test Center and some revenue track sites, rails known to contain detail fractures were placed or left in track for varying periods to provide several data points consisting of measured detail fracture growth lives associated with descriptions of the environmental factors believed to affect the rate of crack growth. The experimental measurements were generally accurate and nearly complete for tests performed under the relatively well

controlled conditions available at the Transportation Test Center. The data from revenue track sites was generally less accurate and much less complete, but still served a useful role in the overall research program. In addition to the crack growth experiments, full scale static tests were performed to determine the breaking strengths of rails containing detail fractures. The field experiments and observations demonstrated that detail fractures do grow slowly (i.e., the safe life concept is valid) in a wide variety of service conditions. A few service conditions were identified as producers of rapid growth and safe lives too short to deal with by means of periodic rail testing. These were generally extreme conditions that would be expected to occur only infrequently.

Laboratory tests were performed to determine the basic crack growth rate properties of rail steel. The specimens used for such tests have a standard shape that permits the test results from different materials and different trails of the same material to be compared without the complications introduced by differences in the shapes of the structures or cracks encountered in service. Five independent investigations of United States rail steel crack growth rate properties over a period of six years led to results which were highly scattered. The present report demonstrates that the extremes of these investigations lead to detail fracture growth life estimates which differ by a factor of ten. Similar results have been obtained from a similar investigation of European rail steel performed by the Office of Research and Experiments of the International Union of Railways.

The field and laboratory results were correlated by means of a mathematical model of the detail fracture based on the engineering discipline of fracture mechanics. Fracture mechanics treats a crack as an idealized discontinuity, i.e., the surfaces of the crack are assumed to be absolutely flat and to be touching each other when the body is not loaded. Also, the crack is assumed to enlarge uniformly, e.g., a crack which begins as a circular shape remains a circular shape. Real cracks in physical bodies do not conform to these mathematical idealizations. Nevertheless, the idealizations can provide useful approximations for predicting the behavior of real cracks, provided that the model can be validated by comparison of predictions with full scale experiments. In the present case, several fracture mechanics formulae which approximate various aspects of a detail fracture in a rail head were combined to create the mathematical model. The model was found to correlate most of the field tests and observations on both crack growth life and breaking strength of rails containing detail fractures. The life results were correlated by material crack growth rate properties from the middle of the range defined by the five independent laboratory studies.

The mathematical model was then used to study the sensitivity of detail fracture crack growth to variations of nine vehicle, track, and other factors which describe the environment for a detail fracture in a rail in service. These factors are:

Vehicular

- Train consist and average axle load
- Dynamic effects of car motions and wheel defects

Track

- Curvature
- Foundation quality
- Rail section
- Rail residual stress

Other

- Thermal tension in continuous welded rail (CWR)
- Location of wheel contact on the rail running surface
- Location of detail fracture in the rail head

The three most influential factors were found to be thermal tension, track curvature, and residual stress.

Strings of CWR are placed in thermal tension when the rail cools below its installation temperature because the string is restrained against natural shrinkage. CWR is generally installed when the rail temperature is between 70 and 90 degrees Fahrenheit. The thermal stress at any later time is generally proportional to the difference between the installation temperature and the rail temperature at the time of interest, although the track will adjust and decrease the stress to some extent.

The results of the study show that the safe crack growth life of a detail fracture becomes much shorter as the percentage of night and/or winter traffic tonnage increases. For example, the safe crack growth lives corresponding to unit coal train traffic on a heavy rail section in tangent track subjected to typical northern Great Plains weather were estimated to be 316 million gross tons (MGT) for 100 percent daytime operations, 60 MGT for equal day and night traffic densities, and 33 MGT for 100 percent night operations.

The strong influence of track curvature arises from the increased lateral loads which trains exert on curved track. These effects generally appear on the curve high rail. The results of the study show that the safe crack growth life of a detail fracture in a curve of 3 to 6 degrees is about half the life of a similar defect in comparable tangent track.

Residual stress is one of the by-products of metalworking by repeated wheel contacts. The pattern of residual stress in the rail head is complex and not yet fully understood. The available experimental results show that residual tension exists in that part of the rail head where detail fractures form and begin to grow. The results also suggest that residual stress may be increased in curve high rails (relative to tangent track), high strength rails (relative to standard strength rails), rails which are roller straightened immediately after manufacture to meet tolerances for use in CWR strings, and/or increases in axle loads above the current maximum permitted by U.S. freight railroad interchange rules.

The results of the study show that residual tension drives the growth of a detail fracture in much the same way as thermal tension. In one field observation from test track, a rail which suffered an early failure from a detail fracture was found to have three times the typical residual tension measured in other rails. The sensitivity study showed that a factor of three increase in residual stress leads to a factor of five decrease in safe crack growth life. The available data is not sufficient to determine whether or not the factor of three increase in residual stress was an isolated case. Further experiments and full-scale laboratory tests are required to gain a better quantitative understanding of the range of residual stress which should be expected in typical service conditions.

1. INTRODUCTION

The Federal Railroad Administration's track safety research program includes a rail integrity project. The objective of the project is to identify practical approaches to the reduction of derailments caused by rail failures. Rail defects originating from mill practices, construction or maintenance actions, or metal fatigue are the sources of rail failures.

Piped rail, transverse fissures, and compound fissures are examples of mill defects. Piped rail results when a center seam created by ingot shrinkage is incompletely fused during hot rolling. The fissure type defects result when improperly controlled cooling or vacuum degassing leaves excess hydrogen in the steel; the hydrogen diffuses to grain boundaries, where it collects as flakes and promotes fissure formation by local intergranular cracking.

Strings of continuous welded rail (CWR) are joined in the field by means of custom designed thermite weld kits. Similar kits and other field welding methods are also used to repair certain localized types of rail defects. Sand-pocket or lack-of-fusion defects can occur in these welds, and are classified as construction or maintenance-related defects.

Fatigue defects generally cannot be ascribed to any specific deviation from practice that could have been identified and corrected during fabrication or maintenance. Fatigue defects form at random times and random locations, but the behavior of a population of defects in a population of rail can be described in terms of probability models [1]. These models display a smoothly increasing rate of defect formation as tonnage is accumulated on a population of rail. Actual rail populations do follow such trends in the aggregate, but complex interplay of track characteristics, vehicle-track interactions, and maintenance tend to make the actual defect rates fluctuate. Studies of railroad defect reports suggest that fatigue defects tend to concentrate in some stretches of track [2], where a given rail population may be small enough to allow such fluctuation.

These same studies also show that the population of rail defects is dominated in the long term by three types of fatigue defects: detail fractures, bolt hole cracks, and vertical split heads. Detail fractures are transverse internal defects located in the rail head and are commonly reported in terms of a percentage of the rail head cross sectional area preceived by ultrasonic testing to be cracked. Bolt hole cracks emanate from holes drilled in the rail web to accommodate joint hardware and are commonly reported in terms of length from the hole. Vertical split heads are longitudinal internal defects in the rail head and are commonly reported in terms of total length. Detail fractures are of particular consequence to modern mainline track, which is increasingly being upgraded to CWR. The experience to date suggests that detail fractures are the single dominant component of the rail defect population in CWR.

The objective of the work reported here is to provide the means for estimating the safe crack growth life of a detail fracture in a variety of track, territorial, and operational environments. In the present context, safe crack growth life means the gross tonnage that would be required to cause a detail fracture to grow from a defined "detectable" size to its critical size under nominal conditions.

Detectable size is related to inspection technology and is taken as a size at which a single inspection has some chance of finding the defect. For current rail inspection technology, the detectable size of a detail fracture is taken to be 10 percent of the rail head area (%HA). Experience suggests that current ultrasonic testing equipment and procedures are able to detect about one out of three 10 %HA detail fractures. Larger defects have correspondingly greater chances to be detected, e.g., 50 %HA and larger detail fractures are likely to be detected at least nine out of ten times.

Critical size is the size at which a defect can be expected to cause a rail failure under the next train. Critical size is determined by maximum stress conditions and thus

depends upon the track, territorial, and operational factors which influence rail stress. A variety of critical crack sizes exists corresponding to the variety of revenue track environments.

Safe crack growth life is the starting point for rational determination of a safe inspection interval. In the present context, safe inspection interval means the amount of tonnage that can be allowed between rail inspections while a reasonable chance to find each defect is still maintained. For example, if two inspections per safe crack growth life with individual probabilities P_1 and P_2 are performed (Figure 1), then the overall detection probability is $P = 1 - (1 - P_1)(1 - P_2)$. It is impossible to guarantee certainty of detection; in practice, the number of inspections per safe crack growth life should be sufficient to achieve $P \geqq 0.99$ under average service conditions.

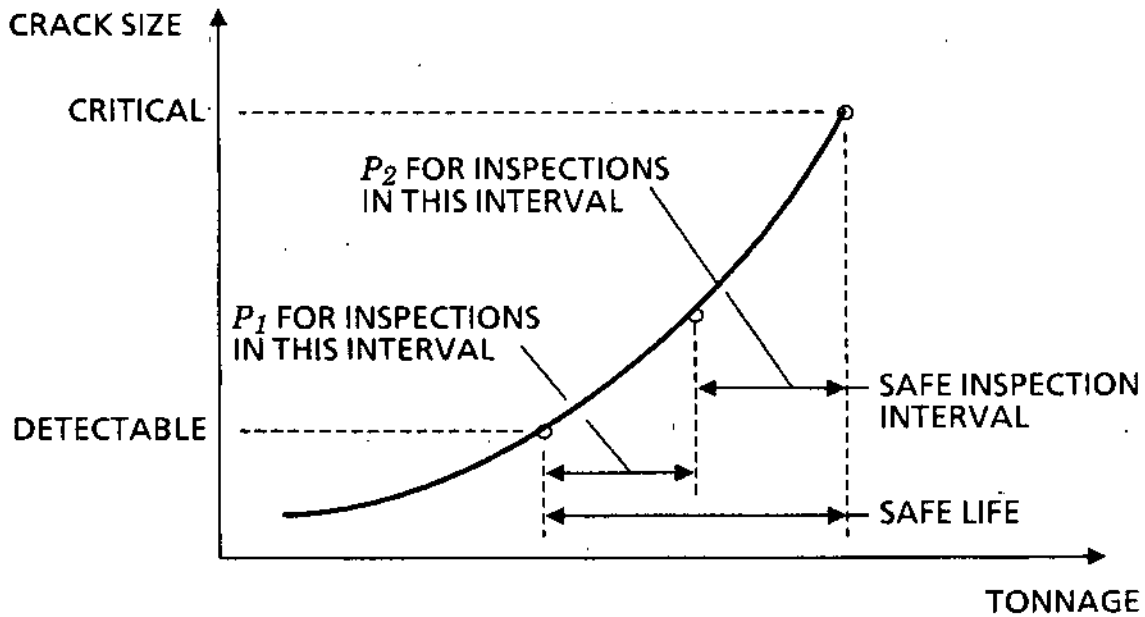

FIGURE 1. SAFE LIFE AND INSPECTION INTERVAL CONCEPTS

The principles of engineering fracture mechanics can be used to estimate safe crack growth life from material crack propagation properties and a description of the fatigue stress environment. A life estimate is commonly given as the number of fatigue stress cycles required to grow a crack from detectable to critical size, based on summation or integration of a rate equation which describes the expected crack size increment per cycle in terms of stress magnitude.

In the present case, the conventions of engineering fracture mechanics have been converted into railroad engineering terms to apply the method to detail fractures growing in rails. The results have been embodied in a computer program for detail fracture safe crack growth life estimation. The program has been validated by comparing its life estimates with actual detail fracture lives measured in a controlled experiment at the Transportation Test Center (TTC) and with other available field and test data on detail fracture behavior [3,4].

This report documents the detail fracture crack growth life calculation model. Section 2 summarizes the TTC experiment and other data on detail fracture behavior. Section 3 explains the crack growth rate equation and its use in relation to basic material properties, varying crack geometry, and service stresses. The specific assump-

tions used to construct an engineering model of the detail fracture are presented. Section 4 explains how service stress environments are constructed and how they are related to railroad engineering descriptions of track, traffic, and territory. Section 5 summarizes the validation of the model and presents results for a variety of typical applications.

2. SUMMARY OF TEST RESULTS

The Atchison, Topeka & Santa Fe, Norfolk & Western, and Southern Pacific railroads collected rails from their revenue tracks for the test program. Each rail contained a detail fracture that had been detected during a scheduled rail inspection. Ten of these rails were installed in a tangent section of the TTC Facility for Accelerated Service Testing (FAST), where they were subjected to FAST train loadings for up to 54.3 million gross tons (MGT) over a six-month period. Six of the ten rails remained in track long enough to provide useful data on detail fracture growth over tonnages ranging up to 53.3 MGT (Section 2.1). Field observations of detail fracture behavior were made in a one-year test of two defects in revenue track on other railroads, and some useful data was collected from two reports of rail failures caused by detail fractures (Section 2.2). About thirty of the collected rails, in addition to the FAST test rails, were tested in the laboratory to determine static strength as a function of defect size (Section 2.3). These test results were previously reported in the open literature [3,4]. All of the test rails were of non-roller-straightened U.S. manufacture and standard composition (Table 1).

TABLE 1. TYPICAL PROPERTIES OF RAIL STEEL ALLOYS.

Alloy	Hardness (BHN)	Yield Strength (ksi)	Ultimate Tensile Strength (ksi)	Composition (Weight %)		
				C	Mn	Si
Standard	255	70	133	0.80	0.90	0.20
Hi-Si	285	75	142	0.75	0.80	0.65
Premium (a)	320 350	93 114	157 175	0.70 0.75	0.65 1.00	0.25 0.70

[a] Ranges shown for three compositions that include various amounts of chromium, molybdenum, and vanadium.

2.1 FAST test results

The FAST experiment was run from mid-June through mid-December 1982. The ten test rails were installed in two CWR strings as shown in Figure 2. Rails SP1, SP10, SP14, and SP22 were removed early for various reasons, and the defects in these rails did not grow enough to provide reliable measurements. The numerical identifications 1 – 6 (Table 2) are used in the sequel to refer to the remaining test rails from which detail fracture growth data was obtained.

During the test period the static wheel load in the FAST consist averaged 30.9 kips. The consist was operated generally between the hours of 5 PM and 5 AM, and the direction of running was reversed approximately once every 1 MGT. The reversal rate is intermediate between revenue operations on double track (infrequent or no reversal) and single track (reversal every few trains). The pattern of reversals on FAST was reflected as a distinctive ridged appearance of the test detail fracture surfaces in the area corresponding to fatigue crack propagation during the test. When a defect was broken open after the test, the ridges were used as boundaries to make direct measurements of the defect size at different points during the test. Each flaw size thus determined was also associated with a cumulative tonnage corresponding to a traffic reversal, starting with the largest flaw size and the last reversal near the end of the test and working backward. Figure 3 and Table 3 summarize these results.

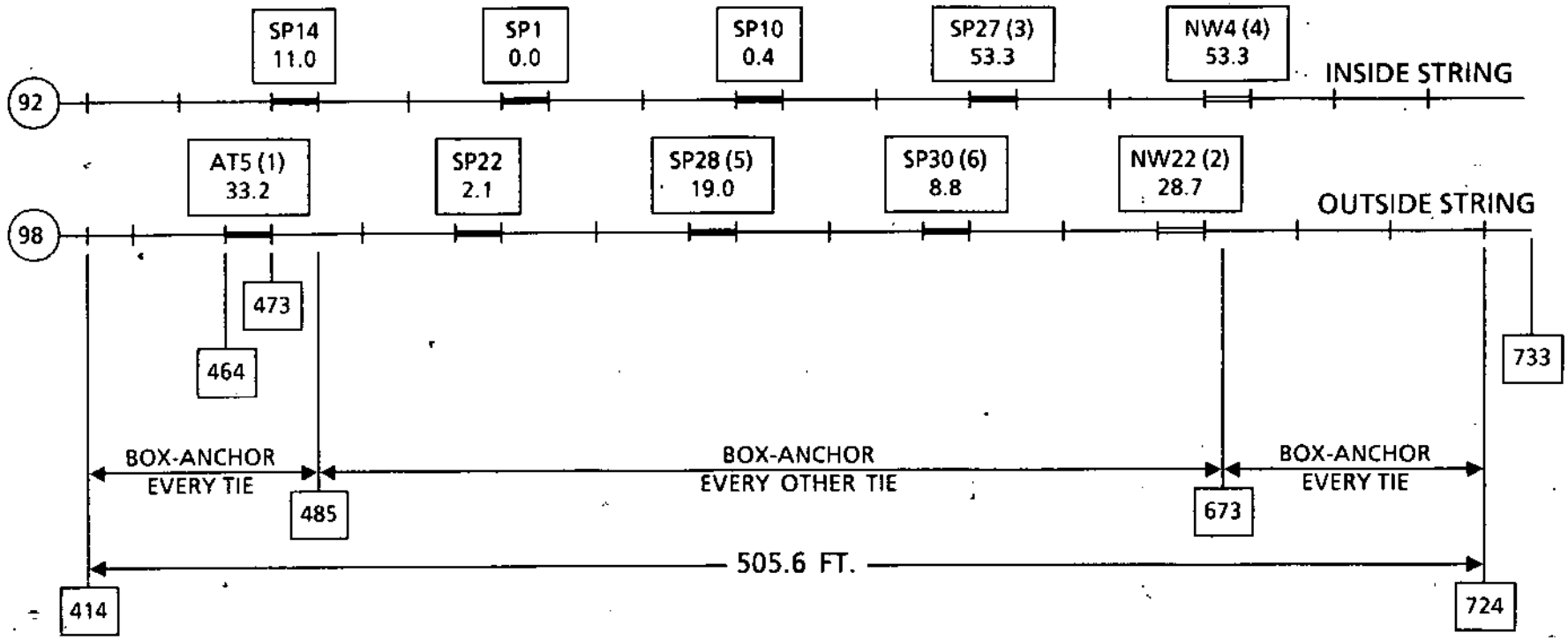

LEGEND:

SPACER RAIL (136 RE SECTION)

TEST RAIL (136 RE SECTION)

TEST RAIL (132 RE SECTION)

AT5 (1) 33.2 ← TEST RAIL (NUMERICAL) IDENTIFICATION
← APPROXIMATE MGT FROM TEST START WHEN RAIL WAS REMOVED FROM TEST

464 ← TIE NUMBER

(98) RAIL TEMPERATURE (°F) WHEN STRING WAS JOINED INTO ADJACENT TRACK

FIGURE 2. INSTALLATION FOR DETAIL FRACTURE GROWTH TEST.

TABLE 2. TEST RAIL IDENTIFICATIONS.

Rail Properties and Prior History	Identification in Figure 3, Table 3, and Text					
	1	2	3	4	5	6
Test I.D.	AT5	NW22	SP27	NW4	SP28	SP30
Rail section	136 RE	132 RE	136 RE	132 RE	136 RE	136 RE
Year rolled	1966	1971	1961	1956	1955	1969
Revenue track location, class, and speed	curve 4 45 mph	curve 3 40 mph	tangent unk. unk.	curve 3 40 mph (a)	unk. unk. unk.	unk. unk. unk.
Revenue MGT	370	462	unk.	462 (a)	unk.	unk.

[a] Since 1971; no information available for 1956-1970.

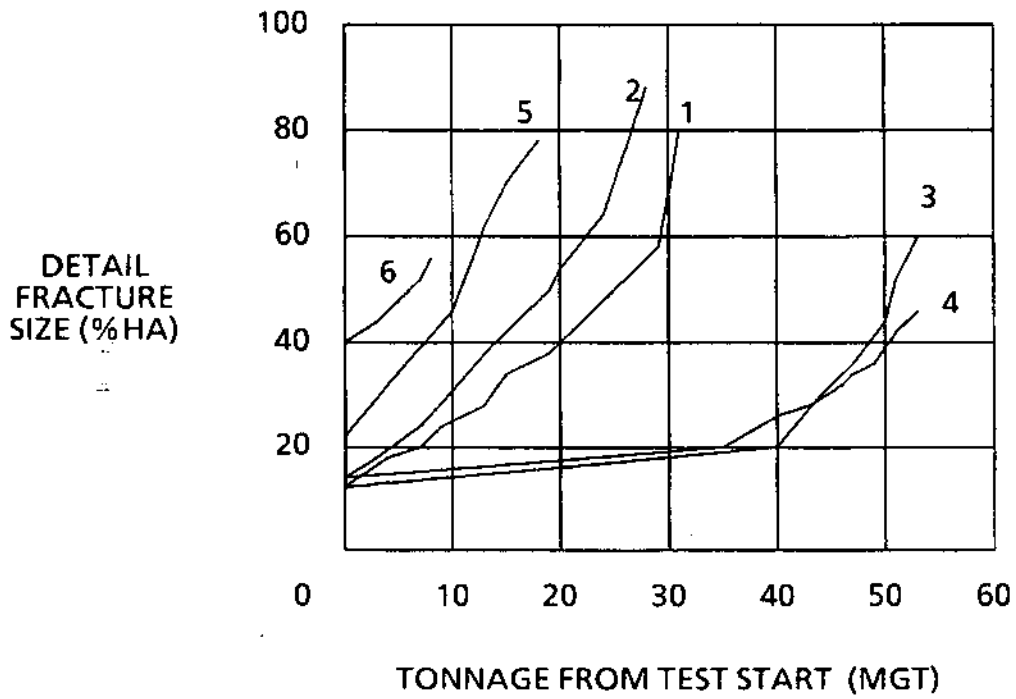

FIGURE 3. DETAIL FRACTURE GROWTH CURVES.

Test rails 1, 2, 5, and 6 exhibited similar rapid crack growth rates, while test rails 3 and 4 exhibited similar slow rates (Figure 2). A section of test rail 1 near the defect was later destructively tested to determine residual stresses (see Section 4.3). Nothing in

TABLE 3. RECONSTRUCTED HISTORIES OF DETAIL FRACTURE GROWTH.

MGT from Test Start	Date	Detail Fracture Size (% HA)					
		1	2	3	4	5	6
0.00	6/7	11.9	14.0	11.4	13.3	23.2	39.3
1.43	7/29	12.6					
2.98	8/2	14.6	18.4				41.4
3.98	8/5	17.5				31.5	44.7
6.98	8/11	19.6					52.5
7.98	8/13		24.7				
8.83	8/16	23.7				45.1	56.7(b)
12.95	8/31	27.6				61.6	
14.80	9/1	33.7	40.5			69.7	
18.98	9/16	37.4	50.0			87.2(b)	
19.90	9/17		54.3				
20.99	9/20	43.0					
24.82	10/1		65.1				
25.82	10/4	50.6					
26.84	10/5		76.7				
27.67	10/6	57.0					
28.73	10/7		88.9(b)				
29.68	10/8	67.1					
33.19	10/20	80.4(a)					
35.22	10/25				20.5		
39.43	11/2			19.1	23.8		
40.09	11/4			21.2	26.0		
43.74	11/17			29.4	28.8		
45.36	11/22			33.0	31.5		
47.49	11/26			36.4	34.1		
49.58	11/30			43.4	36.7		
51.17	12/2			51.5	41.8		
53.31	12/7			61.0(c)	45.9(c)		

[a] Removed after rail failure under train. [b] Removed to avoid rail failure.
[c] Last measurable ridge associated with 53.31 MGT traffic reversal.

the basic properties or prior histories of the rails could be found to account for the difference between the two groups. Test rails 3 and 4 were located in the inside string, however, which was joined to the track at a rail temperature 6 °F lower and was disturbed more by early rail removals than the outside string.

Post-test measurements were also made to determine the approximate shape and center location of the cracked area for as many different ridge boundaries as could be unambiguously characterized as compound ellipses. Figure 4 illustrates the conventions for the ellipse semi-axes *a*, *b*, *c* and center location coordinates *y*, *z**. Depth below the unworn crown, *z**, was chosen in preference to height above the neutral axis, *z*, despite the fact that rail stress due to vertical bending is proportional to *z*. The reason for choosing *z** as a flaw characterization parameter is that detail fractures form as a result of wheel-rail contact stress, which scales with depth below the running surface.

Table 4 summarizes the measurement results. The average and standard deviation for each parameter is given for each of several data groups covering different ranges of flaw size. The data covers defects from 11 %HA to 45 %HA in 132 RE and 136 RE rail. The measurement scheme was checked by calculating the area of each compound ellipse and comparing the result with the actual area measured by planimeter. The calculated areas were found to be within the bounds of about ± 10 percent error. Defects larger than 50 %HA were found to have boundaries too irregular to be classified by this measurement scheme.

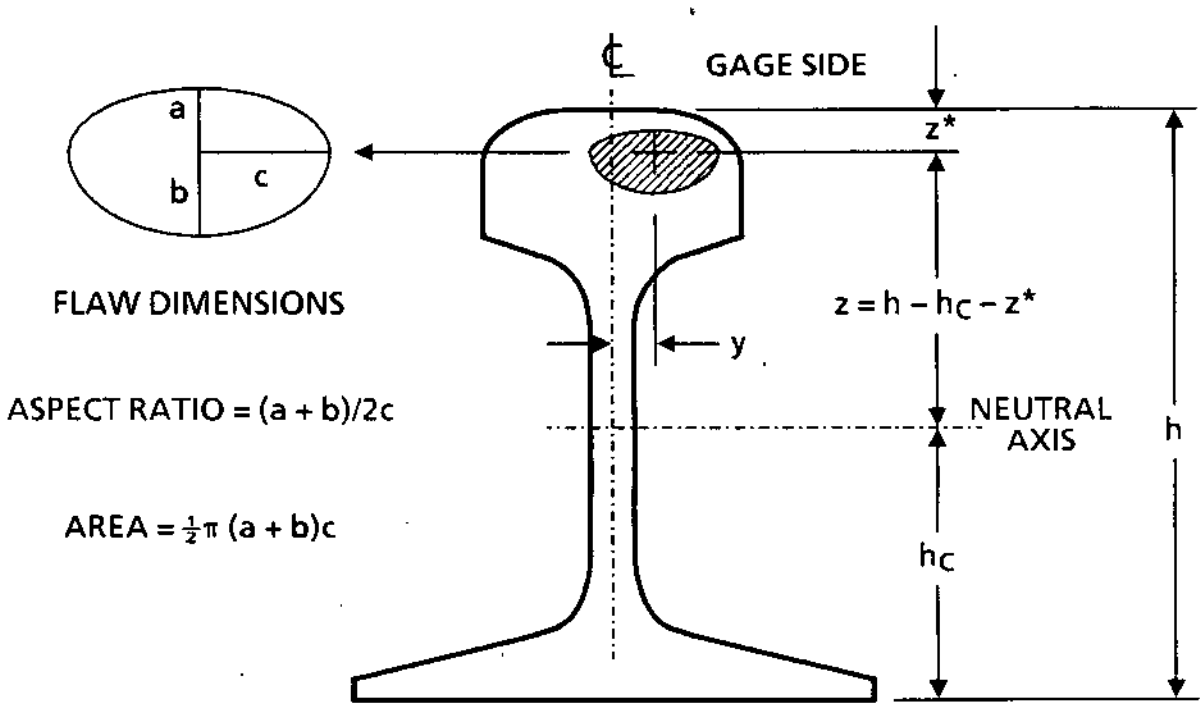

FIGURE 4. CONVENTIONS FOR DETAIL FRACTURE DIMENSIONS AND LOCATION.

The measurement results show that this group of detail fractures has a nearly constant aspect ratio (0.71 with a standard deviation of 0.02, based on the average semi-axis dimensions) in the 11 %HA to 45 %HA size range. However, the center location parameters change as the flaw size changes. Figure 5 illustrates the center location trends. Also shown in the figure are three pairs of parabolic curves which best fit the data in the least-square-error sense: (1) for the aggregate of all data groups; (2) for the measurements made on test rail 1; and (3) for the average of the measurements made on test rails 3 and 4. The aggregate curves will later be assumed to represent the

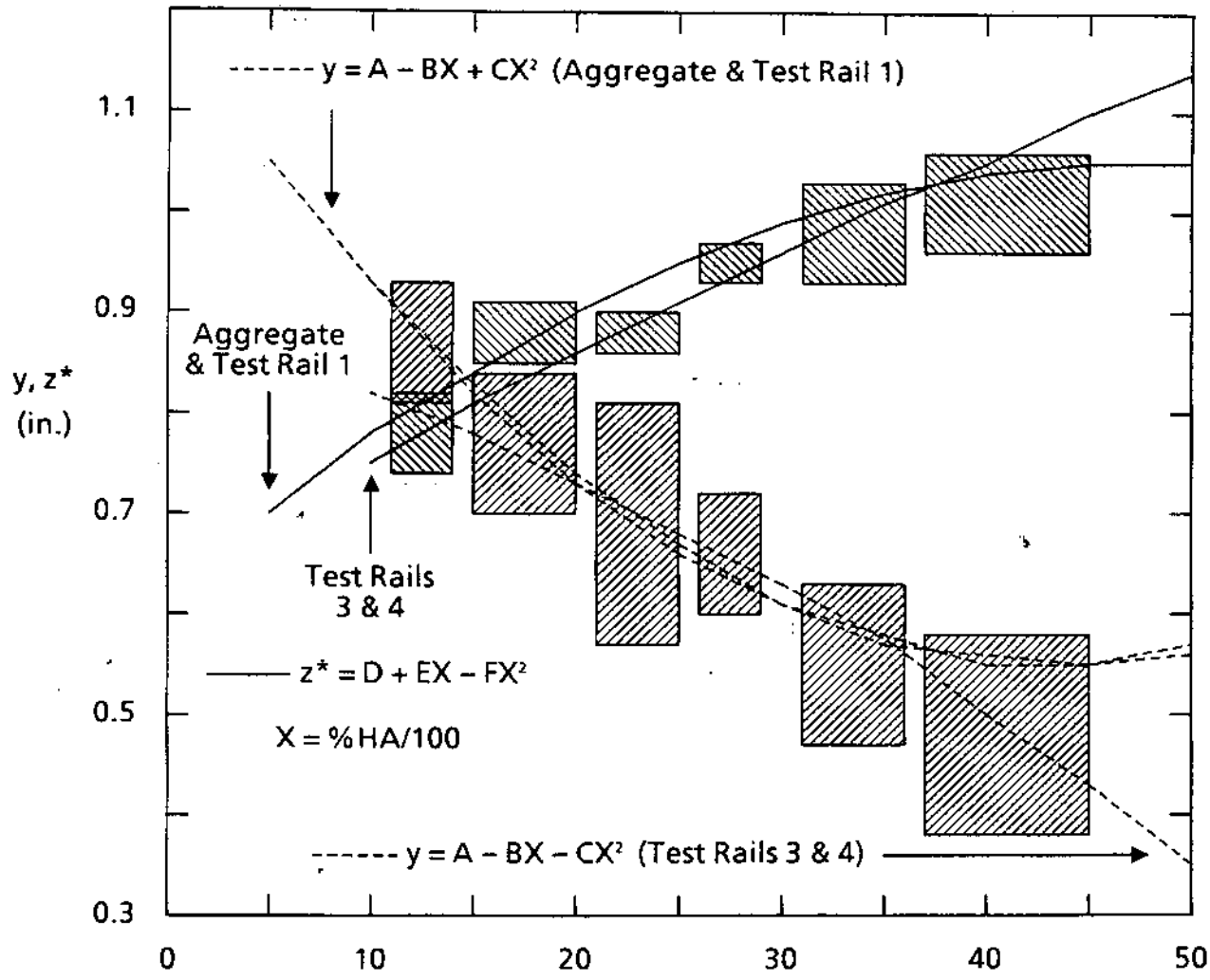

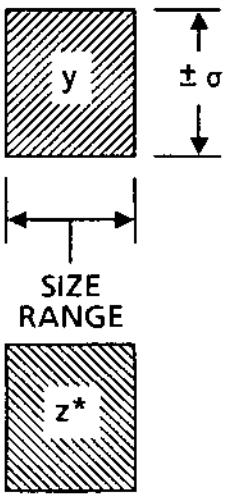

COEFFICIENTS FOR PARABOLIC CURVE FITS						
Data Fitted	A	B	C	D	E	F
Aggregate	1.1874	2.9523	3.4306	0.6213	1.7580	1.7933
Test Rail 1	1.1873	2.9142	3.3321	0.6175	1.7687	1.8004
Test Rails 3 & 4	0.8896	0.5869	0.9723	0.6345	1.1969	0.3829

FIGURE 5. CENTER LOCATION VERSUS FLAW SIZE.

TABLE 4. DETAIL FRACTURE DIMENSION AND LOCATION STATISTICS.

Flaw Size (%HA) (a)	Number of Samples	Measurement Results (inches) (b)				
		a	*b*	*c*	*y*	*z**
11 14	5	0.36 0.04	0.38 0.05	0.52 0.05	0.86 0.07	0.78 0.04
15 20	5	0.42 0.06	0.51 0.03	0.62 0.05	0.77 0.07	0.88 0.03
21 25	6	0.39 0.03	0.58 0.04	0.68 0.06	0.69 0.12	0.88 0.02
26 29	5	0.46 0.04	0.64 0.03	0.76 0.03	0.66 0.06	0.95 0.02
31 36	6	0.48 0.04	0.70 0.08	0.84 0.03	0.55 0.08	0.98 0.05
37 45	5	0.50 0.06	0.78 0.04	0.93 0.07	0.48 0.10	1.01 0.05

[a] Minimum and maximum flaw size in data group.
[b] Average and standard deviation of each measurement.

general population of detail fractures. The curves for test rail 1 are close to the aggregate curves but the curves for test rails 3 and 4 are distinct. The implied difference in effective bending stress might explain the slow growth rate exhibited by the defects in these rails.

The difference between rail neutral temperature T_n and service temperature T can also affect the rate of growth of a detail fracture in CWR. For tangent track, one can reasonably assume that CWR is fully restrained against longitudinal expansion or contraction. The temperature differential then induces a longitudinal thermal stress:

$$S_T = E\alpha(T_n - T) \tag{1}$$

in the rail, where E is Young's modulus, α is the coefficient of linear expansion, and a positive value ($T_n > T$) means tension. For nominal properties of steel, $E\alpha = 0.195$ ksi per Fahrenheit degree.

The inside and outside strings were joined to the track at 92 °F and 98 °F, respectively (Figure 2); these were the neutral temperatures at the start of the experiment. The outside string was thus initially subject to greater thermal tension than the inside string. The early removal of three rails from the inside string (versus one from the outside) is also likely to have caused a more rapid neutral temperature reduction on the inside string. The more rapid growth of the defects in the outside string is consistent with the thermal stress trend, although rail neutral temperature in both strings should have tended to shift toward operating temperature as tonnage accumulated [5].

An indirect estimate of T_n in the outside string was made at 33.19 MGT when test rail 1 failed under the FAST train (Table 3). Following the rail failure, a 1/4-inch gap was

observed between the fracture surfaces when the rail was at a temperature of 38 °F. These observations can be used to estimate the neutral temperature at 33.19 MGT as follows. Each tie to which the rail is anchored is assumed to be able to supply a force up to some value f to resist rail contraction. It is further assumed that the rail will be free to contract, moving the tie, when the limiting resistance value is attained. Before failure the rail is carrying a thermal tension force $F_T = S_T A_R$, where A_R is the rail cross section area. After the failure it is assumed that a number of ties, n, in each direction reach their resistance limit, and that this number is just sufficient to supply a reaction load for the thermal tension in the rest of the string:

$$n = \frac{EA_R\alpha(T_n - T)}{f} \tag{2}$$

Now let ℓ be the center spacing between anchored ties and divide the string into lengths ℓ starting at the broken section. The first such length is stress-free and is thus able to contract by the amount $\alpha\ell\,(T_n - T)$; the second length has an opposing tensile strain f/A_R from the first tie force, and its contraction is accordingly less. The analysis continues to the nth tie, and the individual contractions are then summed to obtain the total contraction:

$$\tfrac{1}{2}\Delta\ell = \ell\left[n\alpha(T_n - T) - \frac{n(n+1)f}{2EA_R}\right] \tag{3}$$

where $\Delta\ell$ is the observed gap. The factor of 1/2 on the left side of Eq. 3 reflects the fact that the expression on the right accounts only for the contraction on one side of the break. Equation 2 can now be used to eliminate n from Eq. 3, which can be solved for the neutral temperature:

$$T_n = T + \frac{1}{2\alpha}\left[\frac{f}{EA_R} + \sqrt{(f/EA_R)^2 + \frac{4f\Delta\ell}{EA_R\ell}}\;\right] \tag{4}$$

The value $f/A_R = 58$ psi was established in a separate investigation by comparing the rail-end gaps predicted by Eq. 3 with measurements of joint pull-aparts in extreme cold weather on the Burlington Northern Railroad's Alliance Division, a well drained Class 4 track which was laid with 132 RE CWR at the time. It is reasonable to apply this value to the FAST situation because of the similarity of roadbed conditions. However, the value requires adjustment to account for the difference in cross section area of 136 RE rail (13.35 in.^{2}) versus 132 RE rail (12.95 in.^{2}):

$$\frac{f}{A_R} = 58 \times \frac{12.95}{13.35} \approx 56.3\ psi \tag{5}$$

The average tie spacing in the test section can be estimated from the length of rail between ties 414 and 724 (Figure 2):

$$\ell = \frac{505.6\ ft. \times 12}{724 - 414} \approx 19.6\ in. \tag{6}$$

As can be seen in Figure 2, however, only a short length of the string (71 ties) around test rail 1 was anchored at every tie while the remainder of the test section was anchored at every other tie. Thus, the effective spacing for resistance to contraction would be 39.2 inches for most of the string, and both spacings must be analyzed.

Application of Eq. 4 yields $T_n = 62$ °F if the nominal tie spacing is assumed or 55 °F if the effective spacing 2ℓ is assumed. Tighter bounds can be obtained by applying Eq. 2 to estimate the number of ties that develop the full resisting force in each case; one thus finds $n = 83$ and 59 ties, respectively, and average effective spacings can be estimated from:

$$\ell_{AV} = \frac{71 \times 19.6 + (2n - 71) \times 39.2}{2n} \quad (7)$$

The results are $\ell_{AV} = 30.8$ and 27.4 inches, respectively. Applying Eq. 4 again then leads to estimates of about 57 and 58 °F, respectively. It is then reasonable to take 57.5 °F as the neutral temperature for the outside string at 33.19 MGT.

The decline of neutral temperature between the start of the test and 33.19 MGT can be estimated based on the results of track buckling research [5], which suggests that traffic reduces the initial neutral temperature during roughly the first 10 MGT after destressing. Table 5 summarizes the assumed neutral temperature shifts for both strings, based on the track buckling research experience and the available data points.

TABLE 5. ASSUMED NEUTRAL TEMPERATURE HISTORY.

MGT (a)	Date	T_n (°F)	
		Inside string	Outside string
0.0	6/7	92.0	98.0
2.3	7/31	80.0	80.0
12.95	8/31	57.5 (b)	57.5 (b)

[a] Cumulative tonnage from test start.
[b] Neutral temperature remains constant to end of test.

The TTC routinely compiles daily high, low, and mean ambient temperature data for use by all experiment managers. Monthly averages of these statistics were calculated to provide a summary description for the June-December 1982 test period. Table 6 presents these statistics together with the cumulative tonnage from the start of the experiment to the end of each period.

2.2 Field observations of detail fracture behavior

In addition to the FAST experiment, parallel revenue track tests were performed on the Bessemer & Lake Erie (B&LE) and the Kansas City Southern (KCS) railroads. A detail fracture in a 131 RE rail was located in tangent CWR track on the B&LE Erie Branch and was monitored for one year by ultrasonic hand testing (UT). The branch line carried about three unit ore trains per week at medium speed during the test period. Less than 2.5 MGT were accumulated while the defect was monitored, and the UT results showed no trend, suggesting that the amount of growth was less than the equipment resolution capability. Based on the UT results, the flaw size was estimated to lie in the range of 19 %HA to 48 %HA. The most useful observation from this test was the absence of rail failure despite cold weather operations on CWR. The roadmaster measured rail temperatures as low as 14 °F during the test period.

TABLE 6. FAST TEST THERMAL HISTORY.

Period	MGT (a)	Monthly Averages of Daily Temperatures (°F)		
		High	Low	Mean
June-July	2.3	87	54	70
Aug.-Sept.	23.8	82	53	68
October	36.6	65	32	48
November	48.5	52	21	36
December	53.3	44	19	32

a From test start to end of period reported.

A detail fracture in a 127 DY rail was located on the KCS mainline between Kansas City and Pittsburg, Kansas, and was monitored for one year by UT. The defect was located in bolted-joint rail on tangent track carrying a mixture of unit train and general freight traffic. At the end of the test period the defect was removed to the laboratory and broken open. A physical measurement of the defect area was made and the ratio of the actual area to the last UT estimate was used to scale the intermediate UT readings. A section of this rail near the defect was also destructively tested to determine residual stress (see Section 4.3). Table 7 summarizes the scaled data, together with the record of cumulative tonnage and rail temperature measurements taken at the time of each UT reading. The rail temperatures in this case are not of direct interest, since bolted-joint rail is not subject to thermal stress. However, the results do illustrate the range of rail operating temperature in revenue service.

TABLE 7. KCS TEST RESULTS.

MGT	Size (%HA)	T	MGT	Size (%HA)	T
0.0	10	---	9.5	29	18
2.5	17	120	15.5	29	38
3.5	17	75	16.0	33	87
4.4	25	74	16.6	33	38
9.0	26	20			

During a search of B&LE lines for suitable test flaws in October 1983, two failed rails that had recently been removed from track were examined. Both failures had resulted from 70 to 80 %HA detail fractures, which had fractured when a section gang applied reverse bending to the rail during tamping operations. The affected rails were 140 RE Curvemaster and had been installed respectively in the 5°30′ entry and 6°00′ reverse of a CWR "S" curve. Review of inspection records showed no prior UT flaw indications, even though the line had carried less than 15 MGT since the last inspection before the rail failures. The observations suggest that these defects grew from 10 to 70 or 80 %HA

within 15 MGT, a rate of growth about twice the rapid rate that was demonstrated for tangent track in the FAST test. This case provides a good benchmark against which models of track curvature effects can be assessed.

A possible case of extreme thermal stress is believed to have been involved in a derailment of a loaded unit coal train in December 1983 on a Burlington Northern line near Trinidad, Colorado [6]. The derailment was caused by failure of a 132 RE section in the high rail of a 6°10' reverse on a downgrade CWR "S" curve. The failure occurred at a detail fracture that had grown in fatigue to only 10 %HA, i.e., what is normally the detectable rather than the critical flaw size. The failure occurred at night when the ambient temperature was – 10 °F. The extremely low ambient temperature suggests the presence of a large thermal tension which could have reduced the critical crack size in this case.

2.3 Static strength of rails containing detail fractures

The KCS and surviving FAST test rails, together with about thirty other rails collected for the test program, were subjected to static reverse bending tests in the laboratory to obtain direct measurements of effective rail strength as a function of flaw size. Each rail was loaded head-down in a four-point bending fixture with the dimensions shown in Figure 6. Breaking strengths P in kips were measured by a load cell. Table 8 summarizes the results. The equivalent rail bending moment is M (inch-kips) = – 13P. When the critical bending moments are combined with the flaw center location measurements (see Figure 5), one obtains another benchmark against which engineering fracture mechanics models of the detail fracture can be assessed.

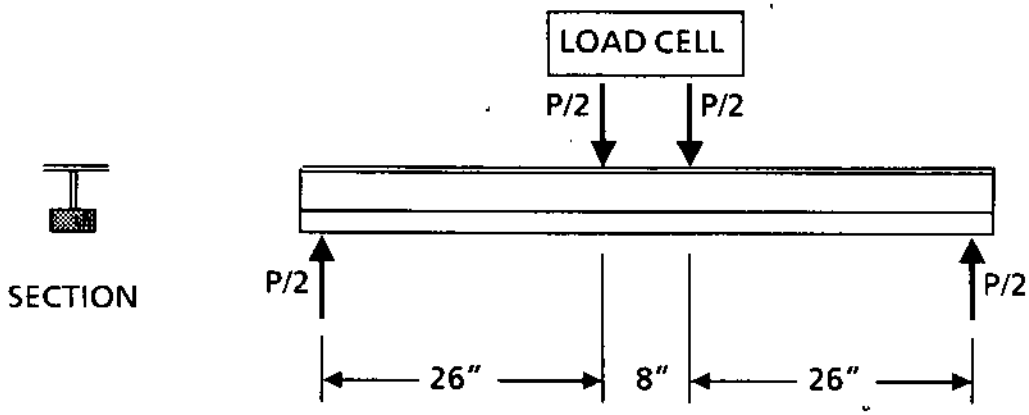

FIGURE 6. SCHEMATIC OF BENDING TEST FIXTURE

TABLE 8. STATIC STRENGTH TEST RESULTS.

136 RE Rails			132 RE Rails		
Test I.D.	Apparent Flaw Size (%HA)	Breaking Load (kips)	Test I.D.	Apparent Flaw Size (%HA)	Breaking Load (kips)
SP6	53	70	NW7	37	97
SP7	78	62	NW8	28	86
SP12	63	52	NW9	22	106
SP15	59	71	NW10	25	86
SP18	24	82	NW12	18	98
SP19	69	53	NW14	25	76
SP31	44	64	NW15	20	108
SP34	44	58	NW16	22	148
SP1	46	52	NW17	25	83
AT4	20	78	NW19	35	80
AT6	13	80	NW1	34	90
SP2	28	73	NW5	3	123
SP27	61 (a)	52	NW13	36	82
SP28	87 (a)	42	NW18	10	88
SP30	57 (a)	30	NW20	58	46
			NW25	26	54
			NW11	54	76
			NW21	18	85
127 DY	Rail		NW4	46 (a)	30
KCS	33 (a)	61	NW22	89 (a)	23

[a] Exact size measured by planimeter

3. CRACK GROWTH RATE EQUATIONS

The effective strength of a structure containing a crack decreases as the size of the crack increases. Engineering fracture mechanics allows the results of laboratory strength tests on cracked specimens to be applied to configurations other than the test specimen by matching the stress intensity factor. A stress intensity factor is the product of an applied stress, the square root of the crack length, and other dimensionless factors that account for crack shape, proximity of the crack to free surfaces, and/or stress distribution shape [7,8]. Handbooks covering a wide variety of configurations are now available [9 – 11].

A crack growth rate equation describes the material behavior observed in constant-amplitude cyclic stress laboratory tests in which visible cracks are grown in fatigue. Just as stress amplitude is used to correlate the results of ordinary fatigue tests, stress intensity factor amplitude or its equivalent can be used to correlate fatigue tests of structures containing slowly growing cracks. The following deals with the expression of rail steel crack growth properties as rate equations (Section 3.1), the extension of such expressions to cover the geometrical effects expected for a detail fracture growing in a rail head (Section 3.2), a method of using the rate equation to estimate safe crack growth life (Section 3.3), and effects that the estimation method does not account for (Section 3.4).

3.1 Basic equations and material properties

The simplest example of an internal crack (and a logical starting point for models of detail fractures smaller than 50 %HA) is the circular penny crack in an unbounded medium. The Sneddon formula [12]:

$$K = 2S\frac{\sqrt{r}}{\sqrt{\pi}} \tag{8}$$

gives the stress intensity factor K for a penny crack of radius r subjected to uniform tensile stress S normal to the crack plane (Figure 7). Also shown is a quarter-circular corner crack of radius r' at the right-angled intersection of two free surfaces of an otherwise unbounded medium. The stress intensity factor for this crack varies along the crack front. The maximum value occurs where the crack front intersects the surfaces; correlation with experimental data has suggested that the maximum stress intensity factor for this case is given approximately by [13]:

$$K = 2.4S\frac{\sqrt{r'}}{\sqrt{\pi}} \tag{9}$$

The quarter-circular crack is a logical starting point for models of detail fractures larger than 50 %HA. For other situations the stress intensity factors for penny and quarter-circular cracks can be expressed in the general form:

$$K = S\,G(r)\sqrt{r} \tag{10}$$

where $G(r)$ is a function that incorporates additional crack geometry and/or stress distribution effects, and where it is understood that r' replaces r in Eq. 10 for the case of a quarter-circular crack.

Material fracture toughness is determined in the laboratory by applying a static load F to a compact tension specimen containing a through-crack of length ℓ (Figure 8). The stress intensity factor for the test specimen is given by [9 – 11]:

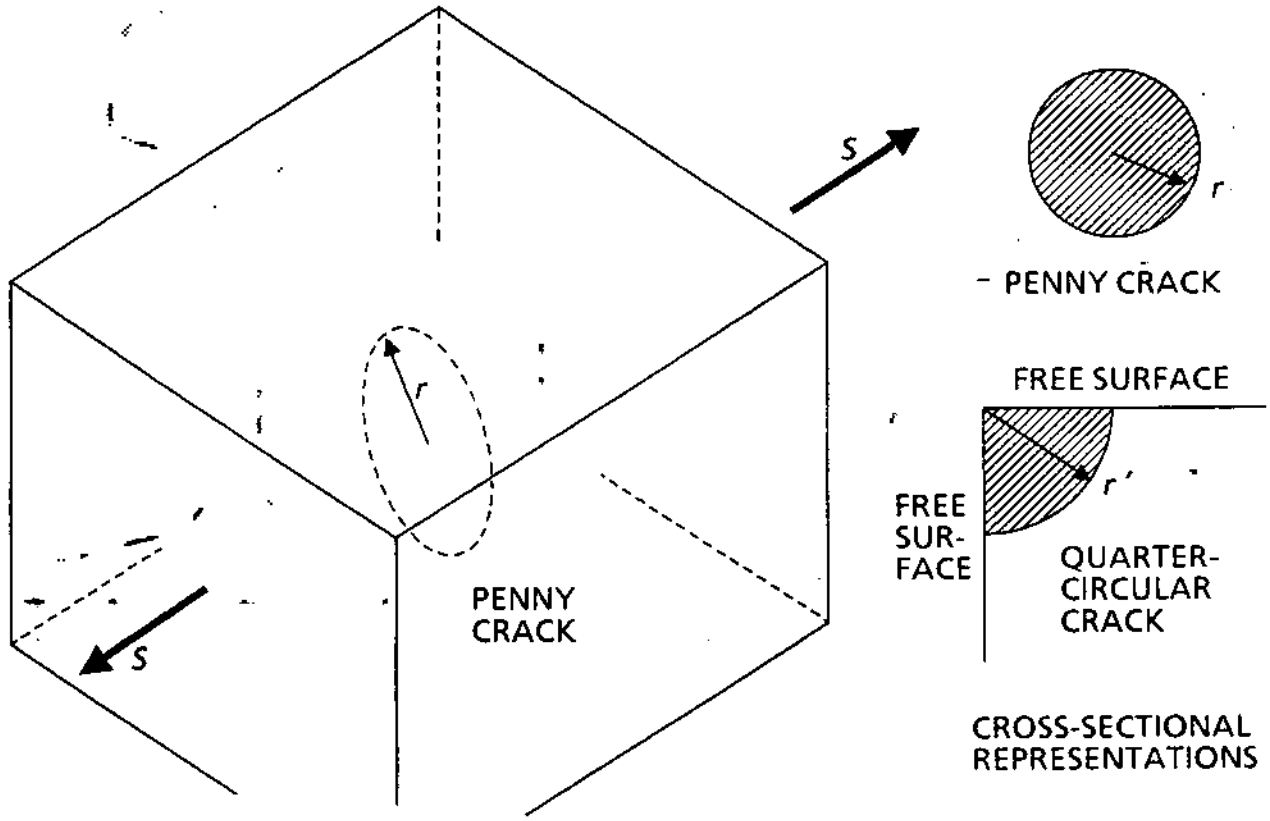

FIGURE 7. PENNY CRACK AND QUARTER-CIRCULAR CRACK.

$$K = \frac{F(2+\ell/W)[0.886+4.64(\ell/W)-13.32(\ell/W)^2+14.72(\ell/W)^3-5.6(\ell/W)^4]}{(1-\ell/W)^{3/2}B\sqrt{W}} = F\,H(\ell) \qquad (11)$$

where B and W are the dimensions shown in the figure. When such a test meets established criteria for the measured load-deflection curve and the crack behavior [14], substitution of the fracture load in Eq. 11 gives the fracture toughness K_{IC} . Values obtained under moderate dynamic conditions are sometimes referred to by the symbol K_{Id} to reflect strain-rate sensitivity. The established values are $K_{IC} \approx 35$ ksi√in. and $K_{Id} \approx 25$ ksi√in. for standard composition rail steel [15,16] (see also discussion in [4]). Substitution of one of these values in Eq. 10 then defines the critical combination of applied stress and crack radius for a penny or quarter-circular crack.

If a compact tension specimen is now subjected to cyclic loading such that the maximum load is less than the critical load, the crack will grow slowly in fatigue. The fatigue stress cycle is described in terms of the stress intensity factor range ΔK and load ratio R:

$$\Delta K = H(\ell)\,\Delta F \;\; ; \;\; R = \frac{F_{min}}{F_{max}} \qquad (12)$$

where F_{min}, F_{max}, and ΔF are defined in Figure 9. Periodic measurements of the crack length and use of Eq. 11 serve to define ΔK and the average crack length increment per

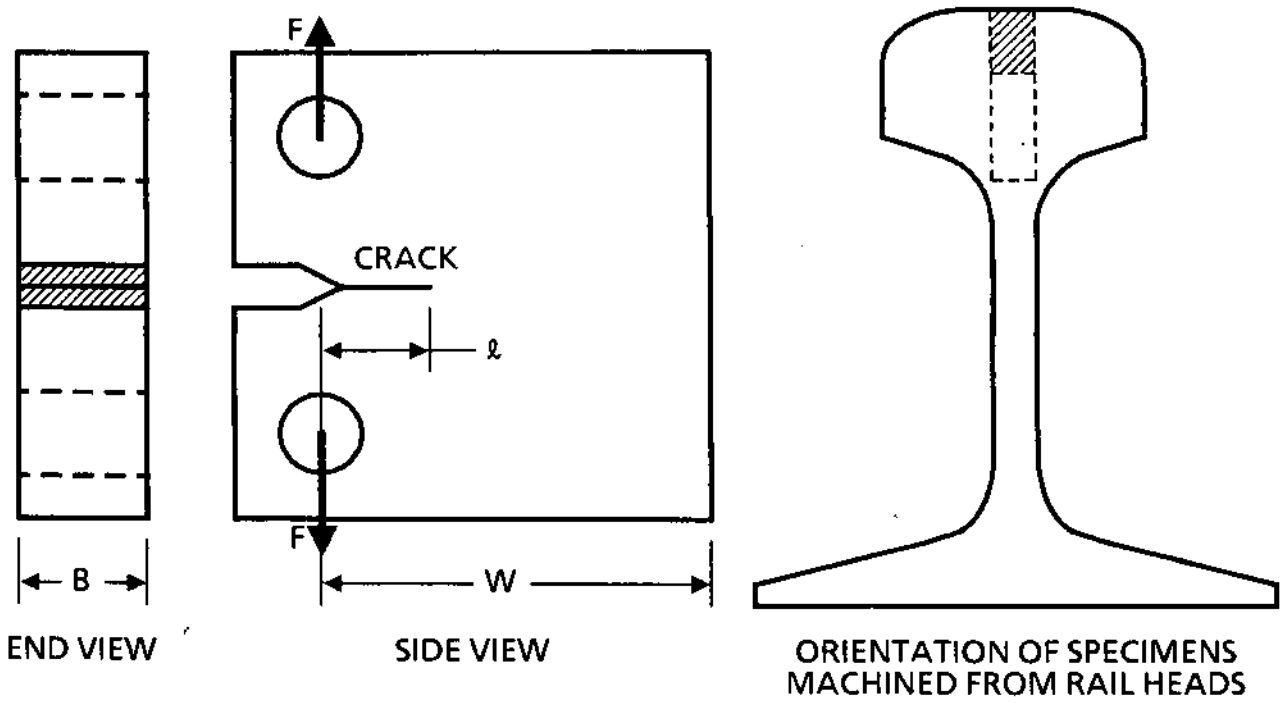

FIGURE 8. COMPACT TENSION SPECIMEN.

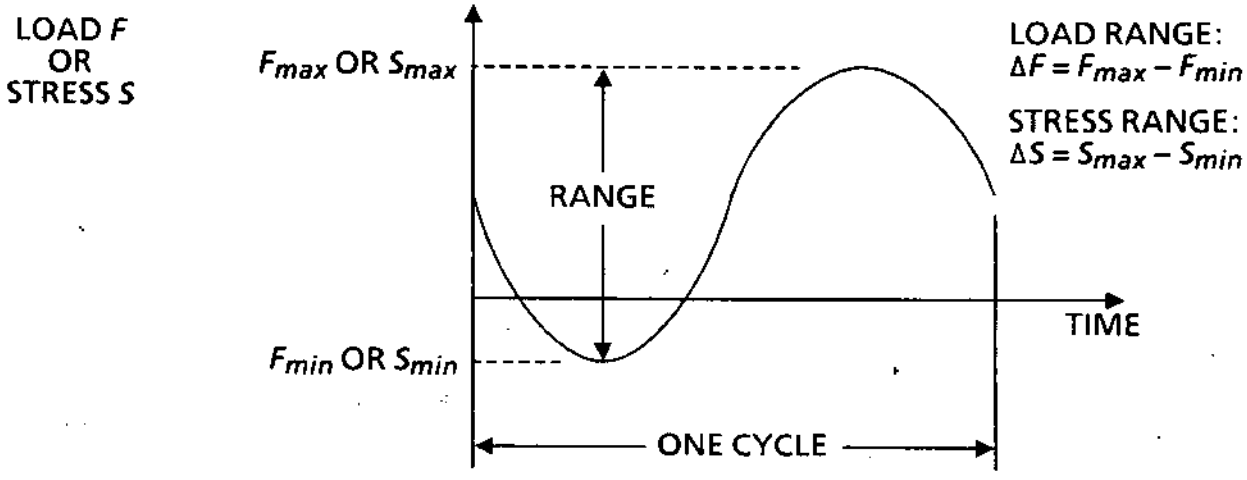

FIGURE 9. DEFINITION OF STRESS CYCLE.

cycle, $d\ell/dn$. The measurements are made over intervals of crack length sufficiently small to warrant the assumption that ΔK is essentially a constant for each data point.

The data obtained from fatigue crack growth experiments can often be described, with some reservations, by rate equations of the general form:

$$\frac{d\ell}{dn} = \frac{C(\Delta K)^P}{(1-R)^Q} \qquad (13)$$

where C, P, and Q are empirically determined constants. Figure 10 schematically compares observed crack growth behavior with the rate model. When $\ell og\,(\,d\ell/dn\,)$ is plotted against $\ell og\,(\,\Delta K\,)$, the test data for a given load ratio tend to fall within an "S"-shaped band defined by a factor of two or less in $d\ell/dn$. Tests are usually performed at $R = 0.05$ and $R = 0.50$ to determine whether high load ratios increase the growth rate. For any given R, Eq. 13 appears as a straight line with slope P on the $\ell og - \ell og$ plot, and the empirical constants are selected to pass the line through the average of the data.

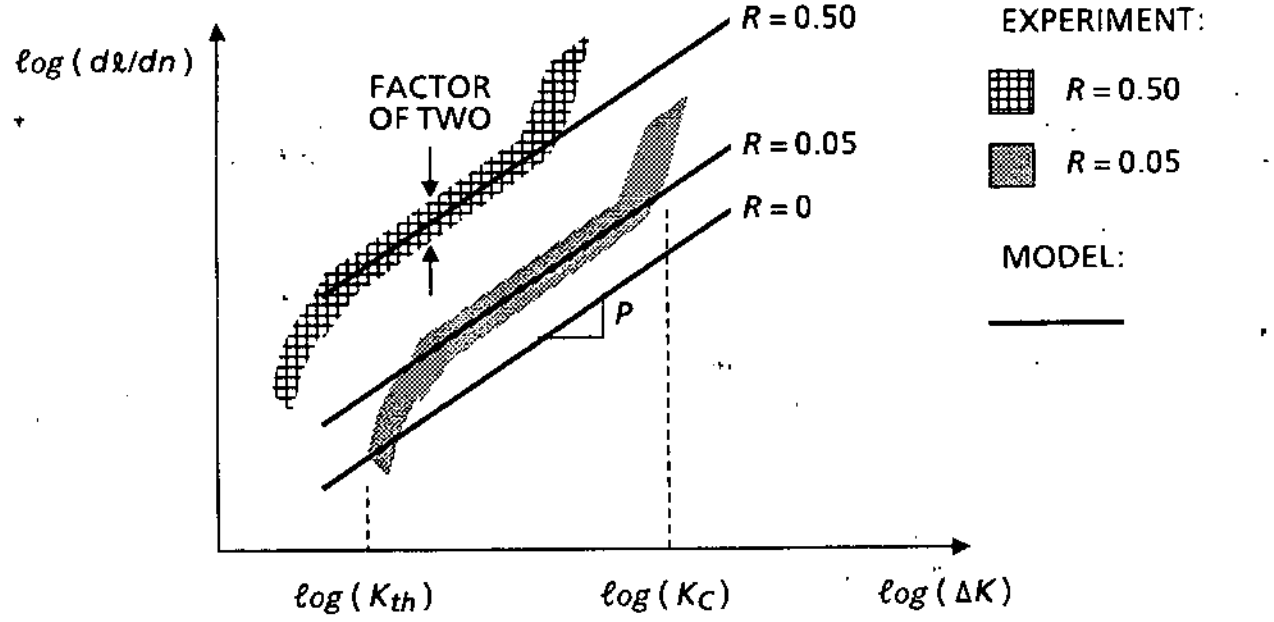

FIGURE 10. RELATION OF RATE EQUATION TO CRACK GROWTH DATA.

Equation 13 accurately reflects the material behavior in the positive-R, slow crack growth regime, but supplementary logic is required to control computer analyses that might apply the model outside this regime. At low ΔK, for example, observed crack growth rates tend to be two to three orders of magnitude smaller than the rates one would extrapolate from the model. The difference is usually accounted for by defining the so-called threshold stress intensity factor, K_{th}, a numerical value of ΔK corresponding to the low end of the $R = 0.05$ data band. In the model, the crack growth rate is either taken to be as given by Eq. 13 or is set to zero if:

$$\Delta K < (1-R)K_{th} \tag{14}$$

This supplementary rule is called sharp threshold cutoff and can also be expressed in the form $K_{max} < K_{th}$.

For similar reasons a fast crack growth stress intensity factor K_C is sometimes defined, and the rate equation itself is modified to make $d\ell/dn \to \infty$ as $\Delta K \to (1\text{-}R)K_C$. Such models can be usefully applied to components that are subjected to large stress ranges and have short lives. However, the modification is not necessary for rails, which are subject to small stress ranges and have long crack growth lives.

The load ratio parameter also requires special attention. A dependence of crack growth rate on R reflects the phenomenon of crack closure. Applying tension opens a crack and also causes the material in a small zone ahead of the crack tip to yield and deform plastically. When the tensile load is released, a part of the plastic zone closest to the crack tip retains compressive residual stress. When the tension is reapplied, part of

the load must be expended to overcome the residual stress before the crack reopens. Since experiments suggest that a crack cannot propagate when closed, only the unexpended portion of the applied load is available to advance the crack. Conversely, the tension is never fully released at high R, and the compression is either smaller or absent. The crack growth rate for a given ΔK can thus be greater at high R than at low R. Elber's crack closure model [17] has demonstrated the validity of these ideas. Elber chose a rate equation of the form:

$$\frac{d\ell}{dn} = C(\Delta K_{eff})^P \tag{15}$$

where ΔK_{eff} is based on the load range $\Delta F_{eff} = F_{max} - F_{op}$ and F_{op} is the crack-opening load. A simplified elastic-plastic analysis based on a line-spring model ahead of the crack tip is used to calculate F_{op}. Since F_{op} is usually greater than F_{min} at low R, ΔK_{eff} is less than ΔK, and the calculated crack growth rate is reduced. The crack closure model can be used to predict $d\ell/dn$ at high R from test results at low R.

The crack closure concept leads one to expect reduced growth rates at negative R, but Elber's model is difficult to apply to such cases. Crack growth tests are also difficult to perform at negative R because the test specimen tends to misalign in the slack condition when the load is changing from tension to compression. Extrapolation of the empirical model, Eq. 13, to negative R is not reliable without confirming data. An alternate procedure is simply to truncate the load or stress cycle, e.g., $\Delta S_{eff} = S_{max}$ and $R_{eff} = 0$ when $S_{min} < 0$ (R-truncation). The R-truncation procedure qualitatively reflects crack closure and is used in the analysis of detail fracture growth.

Five independent investigations of rail steel crack growth properties have been made [16, 18 – 21], and empirical rate models have been fitted to each set of results [4]. The first four groups of investigators performed their tests in laboratory air and reported no R effect (i.e., $Q = 0$ in Eq. 13). The fifth group performed tests in moist air and in vacuo; they found an R effect in moist air but none in vacuo [21]. The previous report on the models [4] incorrectly associated the R effect with the vacuum instead of the moist air environment. Table 9 summarizes the data and model parameters and corrects the error.

The valid data from the laboratory tests sampled 84 service-worn rails of older U.S. manufacture and standard composition. The rate equation constants for models C and D are raw averages of scattered results, and the K_{th} values for these models were assigned by the present authors. Also, model F was assigned $K_{th} = 10$ ksi$\sqrt{\text{in.}}$ instead of the reported value, based on the present authors' judgement that the assigned value better reflects the threshold measurement results.

Comparison of the growth rate constants C in Table 9 suggests a wide range of disagreement between the models. The apparent differences are somewhat misleading, however, since the increase of exponent P with decreasing C tends to compensate. A better comparison is obtained by using the models to calculate life at fixed R and ΔS for a specific crack geometry. The last column in Table 9 shows the relative lives calculated for a penny crack growing from 0.375-inch to 0.65-inch radius at $R = 0$ and $\Delta S = 17.4$ ksi. The crack areas correspond to 10 % HA and 30 % HA detail fractures, respectively, in 132 RE rail; ΔS is the full bending stress range one would expect at 0.5 inch below the crown of a 132 RE rail subjected to one static wheel load from a fully loaded 100-ton car. The factor of 10 in relative life is less than the factor of 18 in C but is still too large to attribute to normal scatter in material properties and test measurements. The comparison is also incomplete, in that it does not distinguish between the presence or absence of an R effect (model F versus model E) and does not assess the effect of different K_{th} values. Under these circumstances, all six models must be compared with the test rail 1 experiment before a choice can be made between them.

TABLE 9. RAIL STEEL CRACK GROWTH PROPERTIES.

Model	Experiment Summary						Model Parameters				Rel. Life
	Ref.	No. of rails tested	Envt.	ΔK_{min} (a,b)	ΔK_{max} (a,b)	K_{th} (a,c)	C (d)	P	Q	K_{th} (a)	
A	16	5	Air	15	50	5.5	13.80 (e)	3.30 (e)	0.00	5.5 (e)	0.35
B	18	5	Air	7	35	7.3	3.70	3.41	0.00	7.3 (e)	1.00
C	19	65 (g)	Air	15	50	---(f)	0.46	5.12	0.00	7.0	0.09
D	20	6	Air	15	40	---(f)	0.76	4.07	0.00	7.0	0.88
E	21	5 (h)	Vacuo	6	40	6.5	1.00	4.00	0.00	6.5 (e)	0.78
F	21	5 (h)	Moist air	6	40	9.0	1.00	4.00	1.63	10.0	0.78

[a] In units of ksi√in.
[b] Smallest and largest ΔK tested.
[c] Measured threshold at $R = 0.05$.
[d] In units of 10^{-11} in.cyc.$^{-1}$(ksi√in.)$^{-P}$.
[e] Parameters reported by investigators.
[f] Threshold measurements not reported.
[g] One duplicate sample and one outlier discarded.
[h] Same five samples.

3.2 Crack geometry effects

Detail fractures are nonplanar, have complex crack-front shapes, and reside in nonuniformly stressed finite bodies with complex boundary shapes. The dimensions and location coordinates of detail fractures also vary from one defect to another and with defect size (Section 2.1). Conversely, basic stress intensity factor formulae characterize planar cracks in uniformly stressed bodies, and well founded adjustments to the basic factors can be derived for only the simplest deviations from these idealized conditions.

Construction of an approximate K model for detail fractures thus requires judicious selection and interpretation of idealized solutions. The penny crack and quarter-circular corner crack stress intensity factors (Eqs. 8 and 9) are logical starting points for detail fracture models. The penny crack can be used to represent internal detail fractures, while the corner crack can be used to represent detail fractures that have broken out to the gage face and running surface of the rail. The transition appears to occur at about 50 %HA; thus, the penny crack model is to be applied to defects ranging from 5 %HA to 50 %HA and the corner crack model to defects ranging from 50 %HA to 80 %HA.

Examinations of detail fracture surfaces also suggest that these defects grow in fatigue primarily as a result of Mode I (tensile) stress, i.e., the longitudinal component

of stress in the rail head. The ridge features observed on the surfaces of the test detail fractures (Section 2.1) suggest that shear stresses also play a role, but a reasonable approach to an engineering fracture mechanics model is to neglect the effects of shear stress and defect nonplanarity on the crack growth rate. It is also appropriate to construct a model that is independent of the crack front shape details. Therefore, the logical basis for relating the model to the defect is the projection of the flaw area on the rail cross section, $A = \pi r^2$ for the penny crack or $A' = \frac{1}{4}\pi(r')^2$ for the corner crack. This choice also has the practical advantage that the area A corresponds to both planimeter measurements of the test defects and, after division by the rail head area, to railroad practice for categorizing detail fractures.

It is now necessary to consider what magnification factors are appropriate to apply to the basic stress intensity factors. Magnification factors for crack shape (Section 3.2.1), nonuniform stress (Section 3.2.2), transition from penny to corner crack (Section 3.2.3), and finite rail cross section (Section 3.2.4) will be discussed. Section 3.2.5 presents a synthesis of the detail fracture model.

3.2.1 Crack shape

Internal detail fractures approximate ellipses in the shape of the crack front (Section 2.1). Therefore, it is worthwhile to consider the effect of the elliptical shape on the stress intensity factor. Let a and b be the semi-major and semi-minor axes of the ellipse, and let θ be an angular coordinate around the perimeter, measured from an origin at the center of the ellipse such that $\theta = 0$ along the semi-major axis and $\theta = \pi/2$ along the semi-minor axis. The stress intensity factor for an elliptical crack in an unbounded body under uniform tension S is given by [22]:

$$K(\theta) = S\sqrt{(\pi b/a)}\,\frac{(a^2\sin^2\theta + b^2\cos^2\theta)^{1/4}}{E_I(\kappa)} \tag{16}$$

where $\kappa^2 = 1 - (b/a)^2$ and

$$E_I(\kappa) = \int_0^{\pi/2} \sqrt{(1 - \kappa^2\sin^2\phi)}\; d\phi \tag{17}$$

is the complete elliptic integral of the first kind [23].

The elliptical crack is fundamentally different from the penny crack in that its stress intensity factor varies with position around the crack front. This poses no problem for strength analysis, since one need only equate $K_{max} = K(\pi/2)$ to K_{IC} or K_{Id} to determine the critical stress for given flaw dimensions. In the case of fatigue, however, Eq. 16 implies that the crack growth rate varies with position around the crack front, i.e., the ellipse aspect ratio b/a should change as the crack grows. Conversely, internal detail fractures appear to maintain a constant aspect ratio (Section 2.1), suggesting that one should average the stress intensity factor around the crack front to deal with fatigue. For this purpose Eq. 16 can be recast in terms of the penny crack stress intensity factor as:

$$K(\theta) = 2M(\theta)S\sqrt{\frac{r}{\pi}} \tag{18}$$

where $r = \sqrt{ab}$ is the radius of a penny crack having the same area as the ellipse and $M(\theta)$ is the shape magnification factor:

$$M(\theta) = \frac{\pi}{2E_I(\kappa)} (b/a)^{1/4} [\sin^2\theta + (b/a)^2 \cos^2\theta]^{1/4} \quad (19)$$

It is appropriate to consider not only the simple average of $M(\theta)$ but also the P^{th} root mean, where P is the exponent of ΔK in the crack growth rate equation. The mean shape magnification factor is defined by:

$$M_S = \frac{\left[\int_0^{2\pi} [M(\theta)]^P \rho \, d\theta\right]^{1/P}}{\left[\int_0^{2\pi} \rho \, d\theta\right]^{1/P}} \quad (20)$$

where

$$\rho = \frac{b}{[\sin^2\theta + (b/a)^2 \cos^2\theta]^{1/2}} \quad (21)$$

is the radius to the perimeter of the ellipse. Equation 20 includes the simple average as a special case ($P = 1$). Table 10 compares this with the root mean third and root mean fifth averages for a range of ellipse aspect ratios. Table 11 summarizes the root mean P^{th} averages applicable to the six crack growth rate models (Table 9) and internal detail fractures ($b/a = 0.7$). The detail fracture model uses $M_S = 0.984$.

TABLE 10. VARIATION OF MAGNIFICATION FACTOR WITH FLAW SHAPE AND STATISTIC.

Ellipse Aspect Ratio, b/a	Magnification Factor, M_S			Ellipse Aspect Ratio, b/a	Magnification Factor, M_S		
	Simple Average	Root Mean 3rd	Root Mean 5th		Simple Average	Root Mean 3rd	Root Mean 5th
0.4	0.875	0.897	0.917	0.7	0.978	0.983	0.986
0.5	0.923	0.938	0.951	0.8	0.992	0.994	0.995
0.6	0.958	0.965	0.972	0.9	0.998	0.998	0.999

TABLE 11. SHAPE MAGNIFICATION FACTORS FOR DETAIL FRACTURES.

Model	A	B	C	D	E and F
P	3.30	3.41	5.12	4.07	4.00
M_S	0.983	0.983	0.986	0.984	0.984

3.2.2 Nonuniform stress

There are four sources of longitudinal stress in the rail head: thermal stress in CWR, wheel-rail contact, rail bending, and residual stresses from cold work. Only the thermal stress is uniform.

The live stresses caused by wheel-rail contact are compressive and decline rapidly with increasing distance from the center of contact when calculated from the Hertz theory of elastic contact between crossed cylinders [24] (the standard railroad engineering practice for estimating wheel-rail contact stress). The longitudinal component of the contact stress is small at the level of a detail fracture center. Live contact stress thus only decreases S_{min} somewhat and likely does not contribute much to the effective stress range for crack growth. Therefore, the effect of live contact stress is neglected in the analysis of detail fracture growth.

Bending stress in the rail head cycles from compression, when a wheel is directly over the transverse plane containing the defect, to tension when the wheel has progressed and the defective section is engaged in reverse bending. There are five contributions to the bending stress (see Section 4.1), of which the two most important are vertical bending about the rail neutral axis and lateral bending about the rail center plane. If one takes S to be the stress due to vertical bending that one would calculate in an uncracked section corresponding to the flaw center location (y,z), then the stress intensity factor for an elliptical flaw of aspect ratio b/a in the combined bending fields [22] can be expressed as the product of Eq. 18 and the stress gradient magnification factor:

$$M(\theta) = \frac{M_V(\theta) + \frac{y}{z}\frac{\beta}{\beta_L}\frac{I_{yy}}{I_{zz}}\frac{L}{V}M_L(\theta)}{1 + \frac{y}{z}\frac{\beta}{\beta_L}\frac{I_{yy}}{I_{zz}}\frac{L}{V}} = \frac{M_V(\theta) + \lambda M_L(\theta)}{1+\lambda} \tag{22}$$

where $1/\beta$ and $1/\beta_L$ are the characteristic vertical and lateral bending wavelengths for the rail on a given foundation, I_{yy} and I_{zz} are the second area moments of the rail section for vertical and lateral bending, L/V is the ratio of lateral to vertical load, and:

$$M_V(\theta) = 1 + \frac{(b/z)\kappa^2 E_I(\kappa)\sin\theta}{(1+\kappa^2)E_I(\kappa) + (1-\kappa^2)E_{II}(\kappa)} \tag{23}$$

$$M_L(\theta) = 1 + \frac{(a/y)\kappa^2 E_I(\kappa)\cos\theta}{(1-2\kappa^2)E_I(\kappa) - (1-\kappa^2)E_{II}(\kappa)} \tag{24}$$

In Eqs. 23 and 24, $\kappa^2 = 1 - (b/a)^2$, E_I is the complete elliptic integral of the first kind (Eq. 17), and:

$$E_{II}(\kappa) = \int_0^{\pi/2} \frac{d\phi}{\sqrt{(1-\kappa^2\sin^2\phi)}} \tag{25}$$

is the complete elliptic integral of the second kind [23].

For 136 RE rail (I_{yy} = 94.9 in.^{4}, I_{zz} = 14.5 in.^{4}) and average wood-tie track (vertical and lateral foundation moduli of 2500 and 2125 psi, respectively), one finds the ratio $(\beta I_w)/(\beta_L I_{zz}) \simeq 4.262$ and:

$$M(\theta) \simeq \frac{1 + 0.233\,(b/z)\sin\theta + 4.262\,(y/z)(L/V)[1 - 0.7302\,(a/y)\cos\theta]}{1 + 4.262\,(y/z)(L/V)} \qquad (26)$$

Table 12 summarizes the *a/y*, *b/z*, and *y/z* ratios for 136 RE rail, based on the aggregate parabolic curves for *y* and *z** in Figure 5. Also shown in the table are values of $\lambda = 4.262(yL/zV)$ for various *L/V* ratios.

TABLE 12. RATIOS FOR CALCULATING $M(\theta)$ FOR DETAIL FRACTURES IN 136 RE RAIL IN TRACK WITH AVERAGE FOUNDATION PROPERTIES.

Flaw Size (% HA)	5	10	20	30	40	50
a/y	0.319	0.508	0.906	1.334	1.694	1.850
b/z	0.072	0.103	0.152	0.192	0.225	0.253
y/z	0.320	0.291	0.240	0.205	0.190	0.195
λ for *L/V* = (a)						
0.05	0.068	0.062	0.051	0.044	0.040	0.042
0.10	0.136	0.124	0.102	0.087	0.081	0.083
0.20	0.273	0.248	0.205	0.175	0.162	0.166
0.30	0.409	0.372	0.307	0.262	0.243	0.249
0.40	0.546	0.496	0.409	0.350	0.324	0.332
0.50	0.682	0.620	0.512	0.437	0.405	0.416

[a] Also $\lambda = 0$ for all flaw sizes when $L/V = 0$.

The same argument can be made for calculating a mean value of the stress gradient magnification factor as was made in Section 3.2.1 for the shape magnification factor. In the present case, however, it is possible for $M(\theta)$ to have negative values along part of the crack front. Negative values mean crack closure and, strictly speaking, that a revised fracture mechanics analysis is required to define the correct stress intensity factor along the open part of the crack front. The mean value can be approximated, however, by defining $M^* = M(\theta)$ for $M(\theta) > 0$, $M^* = 0$ for $M(\theta) \leqq 0$, and calculating:

$$M_G \simeq \frac{\left[\int_0^{2\pi} [M^*(\theta)]^P \rho\, d\theta\right]^{1/P}}{\left[\int_0^{2\pi} \rho\, d\theta\right]^{1/P}} \qquad (27)$$

Similar results can be generated for the corner crack by taking $b = a = r'$, $y = w/2$, and $z = h - h_C$, where w is the rail head width (2.94 in. for 136 RE rail) and $h - h_C$ is the difference between the rail height and the height of the neutral axis above the base

(3.96 in. for 136 RE rail); the upper limit of 2π in Eq. 27 is also replaced by $\pi/2$. These procedures are incorporated in the detail fracture model.

Longitudinal residual stress in the rail head has a complex pattern, the details of which vary from one rail to another (see also discussion in Section 4.3). A common feature emerging from measurements and observations, however, is the existence of residual tension in the region where internal detail fractures grow. The residual tension supplies a driving force for crack growth as it is locally relieved by the increasing crack area. Its effect on the stress intensity factor can be inferred by the method of superposition, which Figure 11 schematically illustrates. The curve marked *S* on the left represents the residual stress distribution in the uncracked rail head. On the right, a crack is assumed to be present and has relieved part of *S*. In the middle is shown the stress that must be added to the intact distribution to produce the net result on the right, viz: a distribution of pressure on the crack surfaces equal in magnitude but opposite in sign to the relieved part of *S*. The example is approximate in that it neglects the possible redistribution of the remaining part of *S*. This approximation is unavoidable without an incremental fracture mechanics solution which can in principle account for stress redistribution as a function of crack size. In practice, such solutions are difficult and time-consuming to calculate, and the worth of such an effort is questionable for an approximate model.

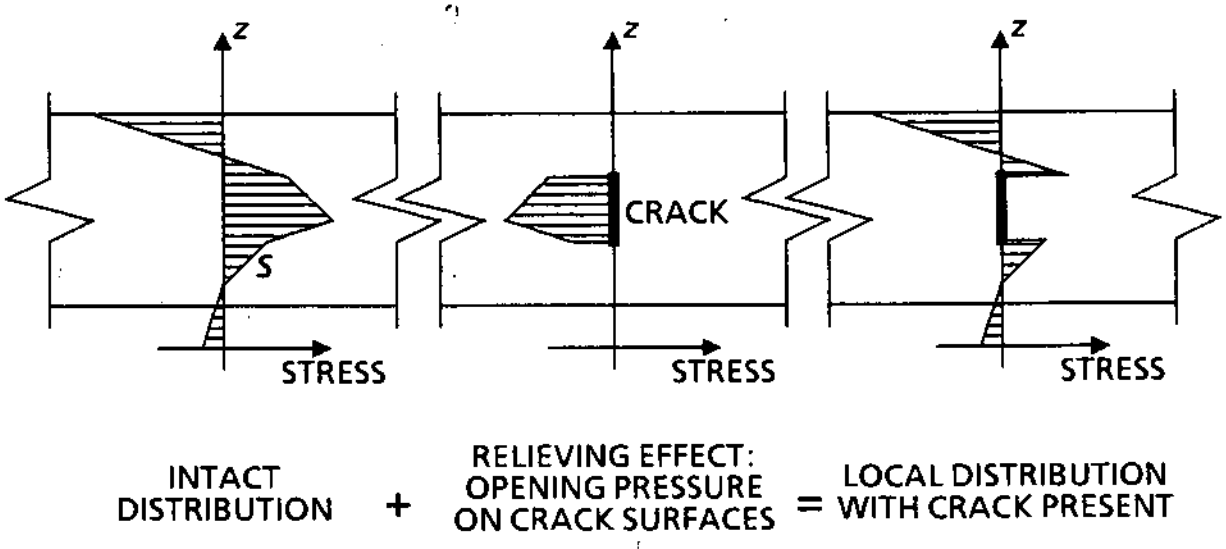

FIGURE 11. SUPERPOSITION METHOD APPLIED TO RESIDUAL STRESS.

A further convenient approximation can be made by averaging the relieved part of *S* over the crack area and using the average, S_R, in place of the distribution. One can then take advantage of the *K* solution for a penny crack subjected to uniform pressure S_R on its surfaces. The form of this solution is identical to Eq. 8, i.e., one can consider the average relieved tension to be just another contribution to the service stress environment. The effect of S_R is like the effect of a constant thermal stress, i.e., it contributes to mean stress and influences the crack growth rate through the stress ratio *R* and/or the threshold (Section 3.1). Also, averaging the relieved tension is a convenient practical way to avoid ambiguities that would arise if one attempted to account for the distribution details. No special magnification factor is required, but S_R is subject to the other magnification factors that apply to uniform stress.

An empirical relation between average relieved residual stress and flaw size was obtained from the experimental data as follows. For test rail 1, the detail fracture boundaries corresponding to 11.9, 33.7, and 80.4 %HA were superimposed on the axial

residual stress contour plot, and the boundary of the 33 %HA detail fracture in the KCS rail (Table 8) was superimposed on a similar plot [4]. For each flaw size A and stress contour S, the area a enclosed by the flaw boundary and the contour was measured with a planimeter.

Intermediate stress values S were linearly interpolated with respect to the enclosed area:

$$S(a/A_H) = C_0 + C_1 \frac{a}{A_H} \tag{28}$$

and the interpolation coefficients C_0 , C_1 were calculated from the measurement results. Table 13 summarizes the coefficients.

For each flaw size A, the average relieved residual stress was calculated by integrating the stress-area interpolations:

$$S_R(A/A_H) = \frac{A_H}{A} \int_0^{A/A_H} \left[C_0 + C_1 \frac{a}{A_H} \right] d\frac{a}{A_H} \tag{29}$$

where the interpolations are extrapolated to the limits as required to complete the calculation. Table 14 summarizes the results. Figure 12 compares the results with the linear empirical relation:

$$S_R = 10 - 12.5 \frac{A}{A_H} \tag{30}$$

which is used in the detail fracture model.

TABLE 13. STRESS INTERPOLATION COEFFICIENTS

Rail	Flaw Size (A/A_H)	Stress Contour (ksi)	Enclosed Area (a/A_H)	Coefficients (a)	
				C_0	C_1
Test rail 1	0.119	10	0.051		
		0	0.115	17.97	−156.25
Test rail 1	0.337	10	0.073		
		0	0.312	13.05	−41.84
		−10	0.325	240.00	−769.20
Test rail 1	0.804	10	0.109		
		0	0.390	13.88	−35.59
		−10	0.742	11.08	−28.41
		−30	0.796	264.80	−370.40
KCS	0.330	15	0.032		
		10	0.124	16.73	−54.17
		0	0.248	20.04	−80.84
		−10	0.292	55.58	−224.22

[a] Each coefficient pair interpolates between preceding and current contours, e.g., $C_0 = 13.05$ and $C_1 = -41.84$ interpolate between 10 ksi and 0 ksi for test rail 1, $A/A_H = 0.337$.

TABLE 14. RESULTS CALCULATED FOR AVERAGE RELIEVED RESIDUAL STRESS

Rail	Flaw Size (A/A_H)	S_R (ksi)
Test rail 1	0.119	8.67
KCS	0.330	4.60
Test rail 1	0.337	5.33
Test rail 1	0.804	−0.48

3.2.3 Crack shape transition

A detail fracture that has broken out to the gage face and running surface conceptually resembles a quarter-circular corner crack, although the actual crack front shape is much more complex and impossible to account for in a simple manner. The left diagram in Figure 13 illustrates the interpretation of the corner crack model. The crack radius r' is chosen so that $A' = \frac{1}{4}\pi(r')^2$ equals the flaw area, and the center point for the nominal stress calculation is located by projection. Although the projected location is physically outside the rail, it is the consistent point for determination of the nominal bending stress to be used in the corner crack stress intensity factor formula.

The middle diagram in Figure 13 illustrates the problem associated with crack shape transition. An internal detail fracture that is close to breakout size should be affected

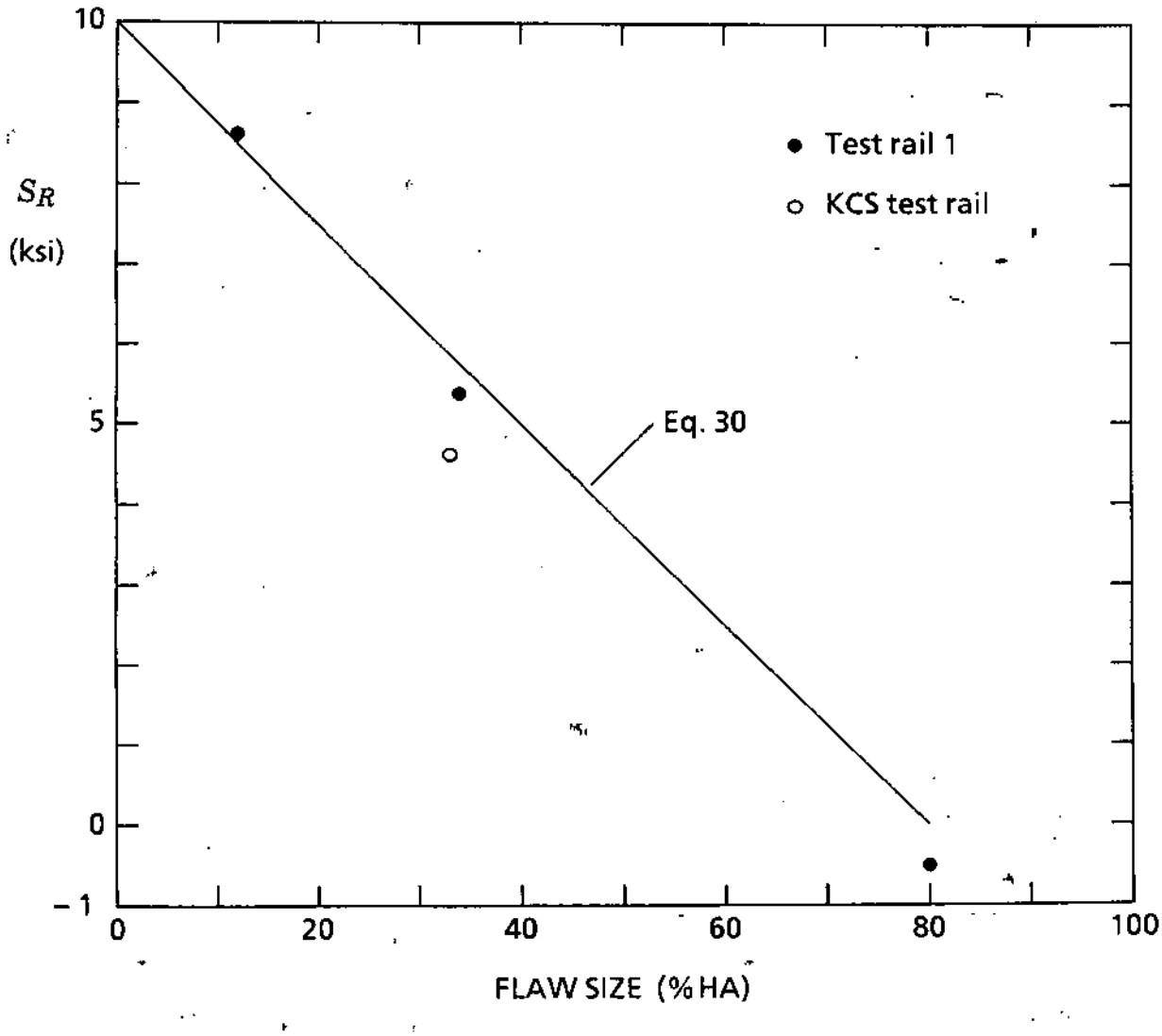

FIGURE 12. COMPARISON OF STRESS RELIEF MODEL WITH CALCULATED RESULTS

by the adjacent free surfaces, as it will be when the crack area increases by a small amount and breakout occurs. Conversely, the corner crack stress intensity factor (Eq. 9) includes the free surface effect as a factor of 1.2 but the penny crack formula (Eq. 8) does not. A fracture mechanics K solution derived for the case of an elliptical crack near a single flat free surface [25] shows that the stress intensity factor is considerably magnified along the part of the crack front closest to the surface. It is difficult to apply this solution to the detail fracture model because of the complex shape of the rail boundary, but some guidance is available from the fact that the authors [25] considered edge distance ratios (equivalent to b/z^*) in the range of 0.4 to 0.9 to be significant. Table 15 summarizes this ratio as calculated from the aggregate z^* parabola in Figure 5, assuming 136 RE rail. The results suggest that magnification should begin to appear when a detail fracture reaches 10 %HA.

A different view emerges from examination of the curves of defect growth in Figure 3. There one can see a tendency for the growth rate to increase between roughly 40 %HA and 50 %HA flaw sizes, suggesting that significant transition magnification begins at 40 %HA. One possible interpretation is that the observed crack growth

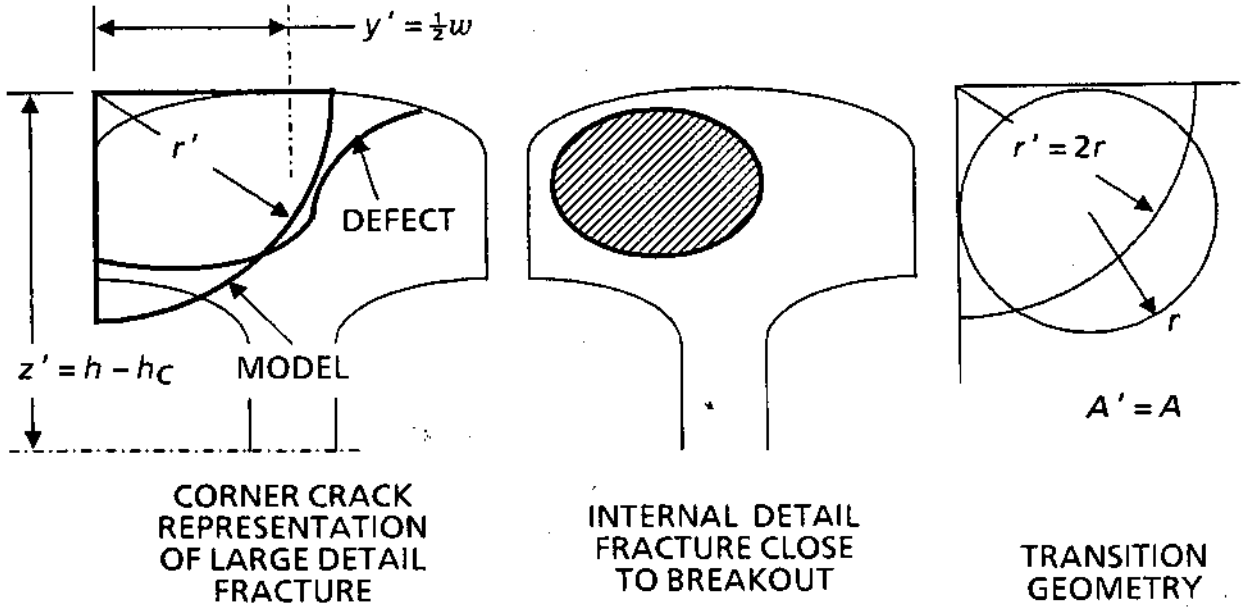

FIGURE 13. TRANSITION FROM PENNY CRACK TO CORNER CRACK.

TABLE 15. EDGE DISTANCE FACTORS FOR DETAIL FRACTURES IN 136 RE RAIL.

Flaw Size (%HA)	5	10	20	30	40	50
b/z^*	0.33	0.42	0.52	0.58	0.63	0.70

behavior reflects averaging of $K(\theta)$ around the crack front while the K solution [25] does not.

The right hand diagram in Figure 13 suggests an approach to selecting an empirical magnification factor that represents the free-surface effect as a transition during the internal defect growth stage. A corner crack of radius $r' = 2r$ has the same area as a penny crack of radius r. For any given flaw size at which the model is to be changed from penny to corner crack (e.g., 50 %HA as was suggested in Section 2), the stress intensity factor ranges calculated for both models should agree:

$$2\, m_t M \Delta S \frac{\sqrt{r}}{\sqrt{\pi}} = 2.4\, M' \Delta S' \frac{\sqrt{r'}}{\sqrt{\pi}} \tag{31}$$

where m_t is the value of the empirical magnification factor M_t at the transition size, M and M' are the products of the other magnification factors applied respectively to the penny and corner crack stress intensity ranges, and ΔS and $\Delta S'$ are the corresponding stress ranges. Therefore, the value of M_t at the transition is given by:

$$m_t = \frac{2.4}{\sqrt{2}} \frac{M'}{M} \frac{\Delta S'}{\Delta S} \tag{32}$$

Since rail bending is the source of the stress ranges, one can follow the logic of Section 3.2.2 to express the ratio $\Delta S'/\Delta S$, keeping in mind that $y' = w/2$ and $z' = h - h_C$ for the corner crack model. One then finds:

$$\frac{\Delta S'}{\Delta S} = \frac{h-h_C}{z} \frac{1 + \frac{w}{2(h-h_C)} \frac{\beta}{\beta_L} \frac{I_{yy}}{I_{zz}} \frac{L}{V}}{1 + \frac{y}{z} \frac{\beta}{\beta_L} \frac{I_{yy}}{I_{zz}} \frac{L}{V}} \tag{33}$$

where y and z are the center coordinates for the penny crack model at the transition size. Table 16 summarizes the $\Delta S'/\Delta S$ ratio for 136 RE rail on average foundation, with the transition flaw size defined to be 50 % HA.

TABLE 16. RATIOS OF $\Delta S'/\Delta S$ FOR TRANSITION FLAW SIZE OF 50 % HA IN 136 RE RAIL ON AVERAGE TRACK FOUNDATION.

L/V	0.00	0.05	0.10	0.20	0.30	0.40	0.50
$\Delta S'/\Delta S$	1.362	1.411	1.456	1.537	1.607	1.668	1.723

The transition magnification factor can be interpolated for defects smaller than the transition size, for example:

$$M_t = \frac{A - A_1}{A_t - A_1} + \frac{A_t - A}{A_t - A_1} m_t \; ; \; A \geq A_1 \tag{34}$$

where A is the defect area, A_t is the area at transition, and A_1 is an arbitrarily chosen area below which no magnification is applied. Equation 34 interpolates linearly from $M_t = 1$ at $A = A_1$ to $M_t = m_t$ at $A = A_t$. This procedure is incorporated in the detail fracture model, with A_1 = 10 % HA.

3.2.4 Finite cross section

The effects of finite cross section are best illustrated by means of the two-dimensional example of a through crack of length ℓ growing across a plate of width w subjected to either uniform tension or bending (Figure 14). The basic stress intensity factor for this case, $K = S\sqrt{\pi \ell}$, refers to a crack in an unbounded plate under uniform tension.

Among the available solutions for the finite-width plate is the following stress intensity factor formula for the case of uniform tension [9 – 11]:

$$K = S\sqrt{\pi \ell} \left[\sqrt{\frac{2w}{\pi l}} \tan \frac{\pi l}{2w} \right] \frac{0.752 + 2.02\,(\ell/w) + 0.37\,[1 - \sin(\pi \ell/2w)]^3}{\cos(\pi l/2w)} \tag{35}$$

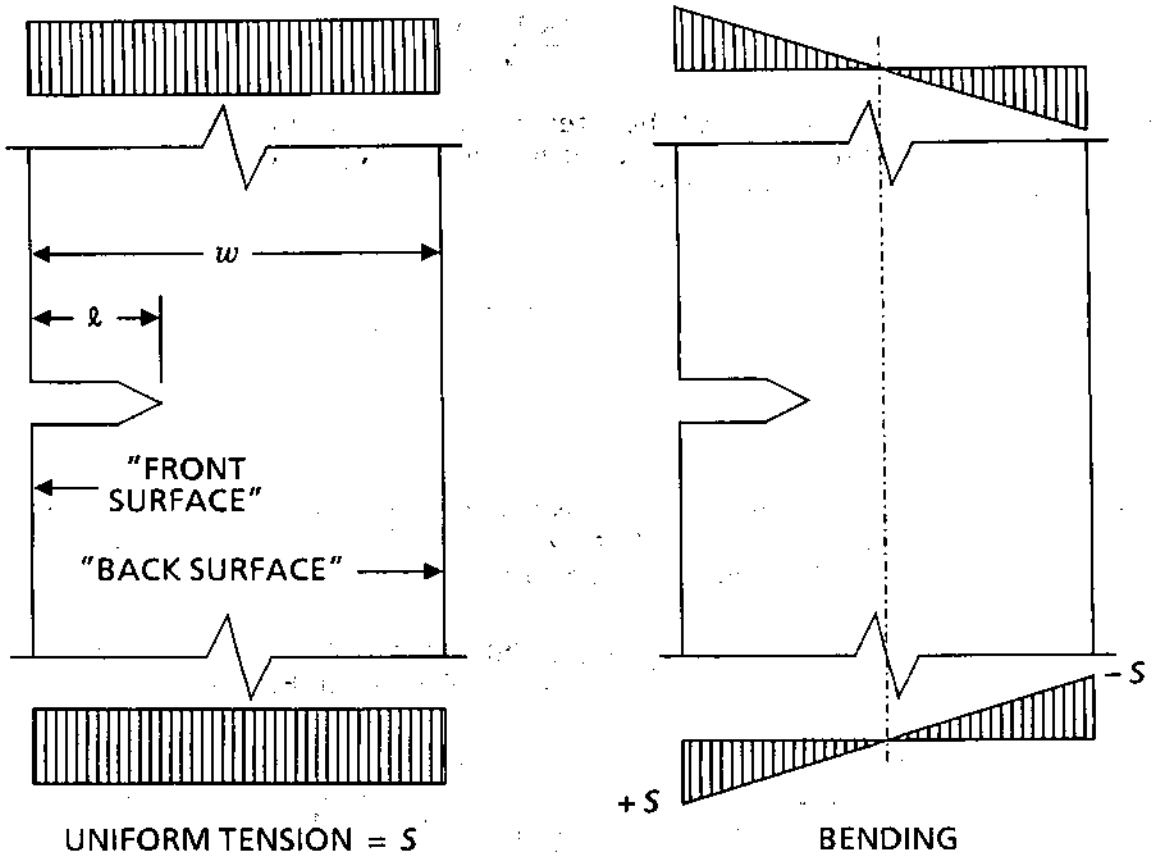

FIGURE 14. EDGE CRACK IN FINITE-WIDTH PLATE

On the other hand, if S is taken to be the maximum stress in a bending stress distribution, a similar solution gives:

$$K = S\sqrt{\pi\ell}\left[\sqrt{\frac{2w}{\pi l}}\tan\frac{\pi l}{2w}\right]\frac{0.923+0.199\,[1-\sin(\pi l/2w)]^4}{\cos(\pi l/2w)} \qquad (36)$$

In both cases K increases without limit as the length of the crack approaches the plate width; this is the so-called "back-surface" magnification factor. Both expressions also include a "front-surface" magnification factor of 1.122, which appears in the right hand numerical ratios as $\ell/w \to 0$. (Note that l'Hopital's rule can be used to show that the bracketed term approaches 1 as $\ell/w \to 0$.)

It appears reasonable to adapt these solutions to the detail fracture model, since detail fractures are asymmetrically located with respect to the rail neutral axis and center plane. Two adjustments are necessary. First, one should recognize that the corner crack stress intensity factor (Eq. 9) already includes a front-surface magnification factor of 1.2, as explained in [13]. Second, an appropriate substitute for the ℓ/w ratio is required. The obvious candidates are the ratio of defect area to rail head cross section area, A/A_H, or to the whole rail area, A/A_R.

With the foregoing adjustments, the detail fracture model incorporates the following finite-section magnification factor based on the uniform stress case:

$$M_1 = \left[\sqrt{\frac{2A_X}{\pi A}}\tan\frac{\pi A}{2A_X}\right]\frac{C_1+2.02\,(A/A_X)+0.37\,[1-\sin(\pi A/2A_X)]^3}{\cos(\pi A/2A_X)} \qquad (37)$$

where in the present case the finite section factor is modeled by $A_X = A_H$ for small and medium penny cracks ($A \leqq 40$ %HA) or $A_X = A_H + 0.5A_R$ for large penny cracks and corner cracks ($A > 40$ %HA), where $C_1 = 0.63$ for penny cracks or 0.83 for corner cracks, and where it is understood that the factor of 2.4 is replaced by 2.0 in Eq. 9. Table 17 summarizes the magnification factors for 132 RE and 136 RE rail sections.

TABLE 17. FINITE AREA MAGNIFICATION FACTORS.

Model	Penny Crack, M_1						Corner Crack, M_1'			
Size (%HA) / Section	5	10	20	30	40	50	50	60	70	80
132 RE	1.025	1.072	1.236	1.513	1.946	1.242	1.457	1.562	1.689	1.842
136 RE	1.025	1.072	1.236	1.513	1.946	1.260	1.475	1.589	1.728	1.895

3.2.5 Detail fracture model

The magnification factors discussed in the preceding sections were combined to model K for a detail fracture growing in a rail head, but two practical difficulties encountered in applying the model led to simplifications. First, trial simulations of the test rail 1 crack growth history exposed artifacts in the transition magnification factor which made it impossible to recapture the shape of the experimental crack growth curve. Ultimately, M_t was discarded, and the transition effect was simulated by averaging life increments calculated from the penny and corner crack models. The average was defined as a linear interpolation such that the penny crack life increment is fully effective for $A \leqq 10$ %HA and the corner crack life increment is fully effective when $A \geqq 50$ %HA.

Second, the fact that the gradient magnification factor M_G depends on L/V introduces ambiguities when L/V is not constant. Such cases arise, for example, when the effects of train loads on curved track are simulated (see Section 4.1.2). The ambiguities arise from the fact that each cycle in the stress spectrum is in general created by two or more wheel loads which can have different values of L/V. Since M_G is not strongly sensitive to L/V (Table 18), the simulation was simplified by making L/V a constant equal to the average value in the train load spectrum.

With these simplifications, the stress intensity factor model for internal detail fractures is given by:

$$K = 2M_S M_1 [S_R + S_T + M_G S]\sqrt{(r/\pi)} \qquad (38)$$

TABLE 18. GRADIENT MAGNIFICATION FACTORS FOR 132 RE RAIL.

Model	Penny Crack, M_G						Corner Crack, M_G'			
Size (%HA)	5	10	20	30	40	50	50	60	70	80
L/V										
0.05	1.000	1.001	1.001	1.002	1.003	1.004	0.966	0.963	0.960	0.957
0.10	1.001	1.001	1.003	1.005	1.007	1.009	0.937	0.931	0.926	0.921
0.20	1.002	1.004	1.009	1.015	1.022	1.027	0.892	0.882	0.873	0.865
0.30	1.003	1.007	1.017	1.029	1.040	1.050	0.858	0.845	0.834	0.824
0.40	1.005	1.011	1.025	1.043	1.060	1.074	0.832	0.817	0.805	0.793
0.50	1.006	1.014	1.034	1.058	1.081	1.099	0.811	0.795	0.782	0.769

where M_S is the shape magnification factor (Section 3.2.1), M_1 is the finite-section magnification factor (Section 3.2.4), S_R is the average relieved residual stress (Section 3.2.2), S_T is the thermal stress, S is the live bending stress, and $r = \sqrt{(A/\pi)}$ is the crack radius for a flaw of area A. For detail fractures that have broken out to the gage face and running surface, the stress intensity factor model is similarly given by:

$$K' = 2\, M_1' [S_R + S_T + M_G' S'] \sqrt{(r'/\pi)} \tag{39}$$

where $r' = 2\sqrt{(A/\pi)}$. These stress intensity factors are used to estimate the crack growth rates dr/dn and dr'/dn for the detail fracture model.

Let S_{min} and S_{max} be the minimum and maximum of the bending stress cycle and $\Delta S = S_{max} - S_{min}$ the stress range. Then from Eqs. 38 and 39 the stress intensity factor ranges are:

$$\Delta K = 2\, M_S M_1 M_G \Delta S \sqrt{(r/\pi)} \tag{40}$$

$$\Delta K' = 2\, M_1' M_G' \Delta S' \sqrt{(r'/\pi)} \tag{41}$$

The stress ratios can also be obtained from Eqs. 38 and 39 and are given by:

$$R = \frac{S_R + S_T + M_G S_{min}}{S_R + S_T + M_G S_{max}} \tag{42}$$

$$R' = \frac{S_R + S_T + M'_G S'_{min}}{S_R + S_T + M'_G S'_{max}} \tag{43}$$

3.3 Life calculation method

In principle one can estimate crack growth life by calculating the crack size increment and updating the current crack size for each cycle of applied stress. In practice, the cycle-by-cycle approach usually requires too much computing time. For example, typical freight traffic would impose from 200 to 400 bending stress cycles per train, or about 42,000 to 83,000 cycles per MGT. To estimate a detail fracture life of order 30 MGT would thus require about 1.3 to 2.5 million calculations of ΔK, R, dr/dn, and updated crack size.

Fortunately, it is easy to devise more efficient calculation procedures. For example, standard aircraft industry practice is to reorganize the stress cycle sequence into blocks of identical cycles; the crack size increment per block can then be calculated as the product of the increment per cycle and the number of cycles per block, under the reasonable assumption that ΔK and R remain nearly constant over a one-block change of crack size. The block calculation method typically reduces the computational effort by a factor of ten.

Further reductions can be made by taking advantage of the mathematical properties of some types of crack models and growth rate equations. If the crack growth model is of the simple form $\Delta K = G(r)\sqrt{r}\Delta S$ and R is independent of crack size, then the crack geometry effects $G(r)\sqrt{r}$ can be separated from the stress effects in rate equations like Eq. 13, e.g.:

$$\frac{dr}{[G(r)\sqrt{r}]^P} = \frac{C(\Delta S)^P}{(1-R)^Q}\, dn \tag{44}$$

It is then easy to show that the left and right hand sides of Eq. 44 can be summed or integrated independently and the result solved for the total number of spectra, N, to grow the crack between specified size limits r_1, r_2:

$$N = \frac{\int_{r_1}^{r_2} \frac{dr}{[G(r)\sqrt{r}]^P}}{C \sum \frac{(\Delta S)^P}{(1-R)^Q}} = \frac{CRACK\ GEOMETRY\ INTEGRAL}{STRESS\ SPECTRUM\ SUM} \tag{45}$$

In the present context, a "spectrum" is an operationally defined group of stress cycles, e.g., one train. Reduction of computational effort is achieved in this case by choosing widely spaced crack size limits for the calculation. In principle, r_1 and r_2 can be taken as the initial and final crack sizes of interest, and Eq. 45 still produces exactly the same answer as the corresponding cycle-by-cycle calculation when N is large enough so that dr/dn can be treated as a continuous function [26]. This approach is called the spectrum integration method.

In practice, the crack geometry and stress effects cannot always be totally decoupled. The detail fracture model is in this category because most of the stress intensity magnification factors are functions of both stress and crack size and because the threshold cutoff procedure censors less of the stress spectrum sum as the crack size

increases. In spite of these difficulties the spectrum integration method can still be applied by dividing the crack life into several size blocks, such that the coupled factors do not change much over a single block. Life calculation for the penny crack model can then be arranged as follows:

$$N = \frac{\int_{r_1}^{r_2} \frac{dr}{[2 M_S \sqrt{r/\pi}]^P}}{C \sum \frac{(M_1 * M_G * \Delta S)^P}{(1-R*)^Q}} \tag{46}$$

where

$$R* = \frac{S_R + S_T + M_G * S_{min}}{S_R + S_T + M_G * S_{max}} \tag{47}$$

and where M^* is a suitably chosen fixed value of M, e.g., $M(r_1)$, $M(r_2)$ or some average over the crack size block. The threshold cutoff procedure is approximated in the same way by censoring from the stress spectrum sum those cycles for which $\Delta K < (1 - R^*)K_{th}$. In a similar manner, life can be calculated for the corner crack model as:

$$N' = \frac{\int_{r_1'}^{r_2'} \frac{dr'}{[2 \sqrt{r'/\pi}]^P}}{C \sum \frac{(M_1' * M_G' * \Delta S')^P}{(1-R'*)^Q}} \tag{48}$$

where

$$R'* = \frac{S_R + S_T + M_G' * S_{min}'}{S_R + S_T + M_G' * S_{max}'} \tag{49}$$

The foregoing procedures are incorporated in the detail fracture model, with the (...)* quantities assigned values corresponding to the middle of the crack size block. The block sizes can be arbitrarily set, but 10 %HA blocks have been generally used in the present study. In the penny crack regime, life calculations are made with both models and the final estimate is defined by the linear interpolation:

$$N_{est} = [1 - \tfrac{1}{2}(A/A_H)]N + \tfrac{1}{2}(A/A_H)N' \tag{50}$$

3.4 Load interaction effects

The spectrum integration and block methods are based on the assumption that each crack size increment depends only on the stresses in the current cycle. Conversely, experiments with spectrum loading often show that the crack growth rate depends on the stresses of prior cycles as well as those of the current cycle. Such phenomena are referred to as load interaction effects.

The best known example of load interaction is the effect of an isolated overload on crack growth in succeeding cycles. Early experiments on aircraft aluminum alloys [27] showed a sharp reduction of the growth rate, followed by a gradual return to the rate one would expect based on constant-amplitude material tests. The result is a retardation in the curve of crack size versus cycles (Figure 15).

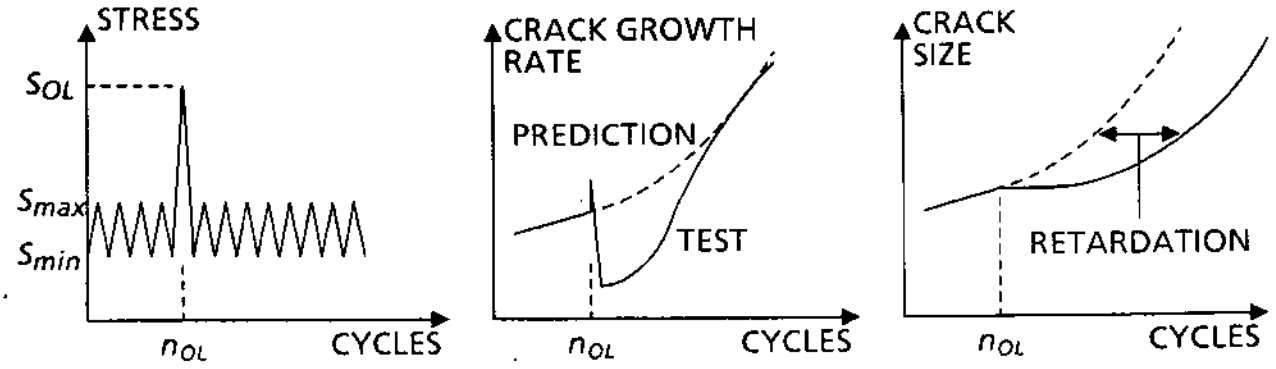

FIGURE 15. CRACK GROWTH RETARDATION.

Elber's crack closure model [17] provides an understanding of the retardation effect and a means for its simulation. The overload cycle creates a large residual compression (and hence also a large opening stress) ahead of the crack front. Thus, ΔK_{eff} decreases in the succeeding cycles until the combination of further crack growth into fresh material and elastic-plastic relaxation returns the crack opening stress to its pre-overload value. In principle, a cycle-by-cycle crack growth calculation can embody Elber's model to track the opening stress history under spectrum loading, at least for positive-R spectra. This approach is time consuming in practice, however, and the crack opening stress is usually approximated by averaging over one spectrum. Averaging is justified by the results of comparative numerical experiments which show that the crack opening stress tends to have a quasi-steady-state history under typical service spectra.

Spectrum average crack opening stress and other empirical models have been used to predict crack growth life for aluminum alloy subjected to aircraft wing spectra with varying degrees of success [28]. Retardation is often observed in laboratory spectrum tests and can be correlated with such models. Common aircraft industry practice for such tests is to organize the cycles for one spectrum (one flight) as the ground-air-ground (GAG) cycle with flight load cycles superimposed in the order of decreasing maximum stress (DMS) rather than real sequence order (RSO). Figure 16 illustrates the difference between these arrangements.

Experimental investigation of load interaction effects should simulate the service environment (ΔK, R) as well as the stress sequence to properly characterize the effect expected in service. The service environment should include the effects of crack geometry and stress distribution on ΔK and R. These effects are difficult to incorporate in the testing of a compact tension specimen (CTS) when the service defect is a detail fracture in a rail head. Accordingly, an approximate simulation was developed, based on the basic penny crack model (Eq. 8) as a representation of the detail fracture. The

principle governing the simulation [29] is to match $K(\ell)$ for the CTS (Eq. 11) with $K(r)$ for the service defect model, leading to:

$$\frac{F}{S} = \frac{2\sqrt{r/\pi}}{H(\ell)} \tag{51}$$

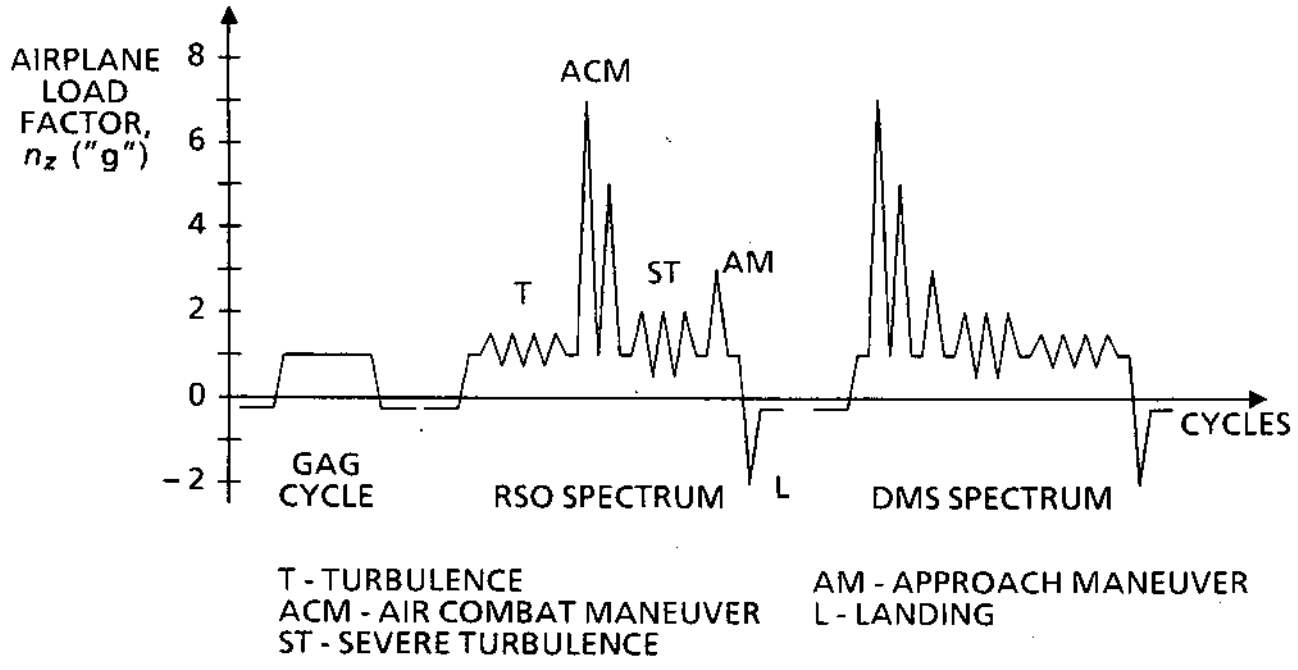

FIGURE 16. FIGHTER AIRCRAFT RSO AND DMS SPECTRUM SEQUENCES.

as the scale factor to convert the service stress spectrum S into a test load spectrum F for a penny crack of radius r and a CTS crack length ℓ. For a given scale factor, Eq. 51 establishes a relation between the test crack length and the equivalent service defect area $A = \pi r^2$. In principle, the load interaction effects are properly simulated when the scale factor is continuously changed so that the number of cycles required to grow the test crack from ℓ_1 to ℓ_2 is the same as the number of cycles required to grow the service defect from the smallest size of interest r_1 to the largest size of interest r_2. In practice, the simulation is approximated by keeping the scale factor constant during each spectrum (one train) and updating the value before the next spectrum.

Laboratory tests of rail steel specimens (Figure 8) were performed under an approximate train spectrum to investigate the effects of load interaction on detail fracture growth [30]. The train represented by the spectrum was a typical FAST consist of 84 vehicles with 421 stress cycles corresponding to approximately 10,000 gross tons. Only the vertical bending component of the rail head live load stress was considered, and the combined effect of thermal and residual stress was represented by a fixed 15 ksi mean stress. The large mean stress created a positive-R spectrum. Table 19 summarizes the cycle count, n, together with S_{min} and S_{max} in DMS order.

Tests were performed under both DMS and RSO spectra, the RSO spectrum having been determined from the consist order. The results were compared with the test rail 1 experiment (Section 2.1) and with a block method life calculation using the model E

and F material properties (Section 3.1). The life calculation was performed without *R*-truncation, although the presence or absence of truncation makes no difference in the present case. The laboratory test results showed that no interaction effects persisted for more than about 750 spectra (7.5 MGT). (The actual limit of persistence is probably much less.)

TABLE 19. LABORATORY TEST SPECTRUM IN DMS ORDER.

n	S_{min} (ksi)	S_{max} (ksi)	*n*	S_{min} (ksi)	S_{max} (ksi)	*n*	S_{min} (ksi)	S_{max} (ksi)	*n*	S_{min} (ksi)	S_{max} (ksi)
2	4.3	15.8	1	4.2	13.4	4	9.4	11.7	1	4.1	11.0
2	4.1	15.4	9	3.8	13.3	4	10.9	11.7	1	6.6	10.7
1	5.5	15.4	1	4.1	13.3	1	10.9	11.6	1	5.1	10.7
1	4.4	15.2	56	10.9	13.3	3	9.9	11.6	1	4.5	10.7
4	3.6	14.6	55	4.2	13.3	1	9.5	11.6	3	4.2	10.7
1	6.6	14.3	2	10.9	13.0	3	10.9	11.6	1	5.3	10.6
1	7.1	14.3	2	4.9	13.0	1	11.0	11.5	3	4.2	10.2
1	5.7	14.3	1	5.2	12.9	3	4.5	11.5	3	4.5	10.2
3	10.3	14.0	2	10.9	12.9	4	8.6	11.4	2	3.6	10.1
55	6.2	14.0	1	5.3	12.9	4	9.4	11.4	1	3.9	10.1
3	3.8	13.9	1	9.9	12.9	55	6.1	11.4	1	4.1	10.1
4	3.7	13.4	3	11.0	12.9	55	4.2	11.4	2	3.6	10.1
12	10.9	13.4	5	10.9	12.7	3	8.9	11.3	2	5.5	10.0
1	3.8	13.4	4	3.8	12.7	1	5.3	11.1	1	4.9	10.0
5	3.7	13.4	1	10.9	12.4	1	7.1	11.1	8	3.7	10.0
1	3.9	13.4	1	5.7	11.7	1	5.7	11.0	4	8.6	9.0

Figure 17 illustrates the comparisons. The scale factor was controlled to simulate crack growth from 20 %HA to about 70 %HA. The RSO laboratory test agreed reasonably well with the test rail 1 growth curve. The DMS laboratory test and the block life calculation agreed with each other, but these two results exhibited a growth rate much slower than the RSO and test rail 1 results. Two conclusions can be drawn from the comparison:

- First, a train spectrum in real sequence order creates interaction effects on the fatigue crack propagation of detail fractures, but the same spectrum in DMS order does not. Further, the interaction effect accelerates rather than retards the growth rate. In other words, the RSO crack propagation life is shorter than the life calculated from spectrum blocks; specifically, the actual life is from 75 to 80 percent of the calculated life.
- Second, one should expect the block and spectrum integration methods of life calculation to overestimate safe crack growth life when the *K* model of the detail fracture is reasonably well calibrated. A scale factor similar to the one exhibited

in the laboratory tests should be expected, i.e., the actual life of a detail fracture should be from 75 to 80 percent of the calculated life.

It should be noted, however, that the scale factor may be different for lighter and/or heavier axle loads. Additional laboratory tests are needed to evaluate the dependence of load interaction on load level.

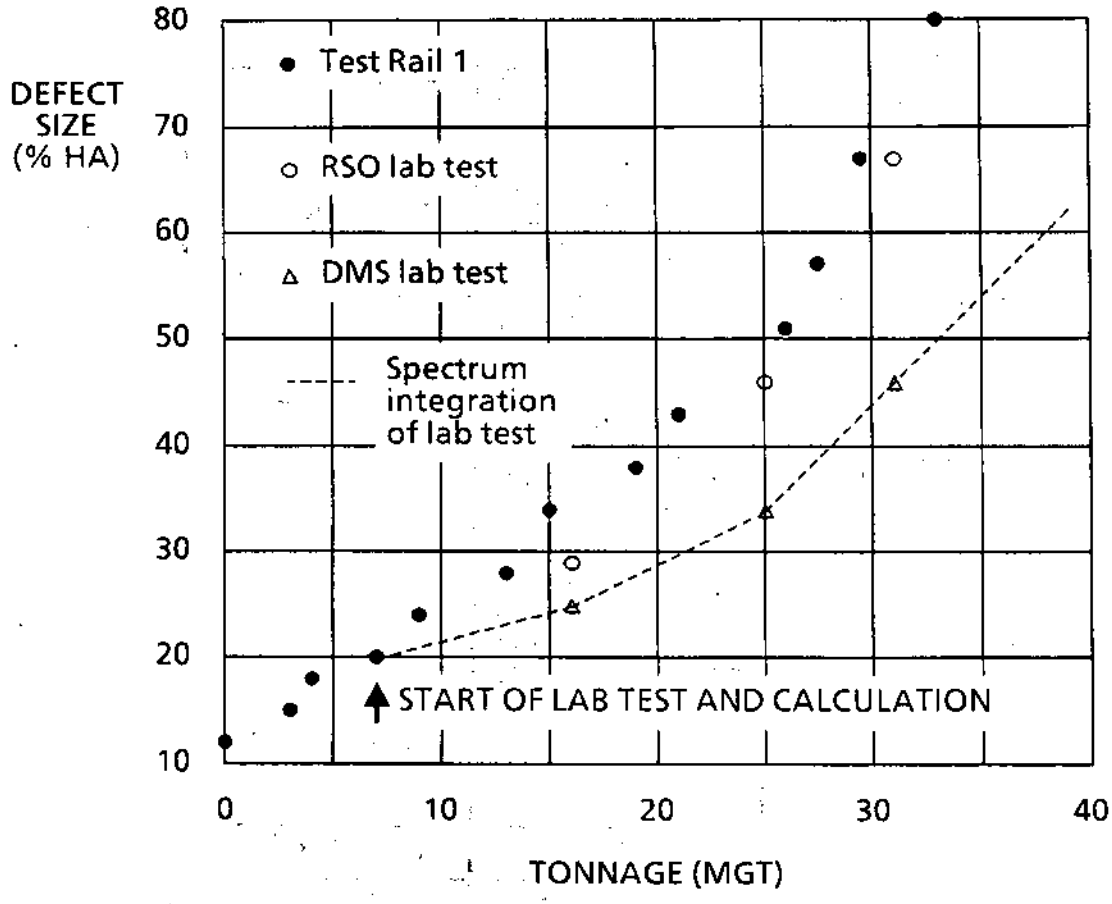

FIGURE 17. LOAD INTERACTION EFFECT FOR DETAIL FRACTURES.

4. THE RAIL HEAD STRESS ENVIRONMENT

An engineering description of longitudinal service stress in the rail head is required to establish typical spectra (S_{min}, S_{max}) or (ΔS, R) for estimating crack growth life. A general approach to such description was outlined earlier [4]. This section discusses procedures for constructing train spectra (including thermal and residual stress effects) for the special case of the FAST experiment (Section 2.1) as well as for representation of typical revenue service environments. The discussion is divided into live load stress (Section 4.1), thermal stress (Section 4.2) and residual stress (Section 4.3).

4.1 Live load stress

Calculation of live load stress due to rail bending is based on the accepted railroad engineering practice of treating the rail as a continuous beam on a continuous elastic foundation [31], as supplemented by the work of Timoshenko and Langer [32] and Hétenyi [33] to deal with the effects of lateral loading. Figure 18 illustrates most of the parameters involved in the beam analysis.

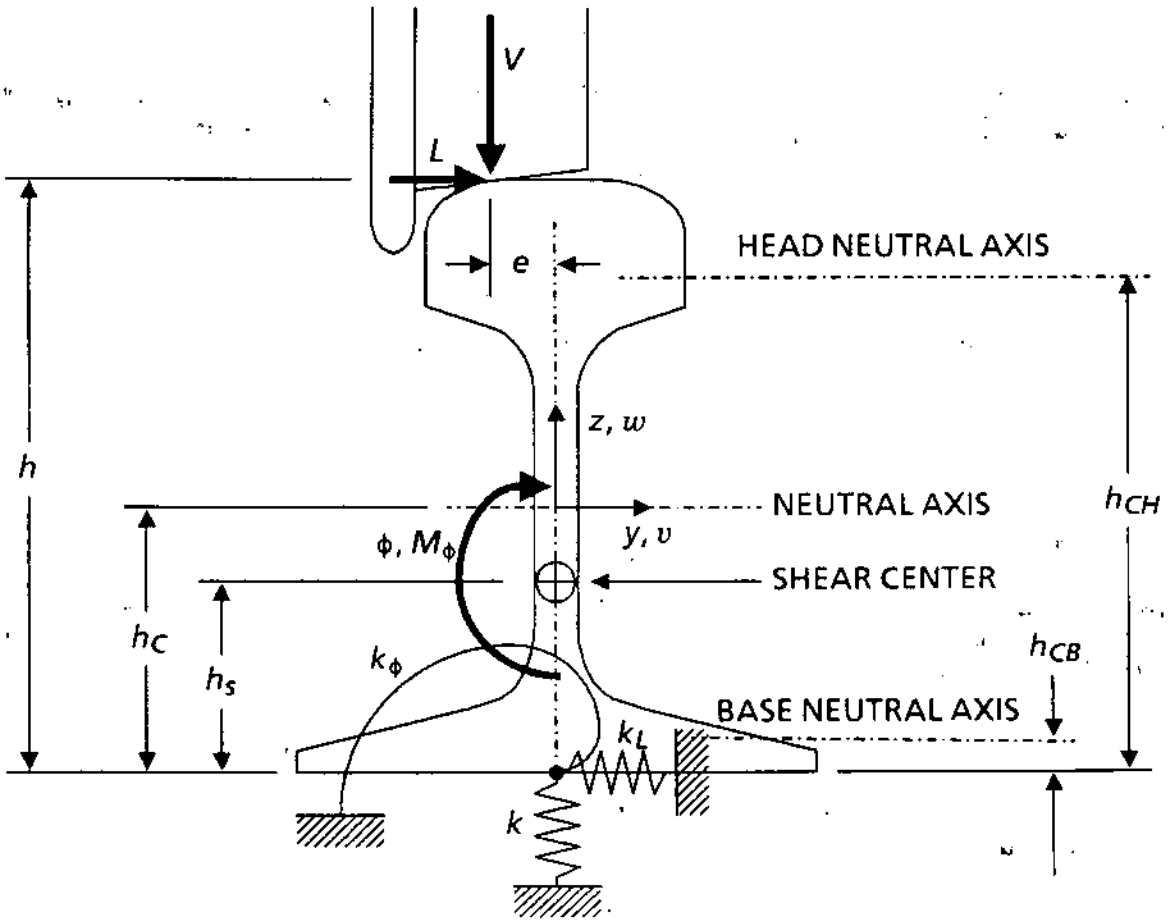

FIGURE 18. RAIL AS A BEAM ON A CONTINUOUS ELASTIC FOUNDATION.

In general, the rail is subjected to a lateral load L as well as a vertical load V from each wheel. These loads also create a twisting moment M_ϕ about the shear center:

$$M_\phi = (h - h_s)L - eV \tag{52}$$

As a result of the combined loads, the rail neutral axis undergoes bending deflections w and v in the vertical and lateral directions, respectively, and the section also undergoes torsional deflection ϕ about the shear center. Based on the earlier discussion [4], the following decoupled set of equations can be derived for these deflections:

$$EI_{yy}\frac{d^4w}{dx^4} + kw = 0 \tag{53}$$

$$EI_{zz}\frac{d^4v}{dx^4} + k_L v = 0 \tag{54}$$

$$D(h_{CH}-h_{CB})^2\frac{d^4\phi}{dx^4} - GJ\frac{d^2\phi}{dx^2} + k_\phi\phi = 0 \tag{55}$$

where x is a longitudinal coordinate, E is Young's modulus (3×10^7 psi), G is the shear modulus (1.154×10^7 psi), I_{yy} and I_{zz} are the second area moments of the section about the neutral axis and center plane, respectively,

$$D = \frac{EI_{zzB}I_{zzH}}{I_{zzB}+I_{zzH}} \tag{56}$$

I_{zzB} and I_{zzH} are the second lateral area moments of the head and base, respectively,

$$J \simeq \frac{A_R^4}{40\sqrt{(I_{yy}^2+I_{zz}^2)}} \tag{57}$$

A_R is the rail section area, and k, k_L, and k_ϕ are respectively the vertical, lateral, and torsional foundation moduli. The dimensions and other geometric properties compiled for a variety of rail sections [34, 35] are listed in Appendix A. Nominal foundation moduli $k_L = 0.85k$ and $k_\phi = 10^5$ in.lb./in.rad. can be used in the flexure equations [36, 37]. Table 20 summarizes appropriate values of the vertical modulus k as a function of general track conditions.

The engineering beam theory does not fully account for the rail behavior near the applied load. The effects of local flexure can be approximated by treating the rail head as a separate beam on the elastic foundation of the web. The vertical and lateral flexure equations for the head-on-web (HOW) effect are:

$$EI_{yyH}\frac{d^4w_H}{dx^4} + k_{HOW}w_H = 0 \tag{58}$$

$$EI_{zzH}\frac{d^4v_H}{dx^4} + k_{LHOW}v_H = 0 \tag{59}$$

TABLE 20. REPRESENTATIVE VERTICAL TRACK FOUNDATION MODULI.

k (ksi)	Track Description
1 to 2	Poor subgrade; deteriorated ballast; deteriorated wood ties; poorly drained; low-tonnage, low-speed branch line.
2 to 3	Typical mainline freight track: well maintained ballast and wood ties; 20 to 40 mph operations; 10 to 20 MGT per year.
3 to 5	Well maintained high-speed, high-tonnage mainline track: ballast and wood ties in excellent condition; 45 to 80 mph operations; 30 to 120 MGT per year. Wood-tie sections of FAST test track.
10	Northeast Corridor concrete-tie track: freight operations up to 60 mph; passenger operations up to 125 mph. Concrete-tie sections of FAST test track.

for deflections w_H and v_H of the rail head neutral axis and center plane. The head-on-web foundation moduli are approximated by:

$$k_{HOW} = \frac{Et_w}{h_w} \; ; \; k_{LHOW} = \frac{Et_w^3}{h_w^3} \tag{60}$$

where t_w and h_w are respectively the thickness and height of the web. The vertical modulus k_{HOW} represents the web compression stiffness, while the lateral modulus k_{LHOW} approximates the cantilever bending stiffness of the web.

For a single pair of loads (L, V) at $x = 0$, the following boundary conditions apply to the flexure equations:

$$\frac{dw}{dx} = 0 \; ; \; EI_{yy} \frac{d^3w}{dx^3} = \frac{V}{2} \tag{61}$$

$$\frac{dv}{dx} = 0 \; ; \; EI_{zz} \frac{d^3v}{dx^3} = -\frac{L}{2} \tag{62}$$

$$\frac{d\Phi}{dx} = 0 \; ; \; D(h_{CH} - h_{CB})^2 \frac{d^3\Phi}{dx^3} - GJ \frac{d\Phi}{dx} = -\frac{M_\Phi}{2} \tag{63}$$

$$\frac{dw_H}{dx} = 0 \; ; \; EI_{yyH} \frac{d^3w_H}{dx^3} = \frac{V}{2} \tag{64}$$

$$\frac{dv_H}{dx} = 0 \; ; \; EI_{zzH} \frac{d^3 v_H}{dx^3} = -\frac{L}{2} \tag{65}$$

at $x = 0$, together with the asymptotic conditions:

$$\lim_{x \to \pm\infty} \{w, v, \Phi, w_H, v_H\} = 0 \tag{66}$$

Strictly speaking, the formulation of w_H and v_H as flexures independent of w and v is mechanically inconsistent, and Eqs. 53 – 66 only approximate the rail behavior. The approximation was assessed by comparing with a three-dimensional finite element analysis [38] and was found to give reasonable estimates of bending stress anywhere in the rail head except in the head-web fillet regions. Therefore, the flexure equations can be used to calculate live load stress for detail fracture crack growth analysis.

The flexure solutions are symmetric with respect to x and take the following forms for $x \geqq 0$:

$$w = -\frac{V\beta}{2k} e^{-\beta x} (\cos \beta x + \sin \beta x) \tag{67}$$

$$v = \frac{L\beta_L}{2k_L} e^{-\beta_L x} (\cos \beta_L x + \sin \beta_L x) \tag{68}$$

$$\Phi = -\frac{M_\phi}{4\beta_1 D (h_{CH} - h_{CB})^2} e^{-\beta_1 x} \left[\frac{\cosh \beta_2 x + (\beta_1 / \beta_2) \sinh \beta_2 x}{\beta_1^2 - \beta_2^2} \right] \tag{69}$$

$$w_H = -\frac{V\beta_{HOW}}{2k_{HOW}} e^{-\beta_{HOW} x} (\cos \beta_{HOW} x + \sin \beta_{HOW} x) \tag{70}$$

$$v_H = \frac{L\beta_{LHOW}}{2k_{LHOW}} e^{-\beta_{LHOW} x} (\cos \beta_{LHOW} x + \sin \beta_{LHOW} x) \tag{71}$$

where $\beta = (k/4EI_{yy})^{1/4}$, $\beta_L = (k_L/4EI_{zz})^{1/4}$, $\beta_{HOW} = (k_{HOW}/4EI_{yyH})^{1/4}$, $\beta_{LHOW} = (k_{LHOW}/4EI_{zzH})^{1/4}$, and

$$\beta_1 = \left[\frac{GJ}{4D (h_{CH} - h_{CB})^2} + \frac{\sqrt{k_\phi / D}}{2 (h_{CH} - h_{CB})} \right]^{1/2} \tag{72}$$

$$\beta_2 = \left[\frac{GJ}{4D(h_{CH}-h_{CB})^2} - \frac{\sqrt{k_\phi/D}}{2(h_{CH}-h_{CB})} \right]^{1/2} \tag{73}$$

For $x<0$, the correct forms are Eqs. 67 – 71 with $+x$ replaced by $-x$. The solutions for w, v, w_H, and v_H are damped spatial oscillations characterized by the wavelengths $2\pi/\beta$, $2\pi/\beta_L$, $2\pi/\beta_{HOW}$, and $2\pi/\beta_{LHOW}$.

The longitudinal stress caused by rail flexure is calculated from the bending moments $EI_{yy}(d^2w/dx^2)$, $EI_{zz}(d^2v/dx^2)$, $EI_{yyH}(d^2w_H/dx^2)$, and $EI_{zzH}(d^2v_H/dx^2)$. Differentiation of Eqs. 67, 68, 70, and 71 and substitution of the wavelength parameters leads to the following bending moment expressions for $x \geqq 0$:

$$M = \frac{V}{4\beta} e^{-\beta x}(\cos\beta x - \sin\beta x) \tag{74}$$

$$M_L = -\frac{L}{4\beta_L} e^{-\beta_L x}(\cos\beta_L x - \sin\beta_L x) \tag{75}$$

$$M_{HOW} = \frac{V}{4\beta_{HOW}} e^{-\beta_{HOW} x}(\cos\beta_{HOW} x - \sin\beta_{HOW} x) \tag{76}$$

$$M_{LHOW} = -\frac{L}{4\beta_{LHOW}} e^{-\beta_{LHOW} x}(\cos\beta_{LHOW} x - \sin\beta_{LHOW} x) \tag{77}$$

The combined bending stress at a location (y, z) in the section is then given by:

$$S = -\left[\frac{Mz}{I_{yy}} + \frac{M_L y}{I_{zz}} + \frac{M_{HOW}(z-h_{CH}+h_C)}{I_{yyH}} + \frac{M_{LHOW} y}{I_{zzH}} \right] \tag{78}$$

There is an additional small contribution to S from restraint of section warping in CWR. This warping stress is given by:

$$S_W \simeq \frac{1}{2} E(y^2+z^2)\left[\frac{d\phi}{dx}\right]^2 \tag{79}$$

where from Eq. 69,

$$\frac{d\phi}{dx} = \frac{M_\phi}{4D(h_{CH}-h_{CB})^2} e^{-\beta_1 x}\left[\frac{\beta_1}{\beta_2} - \frac{\beta_2}{\beta_1}\right] \sinh\beta_2 x \tag{80}$$

The oscillatory nature of the flexural contributions creates the bending stress cycle. For example, it is apparent from Eqs. 74 – 78 that the minimum stress for a point in the upper gage side of the rail head ($y<0$, $z>h_{CH}$) occurs in the section directly under the applied loads ($x=0$). Further, Eq. 74 shows that the principle vertical bending moment

attains its maximum reverse value at the quarter-wave points $x = \pm \pi/2\beta$, and similar reversals occur in the other bending moments at their respective quarter-wave points. The corresponding stresses are the maximum tensile contributions. In practice, one generally finds that the maximum combined stress is located close to the principle quarter-wave points and is approximately 1/5 the magnitude of the minimum stress.

Figure 19 illustrates the longitudinal variation of the bending stress and shows that the spatial oscillation is equivalent to a temporal oscillation at a fixed section when the loads are produced by a wheel traveling along the rail. The second minima occur close to $x = \pm 3\pi/2$ and are generally less than one percent of the principle minimum. Hence, one need consider only the range $-5\pi/4 \leqq x \leqq +5\pi/4$ to construct the live load stresses for crack growth analysis. As shown in the figure, the passage of a single wheel produces two stress cycles $(0, S_{max})$ and (S_{min}, S_{max}).

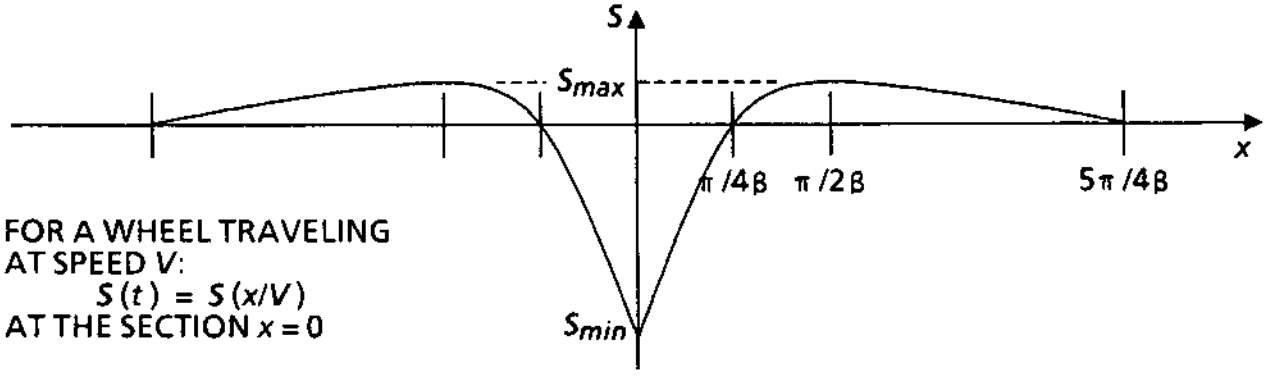

FIGURE 19. DISTRIBUTION OF RAIL HEAD STRESS FROM ONE WHEEL LOAD.

The principle of superposition can be used to construct stress cycle diagrams for the wheel load groups associated with a train passage. Based on numerical studies with actual car and locomotive dimensions, a wheel group comprising the trailing truck of a vehicle and the lead truck of the following vehicle has been found to provide sufficient accuracy. Figure 20 illustrates the typical pattern of five stress cycles associated with a group of four equally loaded wheels located at $x = x_1, x_2, x_3, x_4$. The bending stress at any section x can be found by substituting $\pm(x - x_i)$ in Eqs. 74 – 77 and 80 and summing over $i = 1,2,3,4$.

The stress cycle pattern is generally asymmetric because the wheel loads are not equal. To find the successive S_{max} values in this case, one simply starts at a section $x<0$ to the left of the first peak and tracks the value of S as the section location is advanced to the right in discrete steps. The S_{min} values are always located at x_1, x_2, x_3, x_4. In the detail fracture model, the calculation is started at $x = -100$ inches and is carried out in one-inch steps.

The RSO live stress spectrum for a train can now be constructed in accordance with the following procedure. First, a consist is defined from a menu of representative cars and locomotives. The menu contains the dimensional information needed to establish the wheel spacings, together with the empty (W_E) and loaded (W_L) weight for each vehicle type. Appendix B contains the vehicle menu and consists used in the present study. The static vertical wheel loads for each vehicle are then computed from:

$$V = \frac{1}{8}\left[W_E + L.F.\,(W_L - W_E)\right] \tag{81}$$

for four-axle vehicles, or

$$V = \frac{1}{12}\left[W_E + L.F.\,(W_L - W_E)\right] \tag{82}$$

for six-axle vehicles, where $0 \leqq$ L.F. $\leqq 1$ is the vehicle's load factor.. (Groups of four, five or six wheels must be dealt with in the stress analysis depending on the consist details.) As the load sequence is being created, the vehicle weights are also summed and converted to gross tons to provide the correct engineering scale factor for crack growth life. The static vertical loads are then modified to incorporate dynamic (Section 4.1.1) and lateral (Section 4.1.2) load effects, or to account for extreme loads (Section 4.1.3).

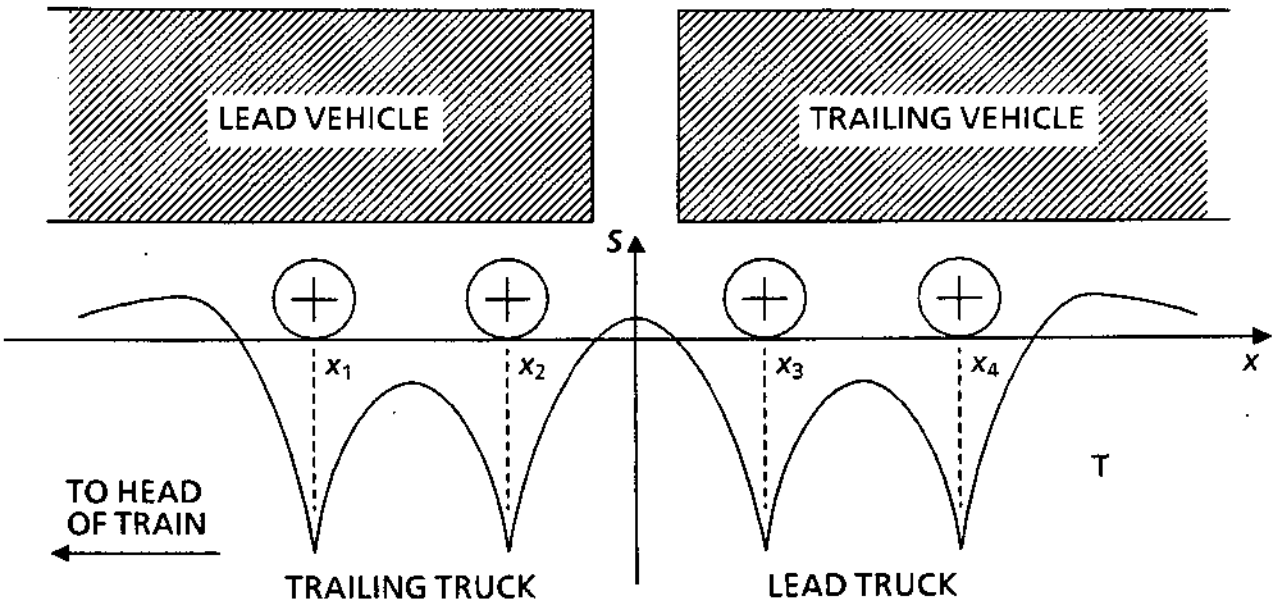

FIGURE 20. STRESS CYCLE PATTERN FROM ADJACENT TWO-AXLE TRUCKS.

4.1.1 Dynamic effects on vertical load

Carbody and truck dynamic motions (pitch, bounce, and rocking) cause the wheel loads to vary at frequencies up to 10 Hz. For a given static wheel load V, this dynamic load $V \pm V_D$ can be modelled as a Gaussian random process with probability density functions of the form:

$$p(V \pm V_D) = \frac{1}{c_v V\sqrt{2\pi}} \exp\left[-\frac{(\pm V_D)^2}{2(c_v V)^2}\right] \tag{83}$$

where the coefficient of variation c_v scales the root mean square dynamic increment in terms of the static load. Values of c_v can be determined empirically by performing Monte Carlo simulation to match computed load occurrence histograms to measured load histograms.

In practice, it is necessary to employ a two-sided Gaussian distribution to account for the observed difference between dynamic load increments and decrements, and separate distributions are usually required to match the behavior of lightly and heavily loaded cars. Figure 21 illustrates the combined probability model concept.

This four-parameter Gaussian model was applied to FAST dynamic loads data which was gathered before the FAST crack growth test was performed. Figure 22 illustrates the result obtained with $(c_{v1}, c_{v2}, c_{v3}, c_{v4}) = (0.0, 0.5, 0.4, 0.2)$ in a Monte Carlo simulation which processed the consist "CTEST1" shown in the accompanying table. The

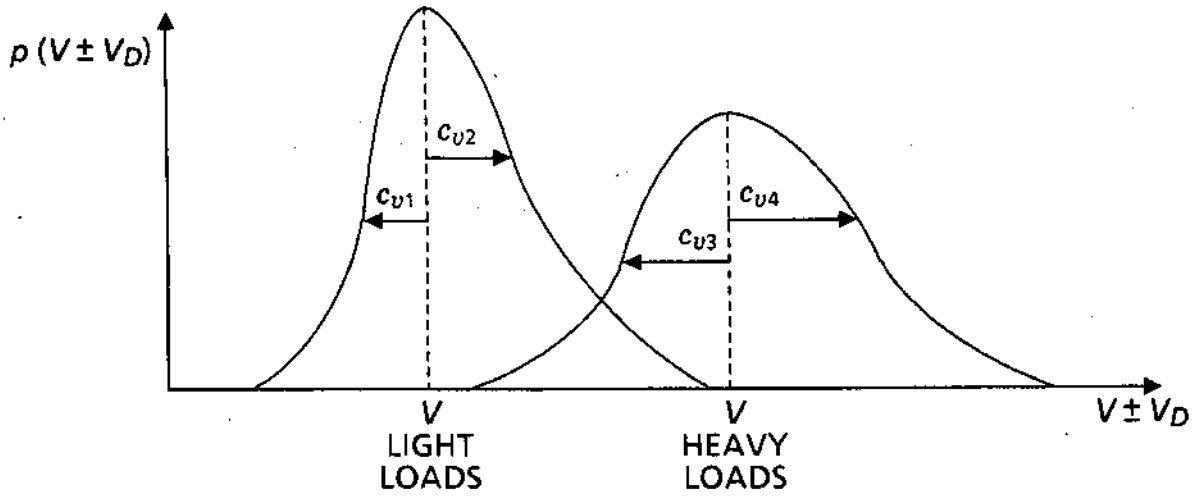

FIGURE 21. FOUR-PARAMETER GAUSSIAN MODEL FOR WHEEL-RAIL DYNAMIC LOADS.

OCCURRENCES PER THOUSAND WHEELS

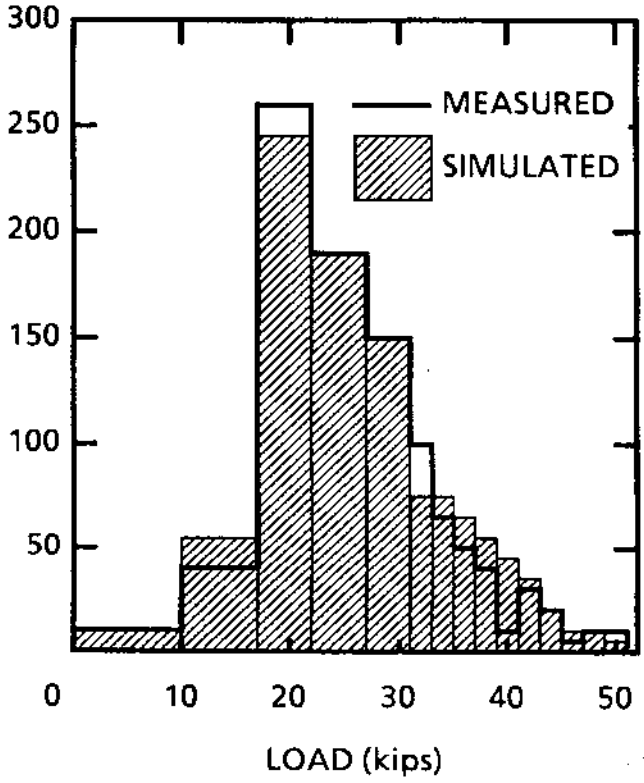

SIMULATION - 27.2 kip AVERAGE
MEASURED - 27.7 Kip AVERAGE

Train Makeup ("CTEST1")

Type	LF†	No.‡	Tons/car	Total tons
LOCO1	1.0	4	125.0	500.0
OHOP1*	0.5	15	83.1	1246.5
TANK1	1.0	2	157.0	314.0
BOXNW	1.0	2	134.5	269.0
OHOP1	1.0	15	131.5	1972.5
BOXNP	1.0	2	110.0	220.0
BOXNW	1.0	2	134.5	269.0
OHOP1*	0.5	10	83.1	831.0
TANK1	1.0	3	157.0	471.0
BOXNW	1.0	2	134.5	269.0
BOXNP	1.0	1	110.0	110.0
OHOP1	1.0	10	131.5	1315.0
TANK1	0.2	2	62.44	124.88
BOXNW	1.0	2	134.5	269.0
BOXNP	1.0	1	110.0	110.0
TANK1	0.2	2	62.44	124.88
OHOP1	0.5	10	83.1	831.0

Total vehicles	85
Total axles	340
Gross tons	9,246.76
Average wheel load (kips)	27.2

†LF = load factor
‡Number of identical vehicles grouped together.

FIGURE 22. APPLICATION OF FOUR-PARAMETER MODEL TO FAST LOADS DATA.

results for c_{vi} are considered to constitute a calibration of vehicle dynamic behavior on the FAST loop during the operational era which included the detail fracture growth test. The average wheel load increased during this era, however, from 27.7 kips to almost 31 kips. Therefore, the train spectrum for simulation of the test environment was constructed by increasing the load factors from 0.5 to 1.0 for the two groups of cars marked by asterisks in Figure 22. The revised consist, "CTEST2", has an average wheel load of 30.8 kips (see Appendix B), but the c_{vi} values quoted above are used to generate the train load spectrum. The FAST load histogram was constructed from wayside measurements made on a concrete-tie tangent section of the track [39].

Using a four-parameter simulation to reconstruct RSO loads leads to a different set of statistics than one finds from analysis of aggregate data. For example, a two-sided Gaussian model (c_v^-, c_v^+) of a histogram defined by:

$$c_v^- = \frac{1}{V_{AV}}\left[\frac{\sum n_i(-V_{Di})^2}{\sum n_i}\right]^{1/2} \quad ; \quad c_v^+ = \frac{1}{V_{AV}}\left[\frac{\sum n_i(+V_{Di})^2}{\sum n_i}\right]^{1/2} \tag{84}$$

is the usual method of analyzing aggregate data, where V_{AV} is the average wheel load, $V_i = V_{AV} \pm V_{Di}$ are the measured loads, n_i are the relative occurrence frequencies, and V_{AV} is estimated from:

$$V_{AV} = \left[\sum n_i V_i\right] \div \left[\sum n_i\right] \tag{85}$$

For the FAST loads in Figure 22, Eqs. 84 give (c_v^-, c_v^+) = (0.27, 0.30). The two-parameter model does not properly associate light and heavy car dynamics with light and heavy wheel loads but is useful for making comparisons with revenue track measurements which lack consist information.

Dynamic loads on revenue track have been measured with instrumentation onboard individual cars running over tens to thousands of track miles ("car data"), as well as with wayside instrumentation surveying hundreds to tens of thousands of wheel passages at fixed track locations ("traffic data"). The static wheel load V is known a priori and $V_{AV} \equiv V$ for car data. For traffic data, V_{AV} is close but not precisely equal to the average of the static loads on the wheels in a survey sample.

Both car and traffic data are often summarized in the form of cumulative probabilities $P(V \pm V_D)$, which are related to histogram summaries $p(V \pm V_D)$ by:

$$P(V \pm V_D) = \int_{-\infty}^{V_D} p(V \pm x)\, dx \tag{86}$$

In such cases the 50th percentile load, $V \pm V_D = V_{50}$, is taken as V_{AV} and extreme percentile loads can be used to estimate the coefficients of variation, e.g.:

$$c_v^- \simeq \frac{V_{50} - V_{0.1}}{3.1 V_{50}} \quad ; \quad C_v^+ \simeq \frac{V_{99.9} - V_{50}}{3.1 V_{50}} \tag{87}$$

Applying Eqs. 87 to cumulative probabilities is equivalent to applying Eqs. 84 to the relative occurrence histogram.

Car data is sometimes summarized in the form of level-crossing exceedance curves. Exceedance curves record the absolute frequencies $N(V \pm V_D)$, e.g. the number of times per mile, at which the continuous load measurement exceeds positive levels $V + V_D$ or falls below negative levels $V - V_D$. Exceedance curves are different from probability

curves and must be analyzed differently to obtain the proper statistics. The following idealized example will illustrate the difference.

Assume that the wheel load on a test car has a triangular waveform of constant frequency N_0 Hz between the loads $V_{min} - \varepsilon$ and $V_{max} + \varepsilon$, where ε is a small number. The relative occurrence frequencies $p(V \pm V_D)$ then conform to the uniform probability function (Figure 23), i.e., any load between V_{min} and V_{max} is equally likely to be measured if the sample is taken at a random time. The coefficients of variation for this distribution are given by:

$$c_v^- = c_v^+ = \frac{1}{\sqrt{3}} \frac{V_{max} - V_{min}}{V_{max} + V_{min}} \tag{88}$$

Similarly, the exceedance counting procedure will record N_0 positive exceedances per second of all levels from $V_{AV} = \frac{1}{2}(V_{min} + V_{max})$ to V_{max} and N_0 negative exceedances per second of all levels from V_{AV} to V_{min}. Thus, the exceedance curve $N(V \pm V_D)$ has the same shape as but a different scale than the probability histogram $p(V \pm V_D)$. The exceedance curve is sometimes differentiated to obtain a peak occurrence frequency curve $n(V \pm V_D)$. In the present example, the peak occurrence curve evidently has the form of spikes at V_{min} and V_{max}. It seems natural to conceptually associate the peak occurrence curve with the probability histogram and, therefore, to apply Eqs. 84 and 85 to obtain the statistics of $n(V \pm V_D)$. The association is wrong, however, and leads to erroneous results, for example:

$$c_v^- = c_v^+ = \sqrt{2} \frac{V_{max} - V_{min}}{V_{max} + V_{min}} \tag{89}$$

in the present case instead of Eq. 88.

Proper coefficients of variation can be obtained in principle by applying Eqs. 84 and 85 to the exceedance curve, rather than the peak occurrence curve. In practice, however, the following alternative procedure is more convenient for treating exceedance data which is assumed to be Gaussian but is not specified in a functional form. Let $V_1 = V_{AV} + V_{D1}$ be a point on the curve corresponding to an exceedance rate N_1 and $V_2 > V_1$ be another such point corresponding to the rate $N_2 < N_1$. Then under the hypothesis of Gaussian behavior,

$$N_1 = \tfrac{1}{2} N_0 \exp\left[- \frac{(V_1 - V_{AV})^2}{2 (c_v^+ V_{AV})^2} \right] \; ; \; N_2 = \tfrac{1}{2} N_0 \exp\left[- \frac{(V_2 - V_{AV})^2}{2 (c_v^+ V_{AV})^2} \right] \tag{90}$$

and Eqs. 90 can be combined to solve for c_v^+:

$$c_v^+ = \frac{1}{V_{AV}} \left[\frac{2 \ell n (N_2 / N_1)}{1 - [(V_2 - V_{AV})/(V_1 - V_{AV})]^2} \right]^{1/2} \tag{91}$$

A similar procedure applies to the negative exceedances (V_1, $V_2 < V_{AV}$). Equation 91 is a single estimate of the underlying coefficient. The estimate is improved by reading several sets of data points (V_1, N_1, V_2, N_2) from the curve and taking c_v as the average of the individual estimates. The coefficient of variation of c_v itself,

$$C.V.(c_v) = \frac{1}{c_{vAV}} \left[\frac{1}{m} \sum_{i=1}^{m} (c_{vi} - c_{vAV})^2 \right]^{1/2} \tag{92}$$

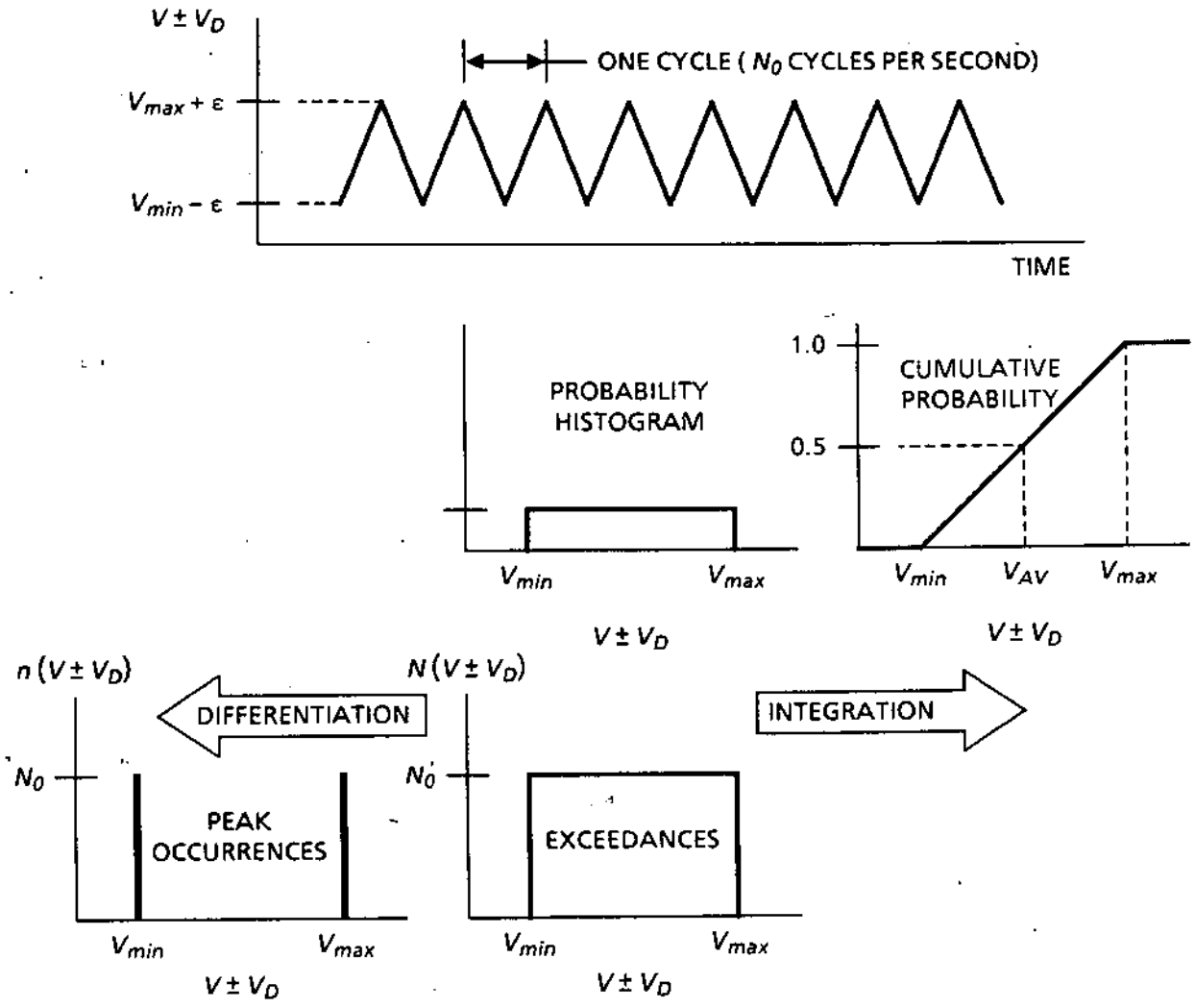

FIGURE 23. ALTERNATE METHODS OF SUMMARIZING DYNAMIC MEASUREMENTS.

also measures the accuracy of the working hypothesis, since C.V.$(c_v) = 0$ if the curve is precisely Gaussian.

The foregoing procedures were applied to the car and traffic data available from a variety of sources [40 – 45]. The measurements include both freight and passenger vehicles on eastern, midwestern, and western revenue tracks, as well as one sample of freight traffic data on the FAST track. Table 21 summarizes these results together with the previous FAST results [39] in order of decreasing average wheel load. The following observations emerge from the summary.

The coefficients of variation are repeatable statistics for the same or similar track and traffic. This is demonstrated by comparing the two FAST measurements (samples 1 and 5).

Comparison of samples 2 and 3 suggests that speed has little effect on car coefficients of variation unless the car is dynamically active in a particular speed range. The tank car that was tested in sample 3 appears to have been dynamically active at high speed. Its positive exceedance curve in the 45 – 60 mph range was strongly non-

Gaussian by virtue of increased exceedance rates for large loads. The investigator attributed this behavior to increased frequency of side bearing contact and/or springs "going solid" [41].

TABLE 21. COEFFICIENTS OF VARIATION FOR DYNAMIC VERTICAL LOAD.

No.	Environment Description	Average Wheel Load (kips)	Speed (mph)	c_v for	
				$-V_D$	$+V_D$
1	FAST, concrete-tie, 1977 [42]; traffic exc. curve	30.5	40 to 45	0.26	0.26
2	Loaded coal hopper car over 1,900 miles on six midwestern and eastern railroads [41]; car exceedance curve	30	15 to 30 30 to 45 45 to 60	0.15 0.13 0.14	0.20 0.17 0.22
3	DOT-112A 33,000-gallon tank car over 114 miles of a midwestern mainline [41]; car exceedance curve	30	15 to 30 30 to 45 45 to 60	0.16 0.17 0.29	0.17 0.25 0.60
4	Hopper car loaded with crushed rock over 182 miles on a western railroad mainline [41]; car cumulative probability curve	30	15 to 30 30 to 45 45 to 60 >60	0.08 0.10 0.11 0.12	0.08 0.10 0.11 0.12
5	FAST, concrete-tie, circa 1977 [39]; traffic histogram (Fig. 21) Simulation for c_{v1} and c_{v2} Simulation for c_{v3} and c_{v4}	27.7	40 to 45	0.27 0.00 0.40	0.30 0.50 0.20
6	NEC, freight, concrete-tie, Edgewood, MD, 1984 [44, 45]; traffic histogram	24.17 24.32	45 to 70	0.38 0.38	0.31 0.33
7	Northeast Corridor, interlocking, passenger and freight, wood-tie, 1975 [42]; traffic exc. curve	20		0.23	0.49
8	Metro-North Railroad, M-2 MU consist, worst 6 miles between New York, NY and New Haven, CT [43]; car cumulative probability curve	18 to 20	35 to 40	0.15	0.15
9	UP, wood-tie, CWR, 1978 [42]; traffic exc. curve	18		0.17	0.47
10	NEC, passenger, concrete-tie, Edgewood, MD, 1984 [44, 45]; traffic histogram	17.86 17.98	70 – 120	0.21 0.22	0.53 0.56
11	FEC, concrete-tie, 1976 [42]; traffic exc. curve	16		0.18	0.55
12	Amtrak Metroliner, MU consist, small data sample on eastern railroad track [40]; car exceedance curve	15 to 17.5	20 to 105	0.02 to 0.05	0.02 to 0.05
13	UP, wood-tie, BJR, 1978 [42]; traffic exc. curve	15		0.14	0.60
14	UP, freight, CWR, 1974 TTD [42]; traffic exc. curve	13		0.23	0.86
15	SP, freight, wood-tie, 1975 [42]; traffic exc. curve	12		0.20	0.79

Comparison of samples 2 and 4 illustrates the effect of varying track conditions on similar cars. The number of miles and railroads included in sample 2 suggests that typical revenue track conditions were surveyed, whereas sample 4 suggests track with excellent surface.

There appears to be no correlation of dynamic loads with wood versus concrete ties. Samples 10 and 11 surveyed traffic at concrete-tie CWR locations on the Northeast Corridor (NEC) and the Florida East Coast (FEC) Railroad. Samples 9 and 14 are traffic surveys at wood-tie CWR locations on the Union Pacific (UP) Railroad with average wheel loads comparable to the averages of samples 10 and 11. The lack of a trend should probably be interpreted only as evidence that some wood-tie track locations can stimulate dynamic activity equal to or greater than the activity at some concrete-tie track locations.

There appears to be no correlation of dynamic activity with bolted-joint rail (BJR) versus continuous welded rail (CWR), but the only clear comparison is between samples 13 and 14. Like the last observation, one should not read into this comparison anything beyond the fact that some CWR locations can cause as much activity as some BJR locations.

Lightly loaded cars tend to be more active than heavily loaded cars. Heavy loading (30-kip static wheel load) is represented by sample 2, medium loading (24 and 18 kips) by samples 6 and 9, and light loading (15, 13, and 12 kips) by samples 13, 14, and 15. There is no clear trend in the negative exceedances, but c_v+ tends to increase as the static or average wheel load decreases. The foregoing samples pertain to freight cars. A similar trend appears in the comparison of freight versus passenger traffic on the same track (samples 6 and 10), although part of the effect in this case might be attributed to the difference in operating speed. Part of the increase in c_v+ at low average load may be an apparent dynamic effect which actually reflects the dispersion of static loads on the wheels sampled.

The passenger vehicle data (samples 8, 10, and 12) require careful interpretation. Sample 12 came from the Metroliner Improvement Program. It thus represents a well maintained suspension with an optimized design, i.e., the best case to be expected for the performance of cars with secondary suspensions. The other samples represent typical service conditions. In spite of the fact that the M-2 car has a reputation as having relatively high dynamic activity, especially on track with poor surface like the test track in sample 8, the surprising result is that the NEC passenger traffic at Edgewood (sample 10) exhibits much more dynamic activity than the M-2 car. Part of the explanation might be the speed difference, yet the difference between well maintained CWR at Edgewood and poorly surfaced track with a high density of interlockings in the M-2 test tends to compensate for the speed effect. The likely explanation of the high NEC activity is a high proportion of Heritage Fleet cars in the traffic. In general, one can infer that the newer passenger rolling stock (Amfleet and MU commuter cars) is much less active as well as much less heavily loaded than freight rolling stock. Therefore, the effect of passenger traffic on rail defect growth need be considered only for track dedicated to passenger service.

The NEC traffic data from Edgewood (samples 6 and 10) included small numbers of extreme loads caused by wheels that were later found to have anomalous circumferential profiles (see discussion in [4]). Based on $V + V_D > 50$ kips as a working definition of extreme load, 0.4 % of the freight wheel loads and 0.2 % of the passenger wheel loads in the samples were extreme. The largest loads in these samples did not exceed 80 kips, although some loads in other samples were estimated to have exceeded 100 kips when the instrumentation was saturated. Two calculations of (V_{AV}, c_v−, c_v+) are shown for each sample. In each case, the first result was obtained from the non-extreme data only, while the second result included the extreme data. These examples illustrate the effect of V_{AV} bias mentioned earlier.

The simulation results are included in the table for comparison with sample 5 to illustrate the fact that the coefficients of variation which provide a good RSO simulation of aggregate behavior are quite different from the aggregate coefficients. In general, one must experiment with the consist and simulation coefficients to match an aggregate behavior.

4.1.2 Lateral loads

The inability of wheels to maintain pure rolling motion when wheelsets with stiff longitudinal restraint negotiate curved track is the major source of lateral wheel/rail loads. Experiments involving instrumented track and test consists and analyses [46, 47] have shown that the largest lateral loads occur between the lead axle of each truck and the high rail of the curve. Based on this research, a relationship between track curvature and *L/V* for the lead wheel on the high rail has been developed for fully loaded 100-ton freight cars. Table 22 summarizes the relationship in a form convenient for linear interpolation for track curvatures between 2.9 and 13.5 degrees.

TABLE 22. VALUES OF *L/V* FOR LOADED 100-TON CARS (V = 33 kips) AS A FUNCTION OF TRACK CURVATURE.

Gentle Curves		Medium Curves		Sharp Curves		Very Sharp Curves	
°C (a)	*L/V*	°C (a)	*L/V*	°C (a)	*L/V*	°C (a)	*L/V*
2.9	0.182	3.7	0.242	8.0	0.409	11.5	0.472
3.1	0.212	4.6	0.302	8.4	0.416	12.0	0.475
3.4	0.222	5.8	0.364	9.5	0.445	12.5	0.478
		7.5	0.406	10.0	0.451	13.0	0.481
				11.0	0.465	13.5	0.485

[a] Track curvature in degrees = 5730 ÷ (radius of curvature in feet).

The data in Table 22 characterizes steady-state performance on dry rail. Well controlled rail flange lubrication can increase the steady-state *L/V* ratio by as much as 10 % to 15 % above the dry value, while lubrication on the rail running surface can decrease the steady-state *L/V* ratio by as much as 60 % below the dry value [48]. Truck hunting and engagements with track alignment and/or gage irregularities can generate dynamic *L/V* ratios well above the steady-state value, with infrequent peaks as high as *L/V* = 1 on tangent track and *L/V* = 2 on curved track [46, 47].

The dynamic activity of lightly loaded cars relative to heavily loaded cars appears to affect lateral as well as vertical loading. Observations by the FAST technical staff have suggested that, for the same speed and track condition, *L/V* for an empty car ($V \approx 8$ kips) tends to be about 50 % larger than *L/V* for a loaded 100-ton car [49]. The light load effect can be accounted for by the empirical magnification factor:

$$M_{L/V} = \frac{83 - (V \pm V_D)}{50} \tag{93}$$

where the vertical load $V \pm V_D$ is in units of kips.

The effects of extreme peak *L/V* require consideration only in the assessment of critical crack size, but the steady-state lateral loads must be included in the analysis of safe crack growth life. Steady-state lateral loads are normally associated only with

curved track, since it is only on curves that L/V routinely attains values large enough to create the risk of gage-widening or rail rollover failures. However, there is also a small steady-state lateral load on tangent track ($0.025 \leqq L/V \leqq 0.05$) which arises from the combination of wheel profile and tie-plate cant. The tangent-track L/V is too small to be of concern for gage widening or rail rollover but is potentially an influential factor on the safe crack growth life of rail defects.

The foregoing effects are easily incorporated in RSO train load spectra after the static vertical loads have been processed as described in Section 4.1.1. For analysis of tangent track, one should assign a lateral load to each vertical load based on a constant factor $0.025 \leqq L/V \leqq 0.05$. For curved track, the factor $M_{L/V}(L/V)$ with L/V interpolated from Table 22 should be assigned to the lead wheel of each truck, while the tangent-track factor is assigned to the trailing wheels.

4.1.3 Extreme loads

Wheels with fresh flat defects and wheels on which flats have been pounded to out-of-round anomalies can create excessive dynamic loads on track. The current AAR interchange rules do not define the out-of-round anomaly as a defect and, in fact, such anomalies are difficult or impossible for car inspectors to detect visually. On the other hand, dynamic load measurements and wheel circumference measurements during followup wheel truing have shown that out-of-round anomalies are the major cause of wheel overloads on the Northeast Corridor and the Florida East Coast Railroad [44, 50].

Figure 24 summarizes some of the Northeast Corridor measurements. The normal variation of wheel loads caused by weight differences and car motions ranged from 10 to 40 kips in the data. The samples reflect typical consist characteristics: a combination of heavy loads and empties for freight and concentration around a median static loading for passenger traffic. The anomalous wheel loads, which ranged from 50 to 80 kips in these samples, occur much less frequently than the normal loads. Also, the distinction between consist characteristics disappears in the anomalous load range. This indicates that the overloads are related to unsprung wheelset mass rather than car weight, since there is relatively little variation in the wheelset masses. In the aggregate, the data implies that anomalous wheel overloads occur at the rate of about three per thousand axle passages.

Other samples have included counts of overloads with magnitudes up to 100 kips, the point at which the instrumentation saturates. Therefore, there is some suspicion that overloads exceeding 100 kips may occur on occasion.

The effect of extreme loads on defect growth life is simulated in the detail fracture model by arbitrarily assigning an overload factor (number of multiples of static load) to selected axles. Overload factors from 2 to 3 should be used on one or two axles in a consist to represent typical magnitudes and occurrence frequencies.

4.2 Thermal stress

Thermal stress is developed in CWR via the difference between rail neutral temperature T_n and rail service temperature T. For fully restrained CWR in tangent track, the thermal stress was given in Section 2.1 as:

$$S_T = E\alpha (T_n - T) \tag{1}$$

where E is Young's modulus, α is the coefficient of linear thermal expansion, and $E\alpha \approx 0.195$ ksi per Fahrenheit degree for rail steel. The thermal stress fluctuates in response to diurnal and seasonal changes of T and T_n. In principle, these thermal stress cycles can drive the propagation of a detail fracture, just as the live-load stress cycles do. In practice, one year of thermal stress cycles generally has somewhat less effect than the live-load stress cycles from one train. It is reasonable to neglect the thermal

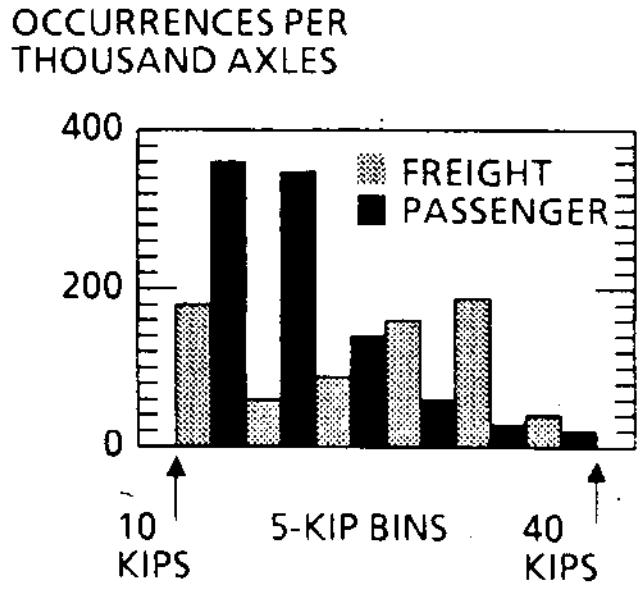

(a) Static Load and Car Dynamic Motion Effects

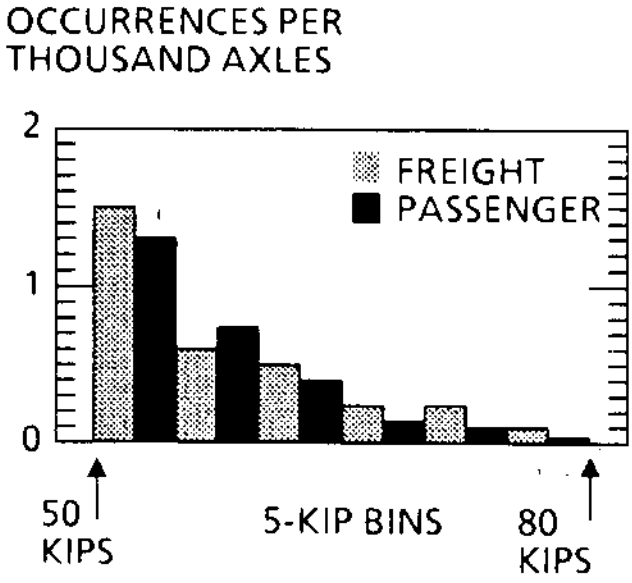

(b) Defective Wheels

FIGURE 24. WHEEL OVERLOADS ON THE NORTHEAST CORRIDOR.

stress cycles, therefore, and to consider only the effect of S_T as a slowly varying mean stress which is superimposed on the live-load stress cycles.

Rail service temperature histories can be estimated from weather data. For example, the U.S. Weather Service publishes daily weather records each month by state. The daily records include high and low ambient temperature, precipitation, and other data for numerous locations. The ambient temperatures are obtained from thermometers that are shielded against exposure to direct solar radiation. Conversely, track is exposed to direct insolation, and rail can reach temperatures 20 to 50 °F higher than the ambient temperature on days with partial sky coverage or clear weather. Therefore, one can take the daily high rail service temperature to be 30 °F above the daily ambient high, except on days for which the records indicate significant precipitation. On days with precipitation and for all nights, the rail service temperature can be taken as equal to the ambient temperature. This procedure gives a rough average of the insolation effect; it does not account for the few cases in which a rapidly moving front might have caused the daily ambient low to occur during the day, or in which night radiational cooling is strong enough to reduce the rail service temperature below the ambient low.

The foregoing procedure was applied to twelve months of Weather Service data, covering the period July 1, 1979 through June 30, 1980, for Broken Bow, Nebraska. Broken Bow is located on the Alliance Division of the Burlington Northern Railroad (a major coal route) and represents typical severe mid-continent climate in the Northern Plains.

Figure 25 illustrates the resulting histograms for daytime and nighttime occurrences of $\Delta T = T_n - T$ obtained from the Broken Bow records, where it is assumed that the rail neutral temperature is constant, $T_n = 60$ °F. The value of 60 °F represents the long-term trend for typical undisturbed tangent track. Under the given assumption, it appears that CWR would be mainly in thermal compression during the day and mainly in thermal tension at night. Figure 26 summarizes the results in terms of monthly averages to illustrate the seasonal effect on rail service temperature. Figure 27 compares the Broken Bow weather with a hypothetical mild environment for which the seasonal variation has been taken equal to half the Broken Bow variation. In this figure, the day and night values of $T_n - T$ have been averaged.

The variation of T_n in both time and location depends on the interaction of such diverse factors as track disturbance during tamping, local destressing of CWR strings when individual rails are replaced, roadbed freeze-thaw cycles, the rolling out of rails by plastic deformation in the rail head caused by wheel-rail contact loads, and the dynamic forces exerted on the rails by passing trains. There is no model available for the prediction of T_n in the general case, but the mechanics equations for changes of T_n via curve radius adjustment have been formulated [5]. A simplified version of that formulation relates the current temperature differential to the track lateral resistance:

$$| \Delta T | = | T_n - T | = \frac{(f_\ell / \ell)\, R}{2EA_R \alpha} \tag{94}$$

where f_ℓ is the peak track lateral resistance per tie, ℓ is the tie center spacing, and R is the curve radius. The current neutral temperature is assumed to be maintained as long as $| \Delta T |$ does not exceed the limit in Eq. 94. If the limit is exceeded, then f_ℓ is replaced by the minimum resistance capacity, and a new value of T_n is calculated such that Eq. 94 is exactly satisfied. The peak and minimum resistances are to be understood as the equivalent of a stick-slip friction model. The track is constrained to build up thermal stress until the thermal force overcomes the peak resistance. When the peak resistance

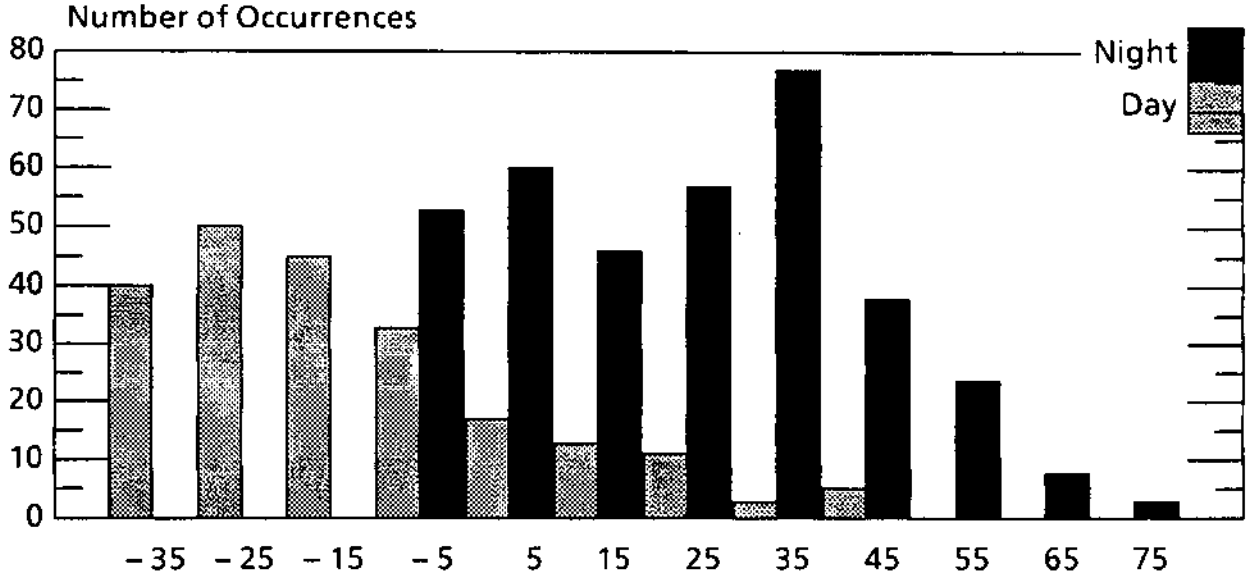

ΔT (°F) for $T_n = 60$ °F (Values define bin centers. Bin widths are ± 5 °F.)

FIGURE 25. OCCURRENCES OF $T_n - T$ AT BROKEN BOW, NE (7/1/79 – 6/30/80).

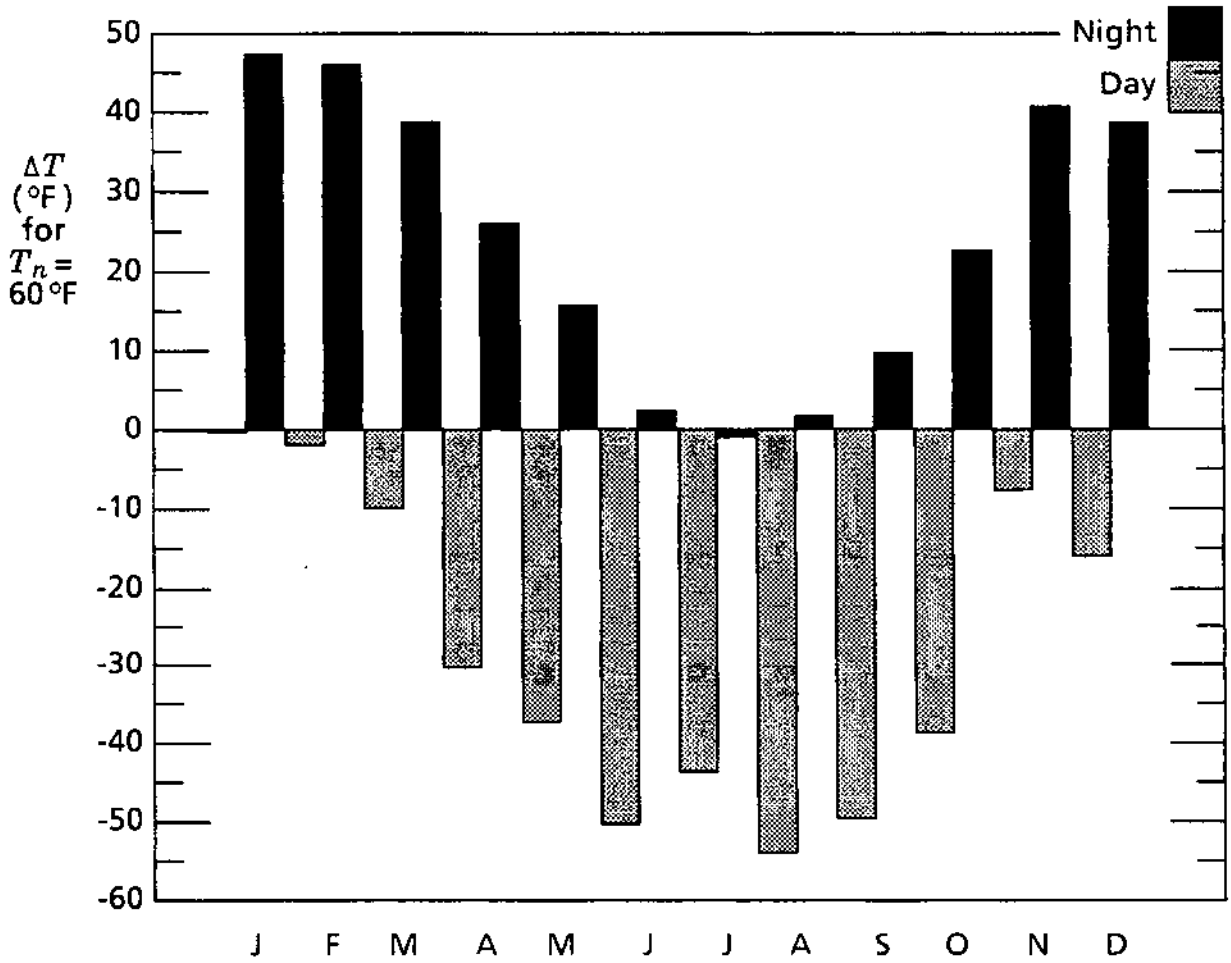

FIGURE 26. SEASONAL EFFECT AT BROKEN BOW.

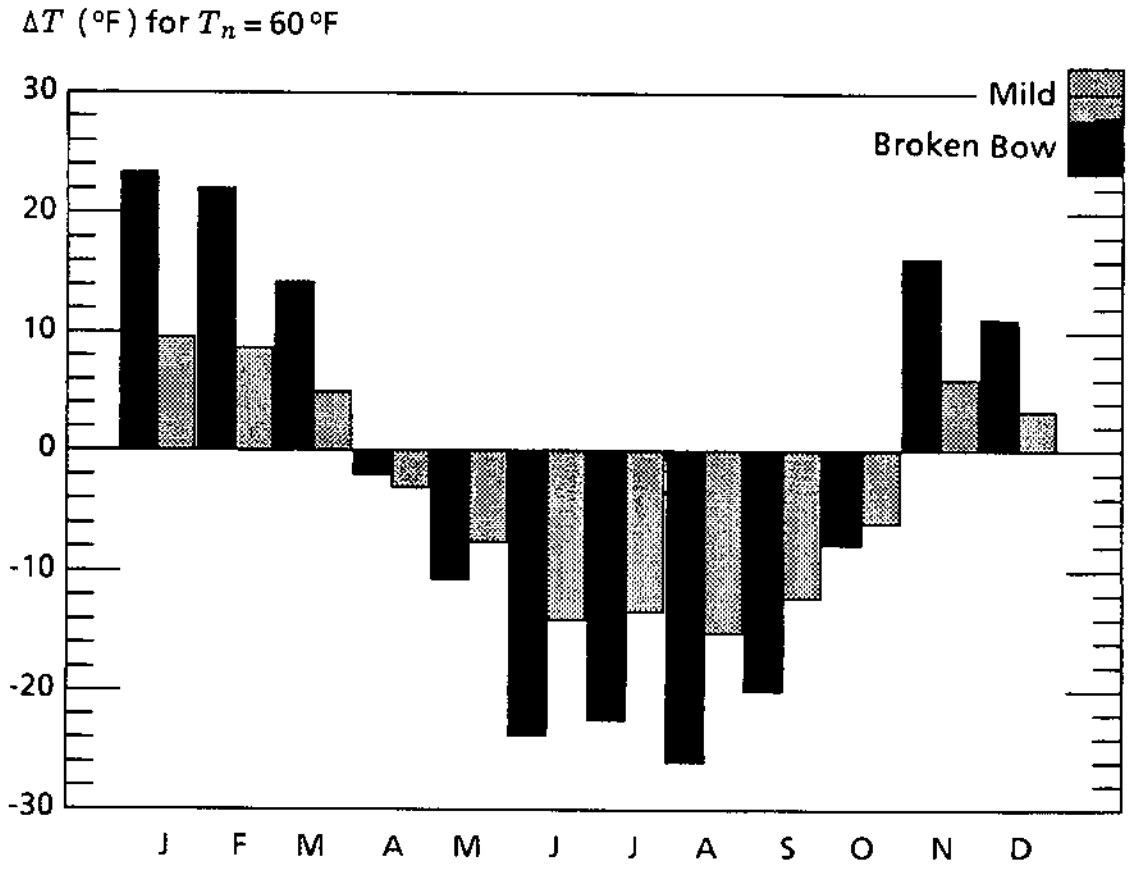

FIGURE 27. BROKEN BOW COMPARED WITH HYPOTHETICAL MILD CLIMATE.

is overcome, the curve radius increases or decreases, as required, until the thermal force has been relieved just enough to balance the track against the minimum resistance.

Example calculations of neutral temperature history were based on the Broken Bow weather records. The rail was assumed to have been newly laid on July 1, 1979, and the ballast was assumed to have been in a disturbed state on that date. The initial neutral temperature was assumed to have been 90 °F, i.e., in the range of conventional practices for CWR installation. Additional ballast disturbances were assumed to have occurred on March 9, 1980 (spring thaw) and April 15, 1980 (resurfacing). The ballast was assumed to have been frozen on all days for which three-day running averages of the daily ambient high and low temperatures were less than 40 and 32 °F, respectively.

Table 23 summarizes the basic resistance capacities used in the calculations. It is assumed that the track has less resistance to inward than to outward motion, reflecting the common practice of having ballast shoulders wider on the outside than the inside of a curve. Ballast disturbance and subsequent consolidation by traffic were modeled by dropping the peak resistances to the corresponding minimum values on the disturbance date and then linearly increasing the resistance back to the peak value over a 2 MGT interval. Frozen ballast was modeled by increasing the basic resistances by a factor of four.

Calculations were made for 5 and 10 degree curves laid with 132 RE rail on ties with 20-inch center spacing. The track was assumed to carry 30 MGT per year. Figures 28 and 29 illustrate the nighttime and daytime $T_n - T$ occurrence histograms. Corresponding histograms for tangent track (assumed to maintain $T_n = 90$ °F

throughout the year) are included for comparison. This assumption is not realistic, but the comparison provides a useful illustration of the compensating effect of the neutral temperature changes in the curved track model. Figure 30 illustrates the T_n histories calculated for the curves. The episodic character of the neutral temperature changes is probably nothing more than an artifact of the model.

Bolted-joint rail with conventional mechanical joints is not subject to significant thermal tension because the rails are generally able to slide through the joints at longitudinal stress levels of the order of 1 ksi, and because there is sufficient sliding play per joint to accommodate cold-weather contraction of the rails. The KCS field test rail (see Table 7 on page 13) provides an example of detail fracture growth in a bolted-

TABLE 23. BASIC LATERAL RESISTANCES ASSUMED FOR CURVED TRACK.

Direction of Motion	Outward	Inward
Peak resistance (a)	1200	600
Minimum resistance (a)	600	300

[a]Resistances in lb. per tie.

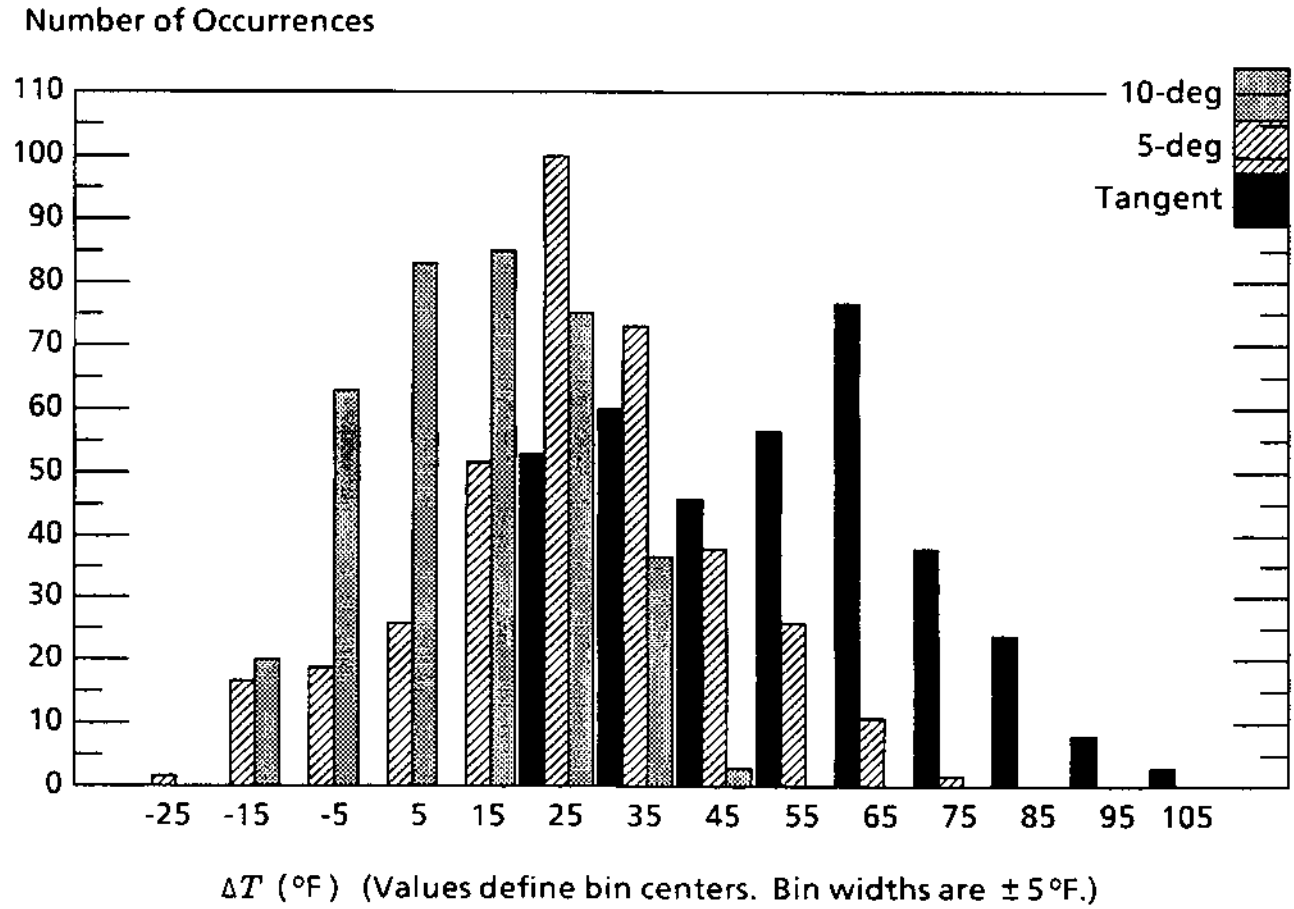

FIGURE 28. EFFECT OF RADIAL BREATHING ON NIGHTTIME $T_n - T$ OCCURRENCES.

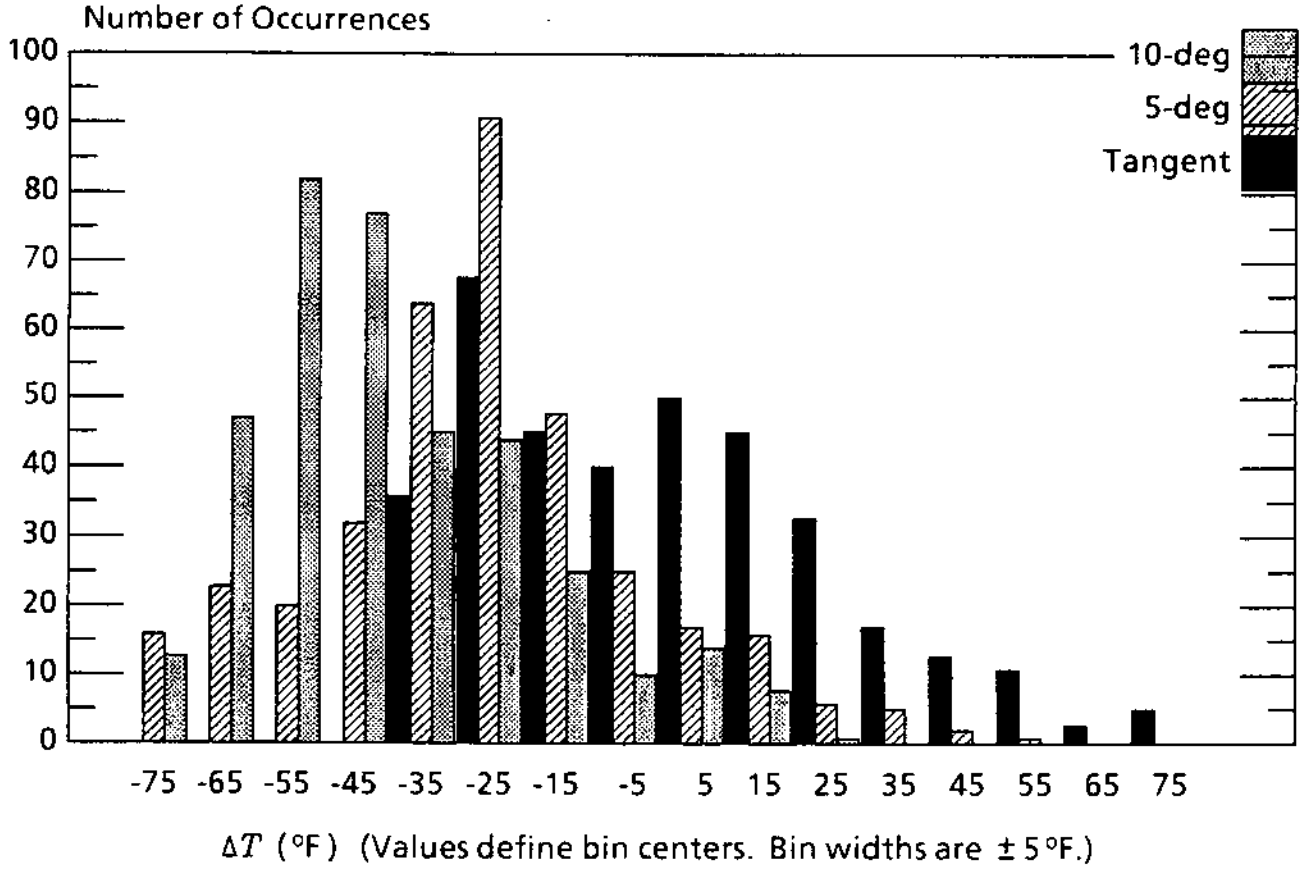

FIGURE 29. EFFECT OF RADIAL BREATHING ON DAYTIME $T_n - T$ OCCURRENCES.

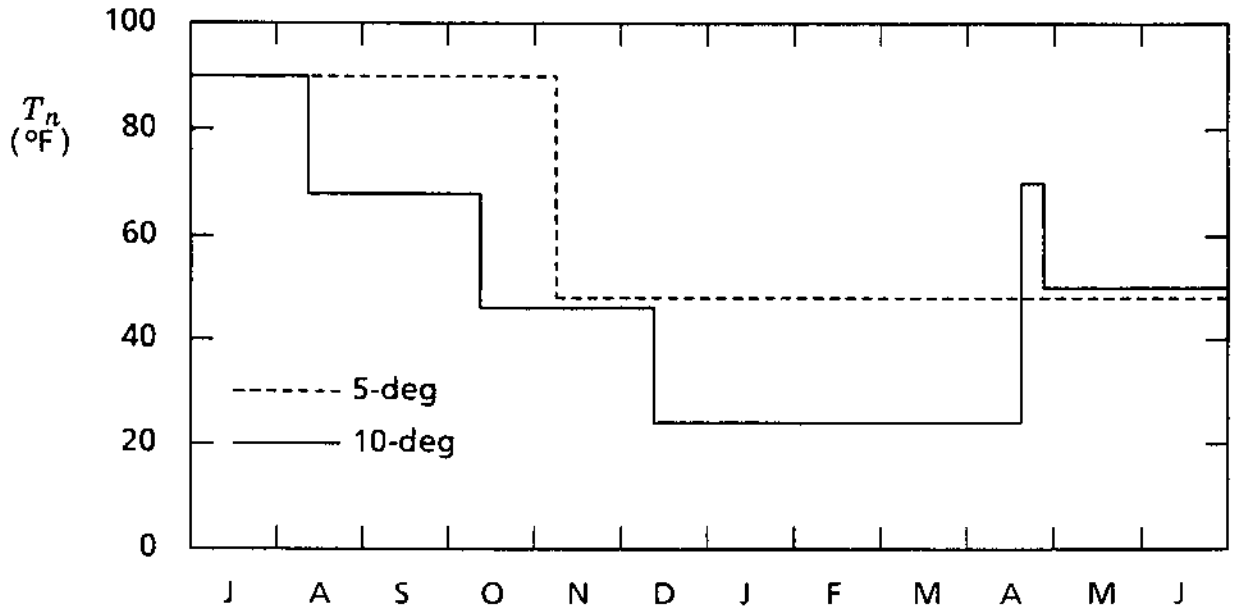

FIGURE 30. NEUTRAL TEMPERATURE HISTORIES.

joint rail. A plot of the defect size versus tonnage is shown in Figure 31. In this case the rate of growth decreased as the crack grew, whereas the FAST test detail fractures in CWR exhibited increasing growth rates (see Figure 3 on page 6). The decreasing growth rate suggests that the KCS rail defect was driven only by live-load and residual stresses, the latter being relieved as the crack grew.

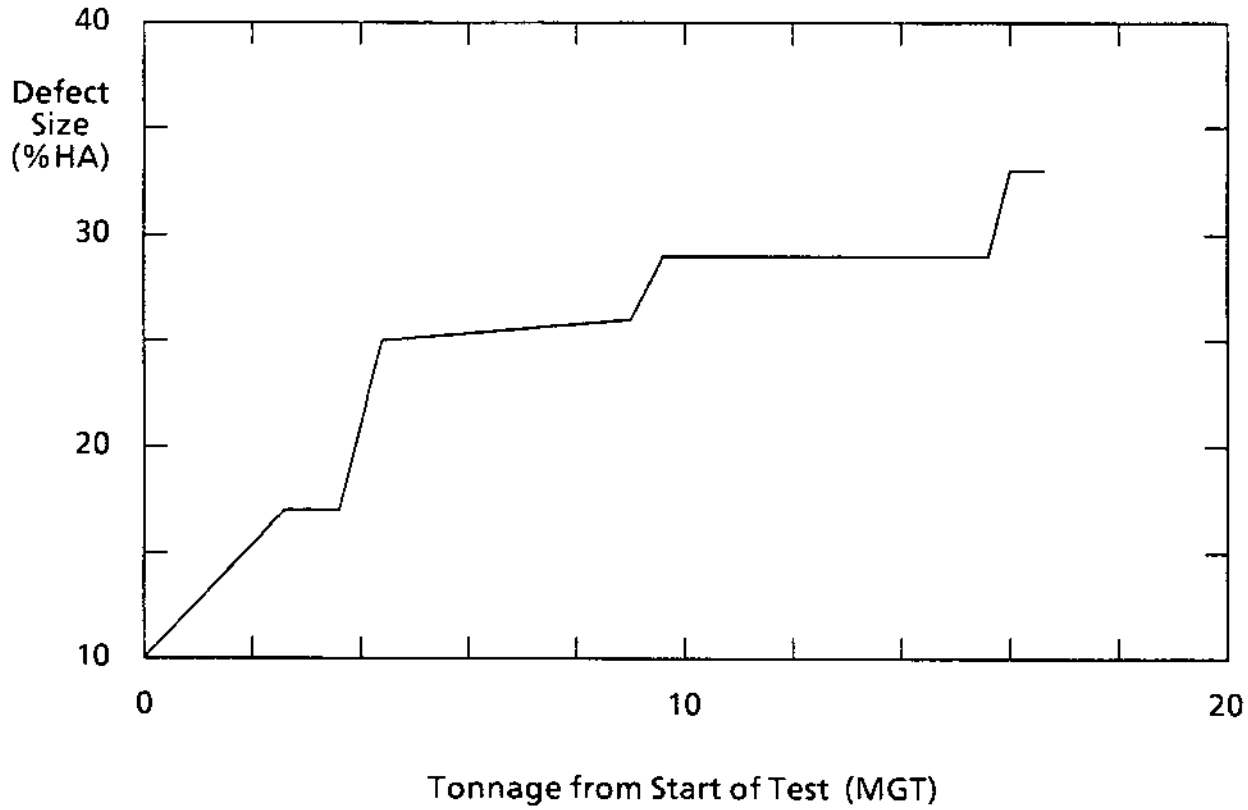

FIGURE 31. HISTORY OF GROWTH OF DETAIL FRACTURE IN KCS TEST RAIL.

4.3 Residual stress

An approximate fracture mechanics model for the crack-driving effect of residual stress was presented in Section 3.2.2, and an empirical relation for the equivalent uniform tension S_R was derived from the available experimental data. However, the experimental results were limited to one sample of the 136 RE section (test rail 1) and one sample of the 127 DY section (the KCS test rail), both of which were tangent rails of standard composition, not heat treated, and not roller straightened. How should the model be adjusted to account for lighter or heavier sections, curve effects, alloy compositions or heat treatments that increase the material strength in the rail head, or the initial residual stresses induced by roller straightening? A simplified elastic-plastic model of the residual stresses caused by wheel-rail contact was developed to provide some general guidelines. A more accurate model based on a finite element method was then formulated to provide detailed stress predictions. Both models treat the rail as an elastic - perfectly plastic medium.

In the simplified model, wheel-rail contact is represented by an elastic stress field derived from the classical Hertz contact formulae [24]. The elastic field is applied at a single location, and a point-by-point elastic-plastic analysis is performed as the contact load is applied and then removed in a single load cycle. Each point analyzed lies directly below the center of contact; along this locus the longitudinal, lateral, and vertical

stresses are principal stresses and, therefore, the elastic-plastic analysis can be done in principal stress space. Analysis of only a few points in isolation from each other lacks the proper enforcement of equilibrium and continuity conditions in the rail section.

The analysis is further simplified by using the Tresca yield conditions:

$$|S_i - S_j| = Y \tag{95}$$

where S_i and S_j are pairs of the principal stresses and Y is the material yield strength, used here as a flow stress instead of the average of the yield and ultimate strengths. The Tresca conditions comprise a right hexagonal cylinder in principal stress space; its axis passes through the origin and makes equal angles with the principal stress axes.

A path representing load application and removal appears as a sequence of vectors in principal stress space (Figure 32). The initial path is elastic (OA), and its direction is determined solely by the ratios of the elastic contact stress components. After the material yields, the actual path is a projection of the extended elastic path onto one of the Tresca planes (AB) or edges (BC). When the load is removed, the stress path (CD) is elastic and thus parallel to the initial path (OA). In some cases the unloading path may reach another Tresca plane or edge, and further unloading entails reverse plasticity along another projected path (DE). The entire path OABCDE can be calculated from the geometry of the Tresca surface. The location of the state corresponding to maximum load (C) is determined by the peak pressure at the center of contact on the surface. Also for this surface point, the final state (D or E) must lie in the longitudinal-lateral stress plane, since the vertical stress at the surface must return to zero when the load is removed. This condition determines the locations of the other final states (D or E) for points below the surface. Details of the model are contained in Appendix C.

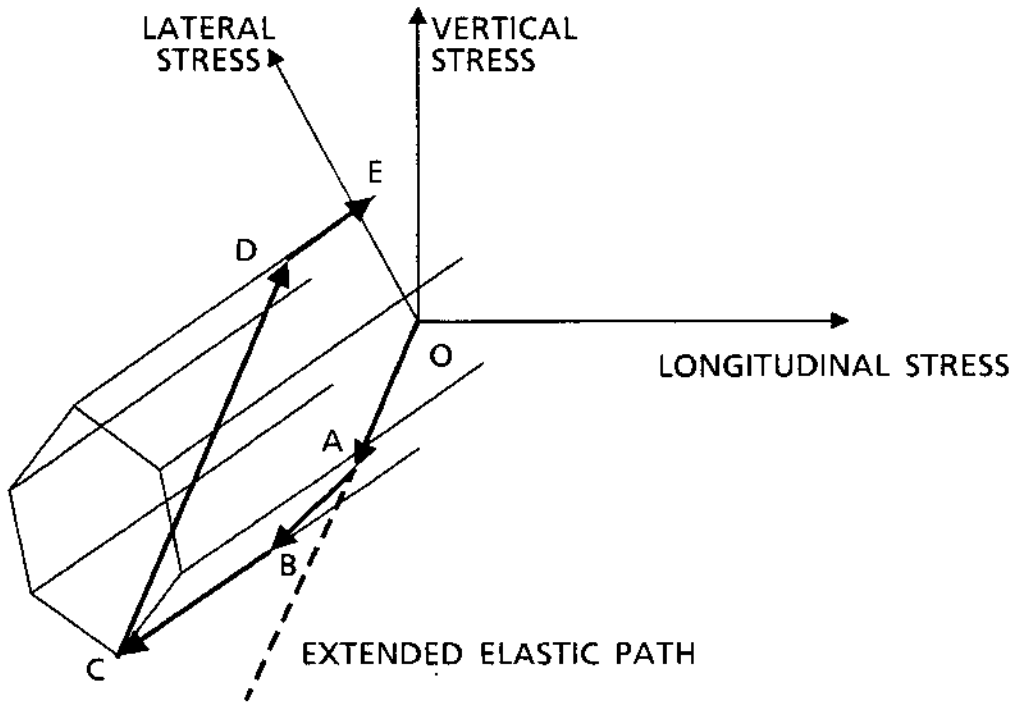

FIGURE 32. ELASTIC - PLASTIC PATH IN PRINCIPAL STRESS SPACE.

The Hertz contact solutions for crossed and parallel cylinders [24] are combined to derive the elastic stress field. The crossed-cylinder solution is used to determine the peak pressure and the major and minor axes of the idealized elliptical contact region. The stress distributions from the parallel-cylinder solution are then used to scale the contact stress field with depth. This combination was suggested by the results recently obtained from a shell crack nucleation model [51].

The simplified model was applied to three cases representing the maximum static wheel loads for freight cars with different capacities (Table 24). The first two cases represent actual rolling stock, while the third represents a hypothetical 125-ton capacity car. Figure 33 shows the calculated longitudinal stress as a function of depth below the surface. Plots abstracted from the experimentally determined stress contours measured on test rail 1 and the KCS test rail are included for comparison. Since there are no definitive center-of-contact locations for these test rails, the abstracts were made along lines passing through the most deeply developed part of the residual tension region in each case, viz: halfway between the center plane and the gage face for test rail 1, and at the center plane for the KCS test rail (see Figure 34).

TABLE 24. CASES ANALYZED WITH SIMPLIFIED MODEL. (a)

Car Capacity (tons)	Wheel Load (Kips)	Wheel Diameter (in.)	Contact Ellipse Dims. (b)		Peak Contact Pressure, p (ksi)	$p \div Y$ (c)
			a (in.)	b (in.)		
70	27.5	33	0.499	0.148	178	2.54
100	33.0	36	0.543	0.157	184	2.63
125	41.0	40	0.601	0.169	192	2.74

[a]All cases analyzed for rail crown radius of 10 inches.
[b]Axes a and b are semi-major (longitudinal) and semi-minor (lateral) axis, respectively.
[c] $Y = 70$ ksi used as material flow stress.

At the surface, the simplified model does not agree with the experimental data, a result which can probably be attributed to different longitudinal-to-vertical stress ratios in the model and the rail. At depths exceeding 1/4 inch, however, the model and experiment are in reasonable agreement and would be even closer if the experimental data had been extrapolated to smooth curves of stress versus depth.

In the finite element model [52], the whole rail section is analyzed, and the conditions of equilibrium and continuity are rigorously enforced at a large number of discrete points in the section. The residual stress field is assumed to be invariant in the longitudinal direction but is unrestricted in the lateral and vertical directions. Longitudinal, lateral, and vertical normal stresses plus shear stresses in the plane of the section are included in the model. The two out-of-plane shear stresses are assumed to be absent, a hypothesis consistent with the assumption of longitudinal invariance.

The wheel-rail contact load is modeled as a surface pressure biparabolically distributed over a rectangular contact region. For convenience the center of contact is made to coincide with a finite element boundary, and the contact rectangle extends one element width to each side. The length of the rectangle is then adjusted to make its area equal to the elliptical area calculated from the crossed-cylinder Hertz contact solution for the same load.

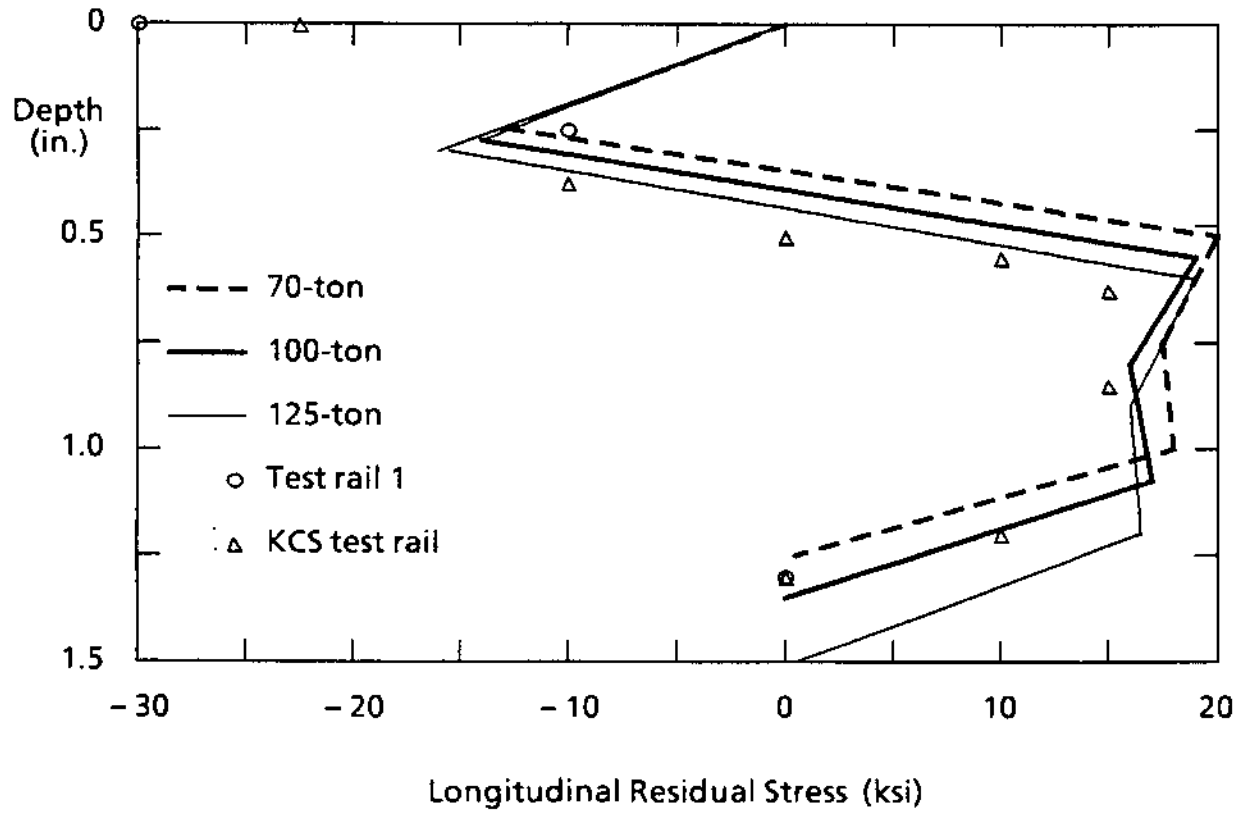

FIGURE 33. COMPARISON OF EXPERIMENTAL STRESSES WITH RESIDUAL STRESSES CALCULATED FROM SIMPLIFIED MODEL.

In a conventional finite element analysis, polynomial interpolations of stress and/or displacement in a typical element are substituted into a mechanical energy expression, the formal minimization of which leads to a set of linear algebraic equations that are solved for the numerical values of stress and/or displacement at discrete points [53]. Minimizing the energy expression is equivalent to enforcing the equilibrium and continuity conditions.

In the present model, however, the energy expression itself is retained and used as an objective function whose minimum is sought, via a search procedure, subject to nonlinear conditions of constraint. The constraints require that the residual stresses alone and the sum of the residual and live-load stresses must lie within the material yield envelope at each discrete point. The lowest-energy solution which satisfies these constraints is postulated to be the shakedown residual stress state in the rail.

The Mises-Hencky yield condition is used to specify the nonlinear constraints:

$$\Phi(S_r) \leq 0 \quad ; \quad \Phi(S_r + S_e) \leq 0 \tag{96}$$

where S_r and S_e denote the residual and live-load (elastic) stresses, respectively, and

$$\Phi(S) = (S_1 - S_2)^2 + (S_2 - S_3)^2 + (S_3 - S_1)^2 + 6S_{12}^2 - 2Y^2 \tag{97}$$

in the present case, where S_1, S_2, S_3, and S_{12} are respectively the longitudinal, lateral, vertical, and in-plane shear components of the stress fields. In the principal stress space (S_1, S_2, S_3) the Mises-Hencky yield condition is a right circular cylinder circumscribing the Tresca planes.

The finite element model and a similar finite difference model were first applied to problems of residual stresses created by bending of a beam and internal pressurization of a cylinder [54, 55], and the methods were validated by comparison with analytical solutions [56]. Recently a trial application was made to the problem of a 132 RE rail section, which was assumed to be subjected to 33-kip contact loads with the center of contact fixed along a longitudinal line halfway between the rail center plane and the gage face [57]. The live-load contact stresses were approximated by using the classical Boussinesq solution for the stresses in an unbounded half space subjected to a single concentrated surface load [24] as an influence function which was scaled by the biparabolic assumed surface pressure distribution and integrated over the contact rectangle. The longitudinal stress component from rail bending (see Section 4.1) was also included.

Figure 34 compares the contours of longitudinal residual tensile stress obtained from the trial analysis with contours obtained from the destructive sectioning of three rails [58, 59]. Good qualitative agreement is evident between the model, test rail 1 (AT5), and the KCS test rail. The major difference between the predicted and experimental results is that the measured patterns are much more spread across the width of the rail head. This spread is believed to have resulted from lateral variation in the center of contact location associated with the variety of worn wheel profiles that run on rails in service.

The 115 RE rail shown in Figure 34 has been included to make the point that the present state of knowledge about rail residual stress is incomplete. The failure of one of three detail fractures growing in this rail derailed the FAST train in 1980. The failure occurred when that defect had reached 20 %HA. A reconstruction of the history of one of the other two defects revealed an unusally rapid rate of growth: from 0.5 %HA to 11 %HA in about 10 MGT [60]. To date no explanation has been found to account for the fact that the longitudinal tensile residual stress in this rail was two to three times the levels observed in test rail 1, the KCS rail, and several similar specimens.

Other aspects of rail residual stress that are not well understood include the effects of changes in material properties induced by the plastic deformation cycles associated with wheel passages and the formation of initial residual stress fields by the roller straightening process. Some work has been done in both areas, but additional research is needed to support quantitative conclusions about the effects of these phenomena on the rail head service stress environment.

The constitutive relations change as permanent plastic deformation accumulates in the material close to the rail running surface. The constitutive relations may eventually stabilize, or if the cyclic strain amplitudes are large enough, the permanent deformation may continue to accumulate until the material fails via metal flow or ductile fracture. Figure 35 presents a schematic illustration of these types of behavior in uniaxial cyclic stress-strain tests. Such behavior has been observed in rail steel specimens [61] as well as many other ductile steel and aluminum alloys. A principal feature of the uniaxial behavior is the reduction of yield strength as the deformation accumulates. For rail steel, the 0.2% offset yield strength generally decreases to about half the as-rolled value when a stable cycle is attained.

There is no unambiguous way to project the material behavior from the uniaxial test regime to the multiaxial environment in the rail head. The most commonly accepted approach is to assume that the uniaxial stress-strain curve can be applied directly to the equivalent stress and strain, S_{EQ} and ε_{EQ}, defined in the present case by:

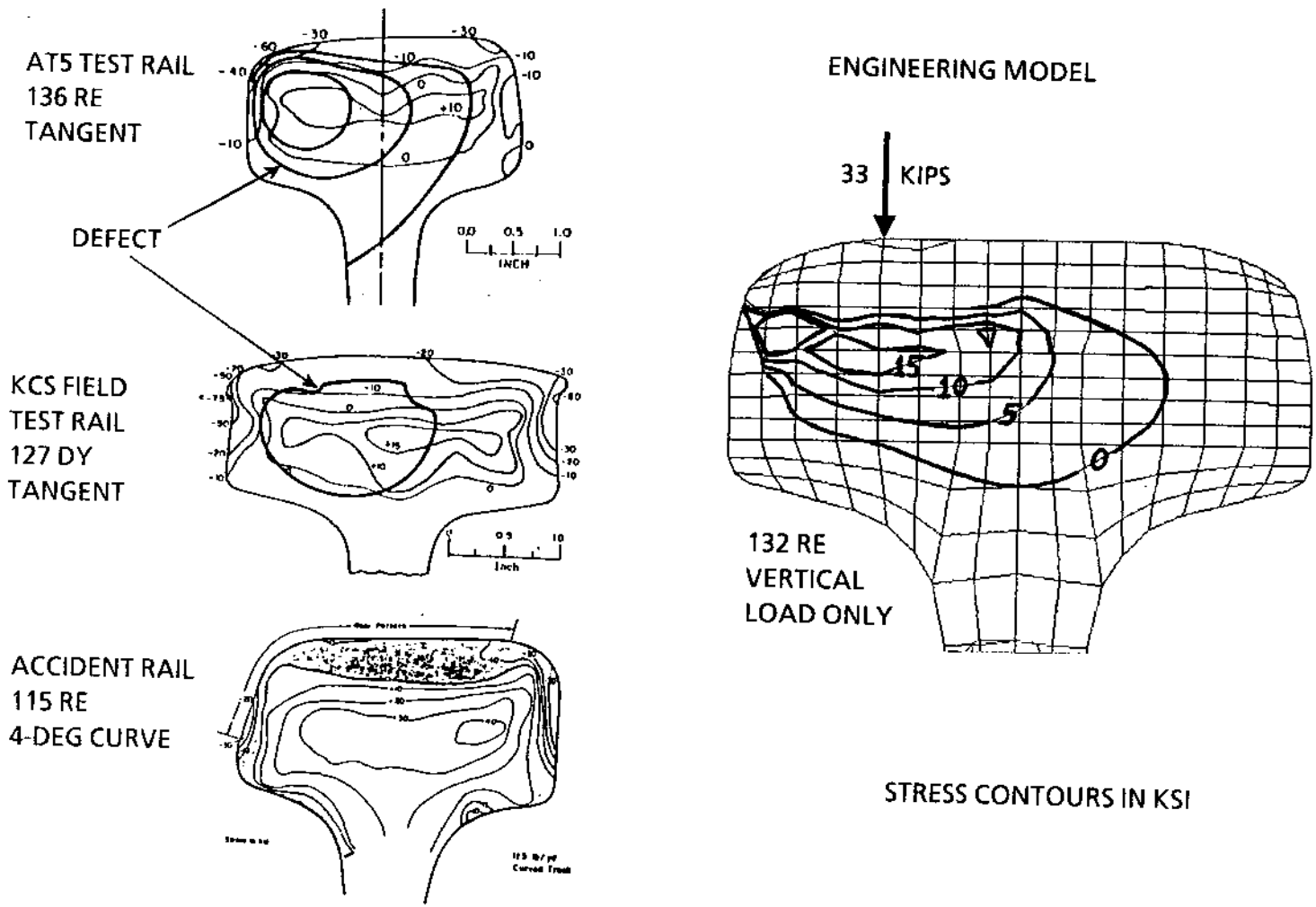

FIGURE 34. COMPARISON OF FINITE ELEMENT PREDICTION OF LONGITUDINAL RESIDUAL STRESS WITH THREE EXPERIMENTAL STRESS CONTOUR MAPS.

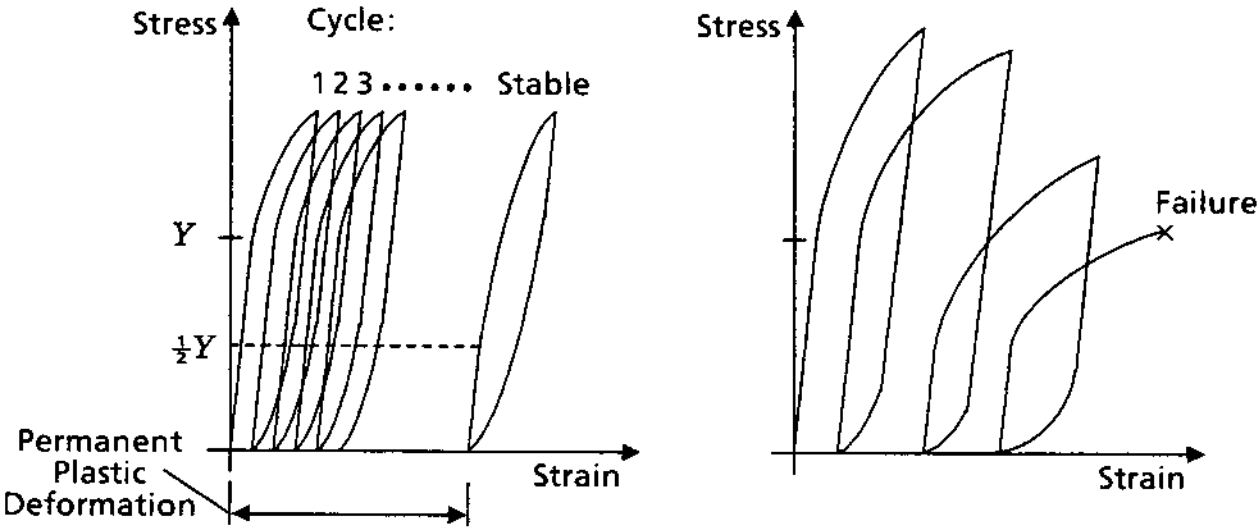

(a) Development of Stable Hysteresis Loop

(b) Continued Deformation to Failure

FIGURE 35. MATERIAL BEHAVIOR IN UNIAXIAL CYCLIC STRESS-STRAIN TEST.

$$S_{EQ}^2 = \frac{1}{2}\left[(S_1 - S_2)^2 + (S_2 - S_3)^2 + (S_3 - S_1)^2 + 6S_{12}^2 \right] \tag{98}$$

$$\varepsilon_{EQ}^2 = \frac{2}{9}\left[(\varepsilon_1 - \varepsilon_2)^2 + (\varepsilon_2 - \varepsilon_3)^2 + (\varepsilon_3 - \varepsilon_1)^2 + 6\varepsilon_{12}^2 \right] \tag{99}$$

A conventional incremental elastic-plastic finite element model of a rolling contact load traversing the surface of a two-dimensional half-space was developed, based on the equivalent stress-strain approach and a kinematic hardening assumption [62]. The model was used to calculate residual stresses corresponding to two representations of the stable hysteresis loop for rail steel: elastic - perfectly plastic behavior and elastic - linear strain hardening behavior, both with a flow stress equal to $Y/2$. For peak contact pressure ratios in the range $3.5 \leqq p/Y \leqq 4.3$, calculations with the elastic - perfectly plastic property indicated that the material would continue to accumulate permanent plastic deformation indefinitely, while calculations with the elastic - linear strain hardening property produced a stable hysteresis loop after two traverses.

These results raise questions about the validity of the first two models, which presume the existence of a true shakedown state in the rail head and seek to find that state via elastic - perfectly plastic calculations. On one hand, the elastic - perfectly plastic material representation in the first two models is actually closer to the linear strain hardening representation in the conventional finite element model (Figure 36), and one expects somewhat lower p/Y ratios based on static wheel loading (Table 24) than the range investigated with the incremental analysis. These arguments tend to favor the approach of seeking a shakedown state. On the other hand, a stable hysteresis loop is not a true shakedown state, and accounting for dynamic effects on

wheel loading would produce p/Y ratios in or above the range investigated with the incremental analysis. These arguments tend to cast doubt on the validity of the results obtained from the shakedown models.

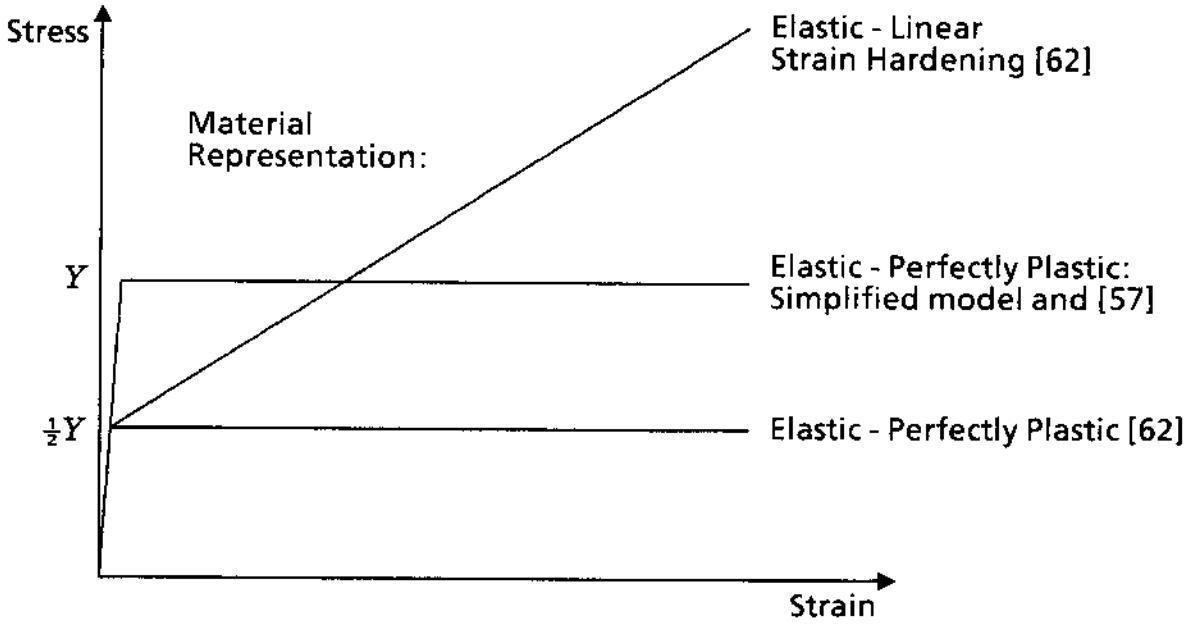

FIGURE 36. MATERIAL MODEL COMPARISON ON UNIAXIAL STRESS-STRAIN DIAGRAM.

A further problem is that none of the analyses include the effects of tangential surface tractions. Solutions for the tractive force distribution and the corresponding internal stresses in the rail head have not been available until a recent publication of one such solution for the case of Hertzian contact pressure combined with tractions at the adhesion limit [63]. Such cases can and should be included in future applications of the residual stress models, especially to investigate the possibility that tractive forces on curve rails might increase the residual stresses to the level observed in the 115 RE accident rail (Figure 34).

In view of the difficulties involved in making predictions of residual stress in the rail head, a program of well controlled full scale experiments is warranted in order to improve the understanding of elastic - plastic behavior under rolling contact and to develop confidence in the engineering models of residual stress formation. Exploratory tests of this type have been performed at the Research Institute of the Polish State Railways, and spot surveys of surface residual stress buildup in the test rails have suggested that a stable state is attained after 2×10^5 to 10^6 wheel passages [64]. More tests of this type, combined with destructive sectioning to determine the internal residual stress field, would provide the required experimental data.

The roller straightening of rails to reduce camber to the tolerances required for CWR installation produces an initial residual stress state that must be accounted for in safety assessments of modern rail production. The combination of a roller straightening stress field and low fracture toughness in a premium alloy rail was cited as a factor contributing to a 1983 rail failure which caused the derailment of an Amtrak passenger train [65, 66], and a technical committee of the International Union of Railways reached a similar conclusion about the general risk posed by the combination of high roller straightening stress and low fracture toughness in new rails [67]. A recent fracture mechanics analysis [68] has confirmed the original hypothesis [65] that the vertical

gradient of longitudinal residual stress can drive unstable web crack propagation in rails with low fracture toughness.

While the 1983 accident focused attention on web fracture, the roller straightening residual stress field can also affect the fatigue crack propagation rate of a transverse defect in the rail head. The longitudinal residual stress is compressive in the web and tensile in the base and head. Wheel-rail contact is known to transform the tensile longitudinal stress to compression in a shallow layer near the running surface. Just how this plastic deformation affects the interior part of the initial stress distribution is not known. The residual stress measurements discussed earlier (Figure 34) were made on rails that were not roller straightened, and similar measurements on roller straightened rails in Europe have been limited to rails that were not subjected to rolling contact service loads. The first measurements of internal residual stresses on service worn roller straightened rails were reported recently [69]. Of two rails investigated, one was of standard composition and apparently saw very little service; the longitudinal stress in this rail was still tensile at the running surface. The second sample was taken from a 136 RE premium alloy rail. The surface stress had been transformed to compression in this case, leaving the customary internal tension region in the rail head (Figure 37). The maximum stress contour of 20 ksi in this case is 30 to 100 percent higher than the corresponding contours in the KCS test rail and test rail 1 (Figure 34), and the tensile region is from about the same to twice the depth of the regions in those rails. Since the premium rail also has a higher yield strength than the test rails, it is not clear whether the changes in the residual stress field arise from the difference in yield strength or the effect of roller straightening stress.

Despite the incomplete state of knowledge about residual stress development in the rail head, there is sufficient agreement between the analyses and the few available experimental results to suggest that the following preliminary conclusions can be drawn as guidelines for describing the variations to be expected in service:

- Rolling contact is the dominant factor affecting the development of residual stress. It follows that the depth of the stress pattern should not depend on the rail section, except insofar as the effective rail radius in the contact zone depends on the section profile. For conventionally designed sections, the effective radius is probably insensitive to section when worn profile effects are considered.
- Subsurface shell formation and the propagation of detail fractures from shells depend to a great extent on the defect location relative to the residual stress pattern. In view of the first conclusion and in the absence of contradictory empirical data, it is reasonable to assume that the existing empirical relations for detail fracture center location (Figure 5) and average relieved residual stress (Eq. 30) as functions of flaw size can be applied to sections somewhat lighter and/or heavier than the 127 DY, 132 RE, and 136 RE sections on which the empirical relations were based.
- A general characteristic of elastic - plastic analyses of bodies subjected to intense local plastic deformation is that the resulting residual stress levels are proportional to the material yield strength. A rail under rolling contact is such a body. Therefore, rails that have been alloyed or heat treated to increase head hardness and yield strength should be expected to have proportionately larger residual stresses. This effect can be represented as a scale factor on Eq. 30, and a preliminary range of 1.3 to 1.5 is suggested for this factor.
- The simplified elastic - plastic analysis model suggests that the contact loads from 125-ton cars may increase the depth of the residual tension region by about 20 percent. This increase can be represented by replacing Eq. 30 with:

$$S_R = 10 - 10.4 \frac{A}{A_H} \tag{100}$$

- The effect of roller straightening can tentatively be assumed to increase the depth of the residual tension region. Further reductions of the numerical factor on A/A_H in Eq. 100 can be used to represent the effect.

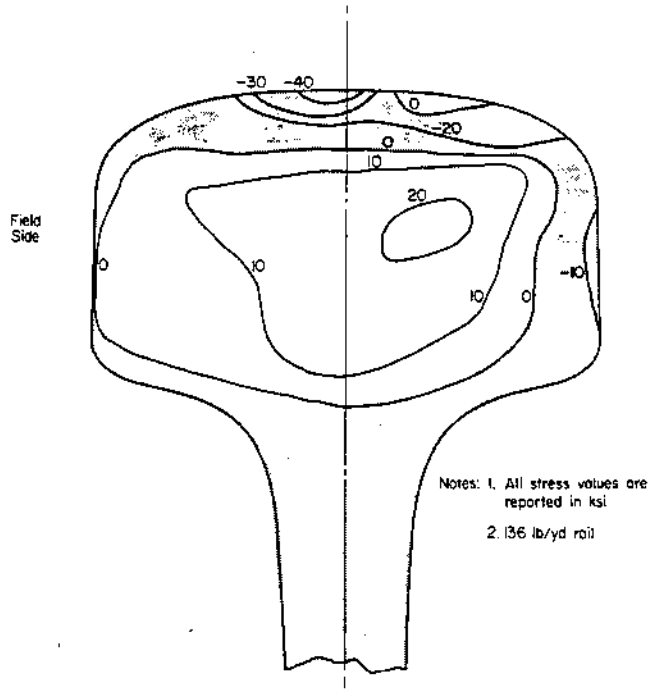

FIGURE 37. LONGITUDINAL RESIDUAL STRESS IN ROLLER STRAIGHTENED ALLOY RAIL.

5. APPLICATION OF DETAIL FRACTURE GROWTH MODEL

After numerical results from early versions of the detail fracture model had been used to guide the selection of stress intensity magnification factors, preliminary estimates of defect life were reported [70, 71], and the model described in Section 3 was implemented as a FORTRAN PC program. The program contains libraries and subroutines which embody various track and environment features, e.g., the rail section properties given in Appendix A, the vehicle dimensions and weights listed in Appendix B, and features of the rail head stress environment described in Section 4. A brief user's guide and the program listing appear in Appendix D.

The case of FAST test rail 1 (see Section 2.1) was analyzed first to validate the detail fracture growth model. Section 5.1 summarizes the validation results. In several other cases of test and field observations, assumptions had to be made to supplement the incomplete knowledge of the service environment. Section 5.2 presents comparisons of the predicted and actual crack growth lives for these cases. A baseline environment description was then established to represent average U.S. revenue freight service conditions, and the sensitivity of detail fracture crack propagation life to service variations was studied by changing one environment factor at a time. Section 5.3 presents the results of the sensitivity study. Section 5.4 presents some additional cases in which the temperature sensitivity results were used to estimate crack growth life in CWR subjected to typical diurnal and seasonal temperature variations.

5.1 Comparison with FAST test

The environment factors affecting detail fracture propagation were discussed in the preceding sections. The specific values applicable to test rail 1 are summarized in the following paragraphs.

Train consist "CTEST2" was used (see Appendix B). This consist represents typical makeups during the FAST test, with an average axle load of 30.8 tons. Vehicle dynamics were represented by the four-parameter model with the values given in Section 4.1.1 (see Table 21). These values were derived to match the known dynamic characteristics on the FAST track. Wheel position (i.e., center of wheel-rail contact) was fixed at half the distance from the rail center plane toward the gage face to represent average running conditions on tangent track.

The track vertical foundation modulus was set at 3 ksi, representing the well maintained dry environment of the FAST track (Table 20). Per the discussion in Section 4.1, the lateral and torsional moduli were taken as 2.4 ksi and 10^5 in.lb./rad., respectively (see discussion on page 42). Tangent track was analyzed, since the test section was tangent track. Lateral load was fixed at 5 percent of vertical load for all axles to reflect the average profile and cant expected on tangent track (see Section 4.1.1).

Monthly average ambient temperature and the reconstructed neutral temperature history (Tables 5 and 6) were used to derive an approximate, piecewise linear history of the temperature differential as a function of tonnage. Averages of the ambient high and low temperature were used to represent the rail temperature, reflecting the then existing practice of operating the FAST train between 4 PM and 6 AM. Figure 38 summarizes the representation for the entire experiment: seven data points with linear interpolations between the points, with the thermal history specified as a function of gross tonnage. For convenience in carrying out the computations, the data in Table 3 was used to translate the tonnage-based history into curves of $T_n - T$ versus flaw size. Figure 39 illustrates the flaw-size-based history for test rail 1. For the analysis of crack propagation, the curve in Figure 39 was converted to tensile stress at the rate of 195 psi per Fahrenheit degree.

Properties for the 136 RE section were used in the analysis. Average relieved residual stress was represented by Eq. 30, the empirical relation which was derived from the test rail 1 residual stress measurements. For the purpose of calculating nominal bending stress at the flaw center location in the penny-crack growth phase, the

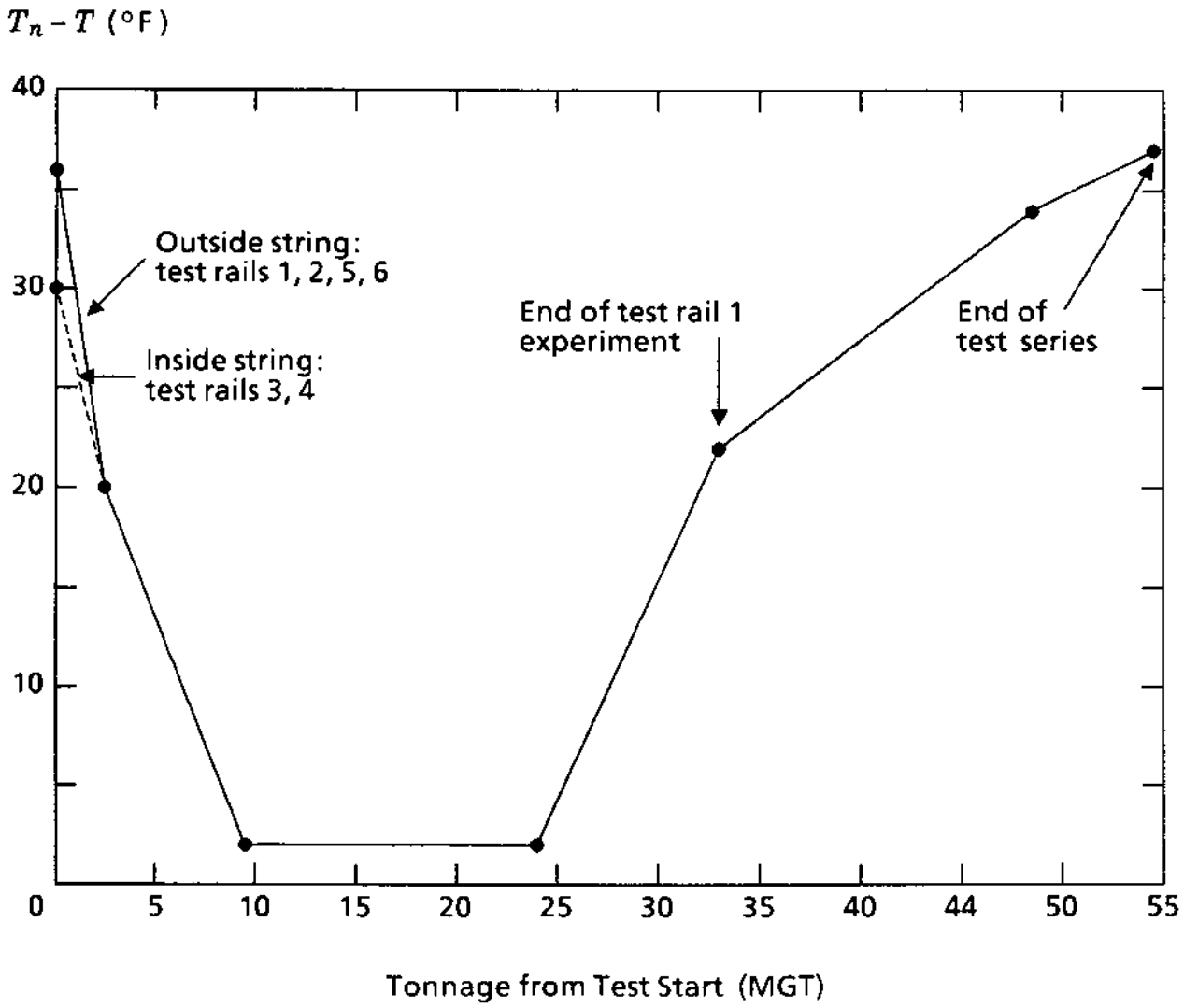

FIGURE 38. HISTORY OF $T_n - T$ REPRESENTING THE FAST EXPERIMENT.

aggregate empirical curves for depth below the unworn crown and offset from the center plane were used (Figure 5).

For computation, the crack growth life was divided into an initial block from 12 to 20 %HA, followed by 10 %HA blocks, and concluding with a block from 70 to 80 %HA. This subdivision agreed closely with the actual initial and final crack sizes in test rail 1 (11.9 and 80.4 %HA) and gave blocks small enough for reasonable numerical accuracy.

The lack of consistency between the various investigations of rail steel crack growth rate properties was noted in Section 3.1. Therefore, calculations were made with all six candidate models, A through F, given in Table 9. Figure 40 compares the calculated lives with the actual performance of the test rail 1 detail fracture. Apparently either model A or model F is the best choice.

As noted in Section 3.4, laboratory tests showed that the actual crack growth life should be 75 to 80 percent of the calculated life because the calculation method does not account for load interaction effects. That reduction factor was arrived at by comparing the laboratory test results with a calculation based on model F. In Figure 41, the calculated results for test rail 1 have been scaled by a factor of 80 percent. This brings

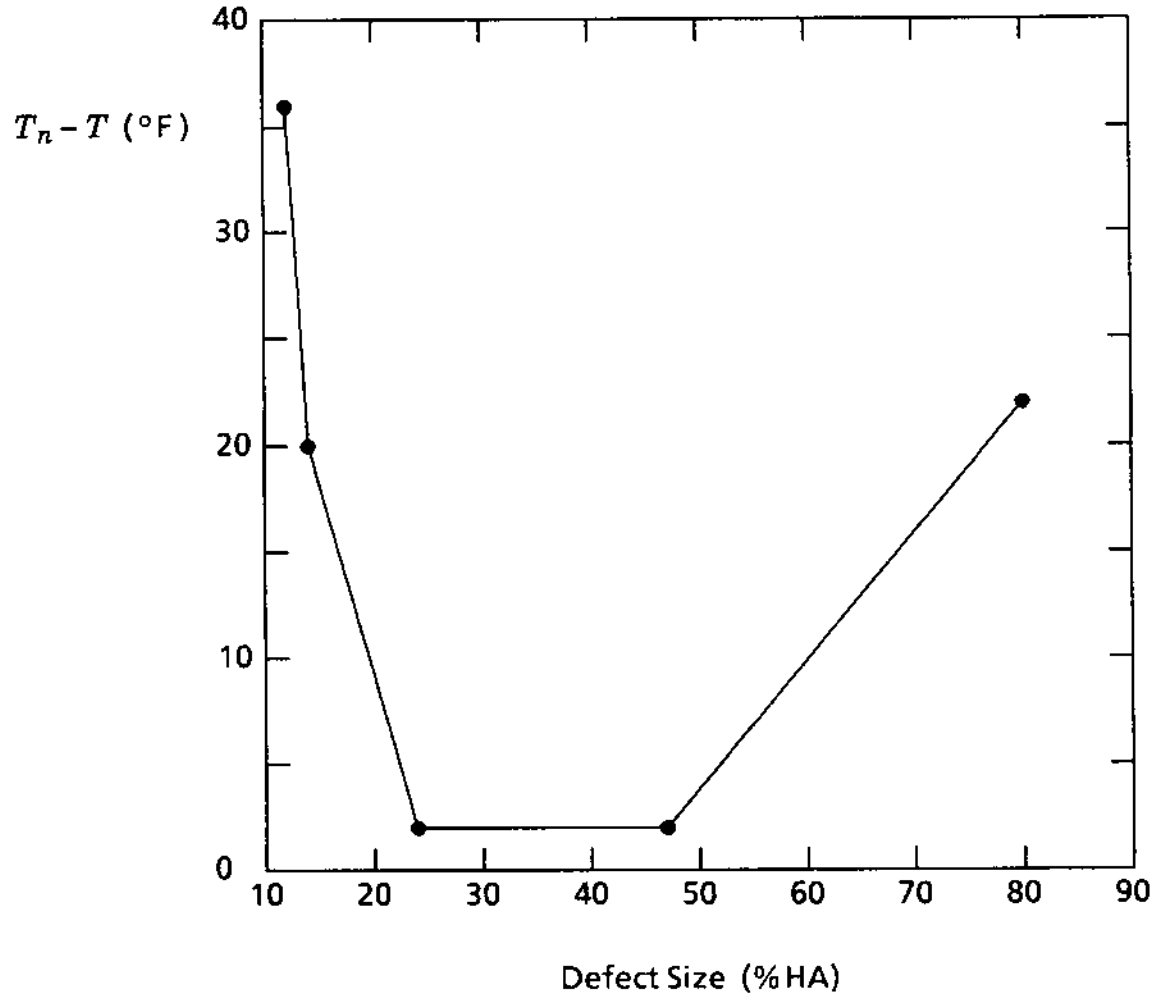

FIGURE 39. HISTORY OF $T_n - T$ REPRESENTING TEST RAIL 1.

the total life calculated by model F into close agreement with the experimental life, and the quality of the detail fracture model can now be judged by comparing the predicted curve with the experiment at intermediate points. A slight artifact, probably attributable to the transition rules (Section 3.2.3) is visible between 30 and 50 %HA, but the correlation is otherwise reasonable. In fairness it should be pointed out that an equally good fit could have been obtained with model A if the load interaction scaling factor had been derived by comparing a model A calculation with the laboratory test results. However, in that case the load interaction effect would have appeared as retardation (actual life longer than calculated life) instead of the acceleration seen with model F. Model F was judged to be the slightly better choice because it is logical to expect acceleration rather than retardation when actual life is compared with a calculation in which negative-R cycles are truncated to $R = 0$. Therefore, calculated crack growth lives in the remainder of Section 5 will be presented based on model F and with the 80 percent scaling factor applied.

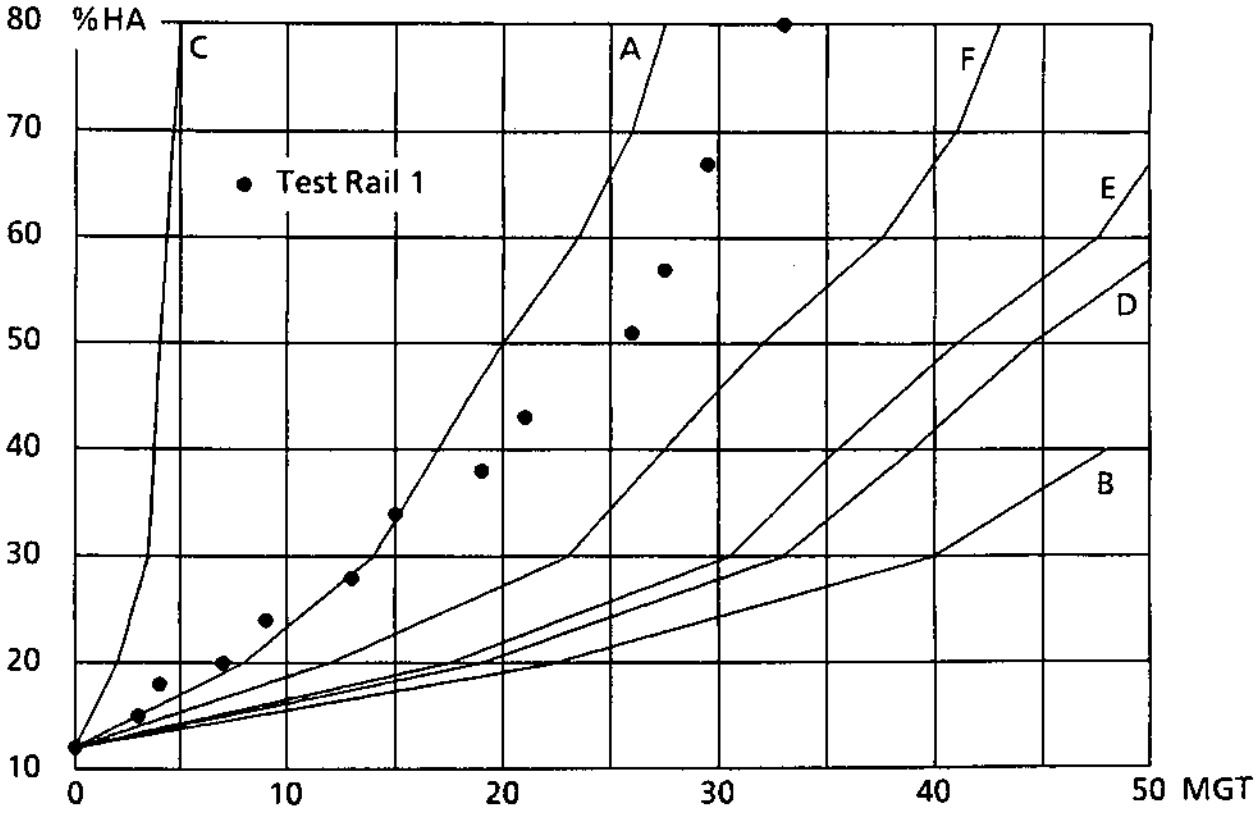

FIGURE 40. COMPARISON OF MODEL PREDICTIONS WITH TEST RAIL 1 RESULTS.

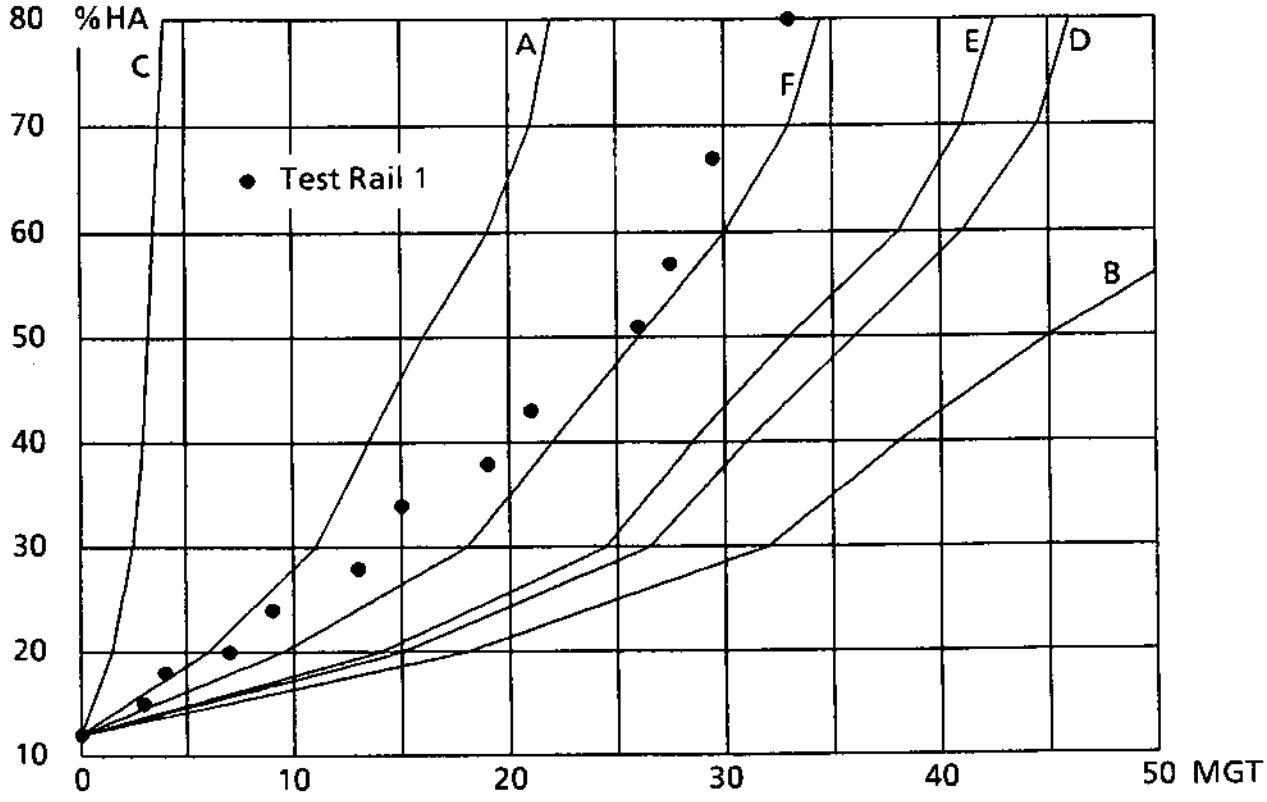

FIGURE 41. COMPARISON AFTER ADJUSTING TO ACCOUNT FOR LOAD INTERACTION.

5.2 Other comparisons

That the detail fracture model with material model F can be made to agree with the test rail 1 experiment is encouraging but does not rule out the possibility of artifacts in the model. Will the predicted crack behavior always agree with observation, no matter what service conditions are simulated? One cannot seriously think so. To expose deviations by making such comparisons is to understand the strengths and weaknesses of the model. Fortunately, the test data and field observations summarized earlier offer several useful comparisons.

Section 2.1 described the results of the FAST experiment. Of the six rails from which crack growth histories were obtained, the detail fractures in test rails 3 and 4 grew more slowly than those in test rails 1, 2, 5, and 6 (see Figure 3). These two groups of rails also had two environment differences. Test rails 3 and 4 were in the inside string, with an initial neutral temperature 6 °F lower than the outside string, which contained the other four rails. The lower neutral temperature implies a thermal stress S_T about 1.2 ksi lower, but this difference does not last long (see Figure 38). Test rails 3 and 4 were also distinct from the other rails with respect to defect center location as a function of defect size (see Figure 5). This difference persists throughout the measurement range, which is also a major part of the fatigue crack growth range.

Crack growth curves for test rails 3 and 4 were calculated from inputs reflecting the above differences. $T_n - T$ curves were reconstructed for defect in accordance with the procedure outlined in Section 4.3, and the alternate empirical relations for defect center location (Figure 5) were used. Figure 42 compares the calculated curves with the test results from Table 3. The model reproduces the slow early growth rate observed in the experiment but gives inaccurate estimates for total life: about 10 percent too long for test rail 3 and 20 percent too short for test rail 4. These discrepancies arise in part from the corner-crack regime of the model, for which the growth rates are too high, and in part from the rules for transition from the penny-crack to the corner-crack stress intensity factor. Note that a small error in the transition can lead to significant life errors when the early growth rate is low.

The residual stresses in test rails 3 and 4 were not measured, but the results for other similar rails [58] suggest that the stresses in these rails should have been similar to the test rail 1 stresses. Accordingly, the empirical description of S_R derived from test rail 1 (see Eq. 30) was used in the calculations for test rails 3 and 4. However, minor variations of the residual stress pattern might still have affected the observed crack growth behavior.

The differences between the test rail 1 and test rails 3, 4 environments were quite modest. Much greater differences appear when test rail 1 is compared with the rail that caused the 1980 FAST derailment (see Section 4.3). The distinguishing factors are: rail section; track curvature; residual stress level; temperature differential history; and defect size range in which the fatigue crack growth history was measured. Table 25 summarizes these differences and the ways in which they affected the simulation of crack behavior in the accident rail.

The calculated crack growth life was about 20 to 30 percent longer than the actual life in this case (Figure 43). The actual life was obtained from post-failure examination of the crack-propagation surface [60], using the ring-counting method outlines in Section 2.1. In this case, however, the investigators reported their results in terms of wheel passages, and the plot in Figure 43 reflects the range of uncertainty about the average axle load in the test train during the growth of the crack.

The model estimates crack growth life in the accident rail reasonably well, considering the degree of extrapolation away from the calibrating conditions of test rail 1. The shapes of the simulated and actual crack growth curves are quite different. The relatively sharp knee in the simulated curve is believed to be a result of the constant $T_n - T$ assumption, rather than a model artifact, since the same effect appears when $T_n - T$ is

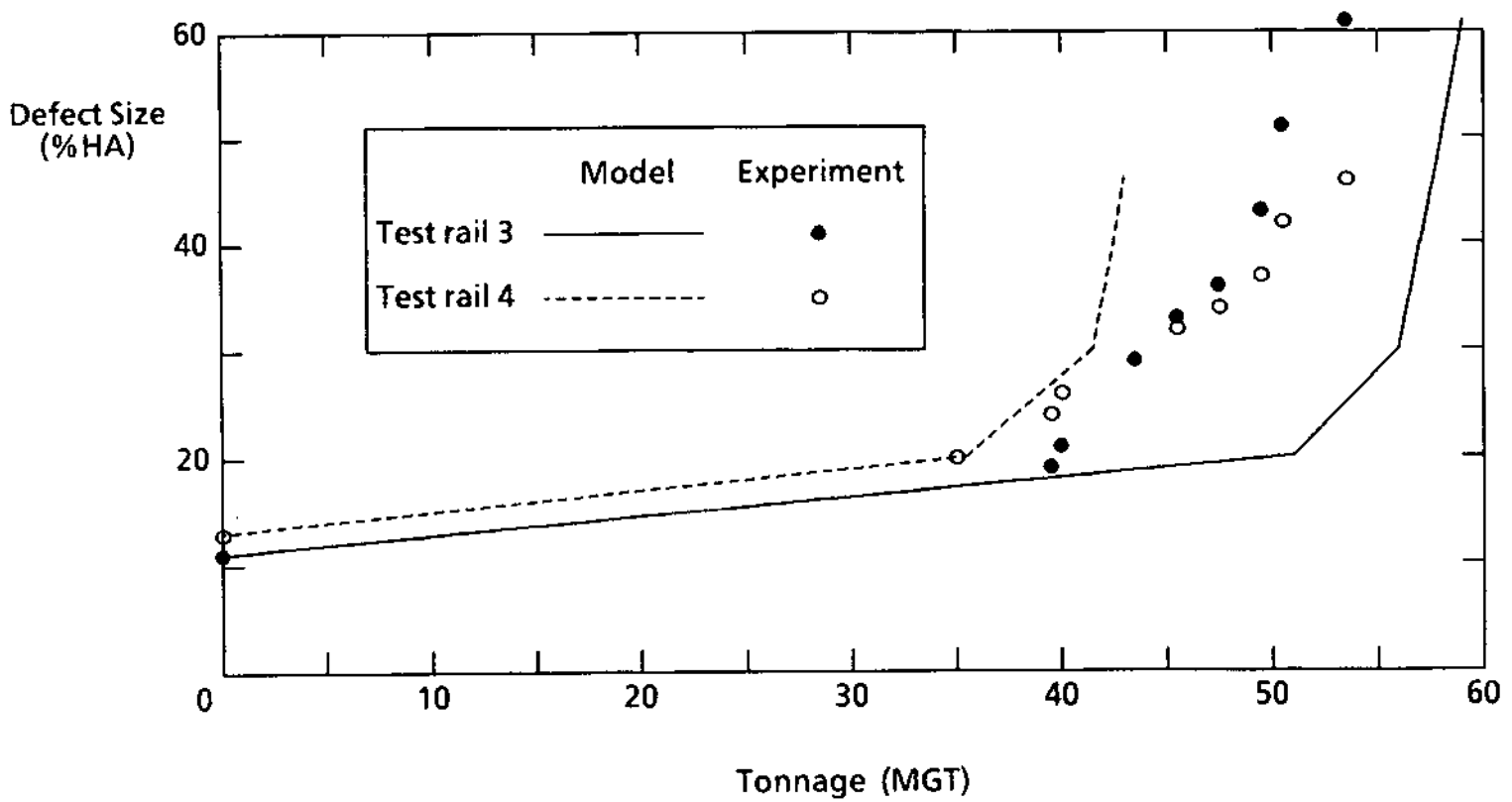

FIGURE 42. COMPARISON OF MODEL WITH EXPERIMENT FOR TEST RAILS 3 AND 4.

TABLE 25. DIFFERENCES BETWEEN TEST RAIL 1 AND ACCIDENT RAIL.

Factor	Environment for		Relative Effect on Simulation of Detail Fracture Growth in Accident Rail
	Test rail 1	Accident rail	
Rail section	136 RE	115 RE	Larger bending stress amplitudes
Curvature	Tangent	4 deg.	Lateral loads increase bending stress
Residual stress	1 ×	3 ×	Magnification factor on S_R increases mean stress
$T_n - T$	Per Fig. 39	Constant 40 °F (a)	Larger thermal stress S_T increases mean stress
Initial defect size (% HA)	11.9	0.5	Smaller ΔK
Final defect size (% HA)	80.4	11.0	Smaller ΔK; growth simulation restricted to penny-crack regime

[a] Based on assumptions of well adjusted track ($T_n = 60$ °F) and cold weather ($T = 20$ °F) for the few days in February during which the crack grew in the accident rail.

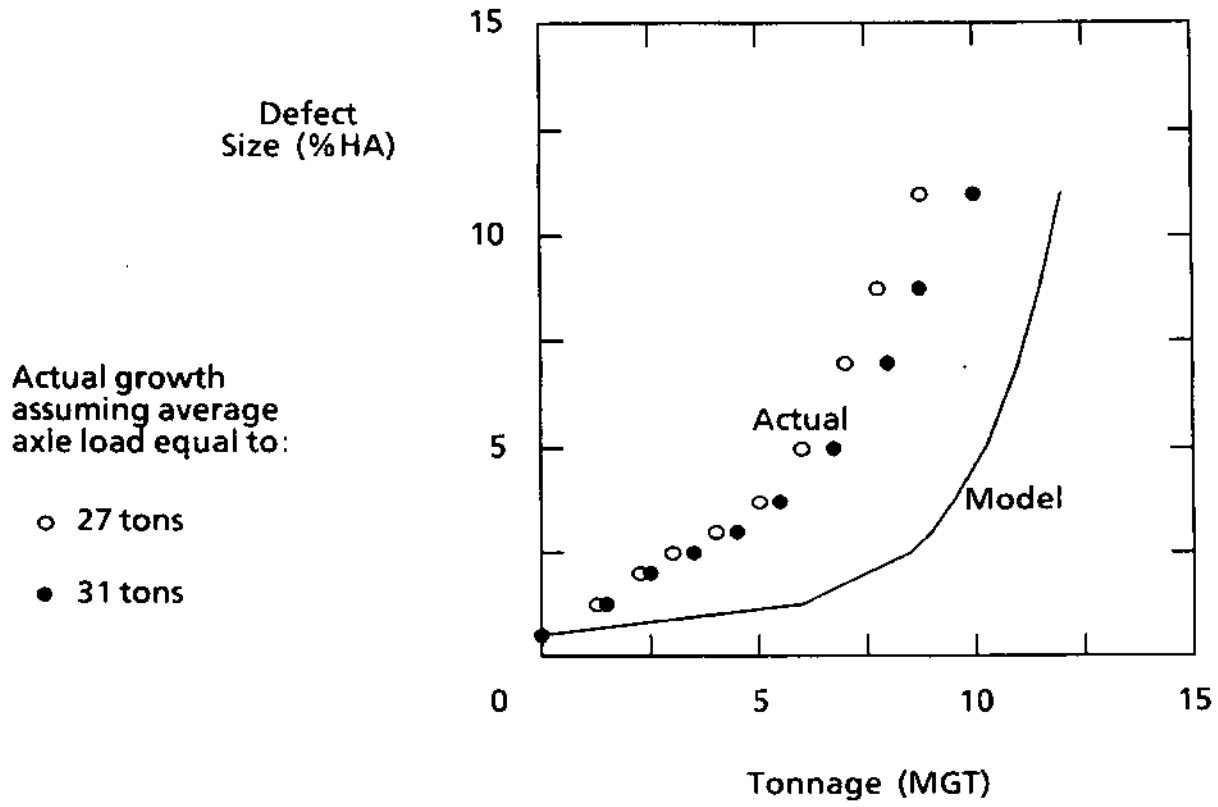

FIGURE 43. COMPARISON OF SIMULATED AND ACTUAL DETAIL FRACTURE GROWTH IN 115 RE ACCIDENT RAIL.

fixed in the crack growth simulation for test rail 1 (Figure 44).

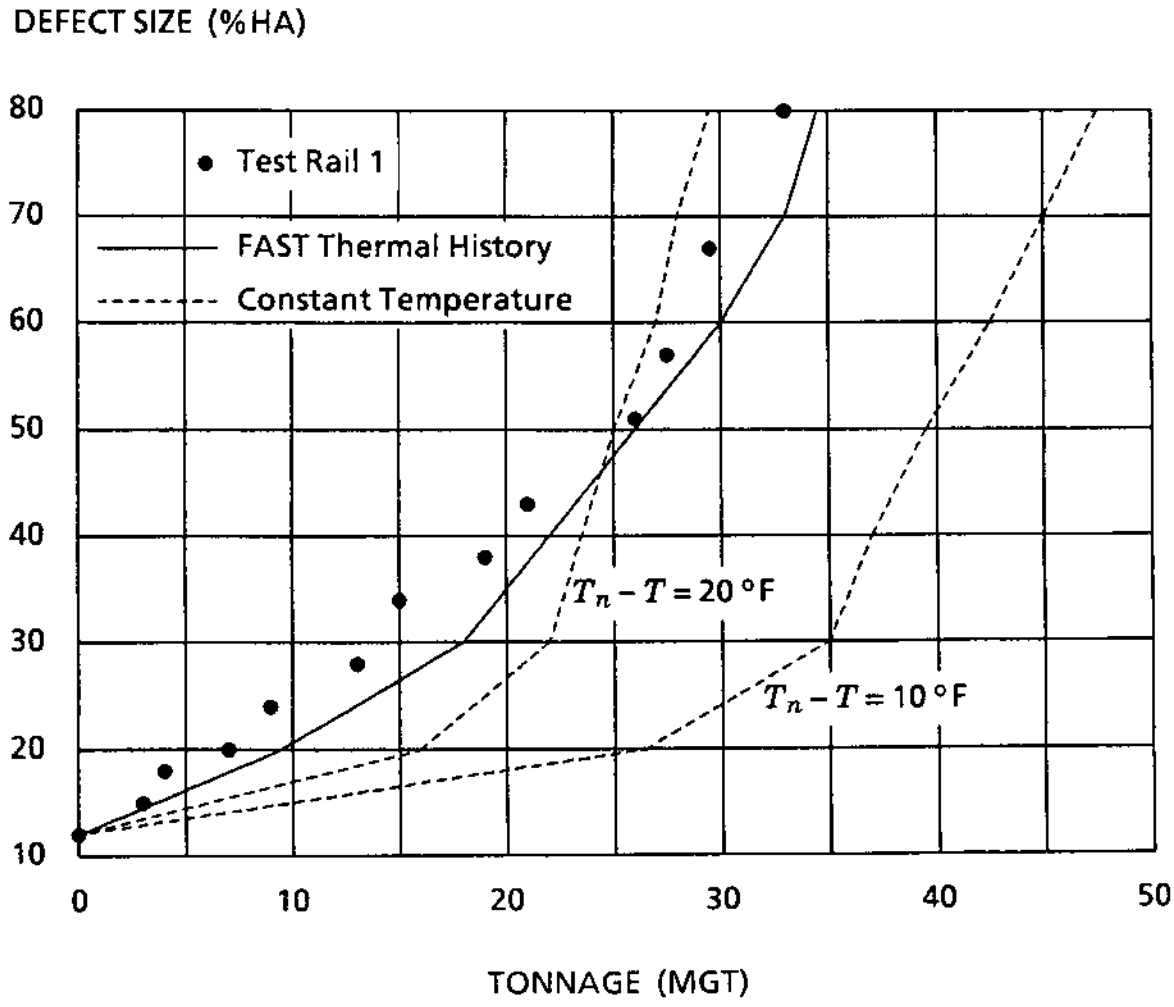

FIGURE 44. EFFECT OF CONSTANT TEMPERATURE DIFFERENCE ON SIMULATION OF CRACK GROWTH IN TEST RAIL 1.

Another example mentioned in Section 2.2 involved the fracture of two rails on a 5°30' – 6° BJR "S" curve on a B&LE Railroad mainline carrying 100-ton unit train traffic. The rails were 140 RE Curvemaster®, a heavy section high-strength rail, and had shown no defect indications on the previous rail test somewhat less than 15 MGT before the fractures. The defects had grown to between 70 and 80 %HA at the time of discovery.

For the purpose of the simulation, it was assumed that the sizes of these defects had reached 10 %HA at 15 MGT before discovery. Figure 45 illustrates several example calculations, in which the assumptions for S_R and S_T were varied as follows:

- Average relieved residual stress, S_R - nominal (Eq. 30) and scale factors of 1.3× and 3×. The 1.3× factor represents the estimated difference between standard and high-strength rails, while the 3× factor represents the highest observed tensile stress in the 115 RE FAST accident rail (see Section 4.3).
- Thermal stress, S_T - values of 1 ksi and 3 ksi; the smaller value represents the expected level when thermal and track-adjustment stress buildup is limited by rail

slippage through joint bars with average friction conditions. The larger value is intended to represent the maximum frictional resistance of rusty joints.

The simulation with residual stress of high-strength rail ($1.3 \times S_R$) combined with nominal S_T buildup comes closest to the field observation. In the light of the 115 RE accident rail case, one can also speculate that the curve loads might have further magnified the stress in the B&LE rails. It is then reasonable to expect that these detail fractures could have grown from an undetectable size to 70 %HA within the 15 MGT since the last rail test. This example lends additional confidence to the model, although it would have little value without the other examples for which the environment conditions were not so ambiguous.

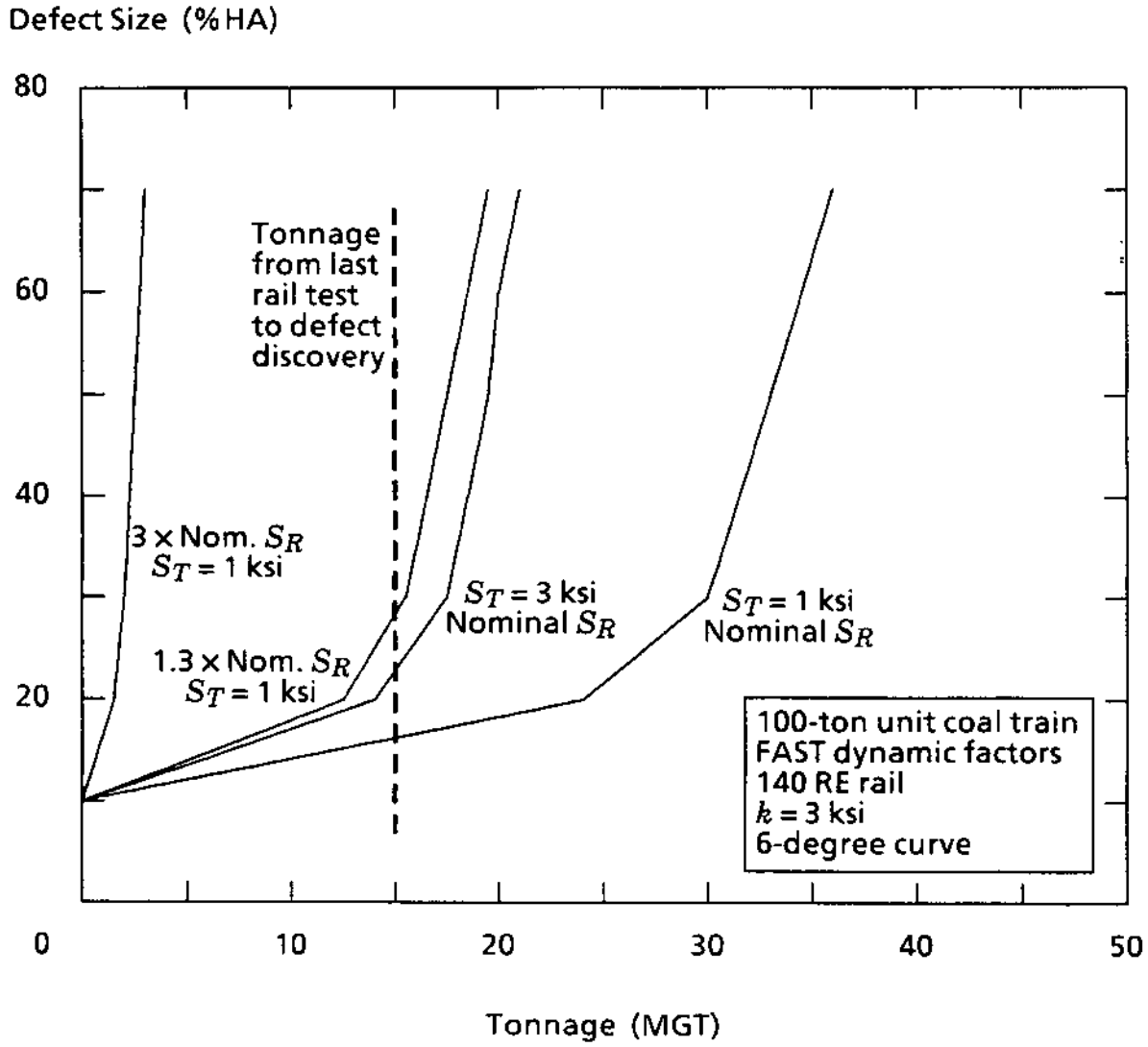

FIGURE 45. COMPARISON OF MODEL WITH FIELD OBSERVATION ON B&LE RR.

The KCS test rail discussed in Section 2.2 is another example of BJR (see Table 7). The traffic details were not documented in this case, except for the general description of mostly mixed freight plus three unit coal trains per week. Since the test lasted one year, these facts suggest that at least 90 percent of the 16.6 MGT accumulated during the experiment was mixed freight. Accordingly, crack growth curves were calculated using the General Freight "B" consist (see Appendix B). A magnification factor of 3 was

applied to the 33rd wheel in the consist to represent a flat, and the FAST car dynamic factors were used. The rail section was a 127 DY, and a vertical foundation modulus of 2 ksi was assumed to reflect a foundation with drainage somewhat poorer than that of the FAST track. No magnification was used on S_R because the one data point from the KCS test rail fell close to the nominal S_R relation, even though the rail was heavily worn (see Figures 12 and 34).

Figure 46 compares calculations for $S_T = 1$, 2, and 3 ksi with the KCS test results. In this case, neither the life estimate nor the shape of the crack growth curve agree with the test results. The probable range of track adjustment stress S_T gives much slower growth rates than the observed rate, and much more than a change of scale factor on S_R would be required to change the simulation to match the observed decreasing trend in the crack growth rate. The discrepancy may reflect a lack of understanding of transient track-adjustment stress in BJR or the need for more detail in modeling residual stress relief, but whatever the reason, this example suggests that one should exercise caution when applying the detail fracture model to BJR or heavily worn rail.

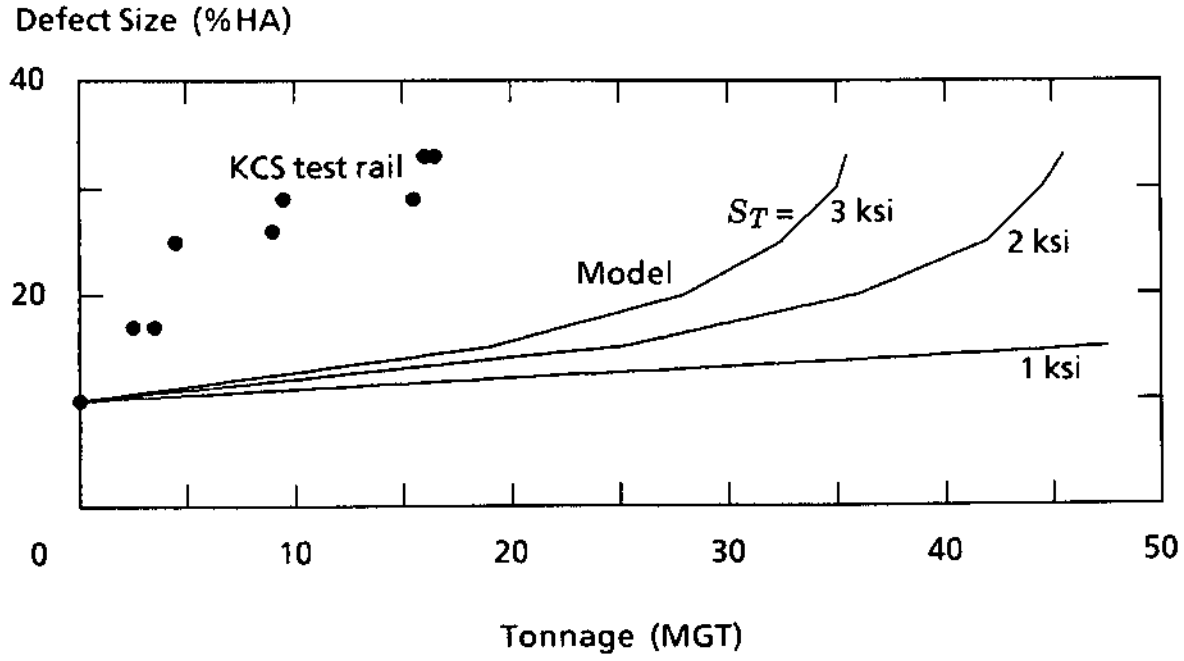

FIGURE 46. COMPARISON OF MODEL WITH FIELD TEST ON KCS RR.

Section 2.3 summarized the results of four-point bending tests to determine the static strength of 36 rails, including FAST test rails 2 through 6 and the KCS test rail. The stress intensity factor part of the detail fracture model can be compared with these results by using the model to calculate the rail breaking load as a function of defect size. In this case, $S_T = 0$ with absolute certainty, but S_R must be assumed. The first such comparison was made using the Sneddon penny-crack stress intensity factor (Eq. 8), assuming $S_R = 0$, and assuming the defect center location to be one inch below the unworn rail crown independent of defect size [3]. That comparison suggested the validity of a model based on the penny-crack formula, at least for detail fractures smaller than 50 %HA.

Figure 47 compares the original and current detail fracture models with the breaking strength test results. Except for rail NW16, the measured strengths fall in a band whose width is approximately a factor of two. The data also exhibits the expected trend of decreasing strength as the defect size increases. The scatter in the data can be

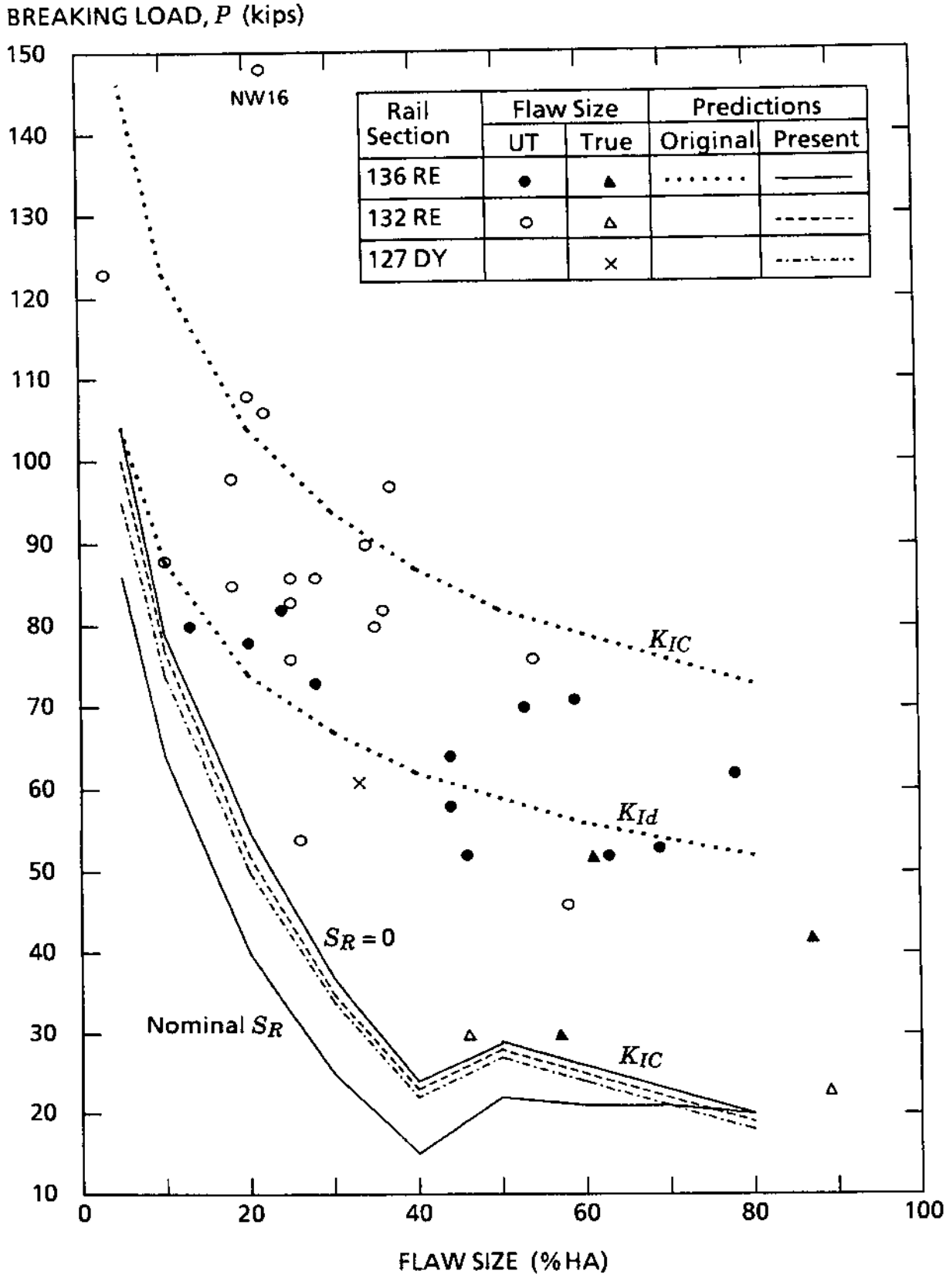

FIGURE 47. COMPARISON OF MODEL WITH STATIC STRENGTH TESTS.

attributed in part to error in UT measurements of flaw size and variations in residual stress.

The original model [3] employed the basic Sneddon stress intensity factor (Eq.8) to predict the breaking strength of a 136 RE section assumed to be free of residual stress and to contain a defect whose center was one inch below the unworn rail crown, independent of the defect size. The fact that strength predictions based on $K_{IC} = 35$ ksi√in. and $K_{Id} = 25$ ksi√in. bounded most of the data from rails with small defects suggested the applicability of the penny crack model. The fact that the measured strengths fell below the lower bound at large defect sizes suggested the need for transition to the corner crack model.

The present model was used to calculate strengths for 127 DY and 132 RE sections with $S_R = 0$ and for a 136 RE section with $S_R = 0$ and S_R as defined by the nominal residual stress relief model (Eq. 30). The results shown in the figure are based on K_{IC}. The $S_R = 0$ cases suggest that little difference between the three sections should be expected, a result which agrees with the measurements. Comparison of these cases with the K_{IC} curve from the original model shows that the present model is much more conservative, i.e., the live-load stress intensity factor K for a given defect size is larger in the present than in the original model. The present breaking strength curve is even lower when the effect of residual stress is accounted for. This curve falls somewhat below the lowest measured strengths.

The discrepancy may arise from averaging K around the crack front, the scheme which was adopted to reflect the tendency of a growing detail fracture to maintain its crack front shape. Conversely, one should base the prediction of breaking strength on the maximum K, as outlined earlier for the simplified case of a body subjected only to bending stress (see discussion in Section 3.2). In the present case, a maximum K analysis would have to account for the fact that residual as well as live stress varies around the crack front. At intermediate defect sizes (30 to 50 %HA), one would be likely to find the top of the crack front in residual compression. One could argue that the maximum K in this situation might be somewhat lower than the average K in the crack growth model, i.e., that the comparison in Figure 47 is not unreasonable.

The Trinidad, Colorado derailment (see Section 2.2) provides one point of comparison for static strength in a curve rail. The 132 RE section failed under a loaded unit coal train at a 10 %HA detail fracture in a 6° 10′ CWR curve at $T = -10$ °F. For the given combination of wheel loading and track curvature, one can take $L/V \approx 0.37$ (Table 22).

Because of the small size of the defect, it is reasonable to use only the penny crack model to make the comparison. From Eq. 38 (see Section 3.2.5), the fracture condition is then given by:

$$S_R + S_T + M_G S = \frac{K_{IC}}{2 M_S M_1 \sqrt{(r/\pi)}} \tag{101}$$

where $r = 0.375$ inch for a 10 HA flaw in the 132 RE section, $M_S = 0.984$ (Table 11), $M_1 = 1.072$ (Table 17), $M_G = \approx 1.01$ (Table 18), and where the flaw center location is given by $(y, z) = (0.9, 3.125)$ inches from the aggregate empirical model in Figure 5. Assuming well adjusted track ($T_n = 60$ °F), $S_T = 13.65$ ksi, and for $K_{IC} = 35$ ksi√in. Eq 101 reduces to:

$$S_R + 1.01\, S = 34.35\ ksi \tag{102}$$

If it is further assumed that the rail failure was precipitated by the maximum reverse bending stress ahead of the lead wheel of a six-axle locomotive ($V = 34.75$ kips) and

that the vertical track foundation modulus was 3 ksi, one finds $S = 3.53$ ksi at the given (y, z) coordinates. Equation 102 then implies that $S_R \approx 30.8$ ksi, i.e., about 3.5 times the nominal value one would calculate from Eq. 30 for a 10 %HA defect.

The foregoing calculations did not include a dynamic load, but even with a large dynamic factor on S, a considerable magnification of the nominal S_R would be required to account for the rail failure. Thus, although uncertainties about the on-site conditions prevent a definitive comparison with the Trinidad case, the result suggests that curve rails do attain higher residual stress levels than tangent rails. In this sense, the comparison is not inconsistent with the situation of the 115 RE accident rail discussed earlier.

5.3 Sensitivity study

Table 26 summarizes the environment factors used as a baseline for the sensitivity study. Most represent typical revenue service on CWR mainline track, but the vehicle dynamic factors and rail temperature differential are exceptions. The baseline vehicle dynamic factors correspond to the known conditions on the FAST track because that is the only example for which the four-parameter car dynamic model (see Section 4.1.1) has been calibrated to experimental data. The FAST conditions are believed to be within the range of revenue freight service conditions but less severe than average revenue freight service. The temperature differential $T_n - T$ should have at least a seasonal variation to be realistic, but a fixed value is used in the baseline. Fixing $T_n - T$ allows one to focus on the sensitivity of crack growth life to thermal stress without the complicating factors of seasonal and/or diurnal variations. The value chosen for the baseline produces a crack growth life estimate comparable to that obtained from the simulation of test rail 1 (see Figure 44).

The baseline simulation produced a life of 52 MGT for a detail fracture to grow from 10 %HA to 80 %HA. Figures 48 through 54 and Tables 27 through 30 summarize the results of the study.

TABLE 26. BASELINE FACTORS FOR SENSITIVITY STUDY.

Category	Factor	Value
Vehicle	Train consist (a) Average axle load (a) Vehicle dynamic factors: Car dynamic coefficients (b) Wheel flats	General Freight "B" 16.5 tons 0.0, 0.5, 0.4, 0.2 None
Track	Curvature Vertical foundation modulus Rail section Average relieved residual stress, S_R Scale factor on S_R	Tangent 3 ksi 136 RE Equation 30 1 ×
Other	Temperature differential, $T_n - T$ Center of wheel contact Defect center location	14 °F Nominal (c) Nominal (d)

[a] Consist determines average axle load; see Appendix B.
[b] See Figure 22.
[c] Halfway from rail center plane to gage face.
[d] Empirical equations from test rails 1, 2, 5, and 6; see Figure 5.

Crack growth life decreases as average axle load increases (Figure 48). The relation is nearly linear, for the cases studied, in the range of typical to extremely heavy loads (16.5 to 38.5 tons per axle). Crack growth life increases disproportionately for average axle loads lighter than 16 tons. This effect arises when the loads are light enough to place significant numbers of stress ranges below the threshold for crack propagation.

The crack growth life under unit trains with empty 100-ton cars (average axle load of 9.9 tons) is about 133 MGT but is only 45 MGT under the same trains when loaded (32.6 ton average axle load). The 3-to-1 difference in life seems like the 3-to-1 difference in average axle load, but the empties actually do very little damage. The relative damage can be better understood by using Miner's rule to estimate the crack growth life for the unit train service on single track. With equal numbers of loads and empties, one finds that the crack growth life is about 53 MGT, of which 40.6 MGT are loads. Thus, the effect of returning the empties on the same track is to reduce the number of loads by slightly less than 10 percent compared to the number which would cause the same detail fracture growth on track dedicated to loaded trains.

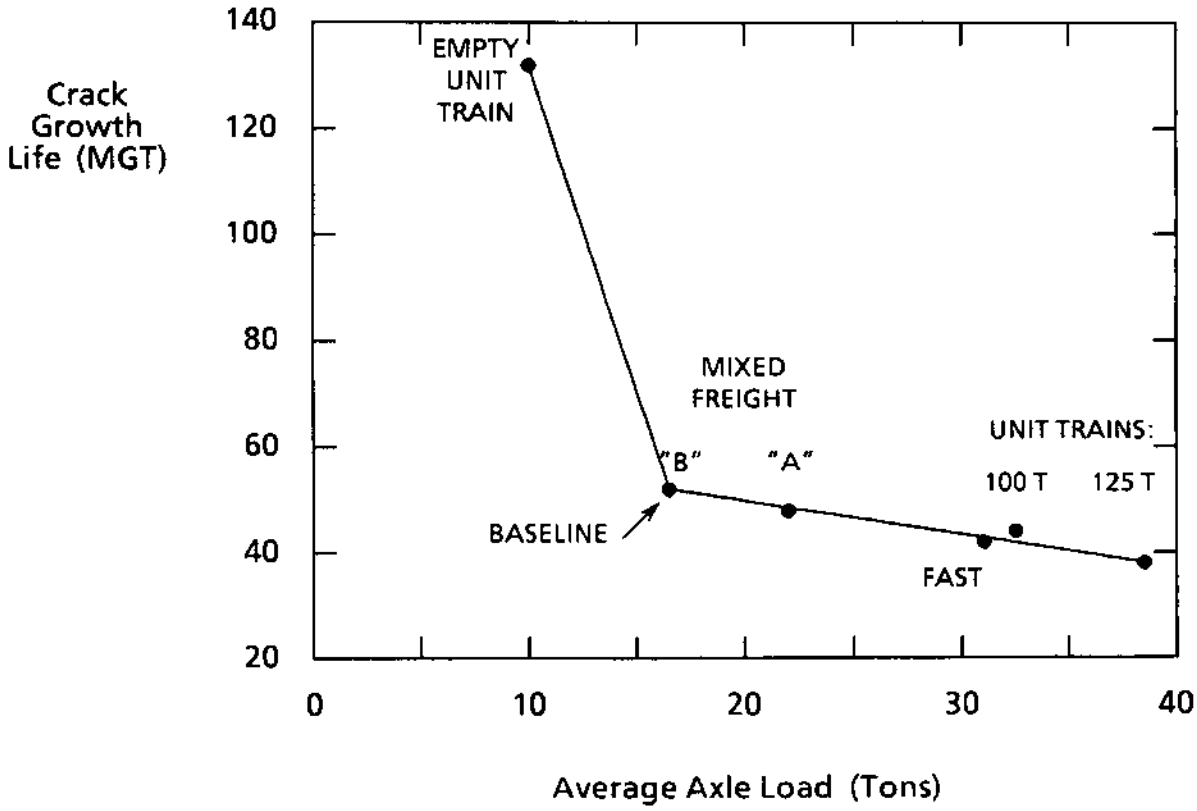

FIGURE 48. EFFECT OF AVERAGE AXLE LOAD.

Table 27 summarizes the effects of the vehicle dynamic factors. Mild car motions on track with exceptionally good geometry and foundation characteristics are represented by dynamic load coefficients with 1/4 of the baseline values. Severe motions are represented by tripling the baseline coefficients for heavy cars (static axle load greater than 27.5 tons). One case is also shown of baseline car motions with anomalous wheels comprising 0.6 percent of the wheel population (one flat in 172 wheel loads). The crack growth life varies by about ± 20 percent over the range of car motion dynamics studied. The flat wheel population incidence decreases the life by 5 percent.

TABLE 27. EFFECTS OF VEHICLE DYNAMICS.

Assumed Environment	Coefficients of Variation				Crack Growth Life (MGT)
	c_{v1}	c_{v2}	c_{v3}	c_{v4}	
Mild	0.0	0.125	0.1	0.05	64.6
Baseline Baseline + wheel flat (a)	0.0	0.5	0.4	0.2	52.0 49.2
Severe	0.0	0.5	1.2	0.6	44.4

[a] The 33rd wheel in the consist. Static load of 27.5 kips; magnification factor of 3.

Crack growth life decreases as track curvature increases (Figure 49). The principal source of this effect is the increase in stress ranges caused by the lateral loads associated with steady-state curve negotiation (see Section 4.1.2) and, therefore, the results apply only to the high rail on curves. The life decrease is limited by L/V saturation at 6 degrees of curvature. For practical purposes, the results suggest that one can evaluate detail fracture crack growth life on mainline curves by means of calculations for 5 degrees of curvature.

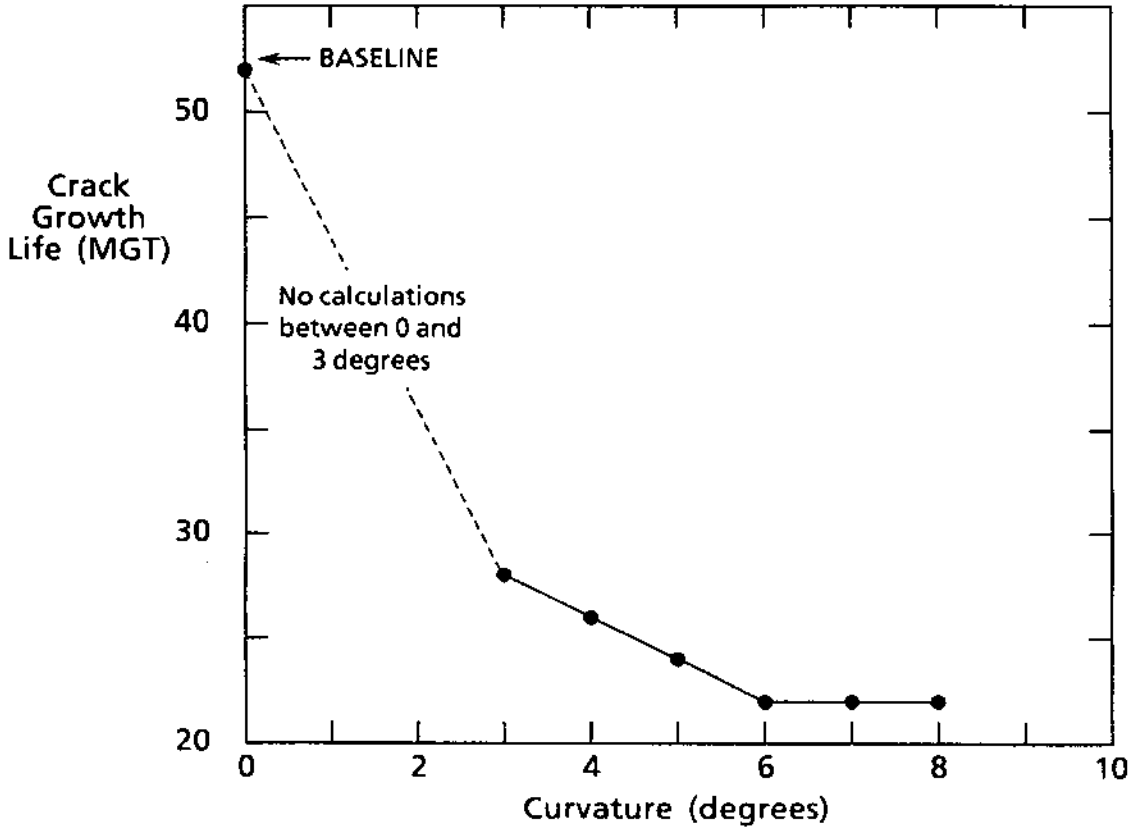

FIGURE 49. EFFECT OF TRACK CURVATURE.

Figure 50 illustrates the sensitivity of crack growth life to foundation stiffness. The life varies by about ± 20 percent over the range of typically maintained wood-tie track ($2 \leqq k \leqq 4$ ksi) and decreases by about 40 percent on poorly maintained track ($k = 1$ ksi). On well maintained concrete-tie track ($k = 10$ ksi), the crack growth life is almost 50 percent longer than the baseline.

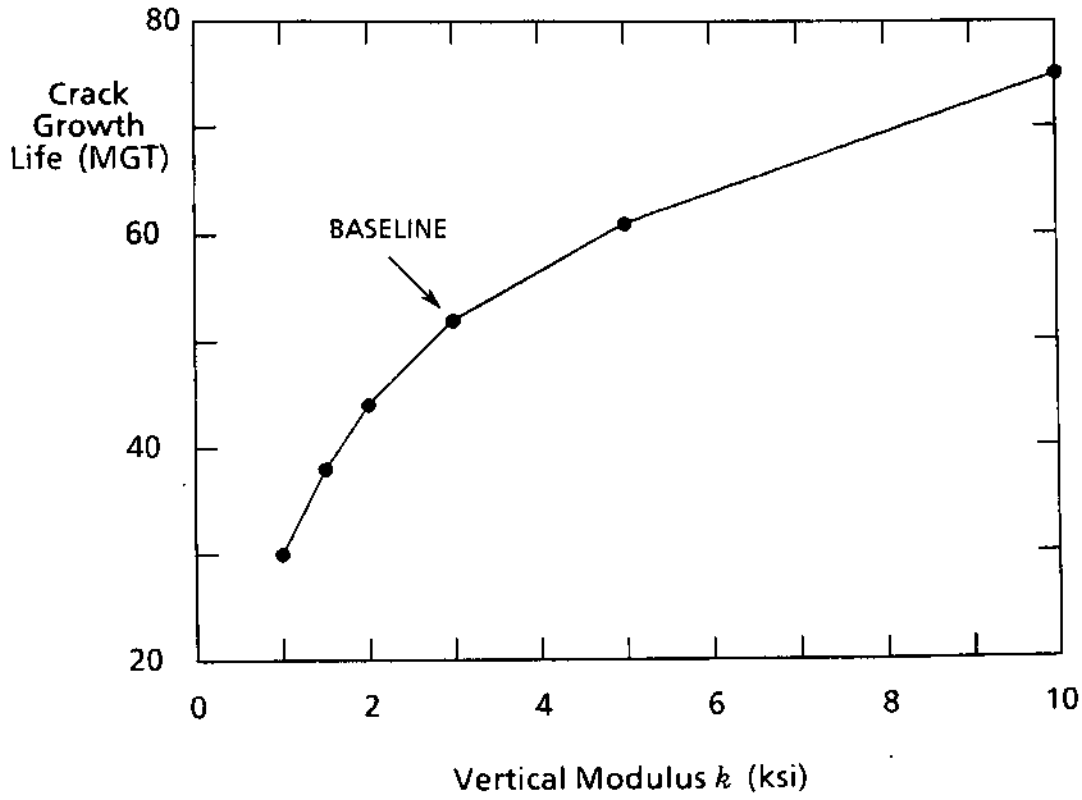

FIGURE 50. EFFECT OF TRACK FOUNDATION MODULUS.

Table 28 summarizes the sensitivity of crack growth life to rail section. Figure 51 also illustrates a plot of these results with respect to the second area moment of the rail section, I_{yy}, which is proportional to the vertical bending stiffness of the rail. The lives calculated for the 127 DY, 132 RE, 136 RE, and 140 RE sections exhibit a spread of about 6 MGT, a figure which can be taken as a measure of the practical resolution limit of the detail fracture model.

TABLE 28. CRACK GROWTH LIFE VERSUS RAIL SECTION.

Section	85 AS	90 AS	100 RE	115 RE	127 DY	132 RE	136 RE	140 RE	155 PS
Life (MGT)	23.7	25.1	33.5	40.9	58.3	57.2	52.0	52.7	63.3

Figure 52 illustrates the sensitivity of crack growth life to the rail head residual stress factors. Equations 30 and 100 are used to represent standard and high-strength rail, respectively, and scale factors from 1 to 3 have been investigated. The extra depth of residual tension assumed to be associated with the high-strength rail has a small effect, decreasing the crack growth life by about 10 percent. Conversely, the scale factor has a strong influence: a factor of 1.3 (difference between standard and high yield strength)

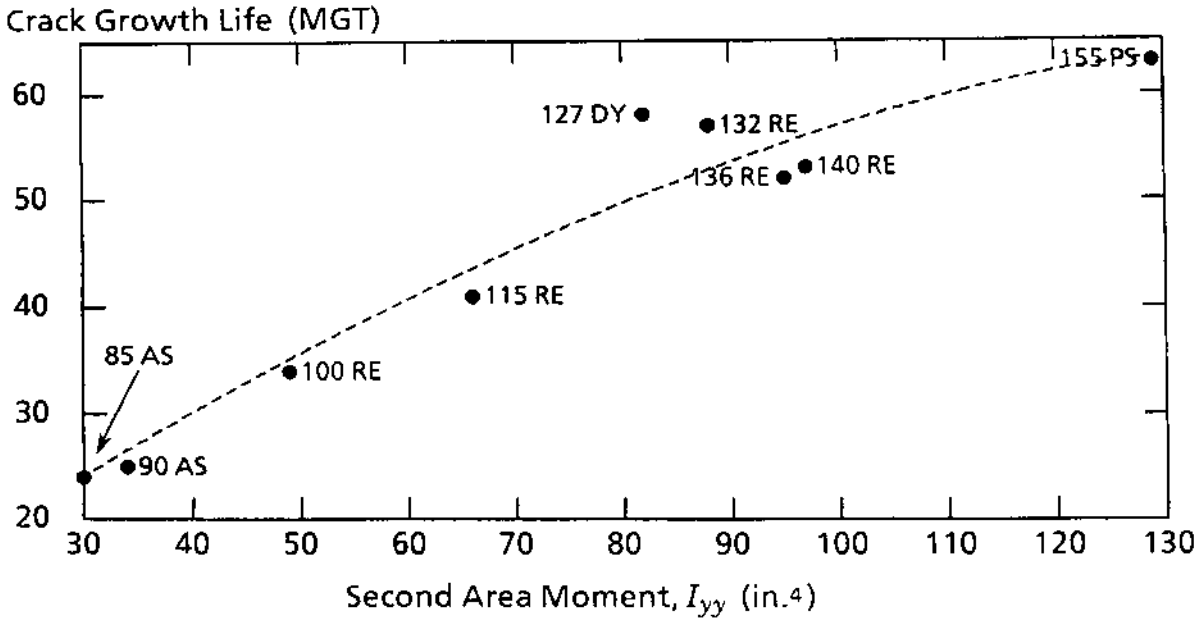

FIGURE 51. CRACK GROWTH LIFE VERSUS RAIL VERTICAL BENDING STIFFNESS.

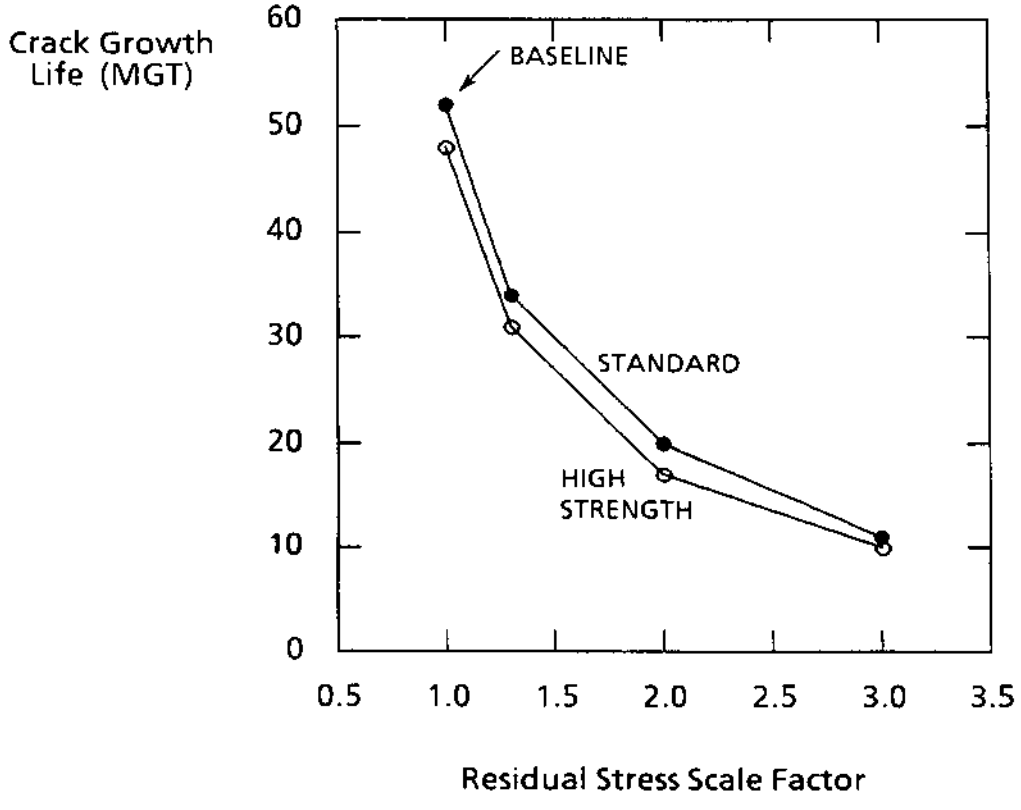

FIGURE 52. EFFECT OF RESIDUAL STRESS.

decreases the crack growth life by about 30 percent; a factor of 3 (possibly the result of wheel-creep tractions on curves) decreases life by about 75 percent. These results suggest that the scale depth of the residual stress distribution is relatively unimportant, whereas the overall magnitude of the stress field has a strong influence on crack growth life.

In the case of zero thermal stress ($T_n - T = 0$), the crack growth life was found to be 156 MGT, i.e., three times the baseline. However, modest thermal tension is sufficient to drastically decrease the life (see Figure 53 on the following page). For example, the baseline life corresponds to $S_T = 2.73$ ksi, and at $S_T = 7.8$ ksi the crack growth life is less than half the baseline value. The last situation corresponds to $T_n - T = 40$ °F, e.g., well adjusted track at a typical winter service temperature of 20 °F.

Table 29 shows the effect of changing the location of the center of wheel-rail contact. The "outside" position represents the typical situation of a heavily worn wheel with false flange operating on the high rail of a curve. Wheels with normal profiles operating on curve high rails would tend to run between the outside and nominal positions. The "inside" position represents either new wheels running on new rail or an extreme case of rail wear in combination with gage widening. Figure 54 illustrates a plot of crack growth life versus lateral position of the center of contact.

TABLE 29. EFFECT OF WHEEL-RAIL CENTER-OF-CONTACT LOCATION.

Loc.	Outside Halfway from rail center plane to field side face	Nominal Halfway from rail center plane to gage side face	Inside In plane of gage side face
Life (MGT)	27.2	52.0	90.0

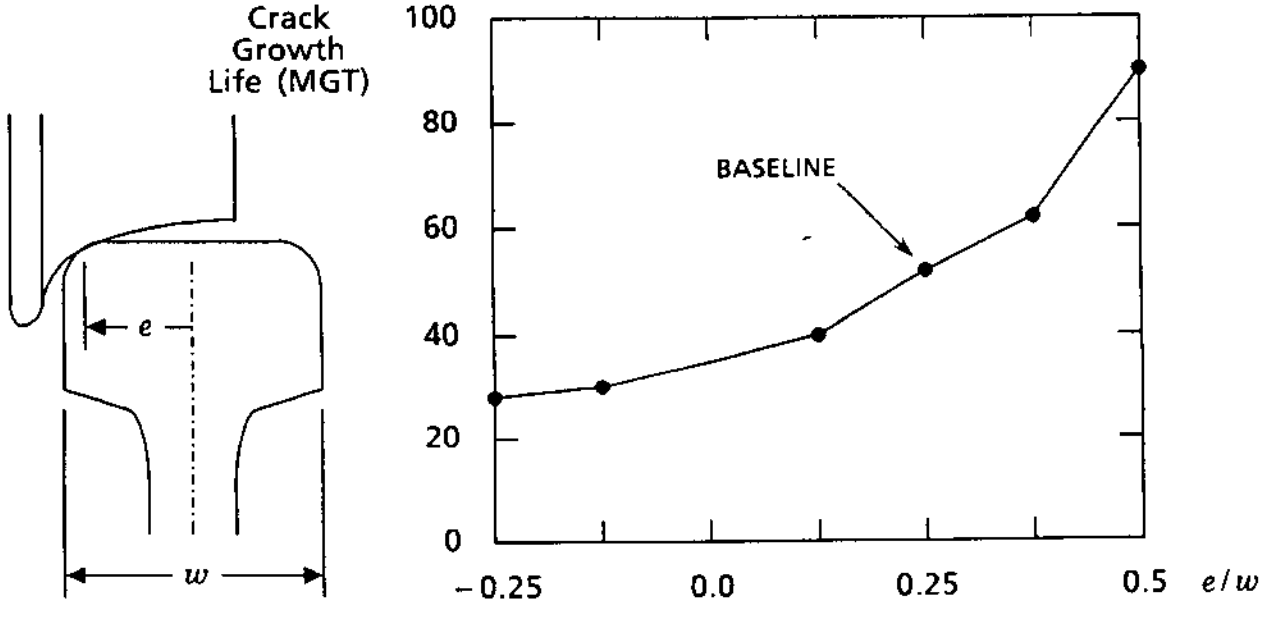

FIGURE 54. CRACK GROWTH LIFE VERSUS WHEEL CONTACT POSITION.

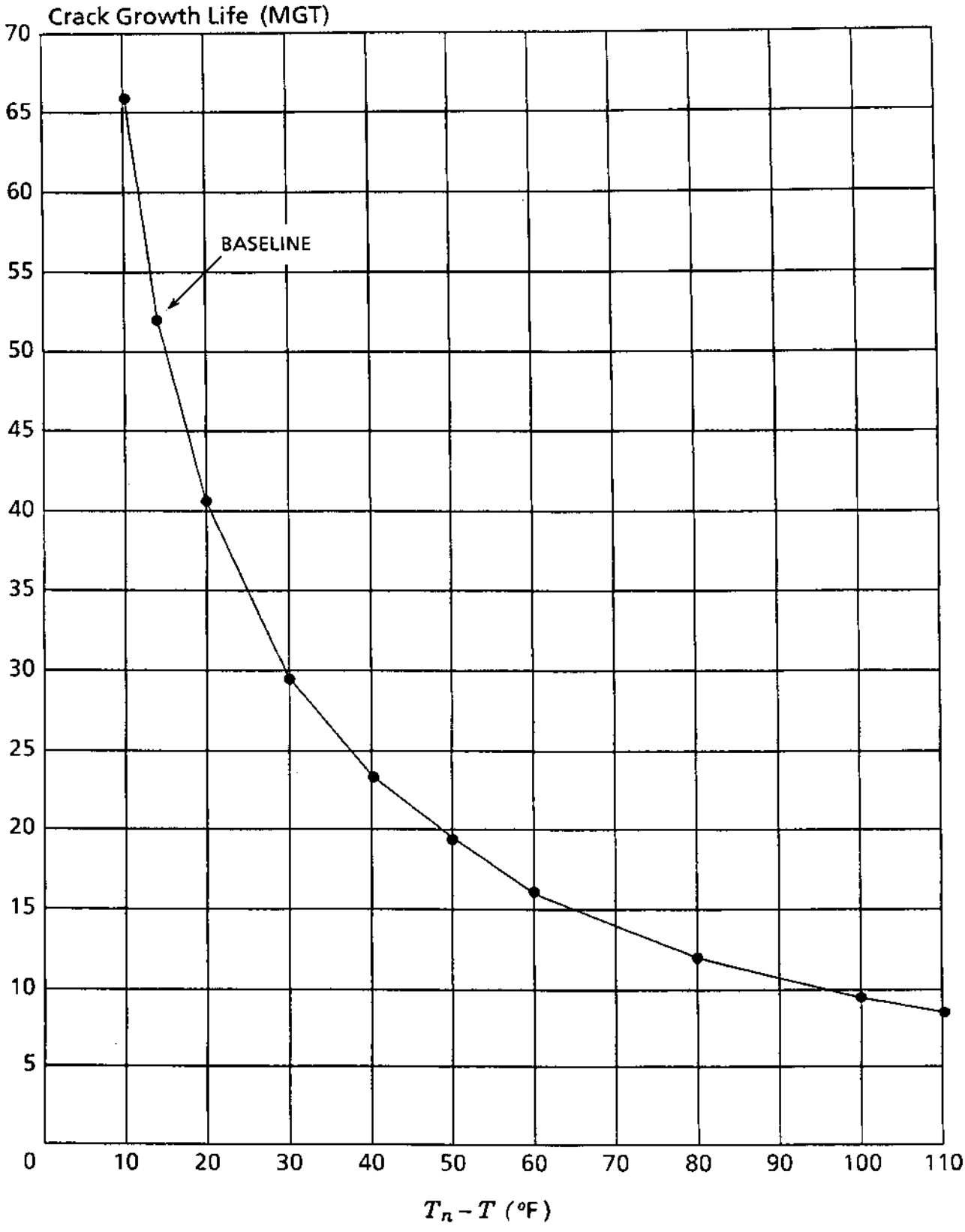

FIGURE 53. EFFECT OF TEMPERATURE DIFFERENTIAL.

Table 30 compares the effect of the nominal and alternative empirical equations for flaw center location parameters as functions of flaw size (see Figure 5). The 10 percent decrease of life for the alternate case is consistent with the effect of the center location change on live stress, but is opposite to the trend of the test rail 3 and 4 experiments.

TABLE 30. EFFECT OF FLAW CENTER LOCATION

Empirical Equations for Center Location	Nominal: Per Test Rails 1,2,5, and 6	Alternate: Per Test Rails 3 and 4
Life (MGT)	52.0	48.9

Figures 55 and 56 summarize the results of the sensitivity study. The ability of each factor to increase or decrease crack growth life, relative to the 52 MGT baseline, is indicated. In Figure 55, the factors have been arranged to illustrate the gradation of decreases from the baseline life. In Figure 56, the factors have been rearranged to illustrate the gradation of crack growth life ranges.

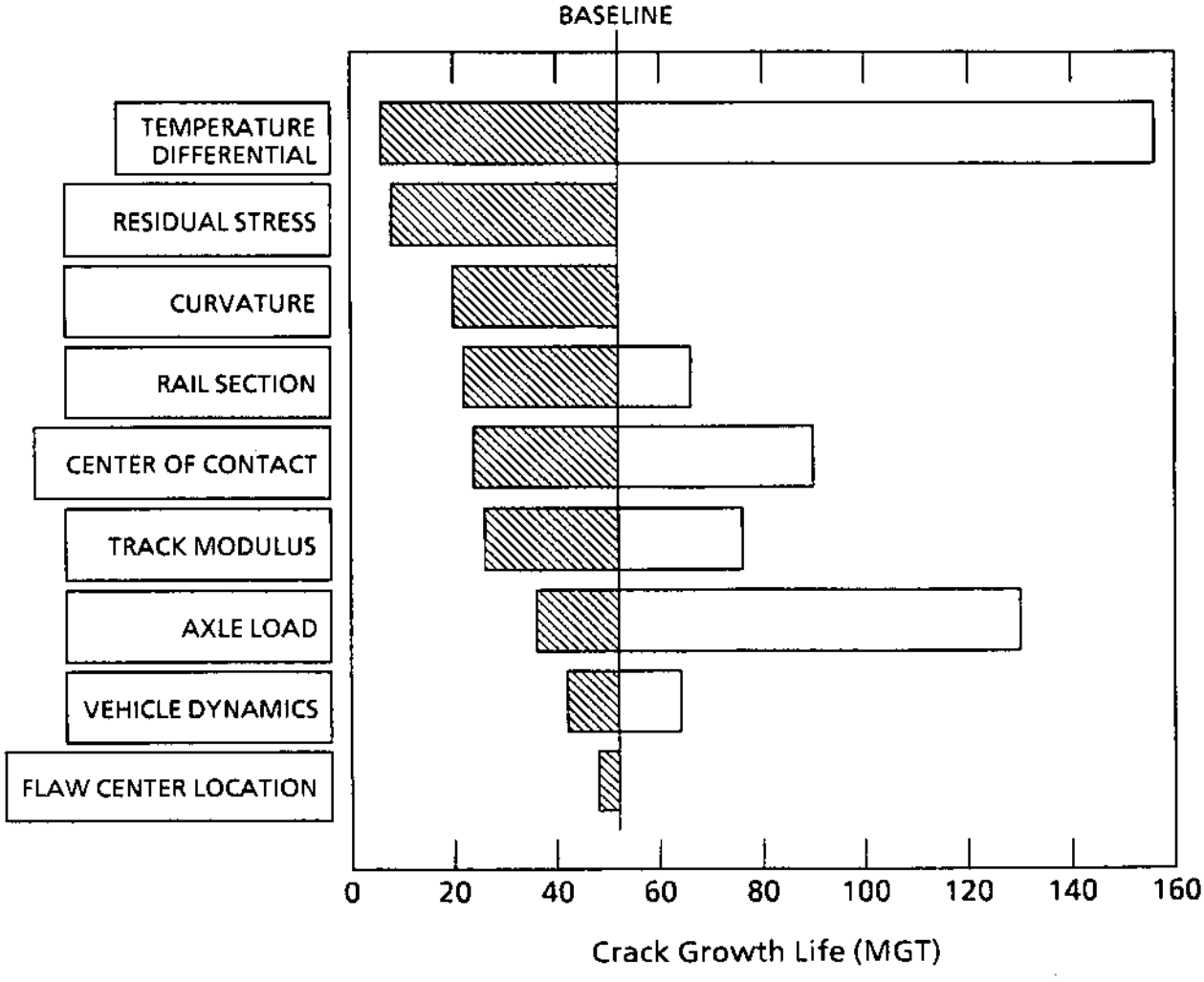

FIGURE 55. RELATIVE EFFECT OF ENVIRONMENT FACTORS ON LIFE REDUCTION.

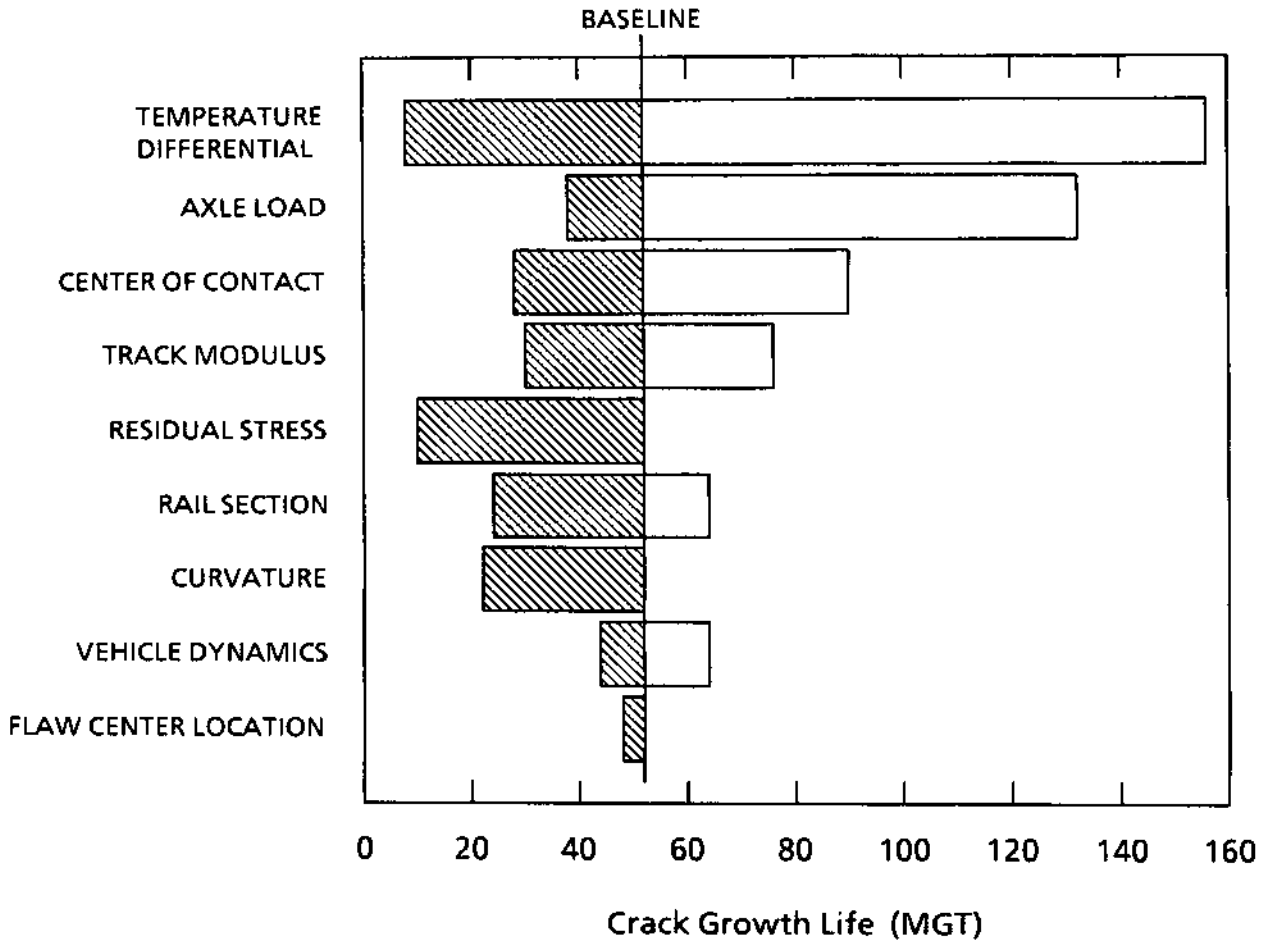

FIGURE 56. RELATIVE LIFE SENSITIVITIES.

5.4 Estimation of Crack Growth Life in Typical Thermal Environments

Thermal stress is the most influential single factor affecting detail fracture crack growth life in CWR and is also the most difficult factor to describe. Corresponding to the range of realizable thermal tension, the range of crack growth life spans an order of magnitude. Histories of thermal tension (or the equivalent, $T_n - T$) for revenue track can at best be characterized only in an average sense, e.g., by histograms of $T_n - T$ occurrences. It is impossible to convert such a description into a specification of temperature differential as a function of defect size, in the manner in which the FAST experiment was treated, without making unjustified assumptions which are likely to have a strong effect on the crack growth life estimate.

Fortunately, an approximate estimation method based on Miner's rule [72] can be constructed to resolve the dilemma. In Section 4.2 it was mentioned that the thermal stress S_T can be treated as a slowly varying mean stress for the purpose of calculating crack growth life. Under this circumstance, one can apply Miner's rule within certain limitations by defining crack growth damage fractions based on $T_n - T$ occurrence histograms and curves of crack growth life versus constant $T_n - T$ values.

Let the environment be described by a discrete set of temperature differentials $(T_n - T)_i$; $i = 1, 2, \ldots, N$. Let m_i be the fraction of service spent at the i^{th} temperature differential and M_i the life, in MGT, for a crack growing at S_T corresponding to $(T_n - T)_i$. The Miner's rule estimate for crack growth life in the given environment is

then calculated in the usual manner as the inverse of the linear damage sum:

$$L = \left[\sum_{i=1}^{N} \frac{m_i}{M_i} \right]^{-1} \tag{103}$$

The test rail 1 simulation will be used as an illustrative example. Figure 57 reproduces from Figure 38 the $T_n - T$ history used in the simulation. For the purpose of the Miner's rule estimate, the history is divided into 11 tonnage blocks, each of which has been assigned a discrete temperature differential. The service fraction for each block is the ratio of the block tonnage to the total tonnage (~33 MGT) elapsed in the experiment.

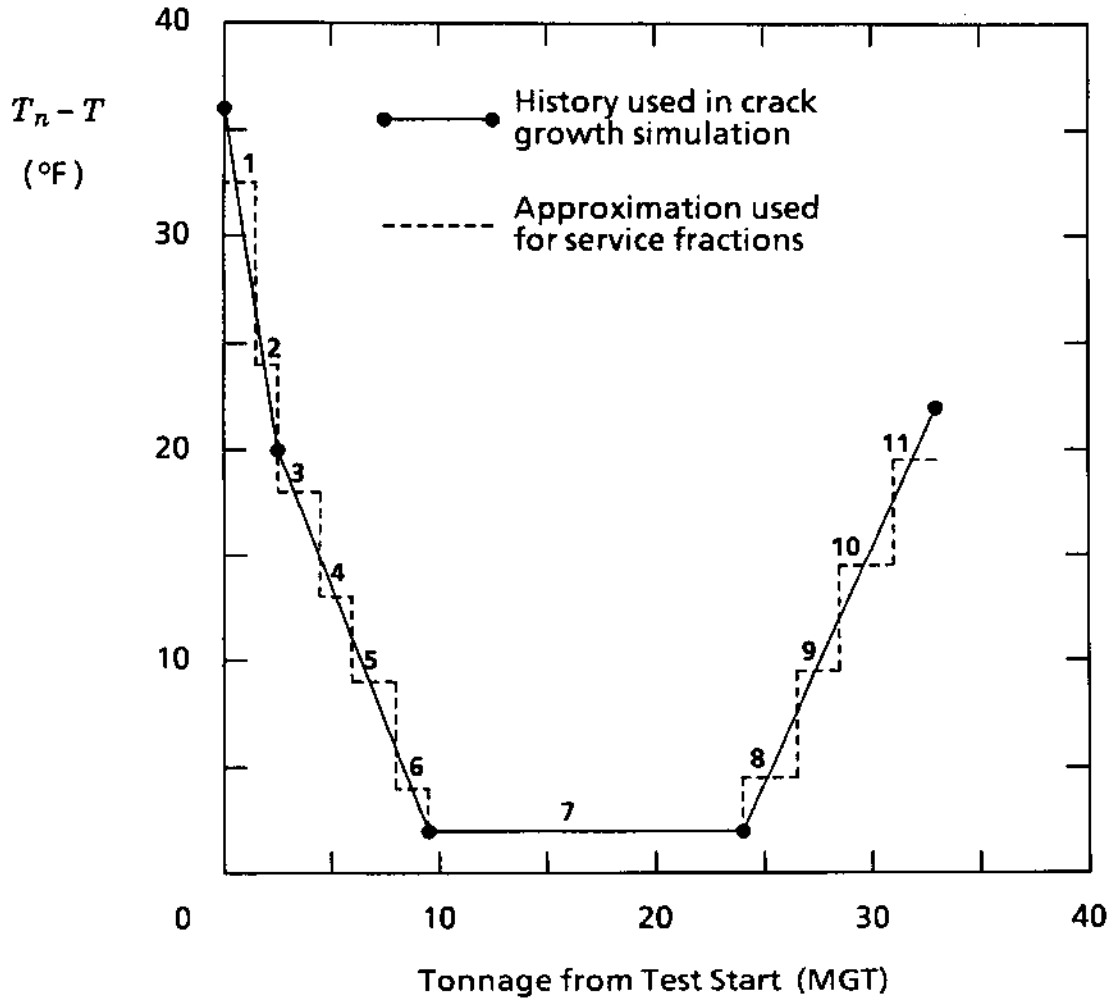

FIGURE 57. ESTIMATION OF SERVICE FRACTIONS FOR TEST RAIL 1.

Figure 58 illustrates the temperature sensitivity curve. This curve was obtained from detail fracture model crack growth calculations with the test rail 1 input factors, except for the use of constant $T_n - T$.

Table 31 summarizes the Miner's rule estimate for test rail 1 crack growth life, based on the service fractions shown in Figure 57 and the temperature sensitivity shown in Figure 58. The estimated life of about 63 MGT is almost twice the 34MGT life calculated from S_T as a function of defect size (see Figure 44). This case provides a severe test

because the strongly biased history of $T_n - T$ creates a sequence dependence in the crack growth history, an effect which the Miner's rule method cannot account for. In practice, however, sequence dependence has little effect on the life estimate because the time history of $T_n - T$ is not strongly biased in revenue service [26].

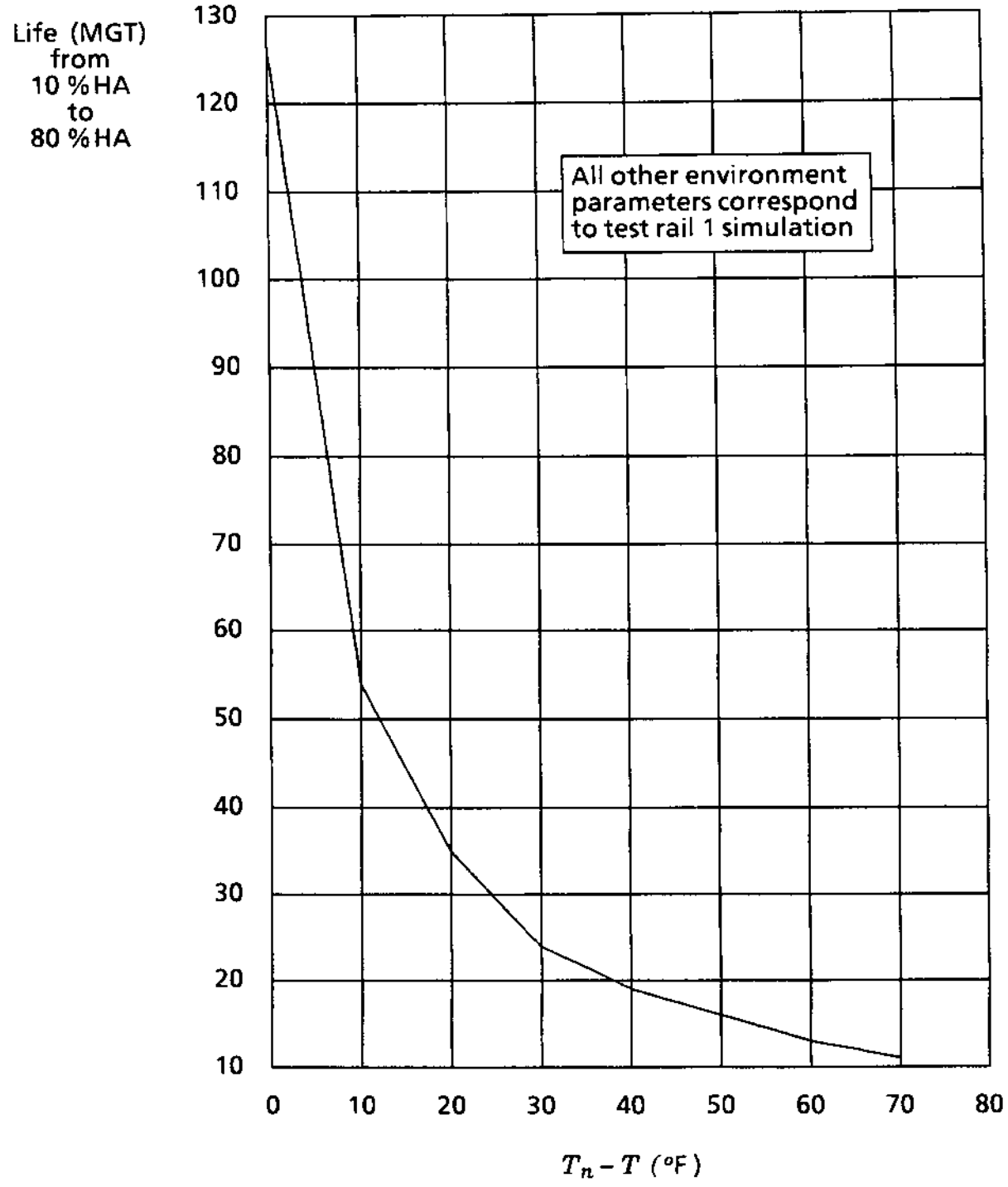

FIGURE 58. LIFE VERSUS TEMPERATURE FOR TEST RAIL 1.

TABLE 31. MINER'S RULE LIFE ESTIMATE FOR TEST RAIL 1.

i	$(T_n - T)_i$ (°F)	m_i	M_i (MGT)	m_i/M_i
1	32	1.15/33	24	0.00145
2	24	1.15/33	31	0.00112
3	18	1.8/33	39	0.00140
4	13	1.8/33	48	0.00114
5	9	1.8/33	62	0.00088
6	4	1.8/33	95	0.00057
7	2	14.5/33	111	0.00396
8	4.5	2.25/33	93	0.00073
9	9.5	2.25/33	54	0.00126
10	14.5	2.25/33	46	0.00148
11	19.5	2.25/33	35	0.00195

$\Sigma m_i/M_i$ 0.01594

Life estimate ..... 62.7 MGT

Miner's rule can be used to make reasonable life estimates for a variety of typical revenue environments and situations if the temperature sensitivity chart includes additional information about the crack behavior:

- How is the consumption of crack growth life distributed over defect size? Does one expect a detail fracture to spend half or most of its life as a small defect? Such questions must be answered in order to evaluate defect detection reliability as a function of rail test equipment reliability and schedule [71].
- Are there significant variations of critical crack size? Does one expect that every detail fracture must reach 80 %HA to cause a rail failure, or are there circumstances in which smaller defects can cause rail failures? A reduction of critical crack size sometimes means a significant reduction of crack growth life.

Figures 59 through 64 are examples of temperature sensitivity charts which enable the engineer to use Miner's rule to answer such questions. Figures 59 and 60 are for 136 RE rail in tangent CWR under mixed freight (General Freight "B" spectrum) and loaded 100-ton unit train traffic, respectively. Figures 61 and 62 are similar charts for the high rail in a 5-degree curve. Each chart contains four curves which define the life of a detail fracture assumed to grow from 10 %HA to four larger sizes: 20, 30, 50, and 80 %HA. Differences can be taken to estimate block lives, e.g. for tangent track under mixed freight at $T_n - T = 10$ °F (Figure 59), growth from 30 to 50 %HA consumes $57 - 51.5 = 5.5$ MGT. Each chart also has a critical crack size cutoff shown as a boldface dashed curve. The cutoff can be interpreted as a life limit in the worst possible case, i.e., if one assumes that the thermal stress necessary to cause failure is always present at the earliest possible moment sufficient to precipitate a rail failure.

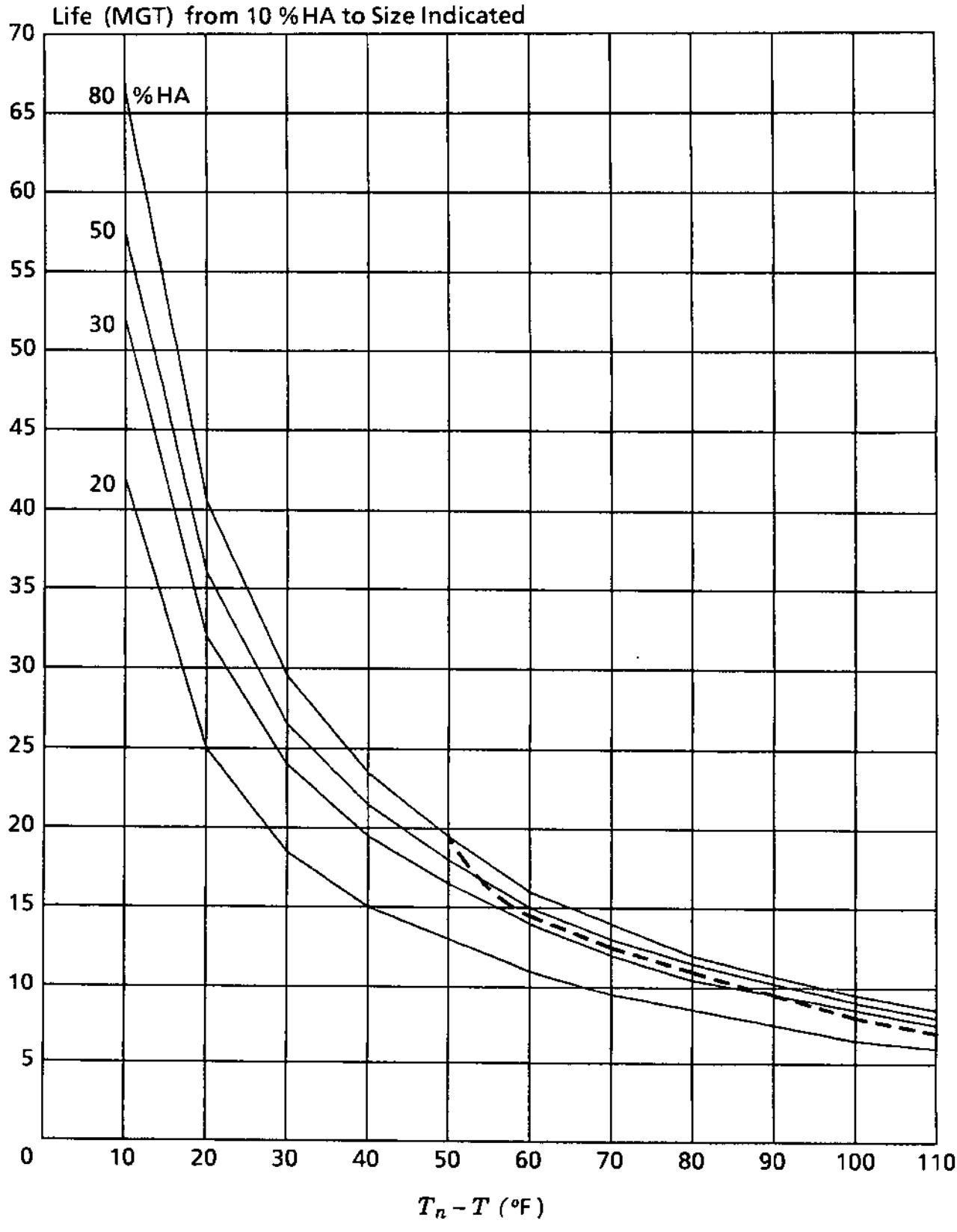

FIGURE 59. DETAIL FRACTURE LIFE (136 RE; TANGENT TRACK; MIXED FREIGHT).

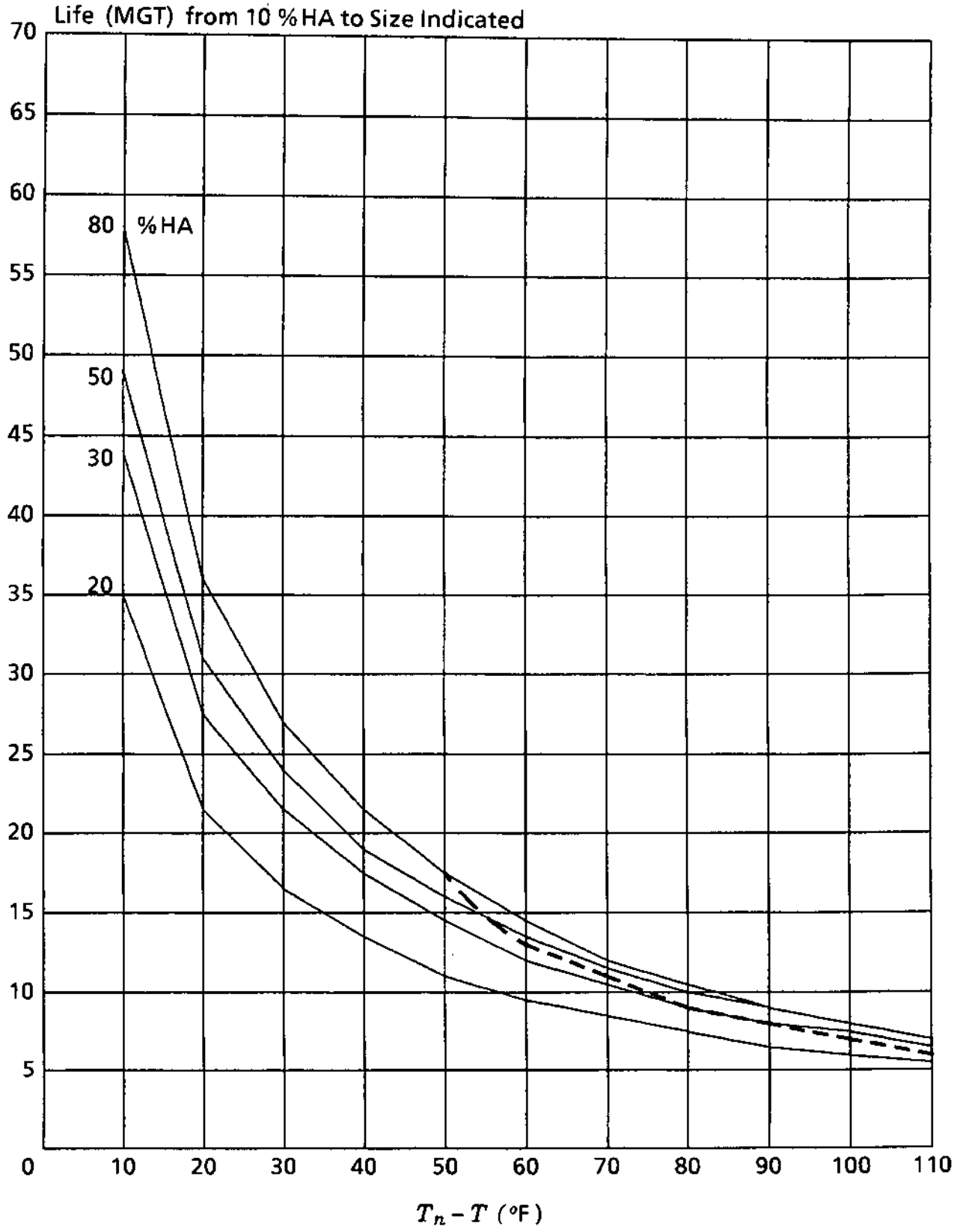

FIGURE 60. DETAIL FRACTURE LIFE (136 RE; TANGENT TRACK; UNIT TRAIN).

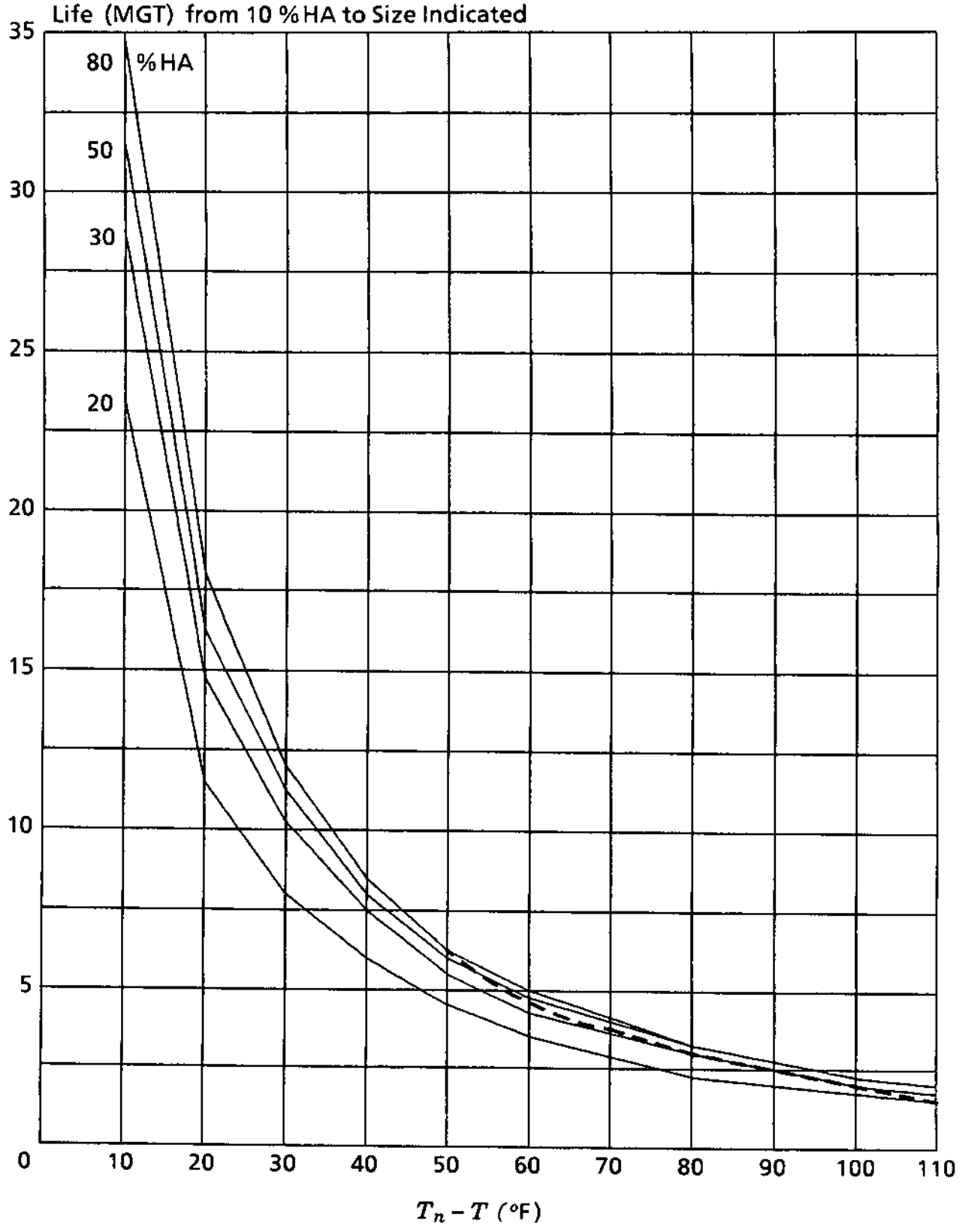

FIGURE 61. DETAIL FRACTURE LIFE (136 RE; 5° CURVE; MIXED FREIGHT).

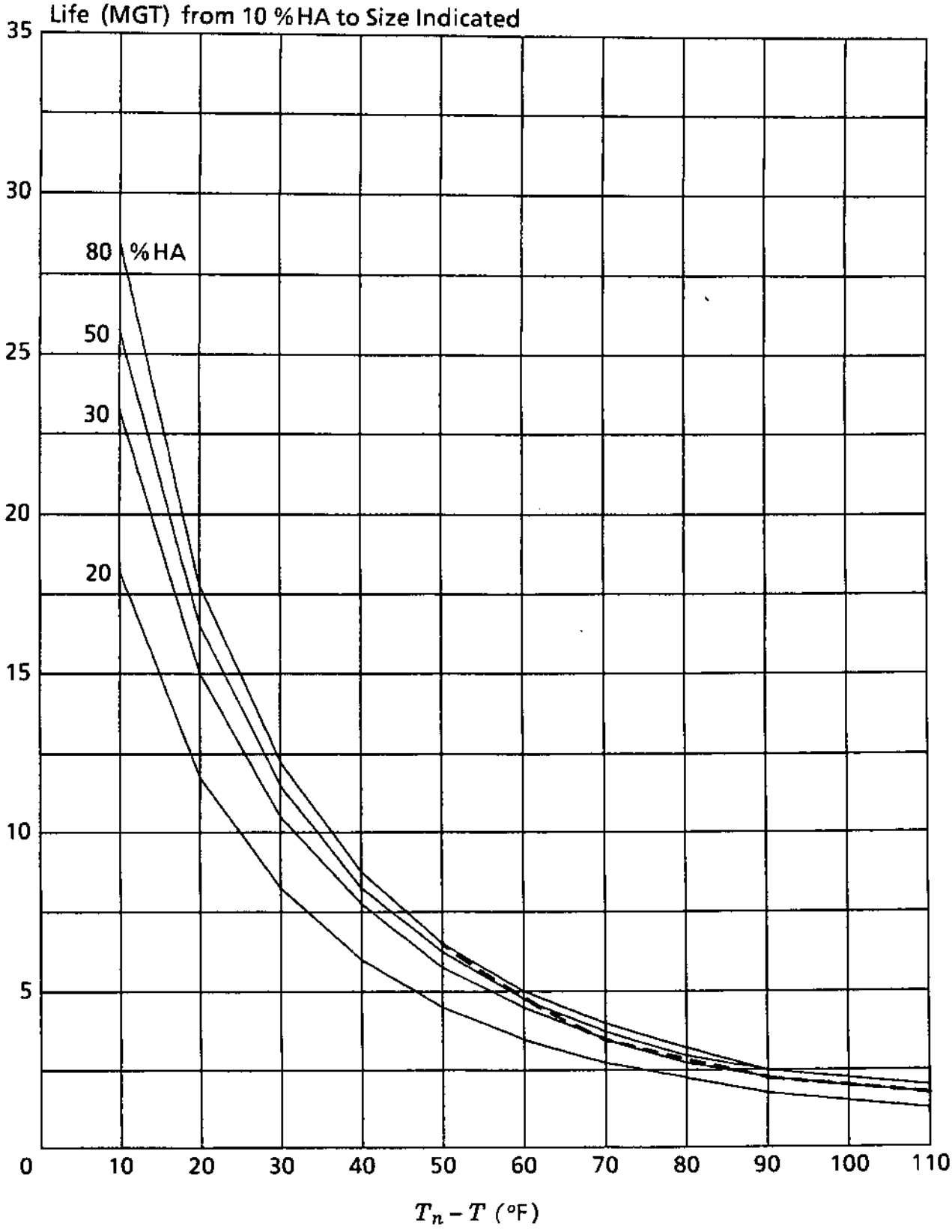

FIGURE 62. DETAIL FRACTURE LIFE (136 RE; 5° CURVE; UNIT TRAIN).

A detailed description of the thermal environment at Broken Bow, NE (a point on the Burlington Northern Railroad's Alliance Division) was presented in Section 4.2. Several examples using that database in conjunction with Figures 60 and 62 will now be presented to illustrate the application of Miner's rule.

First, suppose that an estimate of crack growth life is needed for tangent track which is well adjusted ($T_n = 60$ °F) and which is subjected to the temperature differential occurrences shown in Figure 25 while carrying unit train traffic distributed uniformly over the 24-hour day. The occurrence histograms cover 366 days (February 1980 was a leap month), and there are thus a total of 732 occurrences of daytime and nighttime differentials. The occurrences have been grouped in 10 °F bins, and the temperature differential at the middle of each bin can be used to make the crack growth life estimate. For practical purposes, only those bins for which $T_n - T > 0$ need be counted.

Table 32 summarizes the environmental data and the Miner's rule calculations. The service fractions m_i are obtained by dividing the occurrences by 732. The sum of these fractions is about 0.49, i.e., in the assumed environment the rail is in thermal tension just under half the service time. The constant-temperature lives M_i are read from the 80 %HA curve in Figure 60, except for $T_n - T = 5$ °F, for which 95 MGT is estimated by means of linear interpolation between $M = 58$ MGT at $T_n - T = 10$ °F and $M \approx 132$ MGT at $T_n - T = 0$ °F. The last column of the table gives the damage fractions. The damage sum and its inverse (the life estimate of 60.3 MGT) are given at the bottom.

TABLE 32. MINER'S RULE LIFE ESTIMATE BASED ON OCCURRENCE HISTOGRAM.

$T_n - T$ (°F)	Occurrences in 366 Days			$m_i =$ Total/732	M_i (MGT)	m_i/M_i
	Day	Night	Total			
5	16	60	76	0.1038	95	0.00109
15	12	46	58	0.0792	47	0.00169
25	11	56	67	0.0915	32	0.00286
35	3	78	81	0.1107	24	0.00461
45	5	38	43	0.0587	19	0.00309
55	0	24	24	0.0328	16	0.00205
65	0	8	8	0.0109	13	0.00084
75	0	3	3	0.0041	11.5	0.00036

$\Sigma m/M$ 0.01659

Life ..... 60.3 MGT

Now suppose that the effect of day versus night operation is to be evaluated for the same environment as in the preceding example. The temperature differentials, constant-temperature lives, and occurrences are as given in Table 32, but the scaling factor for m_i is 366 instead of 732. Table 33 summarizes the calculations for these cases. Operating exclusively in the daytime is shown to be a relatively beneficial practice. Less than 13 percent of the daytime temperature differentials put the rail in tension, and

the estimated life is 316 MGT. Conversely, the rail is in tension over 85 percent of the time for a night operation, and the estimated life is only 33.3 MGT.

Miner's rule can also be applied to combine the day and night estimates in various proportions. For example, for the case of equal traffic proportions:

$$L \approx \left[\frac{0.5}{316} + \frac{0.5}{33.3} \right]^{-1} = 60.3 \ MGT \tag{104}$$

which agrees with the result in Table 32.

TABLE 33. INDIVIDUAL LIFE ESTIMATES FOR DAY AND NIGHT TRAFFIC.

$T_n - T$ (°F)	M_i (MGT)	Day		Night	
		m_i	m_i/M_i	m_i	m_i/M_i
5	95	0.0437	0.00046	0.1639	0.00173
15	47	0.0328	0.00070	0.1257	0.00267
25	32	0.0301	0.00094	0.1530	0.00478
35	24	0.0082	0.00034	0.2131	0.00888
45	19	0.0137	0.00072	0.1038	0.00546
55	16	---	---	0.0656	0.00410
65	13	---	---	0.0219	0.00168
75	11.5	---	---	0.0082	0.00071
$\Sigma m/M$		0.00316		0.03001	
Life		316 MGT		33.3 MGT	

How realistic are the foregoing crack growth life estimates, in the light of the first comparison of a similar estimate with the test rail 1 experiment and simulation? The answer in this case depends on how long the estimated life is in relation to the annual tonnage carried by the track. If the annual tonnage is low enough, the crack growth life amounts to several years, the occurrences of all temperature differentials are more or less evenly distributed over all sizes of the growing defect, and the Miner's rule life estimate is reasonable. Conversely, if the annual tonnage is of the same order as the life estimate, one should expect some sequence-bias error from seasonal effects. If Miner's rule is to be usefully applied to such cases, the annualized occurrence histogram should be replaced by an occurrence histogram for one season or one month, and several years of data for the appropriate period should be averaged to smooth out normal weather fluctuations.

The potential for resolution error must also be kept in mind when seasonal presentations of weather data are used to make crack growth life estimates. In practice, one may have only monthly averages of the daily high and low ambient temperatures from which to construct $T_n - T$. Daytime and nighttime seasonal histograms of the Figure 25 occurrence data are illustrated in Figure 26. Table 34 summarizes the Miner's rule life estimate for night operations, based on the seasonal histogram. Correspond-

ing to each monthly average temperature differential, the service fraction is determined by the number of days in the month. In this case, the life estimate of 32.2 MGT is quite close to the 33.3 MGT result obtained from the occurrence histogram.

Such good agreement cannot be relied upon, however, as is shown by a similar comparison of the daytime data. While the daytime occurrence histogram contains a small percentage of service in thermal tension and leads to a life estimate of 316 MGT, the daytime seasonal histogram implies that the rail is never in tension and would lead to an unrealistically long life estimate.

TABLE 34. LIFE ESTIMATE BASED ON SEASONAL HISTOGRAM.

Month	$T_n - T$ (°F)	m_i	M_i (MGT)	m_i/M_i
J	47	31/366	18	0.00471
F	46	29/366	18.5	0.00428
M	39	31/366	22	0.00385
A	26	30/366	31	0.00264
M	16	31/366	45	0.00188
J	3	30/366	110	0.00075
J	−2	31/366	150	0.00056
A	2	31/366	117	0.00072
S	10	30/366	58	0.00141
O	23	31/366	33	0.00257
N	41	30/366	21.5	0.00381
D	39	31/366	22	0.00385

$\Sigma m/M$ 0.03103

Life ..... 32.2 MGT

A better procedure when dealing with seasonal data is to make some estimate for the probability distribution of the temperature differential. For example, let $p(T_n - T)$ and $M(T_n - T)$ be the occurrence probability density and constant-temperature life functions, respectively. Miner's rule can then be formally expressed as:

$$L = \left[\int_{-\infty}^{\infty} \frac{p(T_n - T)}{M(T_n - T)} d(T_n - T) \right]^{-1} \tag{105}$$

and the trapezoid rule can be applied to Eq. 105 to compute the life estimate.

The foregoing example will next be elaborated to illustrate a method for dealing with situations in which the life estimate is of the same order as or shorter than the

annual tonnage. In such cases, let the Miner damage sums be calculated from one month, two months, etc. of seasonal data until twelve such life estimates have been made. Table 35 summarizes the life calculation for the case of four months counted.

TABLE 35. LIFE ESTIMATE BASED ON FIRST FOUR MONTHS.

Month	$T_n - T$ (°F)	m_i	M_i (MGT)	m_i/M_i
J	47	31/121	18	0.01423
F	46	29/121	18.5	0.01296
M	39	31/121	22	0.01165
A	26	30/121	31	0.00800

$\Sigma m/M$ 0.046844

Life ..... 21.3 MGT

Life can then be plotted versus number of months counted; this plot will be referred to as a "life curve". Figure 63 illustrates the plot obtained from analysis of the seasonal nighttime histogram, together with several lines representing different rates of annual tonnage accumulation. The safe crack growth life (in months) is defined by the intersection of the tonnage line with the life curve. Table 36 summarizes the life estimates thus obtained from Figure 63. The life increases as the annual tonnage rate decreases from 120 to 45 MGT per year. At 30 MGT per year, the entire tonnage line falls below the life curve, and the crack growth life estimate for this case is the complete Miner life (Table 34), subject to the caution about sequence bias mentioned earlier. The shape of the life curve in relation to the tonnage lines also suggests that bias might affect the 45 MGT/year case. If a better estimate were desired for this case, one could use the intermediate temperature sensitivities in Figure 60 to construct intermediate life curves for this purpose.

The shape of the life curve is also affected by the starting date used in the calculation. The starting date defines the time at which the defect is assumed to have reached the size of 10 %HA. In general, detail fractures can attain this size at any time of the year, and the January starting date in the preceding example was arbitrarily assumed. A better approach is to calculate life curves for several different starting dates and to obtain the life estimate for each case. Figure 64 shows examples with 60 and 45 MGT per year tonnages. At 60 MGT per year, it so happens that the life based on a January start is close to the most conservative estimate. At 45 MGT per year, however, the most conservative estimate is the life based on an October start. These examples illustrate the importance of a complete analysis, whether the objective is to find the most conservative life estimate or to provide a basis for tailoring rail test intervals to the seasons.

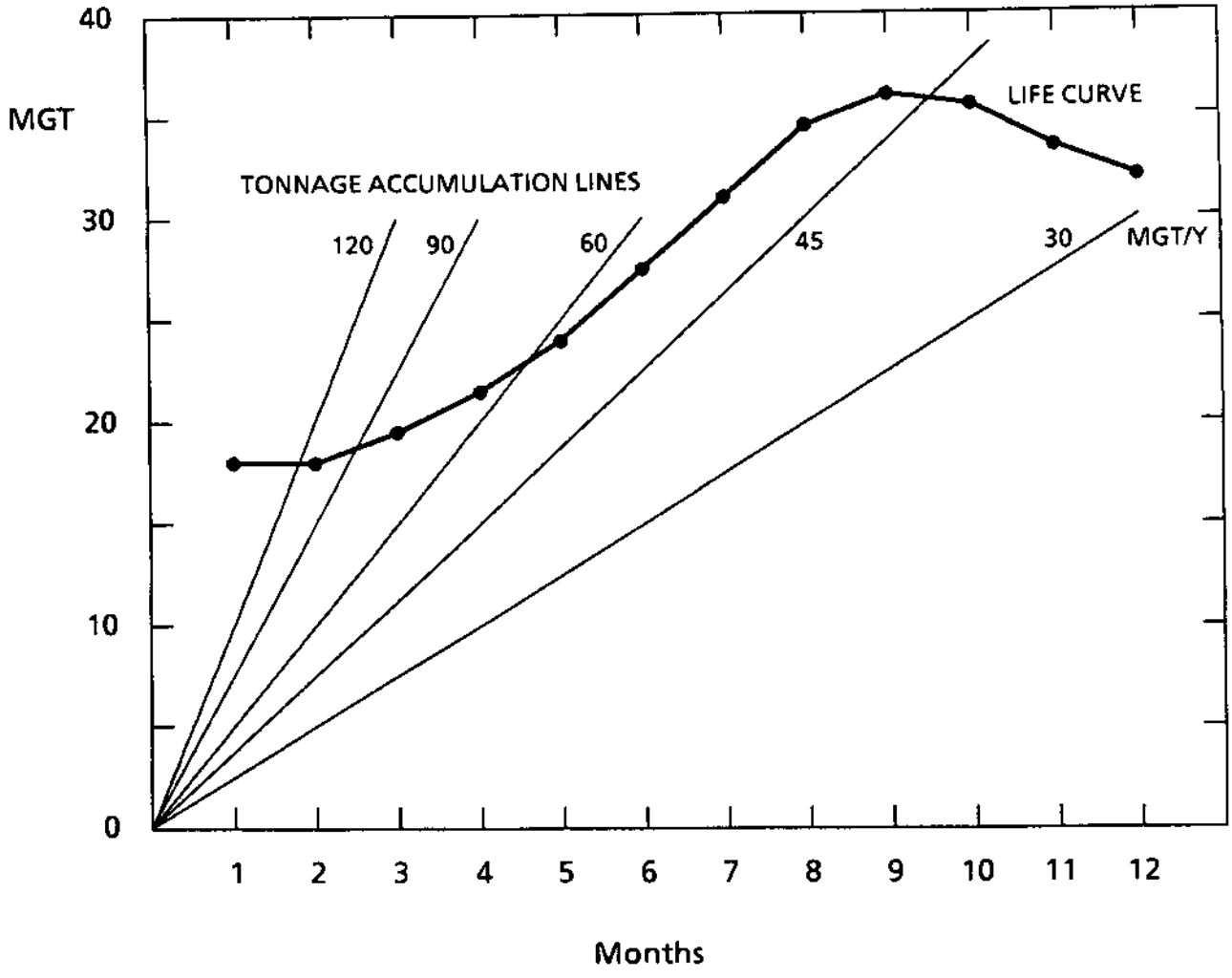

FIGURE 63. GRAPHICAL METHOD FOR LIFE ESTIMATION ON HIGH-TONNAGE TRACK.

TABLE 36. LIFE ESTIMATES OBTAINED FROM FIGURE 63.

Annual Tonnage (MGT/Y)	120	90	60	45
Life in months	1 3/4	2 1/2	4 5/8	9 1/2
Life in MGT	17 1/2	18 3/4	23 1/8	35 5/8

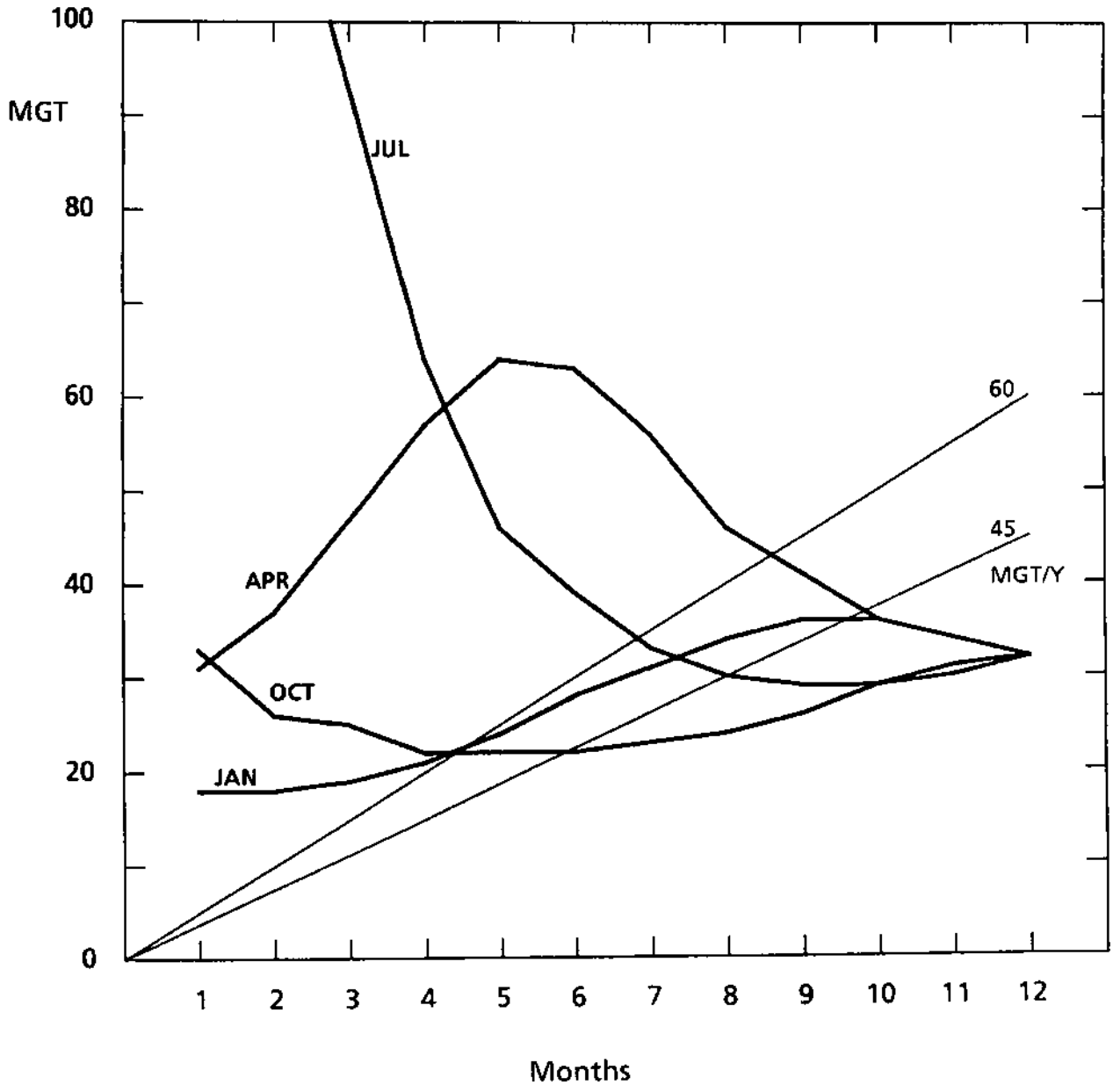

FIGURE 64. VARIATION OF LIFE ESTIMATE WITH ASSUMED STARTING DATE.

TABLE 37. LIFE ESTIMATES OBTAINED FROM FIGURE 64.

Starting Month	Jan	Apr	Jul	Oct
Life in months (60 MGT/Y)	$4\frac{5}{8}$	$8\frac{5}{8}$	$6\frac{3}{4}$	$4\frac{3}{8}$
Life in months (45 MGT/Y)	$9\frac{5}{8}$	$9\frac{3}{4}$	8	$5\frac{7}{8}$
Life in MGT (60 MGT/Y)	$23\frac{1}{8}$	$43\frac{1}{8}$	$33\frac{3}{4}$	$21\frac{7}{8}$
Life in MGT (45 MGT/Y)	$32\frac{1}{12}$	$32\frac{1}{2}$	$29\frac{2}{3}$	$19\frac{7}{12}$

Table 38 illustrates another example involving seasonal histograms. In this case, the environment data have been taken from Figure 27, in which the day and night temperature differentials for each month were averaged. May through October are omitted from the table because these months have no effect on the life estimates. The first case is equivalent (except in resolution) to the occurrence example in Table 32, and the sacrifice of resolution produces an overestimate of the crack growth life (95.5 versus 60.3 MGT). Comparison of the two cases in Table 38 illustrates the beneficial effect of a mild climate, i.e., one with relatively small temperature swings.

TABLE 38. COMPARISON OF DIFFERENT CLIMATES.

Month	Broken Bow Climate			Hypothetical Mild Climate		
	$T_n - T$ (°F)	M_i (MGT)	m_i/M_i	$T_n - T$ (°F)	M_i (MGT)	m_i/M_i
J	23	33	0.00257	10	58	0.00146
F	22	34	0.00233	9	66	0.00120
M	14	50	0.00169	5	95	0.00089
A	−2	150	0.00055	−3	160	0.00051
N	16	45	0.00182	6	46	0.00178
D	11	56	0.00151	3	110	0.00077
$\Sigma m/M$			0.01047			0.00661
Life			95.5 MGT			151 MGT

Table 39 presents a comparison of tangent track with the high rail on a 5-degree curve. In this example, the environment descriptions are occurrence histograms taken from Figure 28. The tangent-track temperature differentials are more severe than those in the preceding examples because the occurrences are based on newly laid CWR ($T_n = 90$ °F). In the curve rail case, neutral temperature adjustment decreases the thermal stress, thus compensating the lateral load effect to some extent, and the curve life estimate is only 20 percent shorter than the tangent-track estimate. Conversely, a 40 to 50 percent reduction of crack growth life is expected for curves in well adjusted track ($T_n = 60$ °F), where the neutral temperature model (Section 4.2) suggests that little or no adjustment of T_n should occur.

TABLE 39. LIFE ON TANGENT TRACK VERSUS 5-DEGREE CURVE.

$T_n - T$ (°F)	Tangent Track			High Rail on 5° Curve		
	Occ.	M_i (MGT)	m_i/M_i	Occ.	M_i (MGT)	m_i/M_i
5	---	---	---	26	36	0.00197
15	---	---	---	52	23.5	0.00605
25	53	32	0.00453	100	15	0.01821
35	60	24	0.00683	73	11	0.01813
45	46	19	0.00661	38	7.5	0.01384
55	56	16	0.00956	26	6	0.01184
65	78	13	0.01639	11	4.5	0.00668
75	38	11.5	0.00903	2	3.5	0.00156
85	24	9.5	0.00690	---	---	---
95	8	8.5	0.00257	---	---	---
105	3	7.5	0.00109	---	---	---

$\Sigma m/M$ ..... 0.06351 ..... 0.07828

Life ..... 15.7 MGT ..... 12.8 MGT

6. DISCUSSION AND CONCLUSIONS

The behavior of detail fractures has been studied to provide estimates of safe crack growth life in a variety of revenue service conditions. Safe crack growth life is the tonnage of train traffic required to grow a detail fracture from a size at which rail test equipment can just find it to a size at which it can cause a rail failure under the next train. Safe crack growth life is the basis from which requirements can be established for the maximum interval between rail tests. The maximum interval is generally a fraction (e.g., half) of the safe crack growth life. This provides additional opportunities to find growing defects, thus compensating for less-than-perfect rail test equipment and/or operator abilities.

Both experiment and analysis have been used to study detail fracture behavior. Field observations and a controlled field test have provided a few data points for crack growth life under realistic service or simulated service conditions. Laboratory tests have characterized the basic crack growth rate properties of rail steel. Fracture mechanics and the theory of rail flexure have been combined with the material properties to construct a mathematical model of the detail fracture growth rate. The model has been calibrated to one field test data point and has been shown to provide reasonable agreement with most of the other field test data and observations. Section 6.1 reviews the comparison of the mathematical model with the experimental results.

The model appears to reflect the behavior of a growing detail fracture sufficiently well to justify its intended use, viz: filling in the gaps between experimental results for safe crack growth life. A sensitivity analysis has been conducted for this purpose by changing the service environment factors one at a time, and analyses of the effect of representative thermal stress histories on crack growth life have also been performed. Section 6.2 reviews the results of these analyses for the purpose of categorizing each environment factor in terms of its controllability (or predictability) and its effect on safe crack growth life. Section 6.3 concludes with a few observations about application of the detail fracture growth model and similar models of other types of rail defects.

6.1 Model evaluation

Although the detail fracture model gave generally consistent estimates for crack growth life, the static strength estimates based on the stress intensity factor part of the model were inconsistent. The predicted breaking strength agreed with test results for rails containing small and large detail fractures but was about half the measured strength for rails containing 20 to 40 %HA detail fractures. The discrepancy implies that the stress intensity should be reduced by a factor of two in the middle range of flaw sizes.

Can such an adjustment be made while the model's life estimation characteristics are preserved? A factor of 1.2 to 1.9 could be obtained by dropping the penny crack finite-section magnification factor (Table 17). However, this adjustment would increase the crack growth life in the middle range from 13 MGT to about 100 MGT in the simulation of test rail 1 (see Figure 41). Accordingly, the total life estimate for the test rail 1 flaw would increase from 33 to 120 MGT. The middle range life could be recalibrated by substituting material model C for model F, but the substitution would also affect other parts of the crack growth curve. The result would be a total life estimate of about 16 MGT, i.e., about half the test result, and the shape of the crack growth curve would no longer agree with the experiment.

Thus, it does not appear possible to match the detail fracture model to static strength as well as crack growth life test results. This reinforces an earlier discussion in which it was noted that static strength fracture mechanics models are based on calculations at the point of maximum stress intensity, while it is often better to base models of a growing crack such as a detail fracture on an average stress intensity. When one also accounts for the local effects of residual stress, it is reasonable to consider the possibility that residual compression near the rail running surface

effectively suppresses fracture initiation at the top of a medium size detail fracture, i.e., the point of maximum stress intensity on these flaws lies deeper in the rail head and the maximum stress intensity factor for fracture initiation is reduced. Conversely, the experimental evidence suggests that the averaging effect remains active for subcritical crack growth in the middle flaw size range. These differences do not arise for small flaws, over which the stress gradients are low, or for large flaws, which have relieved the residual stress.

The detail fracture model has been kept in its present form, since its primary application is to crack growth life estimation. The fact that the model overestimates the static stress intensity factor for medium size flaws means that an artifact is introduced when the model is used to estimate critical crack size (the size of a flaw that will cause immediate rail failure under a given loading condition). Therefore, such estimates should not be used to draw conclusions about rail testing practices based on defect size. Conversely, safe crack growth life is not sensitive to critical crack size (see Figures 59 through 62), and the artifact thus has no significant effect on conclusions about the interval between rail tests.

Comparison of the FAST tests and model predictions yields insight into the practical limits on description of environment factors. The experiment produced two groups of crack growth behavior. One group, represented by test rail 1, exhibited rapid growth with a life of the order of 33 MGT for a detail fracture to grow from 10 to 80 %HA. The other group, consisting of test rails 3 and 4, exhibited slow growth with a life between the same flaw sizes about twice as long as that of the first group. When the known environment factors were input, including the a posteriori histories of thermal stress versus flaw size, the detail fracture model produced reasonable crack growth life estimates for both groups.

However, a careful review of the environment factors suggests that the model should not be able to distinguish between the two groups based on analysis with a priori environment descriptions. There are only two known differences between the test environments of the two FAST defect groups other than the a posteriori thermal stress histories: the initial temperature differential and the flaw center location as a function of flaw size. Test rails 3 and 4 were installed in the inside string (Figure 2) and began the experiment with 6 °F lower temperature differential (about 1.2 ksi less thermal tension) than the other rails (Figure 38). One would expect this difference to slightly increase the lives of the detail fractures in test rails 3 and 4. However, the centers of the flaws in these rails were located somewhat higher above the neutral axis than the centers of the flaws in the first group (Figure 5). This difference was investigated in the sensitivity study, which showed that effect of the test rail 3 and 4 location should be a reduction of about 10 percent in the crack growth life (Table 30).

The net effect of the known differences should thus be small, i.e., one should expect that analyses with a priori environment descriptions to lead to nearly identical life estimates for the two groups of defects in the FAST experiment. In this light, the agreement of the a posteriori analyses with the test results cannot be taken to demonstrate anything about the model beyond internal consistency.

What is the explanation, then, for a model which agrees with a test result when it apparently should not? The sensitivity study has shown that thermal stress is the dominant environment factor in tangent track. Thus, it should not be surprising that the a posteriori imposition of the thermal stress history tends to force the model into agreement. A better description of the environment would likely have included some variations in the residual stress patterns, since test rails 1, 3, and 4 came from three different railroads (Table 2). Also, there might have been some differences in lateral load and/or wheel-rail contact location on the inside versus the outside string. Such differences together with minor differences in the thermal stress history could easily have produced the reduced early rates of defect growth observed in test rails 3 and 4.

The conclusion to be drawn from this view of the results is that, except for precisely controlled and documented experiments, the level of accuracy which can be achieved in the environment description limits the accuracy of the crack growth life estimate. In practice, estimates consistently closer than ± 30 percent of the actual life are not likely.

Similar arguments can be made in the case of the KCS test rail. This bolted-joint rail exhibited an initially rapid defect growth rate with a strong declining trend. The detail fracture model was able to reproduce neither the initial rate nor the trend based on an approximate environment description for bolted-joint track. A lack of understanding of the level of track-adjustment tensile stress in bolted-joint rail was offered earlier as a possible explanation of the discrepancy in the initial growth rate.

In the light of the FAST experiment discussion, details of the residual stress field can also be advanced as a possible explanation of the discrepancy in the growth rate trend. The residual stress description in the detail fracture model is based on an empirical equation which fits residual stress data measured in test rail 1. One other data point, measured on the KCS test rail, fell somewhat below the empirical equation (Figure 12). The KCS test rail also differs from test rail 1 in the location of the crack front relative to the residual stress pattern and shape of the pattern (Figure 34). A study of these differences strongly suggests that the unusual pattern in the KCS test rail could have easily been characterized as an average residual stress that declines at an increasing rate as the defect size increases, and such a model would produce a declining trend in the crack growth rate.

The last point to be discussed in the evaluation of the detail fracture model concerns the comparisons with field observations involving curve high rails. Crack growth life estimates were compared with the FAST rail failure caused by a small detail fracture in an unusually high residual stress field and with a pair of revenue track rail failures for which only sketchy environment descriptions were available. A static strength comparison was also made with a revenue track rail failure that originated from a small detail fracture, i.e., in a range where the model gives reasonable static strength estimates. In each of these cases, calculations based on the model would lead one to expect to happen that which actually did happen. Taken together, these results build confidence in the detail fracture model and suggest that the average curve high rail environment probably includes a 30 percent increase in residual stress; relative to the residual stress in tangent track.

6.2 Assessment of environment factor influences

The sensitivity study investigated the influence of nine environment factors on detail fracture growth life. The results were based on estimates of total life in what is generally considered to be the window of detection opportunity for detail fractures: a defect growing from 10 to 80 %HA. The sensitivities were calculated relative to a baseline approximating average revenue service conditions on U.S. freight railroads: mixed freight traffic with average car dynamic effects running on wood-tie tangent track with good foundation and a heavy rail section in average condition, assuming a contact location corresponding to average worn wheel and rail profiles, and assuming an average temperature differential corresponding to well adjusted CWR in cool weather.

The sensitivity study has divided the environment factors into three groups according to their relative effects. Each factor can also be characterized by its degree of controllability and its degree of predictability. Figure 65 illustrates a schematic comparison of the environment factors in terms of these three attributes. Each factor is represented by a bar whose height is proportional to its effect on crack growth life. The location of the bar on a base plane represents the other two attributes. Bars in the foreground represent factors which can be neither well controlled nor well predicted. Bars displaced to the left represent factors which, although not easily controllable, can nevertheless be reasonably well predicted. Bars in the center background represent factors which can be well controlled and well predicted.

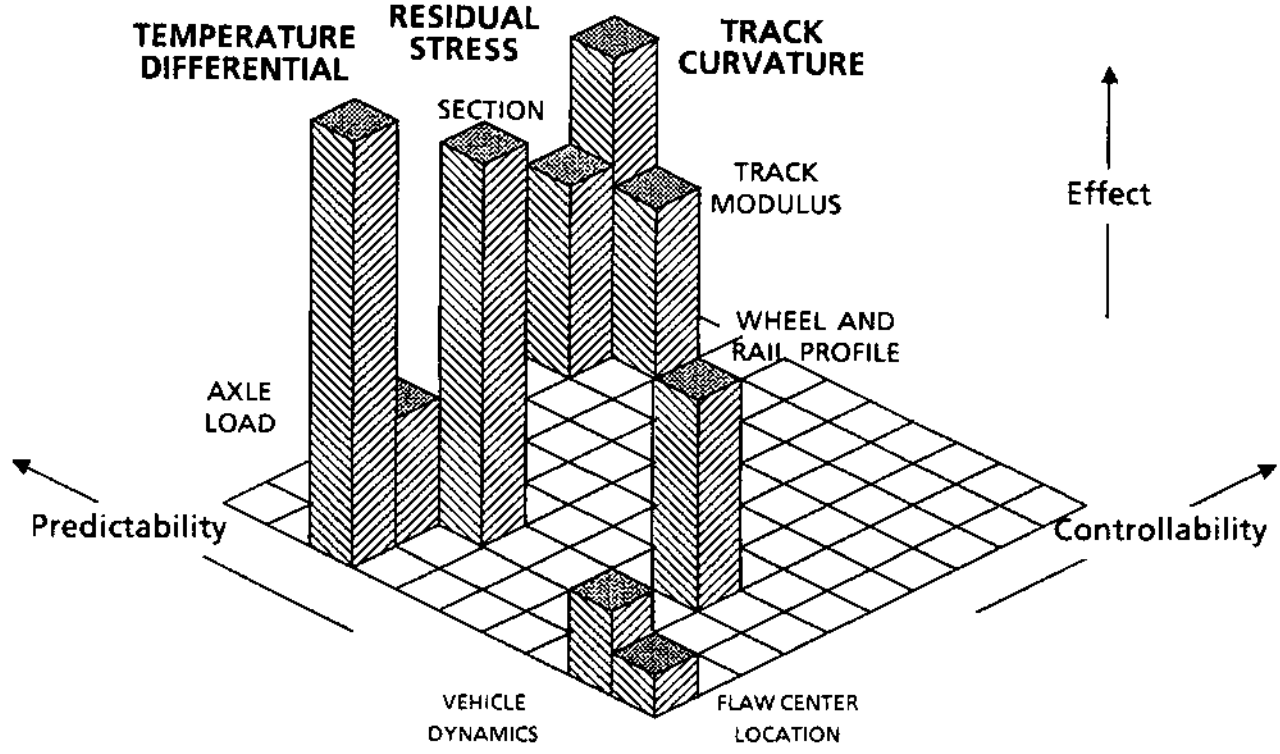

FIGURE 65. EFFECTS AND ATTRIBUTES OF ENVIRONMENT FACTORS.

Temperature differential, rail residual stress, and track curvature have strong effects on detail fracture growth life. Track curvature is controlled and predictable by virtue of track design decisions and track chart records. The curvature factor enters into life estimation only insofar as the question of whether one wants a safe crack growth life for tangent track and gentle curves or for the high rails in sharp curves. Rail residual stress and CWR temperature differential are different. A small degree of control on residual stress might be exercised through mill practices and/or rail grinding in service. Temperature differential is totally subject to the vagaries of the weather. These factors are both predictable to a reasonable degree, however, in the average sense. Hence, when considering questions about rail test intervals it will be appropriate to consider the probable range of effects these factors may have in service and to consider guidelines with flexibility built in to cope with the expected variation of crack growth life.

Rail section, track foundation quality (modulus), center of contact (wheel and rail profile), and average axle load all have moderate effects on detail fracture growth life. The rail section in stretches of track long enough to warrant crack growth life estimates can be identified without ambiguity from track chart information, and scheduled rail replacement programs provide a good degree of control. Foundation quality can be estimated with reasonable accuracy, based on the track engineer's knowledge of his territory, and normal track maintenance programs generally assure that the foundation modulus is kept within reasonable limits. Average axle load is subject to driving by market forces, but the changes are generally slow enough that loadings for the next few years can be extrapolated from the traffic records of the last few years. This group of factors is thus important enough to require care in selecting values appropriate to the track of interest, based on general descriptive data available to the track engineer.

Vehicle dynamics and flaw center location in the rail head have only small effects on detail fracture growth life. They are also the least controllable and the least predictable of the nine environment factors. Under these circumstances, it is appropriate to

use the nominal values of these factors when making crack growth life estimates for detail fractures.

6.3 Concluding remarks

A combination of experiment and fracture mechanics analysis has shown that detail fractures behave in fatigue like sharp cracks, and that reasonable crack growth life estimates can be made for detail fractures based on stress intensity factor formulae. Such estimates cannot be precise, however, because the stress intensity factor approximates the crack driving force and because the service environment can never be precisely specified. In spite of these shortcomings, the crack growth life estimates can still provide some useful guidelines for the scheduling of rail tests. For example, the following guidelines can be drawn from the study results:

- Ideally, curves of three degrees and sharper should be tested twice as often as the tangent track in a line. This might pose severe practical problems as a policy, but it is a reasonable guideline for allocation of rail testing resources exceeding the minimum line inspection requirements.
- For lines which are tested several times per year, the schedule should be concentrated in cold weather on northern and western plains lines. For example, scheduling tests for October, December, February, and June would be a better strategy than scheduling the same four tests at three-month intervals.
- Percentage of night versus day and winter versus summer traffic are important operational factors which should be considered in setting or adjusting the interval between rail tests. All other things being equal, the frequency of rail testing should increase if the proportions of night and/or winter traffic increase.

The detail fracture was selected for intensive study because it is expected to dominate the population of rail defects in modern mainline tracks equipped with CWR and subjected to high axle loads. Many of the results of this study can be applied to other types of rail defects. For example, the mathematical modeling of most of the environment factors could be used to analyze transverse fissure (hydrogen flake) defects in the rail head or lack-of-fusion transverse defects in rail welds. Such studies would, of course, require modification of the defect geometry and center location effects of the stress intensity factor. With consideration of other environment factors which may have a strong influence on crack growth, the conceptual framework developed in this study can be applied to flaws having different orientations and/or locations in the rail. Work along these lines is already in progress for vertical split heads and bolt hole cracks, the types which tend to dominate the defect populations in branchline and older bolted-joint mainline tracks.

The research has produced a physical understanding of detail fracture behavior that has made it possible to approximately forecast changes of safe crack growth life expected from changes in revenue service conditions. The forecasts are accurate enough to serve as inspection interval guidelines, provided that some flexibility is maintained in rail test scheduling procedures to allow the inspection program to adapt to actual crack growth behavior when it deviates from the forecast.

The effect of practical environment factors on residual stress requires additional research. Specifically, of the effects of heavy axle loads, and the curve high rail position, and roller straightening require better quantitative descriptions. The first two factors are currently under study in the 100-ton and 125-ton phases of the FAST High Tonnage Loop rail experiments being conducted at the Transportation Test Center. The third factor will require a coordinated effort of laboratory experiments and analytical work.

APPENDIX A
RAIL SECTION PROPERTIES

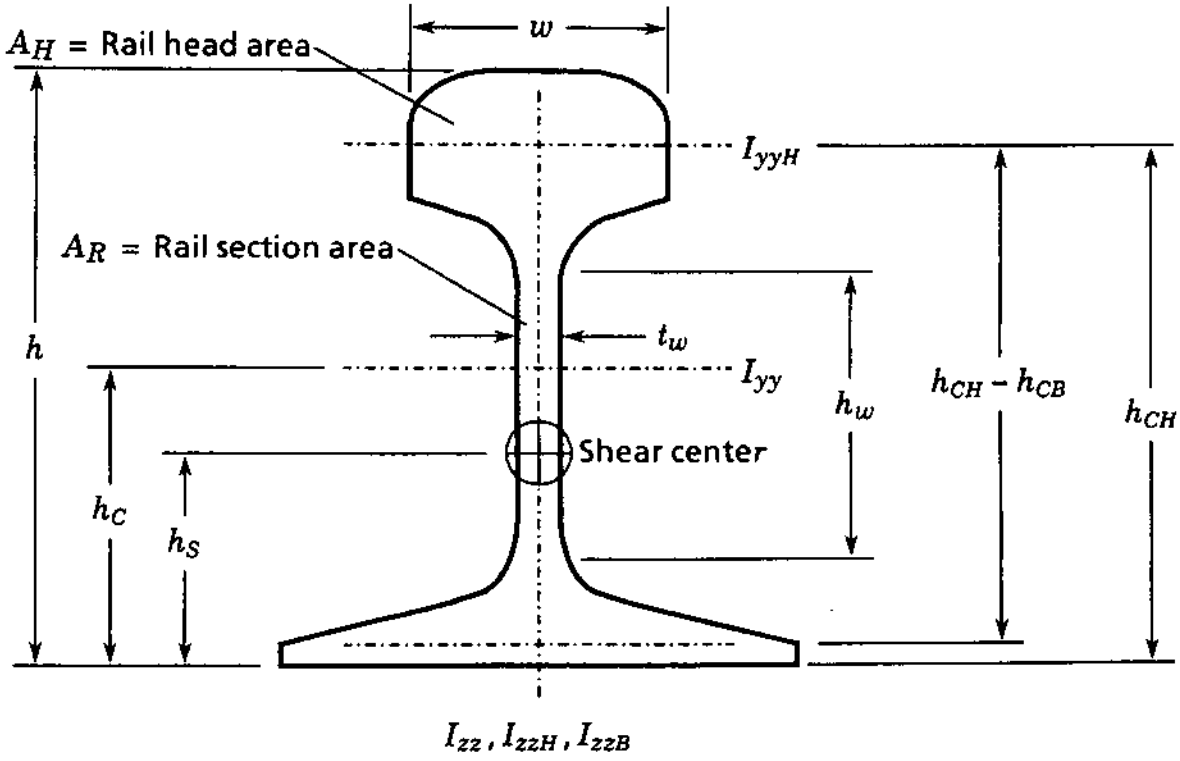

FIGURE A-1. DEFINITIONS OF SECTION PROPERTIES USED IN DETAIL FRACTURE MODEL.

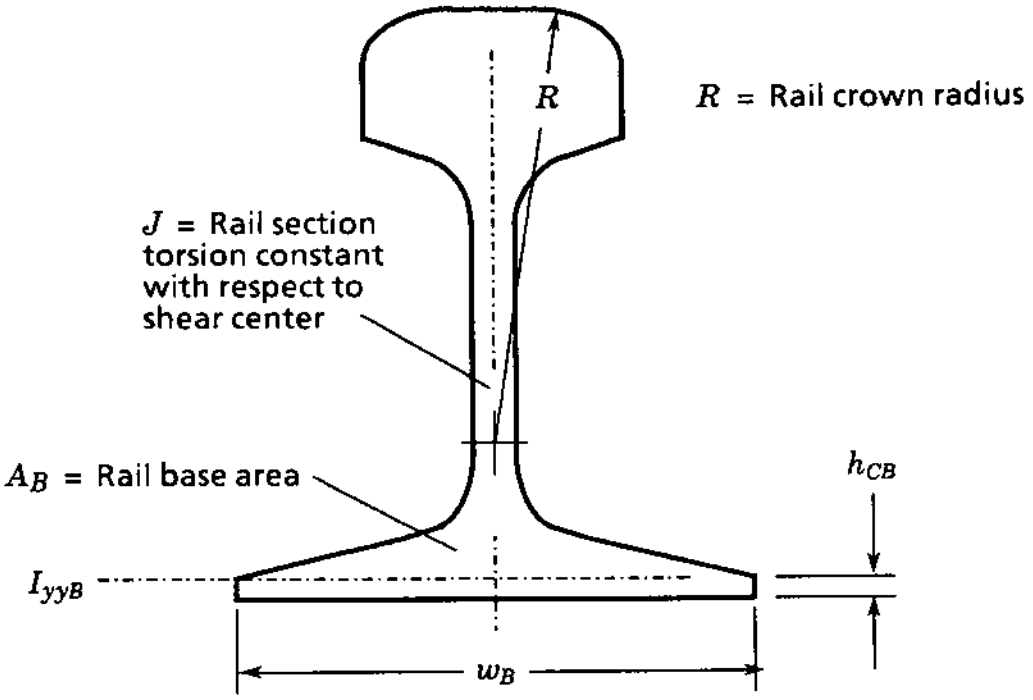

FIGURE A-2. DEFINITIONS OF OTHER SECTION PROPERTIES.

TABLE A-1. RAIL SECTION PROPERTIES.

Property	Units	Value for Section Indicated									
		70 ASCE	85 ASCE	90 ASCE	100 RE	115 RE	127 DY	132 RE	136 RE	140 RE	155 PS
h	in.	4.625	5.188	5.38	6.00	6.625	7.00	7.125	7.3125	7.3125	8.00
h_C	in.	2.22	2.47	2.55	2.75	2.98	3.14	3.20	3.35	3.37	3.51
h_S	in.	1.26	1.37	1.38	1.51	1.55	1.47	1.63	1.69	1.74	1.51
h_w	in.	2.469	2.75	2.86	3.281	3.812	4.16	4.188	4.156	4.062	4.656
$h_{CH} - h_{CB}$	in.	3.71	4.14	4.28	4.84	5.39	5.80	5.86	5.95	5.91	6.57
h_{CH}	in.	4.01	4.46	4.62	5.23	5.80	6.21	6.30	6.39	6.35	7.04
t_w	in.	0.5156	0.5625	0.56	0.5625	0.625	0.66	0.656	0.6875	0.75	0.75
w	in.	2.4375	2.5625	2.63	2.6875	2.7188	3.00	3.00	2.9375	3.00	3.00
A_H	in.^{2}	2.81	3.49	3.77	3.80	3.91	4.26	4.42	4.86	5.00	5.09
A_R	in.^{2}	6.81	8.33	8.83	9.95	11.26	12.50	12.95	13.35	13.80	15.20
I_{yy}	in.^{4}	19.70	30.07	34.39	49.00	65.60	81.57	88.20	94.90	96.80	129.00
I_{yyH}	in.^{4}	0.329	0.558	0.64	0.714	0.729	0.79	0.837	1.17	1.38	1.38
I_{zz}	in.^{4}	4.86	6.95	7.24	9.35	10.40	15.18	14.20	14.50	14.70	20.00
I_{zzH}	in.^{4}	1.24	1.75	2.06	2.12	2.13	2.71	2.84	3.03	3.14	3.14
I_{zzB}	in.^{4}	3.53	5.11	6.43	7.13	7.99	12.20	11.10	11.20	11.10	16.60
R	in.	12	12	12	14	10	10	10	14	10	10
h_{CB}	in.	0.299	0.321	0.34	0.394	0.411	.41	0.436	0.435	0.436	0.465
w_B	in.	4.625	5.1875	5.38	5.38	5.50	6.25	6.00	6.25	6.00	6.75
A_B	in.^{2}	2.59	3.06	3.43	3.92	4.19	4.86	4.86	4.87	4.86	5.81
I_{yyB}	in.^{4}	0.0944	0.133	0.16	0.250	0.292	0.35	0.376	0.378	0.376	0.522
J	in.^{4}	30.1	46.8	53.72	74.1	97.9	131.61	133.6	148.2	146.2	212.8

APPENDIX B

VEHICLE PROPERTIES AND TYPICAL CONSISTS

B.1 VEHICLE PROPERTIES

Dimensional and weight data were collected for a variety of railroad vehicles to represent both typical and unusual rolling stock. Freight cars, passenger cars, and motive power were included. The locomotive and most of the freight car data was obtained from the Car and Locomotive Cyclopedia [73]. The data for passenger and unusual freight cars was abstracted from TSC project files.

Figure B-1 summarizes the conventions used for the vehicle descriptions. The wheel center spacing, truck center spacing, and length over the couplers are denoted by A, B, and C, respectively. These dimensions are given in units of inches. Rail weights empty and loaded are denoted by W_E and W_L, respectively, and are given in kips. The number of axles is denoted by NA.

Table B-1 summarizes the vehicle data, which is contained as a library within the detail fracture model. The first column is a sequence number, which the model software uses to identify the vehicle data. In addition to the parameters specified in Figure B-1, the table includes empty and loaded weights in tons.

The vehicle type codes in the second column are used to specify a consist for input to the detail fracture model software. The acronyms are self-explanatory, except for the following sequence numbers:

36 DODX1 - a six-axle flat car used by the Department of Defense for military movements

37 DODX2 - a variant design for the DoD flat car

38 125T - a hypothetical vehicle with approximate dimensions and weights corresponding to a 125-ton capacity car for unit coal service

39 APLXE - the end platform of a double-stack container car

40 APLXM - the middle platform of a double-stack container car

41 ARROW - heavy rail commuter car (MU type) representing cars like the Metro-North M-2, Jersey Arrow-III, and SEPTA Silverliner-IV.

42 CBQDD - Double-decker rail commuter car, weight and dimensions taken from Chicago, Burlington & Quincy rolling stock.

43 AMTK - Intercity passenger coach, Amfleet-I type.

The APLXE and APLXM entries should be used together to simulate a double-stack container car. A consist of APLXE – APLXM – APLXE approximates the wheel loadings and truck spacings under an articulated five-platform container car (see Figure B-2). The loadings and truck center spacings are intended to be a generic representation of the American President Lines double-stack container car and similar vehicles. These cars are sometimes found as individuals in mixed freight consists but, for the most part, are engaged in unit-train services in consists up to 20 cars.

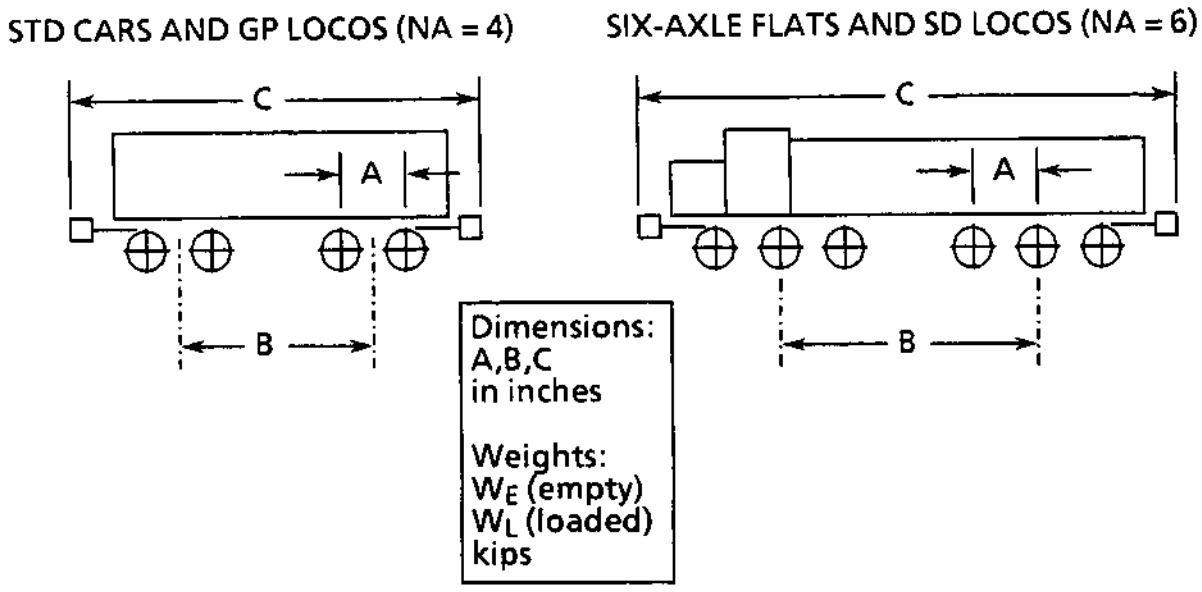

FIGURE B-1. CONVENTIONS FOR VEHICLE WEIGHTS AND DIMENSIONS

DOUBLE-STACK CONTAINER CAR

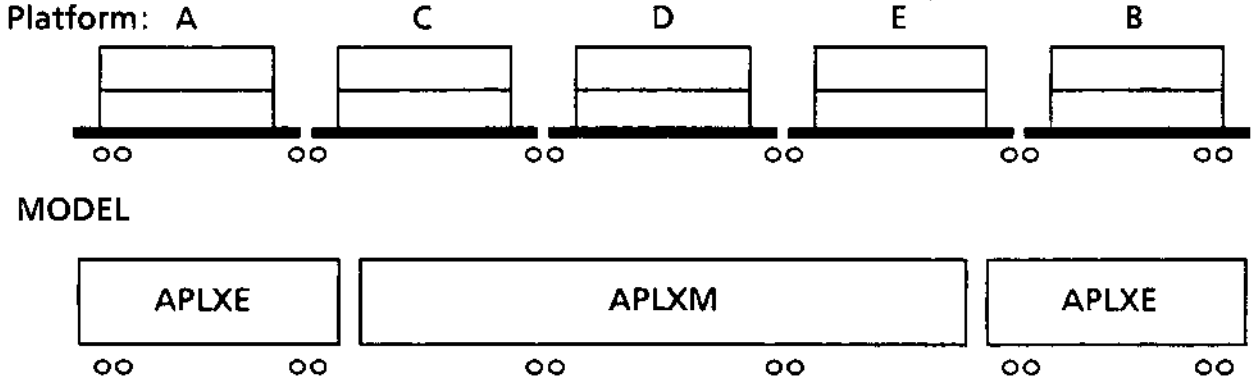

FIGURE B-2. REPRESENTATION OF DOUBLE-STACK CONTAINER CAR

TABLE B-1. VEHICLE WEIGHTS AND DIMENSIONS

No.	Name	A	B	C	W_E	W_L	NA	Tons Empty	Tons Loaded
1	BOXUP	66	377.4	535	53.6	231	4	26.80	115.5
2	BOXNP	68	491.4	654	60.7	220	4	30.35	110.0
3	BOXNW	70	555.0	819	96.1	269	4	48.05	134.5
4	BOXTC	68	772.0	1130	119	219	4	59.50	109.5
5	BOXPS	70	555.4	818	100	263	4	50.00	131.5
6	BOXFG	68	554.8	777	93	219	4	46.50	109.5
7	STOCK	66	372.4	547	44.9	177	4	22.45	88.5
8	GOND1	70	672.4	835	74.8	260	4	37.40	130.0
9	GOND2	68	685.4	849	59.5	214	4	29.75	107.0
10	GONDB	68	659.0	842	71.8	220	4	35.90	110.0
11	CVRG1	68	436.4	599	78.1	220	4	39.05	110.0
12	CVRG2	68	524.0	686	82.7	220	4	41.35	110.0
13	COILG	70	486.0	692	67.6	263	4	33.80	131.5
14	OHOP1	70	469.4	620	69.4	263	4	34.70	131.5
15	OHOP2	70	434.4	585	59.6	263	4	29.80	131.5
16	OHOP3	68	209.4	373	50.2	220	4	25.10	110.0
17	CHOP1	70	540.6	711	64.8	263	4	32.40	131.5
18	CHOP2	70	307.4	458	58.5	263	4	29.25	131.5
19	CHOP3	70	504.0	661	62.2	263	4	31.10	131.5
20	TANK1	70	490.0	790	77.6	314	4	38.80	157.0
21	CABS1	68	278.0	499	55.4	57.4	4	27.70	28.7
22	CABS2	68	278.8	501	55.0	57.0	4	27.50	28.5
23	CABS3	66	233.0	501	48.0	50.0	4	24.00	25.0
24	CABS4	66	278.2	485	56.6	58.6	4	28.30	29.3
25	FLAT1	70	536.0	778	79.5	263	4	39.75	131.5

TABLE B-1. VEHICLE WEIGHTS AND DIMENSIONS (Concluded)

No.	Name	A	B	C	W_E	W_L	NA	Tons Empty	Tons Loaded
26	BKFT1	68	486.0	617	61.5	220	4	30.75	110.0
27	BKFL2	70	736.0	958	87.6	263	4	43.80	131.5
28	PIGB1	70	802.0	1060	76.2	200	4	38.10	100.0
29	LOCO1	108	408.0	710	250	250	4	125.00	125.0
30	LOCO2	96	264.0	536	230	230	4	115.00	115.0
31	LOCO3	168	434.0	722	242	242	4	121.00	121.0
32	LOCO4	81.5	561.9	790	356	356	6	178.00	178.0
33	LOCO5	81.5	621.5	848	390	390	6	195.00	195.0
34	HOPR1	70	469.4	620	58	258	4	29.00	129.0
35	CABS5	66	278.2	485	60	60	4	30.00	30.0
36	DODX1	66	552.0	867	92.7	394.5	6	46.35	197.25
37	DODX2	66	552.0	867	94.7	394.5	6	47.35	197.25
38	125T	70	469.4	620	65.0	315.0	4	32.50	157.5
39	APLXE	70	608.0	888	45.0	242.0	4	22.50	121.0
40	APLXM	70	608.0	1544	60.0	264.0	4	30.00	132.0
41	ARROW	102	714.0	1020	125.0	155.0	4	62.50	77.5
42	CBQDD	102	714.0	1020	110.2	132.4	4	55.10	66.2
43	AMTK	102	714.0	1020	108.0	120.0	4	54.0	60.0

B.2 TYPICAL CONSISTS

Tables B-2 through B-8 summarize the consists used in the present study. Tables B-9 through B-11 are examples of other consists that can be formed from the vehicle menu.

The consist in Table B-2 represents the FAST train as it was before the detail fracture growth rate test. FAST experiment data taken in that era included measurements of dynamic wheel-rail loads, whereas no such loads data were available from the detail fracture growth test period. The Table B-2 consist was used, therefore, to calibrate the dynamic-load coefficients of variation in the detail fracture model. The consist in Table B-3 represents the FAST train as it was during the detail fracture growth test.

Tables B-4 through B-8 represent a range of typical revenue service consists and are arranged in order of decreasing average wheel load. Table B-4 is a hypothetical unit train made up from 125-ton cars. Loaded and empty unit coal trains are represented in Tables B-5 and B-8, respectively. Tables B-6 and B-7 are typical general freight consists.

TABLE B-2. FAST TEST CONSIST CTEST1*

Sequence No.	Menu No.	Type	No. of Cars	Load Factor	Tons per Car	Total Tons
1	29	LOCO1	4	0.0	125.0	500.0
2	14	OHOP1	15	0.5	83.1	1246.5
3	20	TANK1	2	1.0	157.0	314.0
4	3	BOXNW	2	1.0	134.5	269.0
5	14	OHOP1	15	1.0	131.5	1972.5
6	2	BOXNP	2	1.0	110.0	220.0
7	3	BOXNW	2	1.0	134.5	269.0
8	14	OHOP1	10	0.5	83.1	831.0
9	20	TANK1	3	1.0	157.0	471.0
10	3	BOXNW	2	1.0	134.5	269.0
11	2	BOXNP	1	1.0	110.0	110.0
12	14	OHOP1	10	1.0	131.5	1315.0
13	20	TANK1	2	0.2	62.44	124.88
14	3	BOXNW	2	1.0	134.5	269.0
15	2	BOXNP	1	1.0	110.0	110.0
16	20	TANK1	2	0.2	62.44	124.88
17	14	OHOP1	10	0.5	83.1	831.0
Trailing	Tons					8746.76
Total	Tons					9246.76
Total	Trailing	Cars				81
Total	Cars and	Motive	Power			85
Total	Axles					340
Average	Wheel	Load	(kips)			27.2

*For use in calibrating coefficients of variation to dynamic measurements with the FAST consist operating prior to the detail fracture growth rate experiment.

TABLE B-3. FAST TEST CONSIST CTEST2*

Sequence No.	Menu No.	Type	No. of Cars	Load Factor	Tons per Car	Total Tons
1	29	LOCO1	4	0.0	125.0	500.0
2	14	OHOP1	15	1.0	131.5	1972.5
3	20	TANK1	2	1.0	157.0	314.0
4	3	BOXNW	2	1.0	134.5	269.0
5	14	OHOP1	15	1.0	131.5	1972.5
6	2	BOXNP	2	1.0	110.0	220.0
7	3	BOXNW	2	1.0	134.5	269.0
8	14	OHOP1	10	1.0	131.5	1315.0
9	20	TANK1	3	1.0	157.0	471.0
10	3	BOXNW	2	1.0	134.5	269.0
11	2	BOXNP	1	1.0	110.0	110.0
12	14	OHOP1	10	1.0	131.5	1315.0
13	20	TANK1	2	0.2	62.44	124.88
14	3	BOXNW	2	1.0	134.5	269.0
15	2	BOXNP	1	1.0	110.0	110.0
16	20	TANK1	2	0.2	62.44	124.88
17	14	OHOP1	10	0.5	83.1	831.0
Trailing	Tons					9956.76
Total	Tons					10456.76
Total	Trailing	Cars				81
Total	Cars and	Motive	Power			85
Total	Axles					340
Average	Wheel	Load	(kips)			30.8

*Represents the FAST consist during the detail fracture growth rate test.

TABLE B-4. HEAVY AXLE LOAD UNIT TRAIN

Sequence No.	Menu No.	Type	No. of Cars	Load Factor	Tons per Car	Total Tons
1	33	LOCO5	6	1.0	195.0	1170.0
2	38	125T	100	1.0	157.5	15750.0
3	35	CABS5	1	1.0	30.0	30.0
Trailing	Tons					15780.0
Total	Tons					16950.0
Total	Trailing	Cars				101
Total	Cars and	Motive	Power			107
Total	Axles					440
Average	Wheel	Load	(kips)			38.52

TABLE B-5. LOADED UNIT COAL TRAIN

Sequence No.	Menu No.	Type	No. of Cars	Load Factor	Tons per Car	Total Tons
1	33	LOCO5	6	1.0	195.0	1170.0
2	14	OHOP1	110	1.0	131.5	14465.0
3	35	CABS5	1	1.0	30.0	30.0
Trailing	Tons					14495.0
Total	Tons					15665.0
Total	Trailing	Cars				111
Total	Cars and	Motive	Power			117
Total	Axles					480
Average	Wheel	Load	(kips)			32.64

TABLE B-6. GENERAL FREIGHT "A"

Sequence No.	Menu No.	Type	No. of Cars	Load Factor	Tons per Car	Total Tons
1	29	LOCO1	3	1.0	125.0	375.0
2	1	BOXUP	3	0.8	97.76	293.28
3	9	GOND2	2	1.0	107.0	214.0
4	17	CHOP1	5	1.0	131.5	657.5
5	25	FLAT1	3	0.0	39.75	119.25
6	16	OHOP3	5	1.0	110.0	550.0
7	20	TANK1	2	0.8	133.36	266.72
8	28	PIGB1	6	0.5	69.05	414.3
9	6	BOXFG	4	0.0	46.5	186.0
10	8	GOND1	2	0.0	37.4	74.8
11	4	BOXTC	3	1.0	109.5	328.5
12	16	OHOP3	5	0.0	25.1	125.5
13	27	BKFL2	3	1.0	131.5	394.5
14	5	BOXPS	5	1.0	131.5	657.5
15	10	GONDB	2	0.0	35.9	71.8
16	2	BOXNP	5	0.0	30.35	151.75
17	18	CHOP2	4	0.9	121.275	485.1
18	1	CABS3	1	1.0	25.0	25.0
Trailing	Tons					5015.5
Total	Tons					5390.5
Total	Trailing	Cars				60
Total	Cars and	Motive	Power			63
Total	Axles					252
Average	Wheel	Load	(kips)			21.39

TABLE B-7. GENERAL FREIGHT "B"

Sequence No.	Menu No.	Type	No. of Cars	Load Factor	Tons per Car	Total Tons
1	29	LOCO1	2	1.0	125.0	250.0
2	25	FLAT1	3	0.0	39.75	119.25
3	16	OHOP3	5	1.0	110.0	550.0
4	18	CHOP2	2	0.9	121.275	242.55
5	28	PIGB1	6	0.5	69.05	414.3
6	1	BOXUP	3	0.8	97.76	293.28
7	6	BOXFG	4	0.0	46.5	186.0
8	8	GOND1	2	0.0	37.4	74.8
9	4	BOXTC	3	1.0	109.5	328.5
10	16	OHOP3	5	0.0	25.1	125.5
11	10	GONDB	2	0.0	35.9	71.8
12	2	BOXNP	5	0.0	30.35	151.75
13	1	CABS3	1	1.0	25.0	25.0
Trailing	Tons					2582.73
Total	Tons					2832.73
Total	Trailing	Cars				41
Total	Cars and	Motive	Power			43
Total	Axles					172
Average	Wheel	Load	(kips)			16.47

TABLE B-8. EMPTY UNIT COAL TRAIN

Sequence No.	Menu No.	Type	No. of Cars	Load Factor	Tons per Car	Total Tons
1	33	LOCO5	4	1.0	195.0	780.0
2	14	OHOP1	110	0.0	34.7	3817.0
3	35	CABS5	1	1.0	30.0	30.0
Trailing	Tons					3847.0
Total	Tons					4627.0
Total	Trailing	Cars				111
Total	Cars and	Motive	Power			115
Total	Axles					468
Average	Wheel	Load	(kips)			9.89

TABLE B-9. TRAILER VAN UNIT TRAIN

Sequence No.	Menu No.	Type	No. of Cars	Load Factor	Tons per Car	Total Tons
1	32	LOCO4	4	1.0	178.0	712.0
2	28	PIGB1	30	1.0	100.0	3000.0
3	28	PIGB1	20	0.5	69.05	1381.0
4	28	PIGB1	30	1.0	100.0	3000.0
5	24	CABS4	1	1.0	29.3	29.3
Trailing	Tons					7410.3
Total	Tons					8122.3
Total	Trailing	Cars				81
Total	Cars and	Motive	Power			85
Total	Axles					348
Average	Wheel	Load	(kips)			23.34

TABLE B-10. INTERCITY MU COMMUTER

Sequence No.	Menu No.	Type	No. of Cars	Load Factor	Tons per Car	Total Tons
1	41	ARROW	10	1.0	77.5	775.0
Trailing	Tons					775.0
Total	Tons					775.0
Total	Trailing	Cars				10
Total	Cars and	Motive	Power			10
Total	Axles					40
Average	Wheel	Load	(kips)			19.38

TABLE B-11. DOUBLE-STACK CONTAINER CAR UNIT TRAIN

Sequence No.	Menu No.	Type	No. of Cars	Load Factor	Tons per Car	Total Tons
1	33	LOCO4	4	1.0	178.0	712.0
2	39	APLXE	1	1.0	121.0	121.0
3	40	APLXM	1	1.0	132.0	132.0
4	39	APLXE	2	1.0	121.0	242.0
5	40	APLXM	1	1.0	132.0	132.0
6	39	APLXE	2	1.0	121.0	242.0
7	40	APLXM	1	1.0	132.0	132.0
8	39	APLXE	2	1.0	121.0	242.0
9	40	APLXM	1	1.0	132.0	132.0
10	39	APLXE	2	1.0	121.0	242.0
11	40	APLXM	1	1.0	132.0	132.0
12	39	APLXE	2	1.0	121.0	242.0
13	40	APLXM	1	1.0	132.0	132.0
14	39	APLXE	2	1.0	121.0	242.0
15	40	APLXM	1	1.0	132.0	132.0
16	39	APLXE	2	1.0	121.0	242.0
17	40	APLXM	1	1.0	132.0	132.0
18	39	APLXE	2	1.0	121.0	242.0
19	40	APLXM	1	1.0	132.0	132.0
20	39	APLXE	2	1.0	121.0	242.0
21	40	APLXM	1	1.0	132.0	132.0
22	39	APLXE	2	1.0	121.0	242.0
23	40	APLXM	1	1.0	132.0	132.0
24	39	APLXE	2	1.0	121.0	242.0

TABLE B-11. DOUBLE-STACK CONTAINER CAR UNIT TRAIN (continued)

Sequence No.	Menu No.	Type	No. of Cars	Load Factor	Tons per Car	Total Tons
25	40	APLXM	1	1.0	132.0	132.0
26	39	APLXE	2	1.0	121.0	242.0
27	40	APLXM	1	1.0	132.0	132.0
28	39	APLXE	2	1.0	121.0	242.0
29	40	APLXM	1	1.0	132.0	132.0
30	39	APLXE	2	1.0	121.0	242.0
31	40	APLXM	1	1.0	132.0	132.0
32	39	APLXE	2	1.0	121.0	242.0
33	40	APLXM	1	1.0	132.0	132.0
34	39	APLXE	2	1.0	121.0	242.0
35	40	APLXM	1	1.0	132.0	132.0
36	39	APLXE	2	1.0	121.0	242.0
37	40	APLXM	1	1.0	132.0	132.0
38	39	APLXE	2	1.0	121.0	242.0
39	40	APLXM	1	1.0	132.0	132.0
40	39	APLXE	2	1.0	121.0	242.0
41	40	APLXM	1	1.0	132.0	132.0
42	39	APLXE	1	1.0	121.0	121.0
Trailing	Tons					7480.0
Total	Tons					8192.0
Total	Trailing	Cars				60*
Total	Cars and	Motive	Power			64
Total	Axles					264
Average	Wheel	Load	(kips)			31.03

*Model count; actual double-stack car count is 20.

APPENDIX C

SIMPLIFIED ELASTIC - PLASTIC ANALYSIS MODEL

This appendix summarizes the derivation of equations for estimating the residual stresses under the center of contact after a body has been subjected to a single contact load application and removal. The body is assumed to behave as an elastic - perfectly plastic medium which obeys the Tresca yield conditions. The elastic contact stress field under the center of contact is assumed to consist of proportional normal stresses only. It is assumed that the residual stresses can be estimated from a point-by-point analysis of the plastic deviations from a known elastic contact stress field.

B.1 Loading

Let S_1, S_2, S_3 be the longitudinal, lateral, and vertical normal stresses under the center of contact, where the longitudinal and lateral directions define the plane of the contact surface. Let p be the peak contact pressure under any intermediate load and $p = p_{max}$ at maximum load. Since the elastic stresses are assumed to be proportional, the contact solution can be expressed as:

$$S_{1e} = -\alpha \gamma p \qquad S_{2e} = -\beta \gamma p \qquad S_{3e} = -\gamma p \tag{C-1}$$

where α and β are the proportionality factors and γ is a factor which scales the stress field with depth. By definition $S_3 = -p$ ($\gamma = 1$) at the surface. For contact solutions generally, $0 \leqq \alpha, \beta \leqq 1$. Also, $\alpha + \beta < 2$ defines the range of proportionality factors for which yielding is possible.

Since the contact field is assumed to be free of shear stress under the center of contact, S_1, S_2, S_3 are principal stresses. Figure C-1(a) illustrates the Tresca surface in principal stress space: a right hexagonal cylinder whose axis makes equal angles with the stress axes. The cross section dimensions are given in terms of the assumed material flow stress Y. Three of the six planes comprising the Tresca surface, noted by A, B, and C, are defined by the following yield conditions:

$$Plane\ A\text{:}\ S_2 - S_3 = Y \tag{C-2a}$$

$$Plane\ B\text{:}\ S_1 - S_3 = Y \tag{C-2b}$$

$$Plane\ C\text{:}\ S_2 - S_1 = Y \tag{C-2c}$$

The opposite planes will be denoted by A*, B*, C* and have yield conditions with the signs reversed.

Figure C-1(b) illustrates a detail from the surface consisting of the parts of planes A and B in the octant of stress space for which all three principal stresses are compressive. Dashed lines indicate the intersections of these planes with the S_1S_2, S_2S_3, and S_3S_1 planes. Planes A and B are bounded by edges ac and bc* and the common edge ab. Let $\mathbf{i}, \mathbf{j}, \mathbf{k}$ denote unit vectors along the S_1, S_2, S_3 axes. Then vectors $\mathbf{n}_A$, $\mathbf{n}_B$ and $\mathbf{n}_C$ normal to planes A, B, and C can be defined as shown in Figure C-1(b). Also, $\mathbf{e} = \mathbf{i} + \mathbf{j} + \mathbf{k}$ is a vector parallel to the bounding edges.

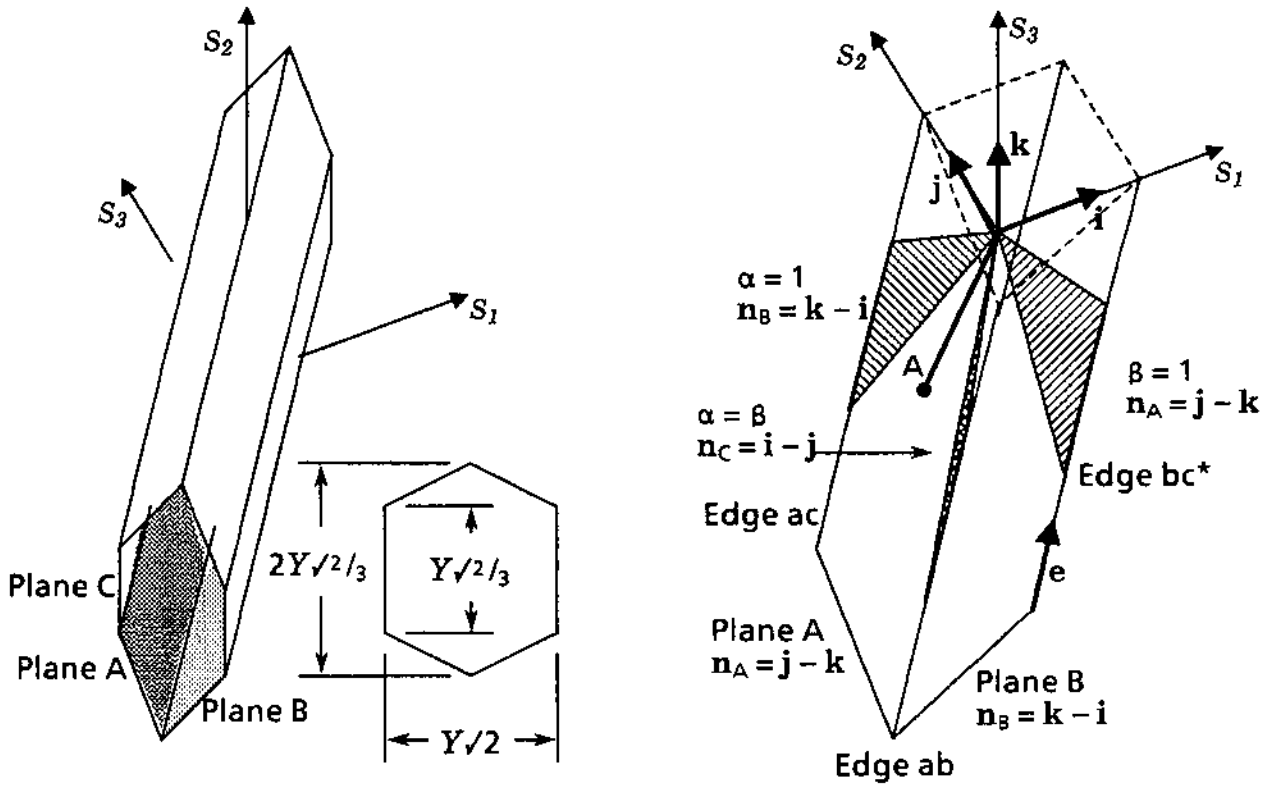

(a) Tresca Yield Surface

(b) Detail of Planes A and B

FIGURE C-1. NOTATION FOR STRESS SPACE AND TRESCA YIELD SURFACE.

As contact load is applied and the stresses under the center of contact begin to increase, the elastic stress state at any depth can be described by the vector:

$$\mathbf{S}_e = S_{1e}\,\mathbf{i} + S_{2e}\,\mathbf{j} + S_{3e}\,\mathbf{k} = -(\alpha\mathbf{i} + \beta\mathbf{j} + \mathbf{k})\gamma p \qquad \text{(C-3)}$$

The first task of the analysis is to find the value of contact pressure at which the material begins to yield. The problem is geometrically equivalent to finding the intersection with the Tresca surface of a line OA directed from the origin along S. Where the intersection A is located depends on which plane is intersected, i.e., on the proportionality factors α and β. As is shown in Figure C-1(b), the plane defined by $\alpha = \beta$ divides the possible locations into subsets: plane A is intersected when $\alpha > \beta$, plane B when $\beta > \alpha$, and edge ab when $\alpha = \beta$. For practical purposes the planes defined by $\alpha = 1$ and $\beta = 1$ also limit the possible directions along S. The case $\alpha > \beta$ will be traced in detail. The initial yield intersection is then defined by Eqs. C-3 and C-2a, which are solved to find:

$$\frac{p}{Y} = \frac{1}{(1-\beta)\gamma} \qquad \text{(C-4)}$$

for the contact pressure at which yield begins. The corresponding stresses are:

$$S_{1A} = -\frac{\alpha}{1-\beta}Y \qquad S_{2A} = -\frac{\beta}{1-\beta}Y \qquad S_{3A} = -\frac{1}{1-\beta}Y \tag{C-5}$$

In accordance with the Prandtl-Reuss equations of incremental plasticity [56], further loading can be described by a stress increment vector in the yield surface plane and a plastic strain increment vector which is normal to the yield surface. Incremental elastic - plastic analysis involves the solution for these increments and is most commonly carried out on curved yield surfaces, e.g., as defined by the Mises-Hencky yield condition. An incremental approach is essential in such cases because, strictly speaking, the stress path on the yield surface is curved, and the stress increments provide a piecewise linear approximation of the stress path. Conversely, the stress path on a Tresca surface consists of one or more straight line segments, the number of segments depending only on the number of Tresca planes and edges traversed. Therefore, elastic - plastic behavior on a Tresca surface can be analyzed in a few steps.

The fact that each stress increment must be proportional to the corresponding elastic strain increment leads to a further simplification if, as is the present case, the plastic strain per se is of no interest. The condition of incremental elastic proportionality has a simple geometrical interpretation, viz: that the stress path on the yield surface is the projection of the extended elastic stress vector. This leads to the following vector analysis procedure for determining the elastic - plastic stress state after initial yielding has occurred (Figure C-2). Let (S_{1e}, S_{2e}, S_{3e}) be the stresses at the extended elastic point B_e and $(S_{1B}, S_{2B}, S_{3B}) = (S_{1A} + \Delta S_1, S_{2A} + \Delta S_2, S_{3A} + \Delta S_3)$ the stresses at the actual elastic - plastic state, point B. Line segment OA is the stress path in the elastic state and line segment AB is the continuation of the stress path on plane A. The direction of AB is defined by the vector product:

$$\mathbf{n}_A \times \frac{\mathbf{S}_e}{\gamma p} \times \mathbf{n}_A = -2\alpha\,\mathbf{i} - (1+\beta)\mathbf{j} - (1+\beta)\mathbf{k} \tag{C-6}$$

Hence, the elastic - plastic stress increments along AB are in the proportions:

$$\Delta S_1 = \frac{2\alpha}{1+\beta}\Delta S_3 \qquad \Delta S_2 = \Delta S_3 \tag{C-7}$$

Since angle ABB_e is a right angle, it is a simple matter to find the elastic - plastic stress increments from the Pythagorean theorem after the sides of triangle ABB_e have been expressed in terms of differences between the stress states defined in Figure C-2. The results are:

$$\Delta S_3 = \tfrac{1}{2}(1+\beta)\gamma p - \tfrac{1}{2}\frac{1+\beta}{1-\beta}Y \tag{C-8}$$

$$S_{1B} = -\alpha\gamma p \qquad S_{2B} = \tfrac{1}{2}Y - \tfrac{1}{2}(1+\beta)\gamma p \qquad S_{3B} = -\tfrac{1}{2}Y - \tfrac{1}{2}(1+\beta)\gamma p \tag{C-9}$$

What happens next if the load continues to increase depends again on the stress proportionality factors (Figure C-3). The stress path AB can be directed toward edge ac or edge ab, as in the first and third cases, or it can be parallel to the edges, as in the

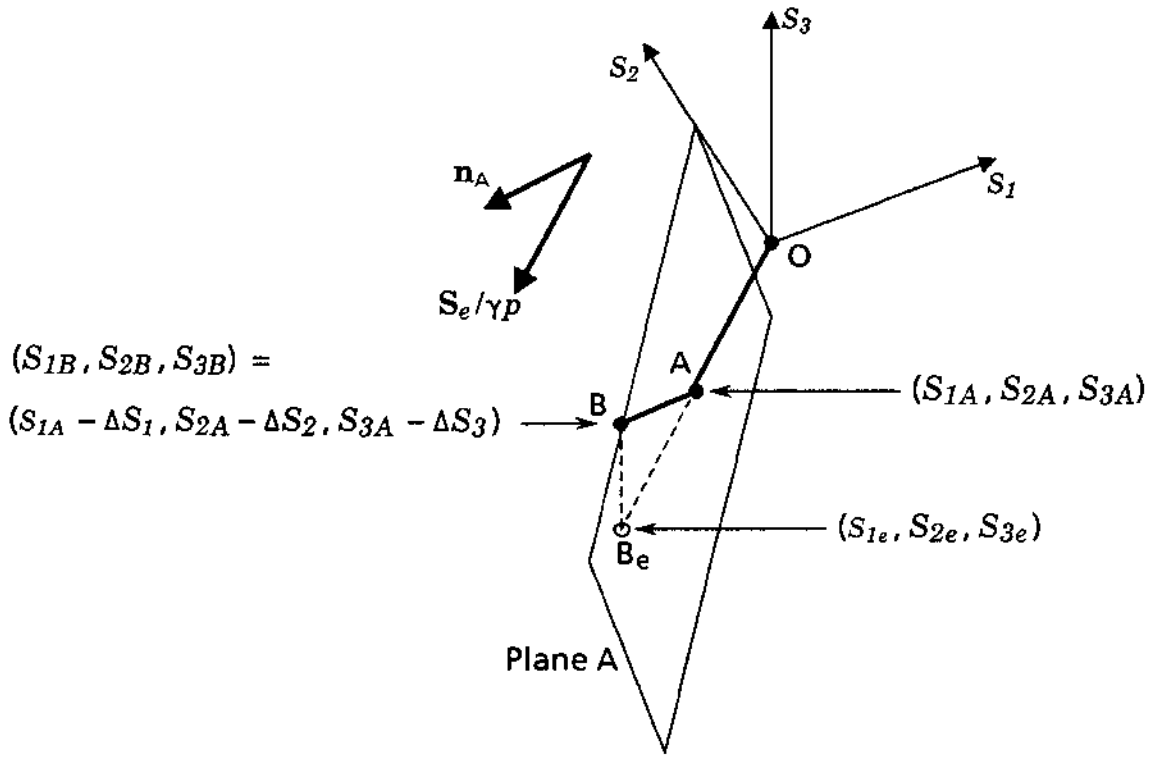

FIGURE C-2. GEOMETRY OF PROJECTION FOR STRESS STATE ON PLANE "A".

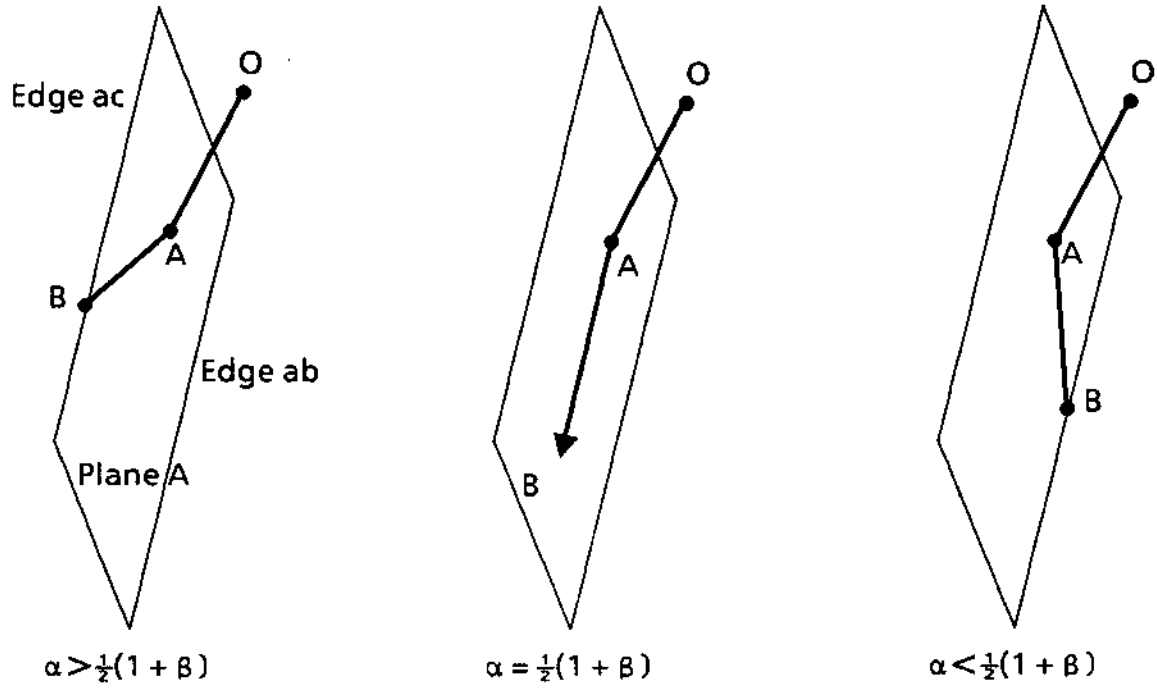

FIGURE C-3. CONDITIONS FOR DETERMINATION OF SUBCASES ON PLANE "A".

second case shown in the figure. In the second case, Eqs. (C-9) express the final loading state when the contact pressure p_{max} is substituted. In the first and third cases, the possibility of the stress path intersecting an edge must be considered.

For the case $\alpha > \frac{1}{2}(1+\beta)$ the Tresca condition for plane C (see Figure C-1) defines the intersection. The contact pressure p and stresses corresponding to the intersection are found by solving Eqs. C-2c and C-9:

$$\frac{p}{Y} = \frac{1}{(2\alpha-1-\beta)\gamma} \tag{C-10}$$

$$S_{1B} = S_{3B} = -\frac{\alpha}{2\alpha-1-\beta}Y \qquad S_{2B} = -\frac{1+\beta-\alpha}{2\alpha-1-\beta}Y \tag{C-11}$$

For the case $\alpha < \frac{1}{2}(1+\beta)$ the Tresca condition for plane B (Eq. C-2b) defines the intersection, and the solution is:

$$\frac{p}{Y} = \frac{1}{(1+\beta-2\alpha)\gamma} \tag{C-12}$$

$$S_{1B} = S_{2B} = -\frac{\alpha}{1+\beta-2\alpha}Y \qquad S_{3B} = -\frac{1+\beta-\alpha}{1+\beta-2\alpha}Y \tag{C-13}$$

If the loading still continues in these cases, the stress path follows a third line segment BC along the intersected edge, until the contact pressure reaches p_{max}. Figure C-4 illustrates the geometrical diagrams which define the stress state at the end point C. In each case the stress increments must be of equal proportions, $\Delta S_1 = \Delta S_2 = \Delta S_3$, and the solution takes the form:

$$S_{1C} = S_{1B} - \Delta S_3 \qquad S_{2C} = S_{2B} - \Delta S_3 \qquad S_{3C} = S_{3B} - \Delta S_3 \tag{C-14}$$

For the case $\alpha > \frac{1}{2}(1+\beta)$ the solution:

$$\Delta S_3 = \frac{1}{3}(1+\alpha+\beta)\gamma p - \frac{1}{3}\frac{1+\alpha+\beta}{2\alpha-1-\beta}Y \tag{C-15}$$

$$S_{1C} = S_{3C} = -\frac{1}{3}Y - \frac{1}{3}(1+\alpha+\beta)\gamma p \qquad S_{2C} = \frac{2}{3}Y - \frac{1}{3}(1+\alpha+\beta)\gamma p \tag{C-16}$$

is obtained from the right triangle BCC_e on the left side of Figure C-4. For the case $\alpha < \frac{1}{2}(1+\beta)$ the solution is:

$$\Delta S_3 = \frac{1}{3}(1+\alpha+\beta)\gamma p - \frac{1}{3}\frac{1+\alpha+\beta}{1+\beta-2\alpha}Y \tag{C-17}$$

$$S_{1C} = S_{2C} = \frac{1}{3}Y - \frac{1}{3}(1+\alpha+\beta)\gamma p \qquad S_{3C} = -\frac{2}{3}Y - \frac{1}{3}(1+\alpha+\beta)\gamma p \tag{C-18}$$

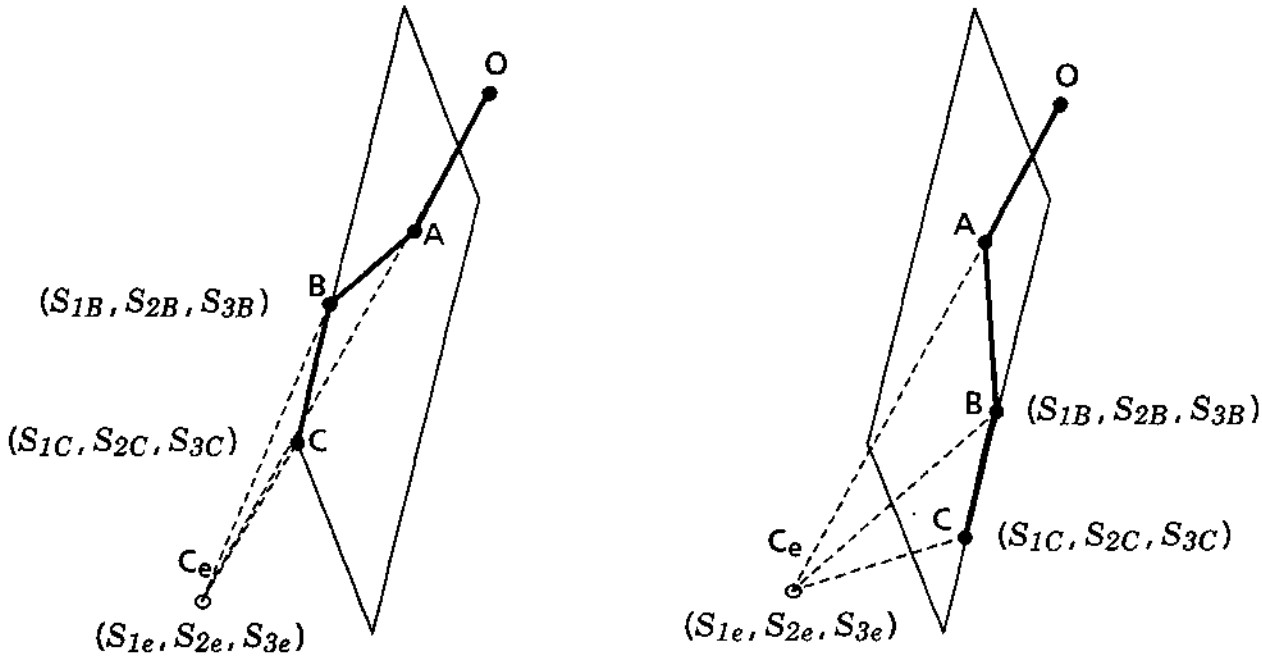

FIGURE C-4. GEOMETRY OF PROJECTION FOR STRESS STATES ON EDGES.

Stress paths which intersect plane B instead of plane A can be analyzed in a similar manner. The solutions for these cases are as follows. For the initial yield point:

$$\frac{p}{Y} = \frac{1}{(1-\alpha)\gamma} \tag{C-19}$$

$$S_{1A} = -\frac{\alpha}{1-\alpha}Y \qquad S_{2A} = -\frac{\beta}{1-\alpha}Y \qquad S_{3A} = -\frac{1}{1-\alpha}Y \tag{C-20}$$

Following yield:

$$S_{1B} = \tfrac{1}{2}Y - \tfrac{1}{2}(1+\alpha)\gamma p \qquad S_{2B} = -\beta\gamma p \qquad S_{3B} = -\tfrac{1}{2}Y - \tfrac{1}{2}(1+\alpha)\gamma p \tag{C-21}$$

For $\beta > \frac{1}{2}(1+\alpha)$:

$$\frac{p}{Y} = \frac{1}{(2\beta-1-\alpha)\gamma} \tag{C-22}$$

$$S_{1B} = -\frac{1+\alpha-\beta}{2\beta-1-\alpha}Y \qquad S_{2B} = S_{3B} = -\frac{\beta}{2\beta-1-\alpha}Y \tag{C-23}$$

$$S_{1C} = \frac{2}{3}Y - \frac{1}{3}(1+\alpha+\beta)\gamma p \qquad S_{2C} = S_{3C} = -\frac{1}{3}Y - \frac{1}{3}(1+\alpha+\beta)\gamma p \tag{C-24}$$

For $\beta < \frac{1}{2}(1+\alpha)$:

$$\frac{p}{Y} = \frac{1}{(1+\alpha-2\beta)\gamma} \tag{C-25}$$

$$S_{1B} = S_{2B} = -\frac{\beta}{1+\alpha-2\beta}Y \qquad S_{3B} = -\frac{1+\alpha-\beta}{1+\alpha-2\beta}Y \tag{C-26}$$

$$S_{1C} = S_{2C} = \frac{1}{3}Y - \frac{1}{3}(1+\alpha+\beta)\gamma p \qquad S_{3C} = -\frac{2}{3}Y - \frac{1}{3}(1+\alpha+\beta)\gamma p \tag{C-27}$$

For the special case $\alpha = \beta$, the stress path intersects edge ab directly. The peak pressure and stresses at the intersection point are given by Eqs. C-4 and C-5 or C-19 and C-20. For further loading the stresses are given by Eqs. C-18 or C-27.

C.2 Unloading

Unloading is defined by increase of the surface normal stress from its value under maximum load, $S_{30} = -p_{max}$, to the final state $S_{30} = 0$. For the purpose of deriving residual stress expressions, however, it will be more convenient to express S_{30} and the vertical stresses at subsurface points in terms of the equivalent elastic-plastic quantities S_{3A}, S_{3B}, or S_{3C} given in the preceding section. The total (elastic) vertical stress increment for unloading, $\Delta S_{3t\,0}$, is then $-S_{3M}$, where M = A, B, or C depending upon the direction taken by the surface loading stress path. Points below the surface will be controlled by depth-scaled increments, $\Delta S_{3t} = \gamma \Delta S_{3t\,0}$. With the understanding that $(\alpha, \beta) = (\alpha_0, \beta_0)$ refers to the stress proportionality factors at the surface, Table C-1 summarizes the expressions for the total unloading increments of vertical stress.

TABLE C-1. TOTAL ELASTIC UNLOADING STRESS INCREMENTS.

State of Surface Point at Maximum Load	ΔS_{3t}
Elastic = 2 Y	γp_{max}
On plane A	$\frac{1}{2}\gamma Y + \frac{1}{2}(1+\beta_0)\gamma p_{max}$
On plane B	$\frac{1}{2}\gamma Y + \frac{1}{2}(1+\alpha_0)\gamma p_{max}$
On edge ac or edge bc*	$\frac{1}{3}\gamma Y + \frac{1}{3}(1+\alpha_0+\beta_0)\gamma p_{max}$
On common edge ab	$\frac{2}{3}\gamma Y + \frac{1}{3}(1+\alpha_0+\beta_0)\gamma p_{max}$

Let S_{1M}, S_{2M}, S_{3M} be the stress state under maximum load (M = A, B, or C) and let S_{1R}, S_{2R}, S_{3R} be the residual stress state after unloading. The unloading process is at least initially elastic. In vector terms, the initial unloading stress path is a line segment parallel to the elastic loading segment OA and contained within the volume enclosed by the Tresca surface. If the stress state remains elastic throughout the unloading process, then the residual stresses are given by:

$$S_{1R} = S_{1M} + \alpha \Delta S_{3t} \qquad S_{2R} = S_{2M} + \beta \Delta S_{3t} \qquad S_{3R} = S_{3M} + \Delta S_{3t} \tag{C-28}$$

If p_{max} is sufficiently large, the stress states at some points may undergo reverse plasticity during unloading. The unloading stress path will then consist of two or more line segments, and the unloading analysis must include calculations of intersections and intermediate stress expressions similar to the ones derived for loading.

Unloading from plane A and its bounding edges will be considered in detail. These cases involve the two planes and four edges marked on the cross sectional view of the Tresca surface shown in Figure C-5(a). As shown in Figure C-5(b), the subset of cases for which $\alpha \geqq \frac{1}{2}(1 + \beta)$,has loading stress paths which trace out half the width of plane A (marked in boldface). The solid-line vectors marked $\alpha = 1$ and $\alpha = \frac{1}{2}(1 + \beta)$ bound the directions of the possible elastic loading segments, and dashed-line vectors with opposite sense indicate the corresponding elastic unloading paths. The unloading path marked $\alpha > \frac{1}{2}(1 + \beta)$ represents a limit of the subset of cases in which the loading path intersected plane A and then traversed to edge ac. A traverse to edge ac is possible as long as α exceeds $\frac{1}{2}(1 + \beta)$ by an infinitesimal amount, i.e., the elastic unloading vector is rotated only an infinitesimal angle from the $\alpha = 1$ unloading vector.

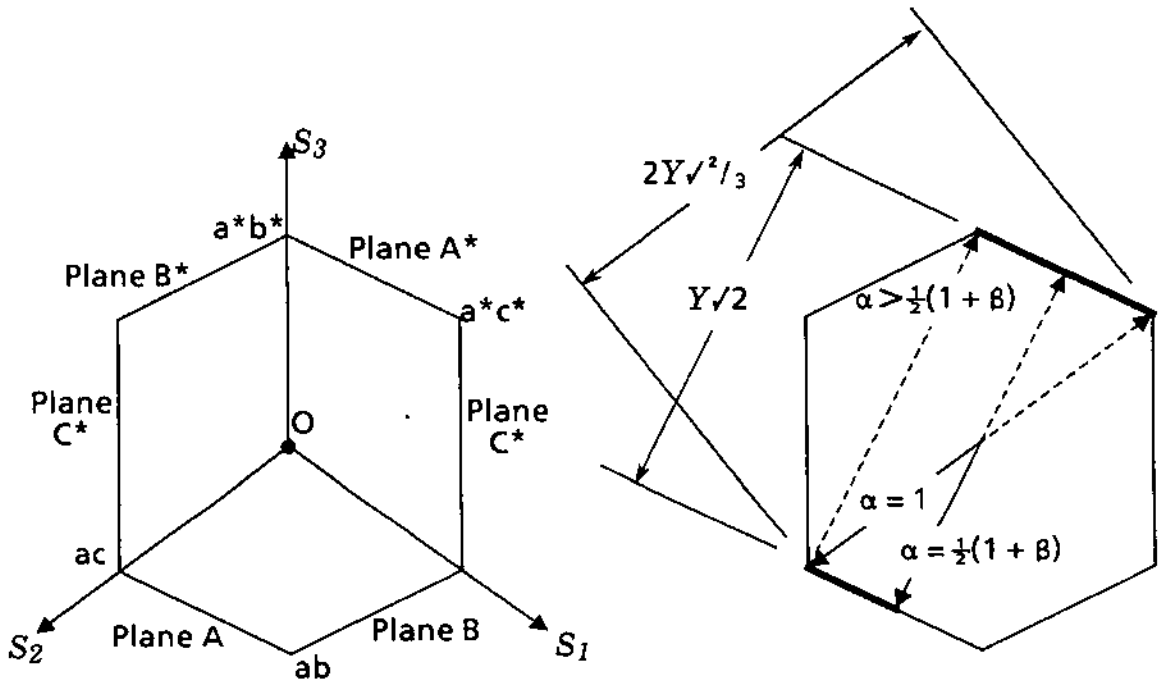

(a) Notation in Cross Sectional View (b) Image of Cases for Which $\alpha \geqq \frac{1}{2}(1 + \beta)$

FIGURE C-5. UNLOADING FROM PLANE "A" STRESS STATES.

Note that in no case can the unloading vector be rotated clockwise with respect to the loading vector because stress paths on the left half of plane A can never be directed toward edge ab (see Figure C-3). Therefore, there are no unloading paths that would intersect plane C*, i.e., the possible paths trace out the full width of plane A* (including its bounding edges) but do not touch other planes.

For the cases $\alpha \leqq \frac{1}{2}(1 + \beta)$ the loading path images the right half of plane A, and the same geometric logic as was used for the left half-plane shows that the unloading paths for these cases also sweep out the entire width of plane A*. Similar arguments can also be made for the cases of unloading from plane B, with a similar result that the unloading paths can intersect only plane B* and its bounding edges.

The lengths of the paths of elastic unloading from plane A can be determined by considering the two bounding cases $\alpha = 1$ and $\alpha = \frac{1}{2}(1 + \beta)$. As shown in Figure C-5, the section dimensions of the Tresca surface are respectively $2Y\sqrt{2}/3$ and $Y\sqrt{2}$ for these two cases. What is actually sought is not the path length per se but ΔS_{3e}, the length of the component parallel to the S_3 axis. This length is calculated from the dot product of the unloading vector $\mathbf{V} = (\alpha\mathbf{i} + \beta\mathbf{j} + \mathbf{k})\Delta S_{3e}$ and a unit vector in the section and unloading planes (Figure C-6). For $\alpha = 1$ the appropriate unit vector is found from $\mathbf{e} \times \mathbf{n_B}$ and is given by:

$$\mathbf{u} = \frac{1}{\sqrt{6}}\left[\mathbf{i} - 2\mathbf{j} + \mathbf{k}\right] \tag{C-29}$$

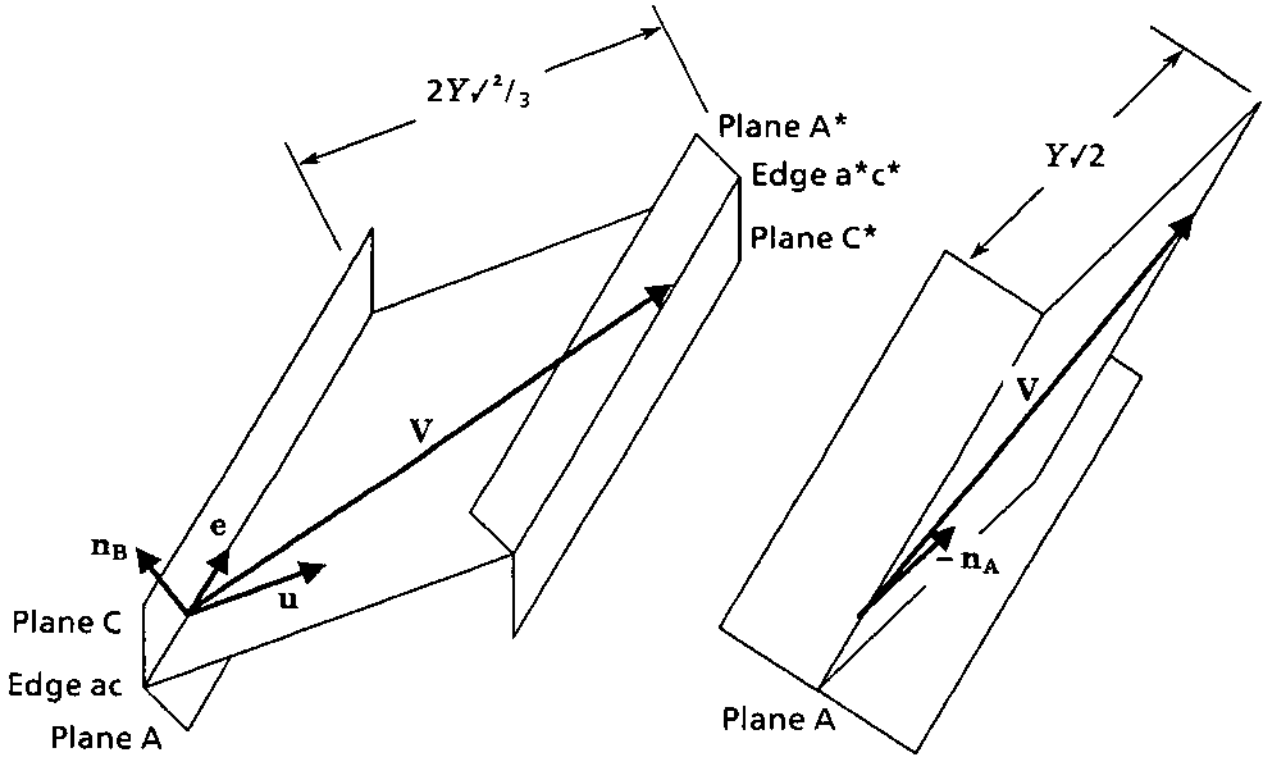

(a) Case of $\alpha = 1$ (b) Case of $\alpha = \frac{1}{2}(1 + \beta)$

FIGURE C-6. ELASTIC UNLOADING PATH LENGTHS.

The dot product then yields

$$\mathbf{V}\cdot\ \mathbf{u} = \frac{\Delta S_{3e}}{\sqrt{6}}\left[1-2\beta+1\right] = 2Y\sqrt{2}/_3 \quad \rightarrow \quad \Delta S_{3e} = \frac{2Y}{1-\beta} \tag{C-30}$$

For $\alpha = \frac{1}{2}(1+\beta)$ the unit vector is simply $-\mathbf{n}_A/\sqrt{2}$ and:

$$\mathbf{V}\cdot\ (-n_A) = \frac{\Delta S_{3e}}{\sqrt{2}}\left[-\beta+1\right] = Y\sqrt{2} \quad \rightarrow \quad \Delta S_{3e} = \frac{2Y}{1-\beta} \tag{C-31}$$

i.e., the same as the preceding case, and in fact ΔS_{3e} is the same for all cases of unloading from plane A, independent of the particular stress path. A similar analysis of the cases involving unloading from plane B leads to a similar result:

$$\Delta S_{3e} = \frac{2Y}{1-\alpha} \tag{C-32}$$

Some other general features of the unloading paths are as follows. If the unloading starts from a state on one of the Tresca edges (ab, ac, bc*), then the reverse plastic path, if there is one, will trace the opposite edge. In such cases the reverse plastic stress increments will be in equal proportions (unloading vector parallel to e). If the unloading starts from a point on plane A, any reverse plastic path will initially lie on plane A*, and the stress increments on that segment will be in the proportions:

$$\Delta S_1 = \frac{2\alpha}{1+\beta}\Delta S_3 \qquad \Delta S_2 = \Delta S_3 \tag{C-33}$$

Furthermore, those paths which proceeded toward edge ac or edge ab during loading will proceed toward the opposite edges (a*c* or a*b*) during the reverse plastic traverse of plane A*. Similarly, unloading from plane B leads to an initial reverse plastic path on plane B* with:

$$\Delta S_1 = \Delta S_3 \qquad \Delta S_2 = \frac{2\beta}{1+\alpha}\Delta S_3 \tag{C-34}$$

and paths directed toward edges ab or bc* during loading will proceed toward edges a*b* or b*c, respectively, in the initial reverse plastic segment.

With the foregoing preliminaries completed, it remains to define the path segment limits and the stress state expressions for each type of unloading case that can be constructed from the combination of loaded states at the surface and the depth of interest. First, it follows from Eqs. C-30 through C-32 that the limits for initiation of reverse plasticity are:

$$\frac{p}{Y} = \frac{2}{(1-\beta)_Y} \ (Plane\,A) \qquad \frac{p}{Y} = \frac{2}{(1-\alpha)_Y} \ (Plane\,B) \tag{C-35}$$

where the loaded-state planes have been designated in each case. Since these values are twice the corresponding initial plastic limits for loading (see Eqs. C-4 and C-19), it follows that no reverse plasticity can occur at any depth if the surface point remained elastic at maximum load. It is also apparent that, regardless of the surface point state,

no point at any depth will undergo reverse plasticity unless it experienced plasticity during loading.

Reverse plasticty is possible in the cases for which the material has yielded at both the surface point and the point of interest. Those cases can be divided into four classes according to the stress states under maximum load: surface and point of interest both on plane A ("AA"); both on plane B ("BB"); surface on plane A but point of interest on plane B "AB"); and surface on plane B but point of interest on plane A ("BA").

Class AA will first be considered in detail. Since the loaded states are on plane A, the maximum elastic unloading stress increment, ΔS_{3e}, is given by Eq. C-31, and the following elastic limits are obtained by equating one of these expressions to the appropriate expression in Table C-1:

Loaded surface state on plane A ($\alpha_0 \geq \beta_0$)

$$\frac{p}{Y} = \frac{1}{1+\beta_0}\left[\frac{4}{(1-\beta)_Y} - 1\right] \tag{C-36}$$

Loaded surface state on edge ac ($\alpha_0 \geq \frac{1}{2}[1+\beta_0]$)

$$\frac{p}{Y} = \frac{1}{1+\alpha_0+\beta_0}\left[\frac{6}{(1-\beta)_Y} - 1\right] \tag{C-37}$$

Loaded surface state on edge ab ($\alpha_0 \leq \frac{1}{2}[1+\beta_0]$)

$$\frac{p}{Y} = \frac{1}{1+\alpha_0+\beta_0}\left[\frac{6}{(1-\beta)_Y} - 2\right] \tag{C-38}$$

The corresponding expressions for class BB are obtained from the AA cases by permutation of symbols:

Loaded surface state on plane B ($\beta_0 \geq \alpha_0$)

$$\frac{p}{Y} = \frac{1}{1+\alpha_0}\left[\frac{4}{(1-\alpha)_Y} - 1\right] \tag{C-39}$$

Loaded surface state on edge bc* ($\beta_0 \geq \frac{1}{2}[1+\alpha_0]$)

$$\frac{p}{Y} = \frac{1}{1+\alpha_0+\beta_0}\left[\frac{6}{(1-\alpha)_Y} - 1\right] \tag{C-40}$$

Loaded surface state on edge ab ($\beta_0 \leq \frac{1}{2}[1+\alpha_0]$)

$$\frac{p}{Y} = \frac{1}{1+\alpha_0+\beta_0}\left[\frac{6}{(1-\alpha)_Y} - 2\right] \tag{C-41}$$

Classes AB and BA can be derived in a similar manner. The limits for class AB are:

Loaded surface state on plane A ($\alpha_0 \geq \beta_0$)

$$\frac{p}{Y} = \frac{1}{1+\beta_0}\left[\frac{4}{(1-\alpha)_Y} - 1\right] \tag{C-42}$$

Loaded surface state on edge ac ($\alpha_0 \geq \frac{1}{2}[1 + \beta_0]$)

$$\frac{p}{Y} = \frac{1}{1+\alpha_0+\beta_0}\left[\frac{6}{(1-\alpha)_Y} - 1\right] \tag{C-43}$$

Loaded surface state on edge ab ($\alpha_0 \leq \frac{1}{2}[1 + \beta_0]$)

$$\frac{p}{Y} = \frac{1}{1+\alpha_0+\beta_0}\left[\frac{6}{(1-\alpha)_Y} - 2\right] \tag{C-44}$$

The limits for class BA are:

Loaded surface state on plane B ($\beta_0 \geq \alpha_0$)

$$\frac{p}{Y} = \frac{1}{1+\alpha_0}\left[\frac{4}{(1-\beta)_Y} - 1\right] \tag{C-45}$$

Loaded surface state on edge bc* ($\beta_0 \geq \frac{1}{2}[1 + \alpha_0]$)

$$\frac{p}{Y} = \frac{1}{1+\alpha_0+\beta_0}\left[\frac{6}{(1-\beta)_Y} - 1\right] \tag{C-46}$$

Loaded surface state on edge ab ($\beta_0 \leq \frac{1}{2}[1 + \alpha_0]$)

$$\frac{p}{Y} = \frac{1}{1+\alpha_0+\beta_0}\left[\frac{6}{(1-\beta)_Y} - 2\right] \tag{C-47}$$

Now suppose that one of the limits for initiation of reverse plasticity given in Eqs. C-36 through C-47 is exceeded. The stress state at initiation (D) is then given by:

$$S_{1D} = S_{1M} + \alpha\,\Delta S_{3e} \qquad S_{2D} = S_{2M} + \beta\,\Delta S_{3e} \qquad S_{3D} = S_{3M} + \Delta S_{3e} \tag{C-48}$$

where M = A, B, or C as before and ΔS_{3e} is given by Eq. C-31 (classes AA and AB) or Eq. C-32 (classes BA and BB). Also, the unloading increment which remains to be accounted for on the reverse plastic path is given by:

$$\Delta S_3 = \Delta S_{3t} - \Delta S_{3e} \tag{C-49}$$

The cases involving plane A at the depth of interest (classes AA and BA) will be considered in detail. If the loaded state was on plane A or traversed plane A to reach an edge, the reverse plastic path must start on plane A*, i.e., the unloading stress increments on this path segment must be in the proportions given by Eqs. C-7. An

intermediate state can then be defined as follows:

$$S_{1E} = S_{1M} + \frac{2\alpha}{1+\beta}(\Delta S_{3t} - Y) \qquad S_{2E} = S_{2M} + \Delta S_{3t} - 2Y \qquad S_{3E} = S_{3M} + \Delta S_{3t} \tag{C-50}$$

where Eqs. C-31 and C-48 have been substituted. The residual stresses are the same as the intermediate state stresses, $(S_{1R}, S_{2R}, S_{3R}) = (S_{1E}, S_{2E}, S_{3E})$, if the reverse plastic path ends on plane A*. Otherwise, Eqs. C-50 must be combined with one of the Tresca yield conditions to establish the stress state at an edge intersection point, and a final increment in the proportions $\Delta S_1 = \Delta S_2 = \Delta S_3 =$ along the edge is calculated to obtain the residual stresses. Strictly speaking, one must also establish the limiting values of p/Y corresponding to the intersections. However, since individual expressions are required for each combination of surface loaded state and state at depth of interest, it is easier in this case simply to calculate the "E" state and check to see whether it violates a Tresca condition. If one of the Tresca conditions is violated, the correct residual stress expressions can be reduced to one of the following forms:

Residual stress state on edge a*c* ($\alpha > \frac{1}{2}[1+\beta]$)

$$S_{1R} = S_{2M} + \Delta S_{3t} - Y \qquad S_{2R} = S_{2M} + \Delta S_{3t} - 2Y \qquad S_{3R} = S_{3M} + \Delta S_{3t} \tag{C-51}$$

Residual stress state on edge a*b* ($\alpha < \frac{1}{2}[1+\beta]$)

$$S_{1R} = S_{3M} + \Delta S_{3t} - Y \qquad S_{2R} = S_{2M} + \Delta S_{3t} - 2Y \qquad S_{3R} = S_{3M} + \Delta S_{3t} \tag{C-52}$$

If the loaded state reached edge ac directly ($\alpha = 1$) or edge ab directly ($\alpha = \beta$), then the entire reverse plastic path lies along the opposite edge, and the residual stresses are:

$$S_{1R} = S_{1M} + \Delta S_{3t} - \frac{2(1-\alpha)}{1-\beta}Y \qquad S_{2R} = S_{2M} + \Delta S_{3t} - 2Y \qquad S_{3R} = S_{3M} + \Delta S_{3t} \tag{C-53}$$

The results for classes AB and BB are similar and are summarized as follows:

Loaded state on plane B ($\beta > \alpha$)

$$S_{1E} = S_{1M} + \Delta S_{3t} - 2Y \qquad S_{2E} = S_{2M} + \frac{2\beta}{1+\alpha}(\Delta S_{3t} - Y) \qquad S_{3E} = S_{3M} + \Delta S_{3t} \tag{C-54}$$

Residual stress state on edge b*c ($\beta > \frac{1}{2}[1+\alpha]$)

$$S_{1R} = S_{1M} + \Delta S_{3t} - 2Y \qquad S_{2R} = S_{1M} + \Delta S_{3t} - Y \qquad S_{3R} = S_{3M} + \Delta S_{3t} \tag{C-55}$$

Residual stress state on edge a*b* ($\beta < \frac{1}{2}[1+\alpha]$)

$$S_{1R} = S_{1M} + \Delta S_{3t} - 2Y \qquad S_{2R} = S_{3M} + \Delta S_{3t} - Y \qquad S_{3R} = S_{3M} + \Delta S_{3t} \tag{C-56}$$

Loaded state reached edge bc* directly ($\beta = 1$) or edge ab directly ($\beta = \alpha$)

$$S_{1R} = S_{1M} + \Delta S_{3t} - 2Y \qquad S_{2R} = S_{2M} + \Delta S_{3t} - \frac{2(1-\beta)}{1-\alpha}Y \qquad S_{3R} = S_{3M} + \Delta S_{3t} \tag{C-57}$$

APPENDIX D

COMPUTER PROGRAM FOR DETAIL FRACTURE GROWTH MODEL

```
C*
C*    MAINLINE PROGRAM FOR DETAIL FRACTURE CRACK GROWTH ANALYSIS
C*    TSC VERSION 6 =  MARCH 1988
C*
      COMMON/BLCK1/ SR(3000),NR(3000),MAXR,SM(3000),NM(3000)
      COMMON/BLCK2/ NFW,IFLAT(20),FWRL(20),FWMF(20),MFLAG
      COMMON/BLCK3/ SIG(4),RBOA,ELOC,TRKC,RLOVT,RLOVA,RAIL
      COMMON/BLCK4/ BL,BR,BM
      COMMON/BLCK5/ C,P,Q,TK1,CPHA,XRS,ITH,ETHERM
      COMMON/BLCK6/ GTONS,NAXLES,LGRPS
      COMMON/BLCK7/ WRL(600),RLOV(600),X(600),LG(131)
      COMMON/BLCK8/ DA(130),DB(130),DC(130)
      COMMON/BLCK9/ COEF(3,3)
      COMMON/BLCK0/ IO2,DMY1,NFLAG
      COMMON/RAIL1/ CWARP,D,E,FK0,FK1,FK2
      COMMON/RAIL2/ FDT,GDT,HDT
      COMMON/RAIL3/ YI,ZI,HIZ,BIZ,HIY,AREA,HAREA
      COMMON/RAIL4/ HGT,ZNA,ZBR,TWB,HWB,HWD
      COMMON/RAIL5/ BETA1,BETA2,BHOWV,BHOWL
      COMMON/CRAX1/ NCRX,PHA(20)
      CHARACTER*5 RAIL
C
C     VARIABLE DEFINITIONS:
C
C     TITLE     = JOBNAME TITLE
C     CTYP      = CAR TYPE
C     EL        = LOAD STATE OF CAR IN PERCENTAGE
C     NUM       = NUMBER OF IDENTICAL CARS
C     SIG(1)    = DYNAMIC LOAD FACTOR TO DECREASE BELOW MEAN LOAD
C     SIG(2)    = DYNAMIC LOAD FACTOR TO INCREASE BELOW MEAN LOAD
C     SIG(3)    = DYNAMIC LOAD FACTOR TO DECREACE ABOVE MEAN LOAD
C     SIG(4)    = DYNAMIC LOAD FACTOR TO INCREASE ABOVE MEAN LOAD
C     NFW       = NUMBER OF FLAT WHEELS
C     IFLAT     = FLAT WHEEL #
C     FWRL      = WHEEL LOAD OF FLAT WHEEL
C     FWMF      = FLAT WHEEL MULTIPLICATION FACTOR
C     THERM     = THERMAL STRESS
C     ETHERM          = CONSTANT THERMAL STRESS VALUE
C     RS        = RESIDUAL STRESS
C     XRS       = RESIDUAL STRESS MULTIPLICATION FACTOR
C     TRKC      = TRACK CURVATURE (DEGREES)
C     RLOVT     = LATERAL-TO-VERTICAL TANGENT WHEEL LOAD RATIO
C     RLOVC     = LATERAL-TO-VERTICAL CURVATURE WHEEL LOAD RATIO
C     RLOVA     = AVERAGE LATERAL-TO-VERTICAL WHEEL LOAD RATIO
C     ELOC      = WHEEL/RAIL LOAD APPLICATION POINT (IN.)
C                 (FROM CENTER OF RAIL TO GAGE SIDE)
C     ZZ        = DISTANCE FROM TOP OF RAIL TO CRACK CENTER
C     YY        = DISTANCE FROM VERTICAL CENTERLINE TO CRACK CENTER
C     SMAXM     = LARGEST STRESS IN SPECTRUM
C     SR        = STRESS RANGES
C     MAXR      = NUMBER OF STRESS RANGES
C     SM        = MEAN STRESSES
C     RBOA      = ELLIPSE ASPECT RATIO (b/a)
C     RAIL      = RAIL WEIGHT/SECTION IDENTIFIER (5= CHAR ALFANUMERIC)
C     CWARP     = WARPING CONSTANT OF RAIL
C     D         = TORSION CONSTANT OF RAIL
C     E         = MODULUS OF ELASTICITY
C     YI        = VERTICAL BENDING INERTIA (IN**4)
C     ZI        = LATERAL BENDING INERTIA (IN**4)
C     HIY       = VERTICAL BENDING INERTIA OF HEAD OF RAIL ONLY (IN**4)
```

```
C     HIZ       = LATERAL BENDING INERTIA OF HEAD OF RAIL ONLY (IN **4)
C     BIZ       = LATERAL BENDING INERTIA OF BASE OF RAIL ONLY (IN **4)
C     AREA      = TOTAL RAIL CROSS SECTIONAL AREA (IN**2)
C     HAREA     = RAIL HEAD CROSS SECTIONAL AREA (IN**2)
C     HGT       = TOTAL RAIL HEIGHT (INCHES)
C     ZNA       = DISTANCE BETWEEN RAIL BASE AND NEUTRAL AXIS (IN.)
C     GDT       = DISTANCE FROM RAIL BASE TO SHEAR CENTER (IN.)
C     HDT       = DISTANCE BETWEEN CENTROIDS OF HEAD AND BASE (IN.)
C     TWB       = AVERAGE THICKNESS OF WEB OF RAIL (IN.)
C     HWB       = HEIGHT OF WEB OF RAIL (IN.)
C     ZBR       = DISTANCE FROM BASE OF RAIL TO CENTROID OF HEAD (IN.)
C     HWD       = WIDTH OF HEAD OF RAIL (IN.)
C     FDT       = DISTANCE FROM LOAD POINT TO SHEAR CENTER (IN.)
C     FK0       = VERTICAL FOUNDATION MODULUS (PSI)
C     FK1       = LATERAL FOUNDATION MODULUS (PSI)
C     FK2       = TORSIONAL FOUNDATION MODULUS (LB-IN/RAD-IN)
C     NCRX      = NUMBER OF CRACK SIZES
C     PHA       = CRACK SIZES
C     BL        = W/R LOAD HISTOGRAM BIN WIDTH (KIPS)
C     BR        = STRESS RANGE BIN WIDTH (KSI)
C     BM        = MEAN STRESS BIN WIDTH (KSI)
C     C         = CRACK GROWTH RATE CONSTANT (KSI-IN**1.5/CYCLE)
C     P         = CRACK GROWTH RATE EXPONENT (GT.2)
C     Q         = EXPONENT FOR R-EFFECT IN DA/DN EQUATION
C     TK1       = KTH PARAMETER IN THE DA/DN EQUATION
C     CPHA      = CHANGE OF STAGE (%HA)
C     GTONS     = CONSIST GROSS WEIGHT (TONS)
C     NAXLES    = TOTAL NUMBER OF AXLES IN CONSIST
C     LGRPS     = TOTAL NUMBER OF LOAD GROUPS IN CONSIST
C     WRL       = WHEEL/RAIL LOADS VECTOR (KIPS)
C     RLOV      = LATERAL/VERTICAL LOAD RATIO ARRAY
C     X         = VECTOR OF RELATIVE LOCATIONS (BY GROUP) OF
C                 W/R LOADS (INCHES)
C     LG        = VECTOR OF LOAD GROUPS
C     DA,DB,DC  = CAR DIMENSION VECTORS (INCHES)
C     SUM       = VECTOR OF PALMGREN-MINER STRESS SUMS
C     GTHN      = CRACK GEOMETRY INTEGRAL
C     FMAGS     = SHAPE MAGNIFICATION FACTOR
C     FMAG1     = FINITE-SECTION MAGNIFICATION FACTOR
C     FMAGG     = NONUNIFORM STRESS MAGNIFICATION FACTOR
C     COEF      = ARRAY OF COEFFICIENTS FOR QUADRATIC FUNCTIONS
C     FX1       = CALCULATES RESIDUAL STRESS AS A FUNCTION OF CRACK SIZE
C     FX2       = CALCULATES DEPTH AS A FUNCTION OF CRACK SIZE
C     FX3       = CALCULATES YLOC AS A FUNCTION OF CRACK SIZE
C     FX4       = CALCULATES THERMAL STRESS AS A FUNCTION OF CRACK SIZE
C
100   CALL INPUT(JFLAG)
      CALL LOAD
      IF(JFLAG.EQ.1) GO TO 200
      CALL DEFGRO
200   STOP
      END
```

```
C*
C*    SUBROUTINE TO HANDLE INPUT DATA MANIPULATION
C*
      SUBROUTINE INPUT(JFLAG)
      COMMON/BLCK1/ SR(3000),NR(3000),MAXR,SM(3000),NM(3000)
      COMMON/BLCK2/ NFW,IFLAT(20),FWRL(20),FWMF(20),MFLAG
      COMMON/BLCK3/ SIG(4),RBOA,ELOC,TRKC,RLOVT,RLOVA,RAIL
      COMMON/BLCK4/ BL,BR,BM
      COMMON/BLCK5/ C,P,Q,TK1,CPHA,XRS,ITH,ETHERM
      COMMON/BLCK6/ GTONS,NAXLES,LGRPS
      COMMON/BLCK7/ WRL(600),RLOV(600),X(600),LG(131)
      COMMON/BLCK8/ DA(130),DB(130),DC(130)
      COMMON/BLCK9/ COEF(3,3)
      COMMON/BLCK0/ IO2,DMY1,NFLAG
      COMMON/RAIL1/ CWARP,D,E,FK0,FK1,FK2
      COMMON/RAIL2/ FDT,GDT,HDT
      COMMON/RAIL3/ YI,ZI,HIZ,BIZ,HIY,AREA,HAREA
      COMMON/RAIL4/ HGT,ZNA,ZBR,TWB,HWB,HWD
      COMMON/RAIL5/ BETA1,BETA2,BHOWV,BHOWL
      COMMON/CRAX1/ NCRX,PHA(20)
      CHARACTER CTRL(13)*4,RAIL*5,WORD*4,BLANK*1,
     1     CTYP*5,CTYPE(130)*5,DMY1*6,DMY2*6
      DIMENSION CWGT(130),ANS(4),STATE(130)
      DIMENSION NAX(130),NO(130),TITLE(16)
      DATA CTRL/'NAME','CNST','DYNF','RAIL',
     1   'CRAK','BINS','PROP','EDIT','REVU',
     2   'ALTR','FILE','CALC','STOP'/
      DATA BLANK/' '/
C
C     DEFINE DEFAULT VALUES
C
      SIG(1)=0.0
      SIG(2)=0.5
      SIG(3)=0.4
      SIG(4)=0.2
      NFW=0
      ITH=0
      XRS=1.0
      TRKC=0.0
      RLOVT=0.05
      ELOC=HWD/4.
      RBOA=0.7
C
      RAIL='136RE'
C
      CALL RAILIB(RAIL,YI,ZI,HIY,HIZ,BIZ,AREA,HAREA,HGT,ZNA,
     1     GDT,HDT,TWB,HWB,ZBR,HWD,FDT,CWARP,D,E,IFLAG)
C
C     FOUNDATION MODULI
C     FK0 = VERTICAL
C     FK1 = LATERAL
C     FK2 = TORSIONAL
C
      FK0=3000.
      FK1=0.85*FK0
      FK2=0.1E+6
C
C     BIN WIDTHS
C
      BL=1.
```

```
      BR=1.
      BM=1.
C
C     CRACK PROPAGATION PROPERTIES
C
      C=1.0E-11
      P=4.
      Q=1.63
      TK1=10.
C
      CPHA=0.5
      NCRX=4
      PHA(1)=0.119
      DO 10 I=2,NCRX
10          PHA(I)=FLOAT(I)/10.
C
C     COEFFICIENTS FOR FX1,FX2,FX3 FUNCTIONS
C
      COEF(1,1)=10.00
      COEF(1,2)=-12.50
      COEF(1,3)=0.0
      COEF(2,1)=0.62
      COEF(2,2)=1.76
      COEF(2,3)=-1.79
      COEF(3,1)=1.19
      COEF(3,2)=-2.95
      COEF(3,3)=3.43
C
      GTONS=0.
      NAXLES=0
      LGRPS=0
      JFLAG=0
      LINE=0
C
20    WRITE(6,30) (CTRL(I),I=1,7)
      WRITE(6,30) (CTRL(I),I=8,13)
30    FORMAT(1X,7(A4,2X))
      WRITE(6,40)
40    FORMAT(1X,'TYPE CONTROL KEYWORD (A4):')
      READ(5,50) WORD
50    FORMAT(A4)
      DO 60 I=1,18
          IF(WORD.NE.CTRL(I)) GO TO 60
          KEY=I
          GO TO 80
60    CONTINUE
      WRITE(6,70)
70    FORMAT(1X,'INVALID ENTRY, TRY AGAIN')
      GO TO 20
C
80    GO TO (100,200,400,600,700,800,900,
     1 1000,1100,1200,1300,2000,3100) KEY
C
C     "NAME" OPTION
C
100   WRITE(6,110)
110   FORMAT(1X,'TYPE JOBNAME TITLE (16A5):')
      READ(5,120) (TITLE(I),I=1,16)
120   FORMAT(16A5)
      GO TO 20
```

```
C
C     "CNST" OPTION
C
200   NE=0
210   WRITE(6,220)
220   FORMAT(1X,'INPUT CAR TYPE (A5):')
      READ(5,230) CTYP
230   FORMAT(A5)
      IF(CTYP.NE.BLANK) GO TO 240
      LINES=LINE
      GO TO 20
240   WRITE(6,250)
250   FORMAT(1X,'INPUT LOAD STATE (F):')
      READ(5,260) EL
260   FORMAT(F7.3)
      IF(EL.LE.1.AND.EL.GE.0.0) GO TO 270
      WRITE(6,70)
      GO TO 240
270   CALL CARLIB(CTYP,EL,WGT,WRLD,DIMA,DIMB,DIMC,NAXLES,IFLAG)
      IF(IFLAG.NE.1) GO TO 280
      WRITE(6,70)
      GO TO 210
280   WRITE(6,290)
290   FORMAT(1X,'INPUT NO. OF IDENTICAL CARS:')
      READ(5,300) NUM
300   FORMAT(I3)
      LINE=LINE+1
      CTYPE(LINE)=CTYP
      STATE(LINE)=EL
      CWGT(LINE)=WGT
      WRL(LINE)=WRLD
      DA(LINE)=DIMA
      DB(LINE)=DIMB
      DC(LINE)=DIMC
      NAX(LINE)=NAXLES
      NO(LINE)=NUM
C
C     ASSIGN LATERAL/VERTICAL RATIO FOR EACH WHEEL
C
      NE=NE+NAXLES*NUM
      NB=NE-NAXLES*NUM+1
      II=0
      RLOVCUM=0.0
      DO 310 I=NB,NE
            IF(TRKC.EQ.0.0) THEN
               RLOV(I)=RLOVT
               GO TO 310
            END IF
            II=II+1
            IF(WRL(LINE).GE.33.0.AND.II.EQ.1) RLOV(I)=RLOVC
            IF(WRL(LINE).LT.33.0.AND.II.EQ.1) RLOV(I)=RLOVC*(83.
     1     -WRL(LINE))/50.
            IF(II.NE.1) RLOV(I)=RLOVT
            IF(NAXLES.EQ.4.AND.II.EQ.2) II=0
            IF(NAXLES.EQ.6.AND.II.EQ.3) II=0
            RLOVCUM=RLOVCUM+RLOV(I)
310   CONTINUE
      RLOVA=RLOVCUM/(NE-NB)
      WRITE(6,320)
320   FORMAT(1X,'NEXT VEHICLE')
```

```
      GO TO 210
C
C     "DYNF" OPTION
C
400   DO 420 I=1,4
            WRITE(6,410) I
410         FORMAT(1X,'ENTER SIG',I1,': ')
            READ(5,260) SIG(I)
420   CONTINUE
      WRITE(6,430)
430   FORMAT(1X,'INPUT NUMBER OF FLAT WHEELS: ')
      READ(5,300) NFW
      IF(NFW.LE.0) GO TO 500
      DO 490 I=1,NFW
            WRITE(6,440)
440         FORMAT(1X,'INPUT FLAT WHEEL #: ')
            READ(5,300) IFLAT(I)
450         WRITE(6,460) IFLAT(I)
460         FORMAT(1X,'INPUT WHEEL (',I3,') LOAD MAGNITUDE OR ',
     1           'MULTIPLICATION FACTOR',/,1x,'(1 AND 2 RESPECTIVELY) : ')
            READ(5,300) MFLAG
            IF(MFLAG.NE.1.AND.MFLAG.NE.2) THEN
               WRITE(6,70)
               GO TO 450
            END IF
            IF(MFLAG.EQ.1) THEN
               WRITE(6,470) IFLAT(I)
470            FORMAT(1X,'INPUT WHEEL LOAD (',I3,') : ')
               READ(5,260) FWRL(I)
            ELSE
               WRITE(6,480) IFLAT(I)
480            FORMAT(1X,'INPUT WHEEL LOAD (',I3,') MULTIPLICATION',
     1              ' FACTOR : ')
               READ(5,260) FWMF(I)
            END IF
490   CONTINUE
500   WRITE(6,510)
510   FORMAT(1X,'INPUT THERMAL STRESS VALUE (1=YES,0=NO) ?')
      READ(5,300) ITH
      IF(ITH.EQ.1) THEN
        WRITE(6,520)
520     FORMAT(1X,'ENTER THERMAL STRESS (IN KSI) : ')
        READ(5,260) ETHERM
      END IF
      WRITE(6,530)
530   FORMAT(1X,'MULTIPLICATION FACTOR FOR RESIDUAL STRESS :')
      READ(5,260) XRS
      WRITE(6,540)
540   FORMAT(1X,'INPUT TRACK CURVATURE (IN DEGREES) : ')
      READ(5,260) TRKC
      IF(TRKC.NE.0.0) CALL TRKCVE(TRKC,RLOVC)
      WRITE(6,550)
550   FORMAT(1X,'INPUT LATERAL/VERTICAL LOAD (TANGENT) RATIO: ')
      READ(5,260) RLOVT
      WRITE(6,560)
560   FORMAT(1X,'INPUT VERTICAL LOAD OFFSET (INCHES): ')
      READ(5,260) ELOC
      WRITE(6,570)
570   FORMAT(1X,'INPUT ELLIPSE ASPECT (b/a) RATIO : ')
      READ(5,260) RBOA
```

```
      GO TO 20
C
C     "RAIL" OPTION
C
600   WRITE(6,610)
610   FORMAT(1X,'ENTER RAIL SIZE/SECTION CODE:')
      READ(5,230) RAIL
      CALL RAILIB(RAIL,YI,ZI,HIY,HIZ,BIZ,AREA,HAREA,HGT,ZNA,
     1      GDT,HDT,TWB,HWB,ZBR,HWD,FDT,CWARP,D,E,IFLAG)
      IF(IFLAG.NE.1) GO TO 620
      WRITE(6,70)
      GO TO 600
620   WRITE(6,630)
630   FORMAT(1X,'INPUT VERTICAL FOUNDATION MODULUS (PSI): ')
      READ(5,260) FK0
      WRITE(6,640)
640   FORMAT(1X,'INPUT LATERAL FOUNDATION MODULUS (PSI) : ')
      READ(5,260) FK1
      WRITE(6,650)
650   FORMAT(1X,'INPUT TORSIONAL FOUNDATION MOD. (LB-IN/RAD-IN): ')
      READ(5,260) FK2
      GO TO 20
C
C     "CRAK" OPTION
C
700   WRITE(6,710)
710   FORMAT(1X,'INPUT NUMBER OF CRACK SIZES: ')
      READ(5,300) NCRX
      DO 730 I=1,NCRX
            WRITE(6,720) I
720         FORMAT(1X,'INPUT CRACK SIZE ',I3,' (%HA): ')
            READ(5,260) PHA(I)
730   CONTINUE
      WRITE(6,740)
740   FORMAT(1X,'INPUT STAGE 1 TO STAGE 2 (%HA): ')
      READ(5,260) CPHA
      GO TO 20
C
C     "BINS" OPTION
C
800   WRITE(6,810)
810   FORMAT(1X,'ENTER BIN WIDTHS')
      WRITE(6,820)
820   FORMAT(5X,'W/R LOAD HISTOGRAM (KIPS):')
      READ(5,250) BL
      WRITE(6,830)
830   FORMAT(5X,'STRESS RANGE (KSI):')
      READ(5,260) BR
      WRITE(6,840)
840   FORMAT(1X,'MEAN STRESS (KSI):')
      READ(5,260) BM
      GO TO 20
C
C     "PROP" OPTION
C
900   WRITE(6,910)
910   FORMAT(1X,'INPUT CRACK GROWTH CONSTANT:')
      READ(5,920) C
920   FORMAT(E10.3)
930   WRITE(6,940)
```

```
940   FORMAT(1X,'INPUT CRACK GROWTH RATE EXPONENT:')
      READ(5,260) P
      IF(P.GT.2.) GO TO 950
      WRITE(6,70)
      GO TO 930
950   WRITE(6,960)
960   FORMAT(1X,'INPUT R-EFFECT EXPONENT: ')
      READ(5,260) Q
      WRITE(6,970)
970   FORMAT(1X,'INPUT KTH PARAMETER:')
      READ(5,260) TK1
      GO TO 20
C
C     "EDIT" OPTION
C
1000  WRITE(6,1010)
1010  FORMAT(1X,'INPUT LINE NUMBER OF CONSIST:')
      READ(5,300) LINE
      IF(LINE.EQ.0) GO TO 20
      IF(LINE.GT.0) GO TO 1040
      J=LINES-1
      IF(ABS(LINE).EQ.LINES) GO TO 1030
      DO 1020 I=LINE,J
                CTYPE(I)=CTYPE(I+1)
                STATE(I)=STATE(I+1)
                CWGT(I)=CWGT(I+1)
                WRL(I)=WRL(I+1)
                DA(I)=DA(I+1)
                DB(I)=DB(I+1)
                DC(I)=DC(I+1)
                NAX(I)=NAX(I+1)
                NO(I)=NO(I+1)
1020  CONTINUE
1030  LINES=J
      GO TO 1000
1040  WRITE(6,220)
      READ(5,230) CTYP
1050  WRITE(6,250)
      READ(5,260)EL
      IF(EL.GE.0.00.AND.EL.LE.1.00)GO TO 1060
      WRITE(6,70)
      GO TO 1050
1060  CALL CARLIB(CTYP,EL,WGT,WRLD,DIMA,DIMB,DIMC,NAXLES,IFLAG)
      IF(IFLAG.NE.1) GO TO 1070
      WRITE(5,70)
      GO TO 1000
1070  WRITE(5,290)
      READ(5,300) NUM
      CTYPE(LINE)=CTYP
      STATE(LINE)=EL
      CWGT(LINE)=WGT
      WRL(LINE)=WRLD
      DA(LINE)=DIMA
      DB(LINE)=DIMB
      DC(LINE)=DIMC
      NAX(LINE)=NAXLES
      NO(LINE)=NUM
      IF(LINE.LT.LINES) GO TO 1000
      LINES=LINE
      GO TO 1000
```

```
C
C     "REVU" OPTION
C
1100  WRITE(6,1110)
1110  FORMAT(/1X,19HCONSIST INFORMATION)
      WRITE(6,1120)
1120  FORMAT(/1X,4HTYPE,4X,3HPT.,3X,3HNAX,2X,2HNO)
      WRITE(6,1130) (CTYPE(J),STATE(J),NAX(J),NO(J),J=1,LINES)
1130  FORMAT(1X,A5,3X,F4.2,2X,I2,2X,I3)
      IO1=6
      IAAA=11
      GO TO 1420
1180  CONTINUE
      GO TO 20
C
C     "ALTR" OPTION
C
1200  WRITE(6,1210)
1210  FORMAT(1X,'TYPE CODE FOR FUNCTION',
     1  /1X,' 1 = RESIDUAL STRESS FUNCTION',
     1  /1X,' 2 = DEPTH FUNCTION',
     1  /1X,' 3 = YLOC FUNCTION: ')
      READ(5,300) I
      IF(I.EQ.0) GO TO 20
      DO 1240 J=1,3
            WRITE(6,1230) J
1230        FORMAT(1X,'ENTER COEFFICIENT ',I2,' : ')
            READ(5,260) COEF(I,J)
1240  CONTINUE
      GO TO 1180
C
C     "FILE" OPTION
C
1300  WRITE(6,1310)
1310  FORMAT(1X,'WRITING DATA INTO DATA FILE...')
      WRITE(6,1320)
1320  FORMAT(1X,'ENTER FILENAME (A5):')
      READ(5,230) DMY1
      OPEN(UNIT=18,FILE=DMY1)
      REWIND 18
      IO1=18
      IAAA=13
      WRITE(IO1,1110)
      WRITE(IO1,1120)
      WRITE(IO1,1130) (CTYPE(I),STATE(I),NAX(I),NO(I),I=1,LINES)
      NCARS=0
      NAXLES=0
      DO 1360 LINE=1,LINES
            NCARS=NCARS+NO(LINE)
            IF(NCARS.LE.130) GO TO 1340
            WRITE(6,1330)
1330        FORMAT(1X,'TOO MANY CARS, TRANSFERING TO "EDIT"
     1           OPTION')
            GO TO 1000
1340        GTONS=GTONS+NO(LINE)*CWGT(LINE)
            NAXLES=NAXLES+NO(LINE)*NAX(LINE)
            IF(NAXLES.LE.600) GO TO 1360
            WRITE(6,1350)
1350        FORMAT(1X,'TOO MANY AXLES, TRANSFERING TO "EDIT"
     1           OPTION')
```

```
                    GO TO 1000
1360  CONTINUE
      GTONS=GTONS/2.
      WRITE(IO1,1370) NCARS
1370  FORMAT(/1X,'TOTAL NO. OF CARS = ',I5)
      WRITE(IO1,1380) GTONS,NAXLES
1380  FORMAT(1X,'CONSIST GROSS WEIGHT = ',E12.5,' TONS',
     1   /1X,'TOTAL NO. OF AXLES = ',I5)
      L=NCARS
      M=NAXLES
      DO 1410 LM=1,LINES
C                 K = COUNTER FOR NUMBER OF AXLES
                  LINE=LINES+1-LM
C                 LOOP TO EXPAND CONSIST INPUT TO ONE CAR PER LINE
                  J=L+1-NO(LINE)
                  DO 1390 I=J,L
                        CTYPE(I)=CTYPE(LINE)
                        STATE(I)=STATE(LINE)
                        CWGT(I)=CWGT(LINE)
                        DA(I)=DA(LINE)
                        DB(I)=DB(LINE)
                        DC(I)=DC(LINE)
                        NAX(I)=NAX(LINE)
1390              CONTINUE
                  L=J-1
                  K=M+1-NO(LINE)*NAX(LINE)
C                 LOOP TO EXPAND W/R LOADS TO ONE AXLE PER LINE
                  DO 1400 I=K,M
                        WRL(I)=WRL(LINE)
1400              CONTINUE
                  M=K-1
1410  CONTINUE
1420  WRITE(IO1,1430)
1430  FORMAT(//1X,'SUMMARY OF INPUT DATA')
1440  WRITE(IO1,120) (TITLE(I),I=1,16)
      WRITE(IO1,1450)
1450  FORMAT(/1X,'DETAIL FRACTURE CRACK GROWTH ANALYSIS'/)
      WRITE(IO1,1460)
1460  FORMAT(/1X,'LOADING PARAMETERS:')
      WRITE(IO1,1470) ELOC
1470  FORMAT(/1X,'WHEEL/RAIL LOAD APPLICATION POINT       = ',
     1  F7.3,' IN.')
      WRITE(IO1,1480) RBOA
1480  FORMAT(1X,'b/a RATIO',32X,' = ',F7.3)
      WRITE(IO1,1490) TRKC
1490  FORMAT(1X,'TRACK CURVATURE (IN DEGREES)',13X,' = ',F7.3)
      WRITE(IO1,1500) RLOVT
1500  FORMAT(1X,'LATERAL/VERTICAL LOAD (TANGENT) RATIO',4X,' = '
     1  ,F7.3)
      IF(TRKC.NE.0.0) WRITE(IO1,1510)RLOVA
1510  FORMAT(1X,'AVERAGE L/V LOAD RATIO',19X,' = ',F7.3)
      WRITE(IO1,1520) SIG(1)
1520  FORMAT(1X,'SIGMA TO DECREASE BELOW MEAN LOAD',8X,' = ',F7.3)
      WRITE(IO1,1530) SIG(2)
1530  FORMAT(1X,'SIGMA TO INCREASE BELOW MEAN LOAD',8X,' = ',F7.3)
      WRITE(IO1,1540) SIG(3)
1540  FORMAT(1X,'SIGMA TO DECREASE ABOVE MEAN LOAD',8X,' = ',F7.3)
      WRITE(IO1,1550) SIG(4)
1550  FORMAT(1X,'SIGMA TO INCREASE ABOVE MEAN LOAD',8X,' = ',F7.3)
      IF(ITH.EQ.1) WRITE(IO1,1560) ETHERM
```

```
1560  FORMAT(1X,'THERMAL STRESS',27X,' = ',F7.3,' KSI')
      WRITE(IO1,1570) XRS
1570  FORMAT(1X,'RESIDUAL STRESS MULTIPLICATION FACTOR',4X,' = ',F7.3)
      WRITE(IO1,1572) (COEF(1,I),I=1,3)
1572  FORMAT(1X,'RESIDUAL STRESS FUNCTION COEFFICIENTS',4X,' = ',
     1  3(F7.3,1X))
      WRITE(IO1,1574) (COEF(2,I),I=1,3)
1574  FORMAT(1X,'DEPTH FUNCTION COEFFICIENTS',14X,' = ',3(F7.3,1X))
      WRITE(IO1,1576) (COEF(3,I),I=1,3)
1576  FORMAT(1X,'Y-LOCATION FUNCTION COEFFICIENTS',9X,' = ',3(F7.3,1X))
      IF(NFW.NE.0) WRITE(IO1,1580)NFW
1580  FORMAT(1X,I2,' FLAT WHEELS : ')
      DO 1610 I=1,NFW
                IF(MFLAG.EQ.1) WRITE(IO1,1590)IFLAT(I),FWRL(I)
1590            FORMAT(1X,'  WHEEL ',I3,' = ',F9.2,' KIP')
                IF(MFLAG.EQ.2) WRITE(IO1,1600)IFLAT(I),FWMF(I)
1600            FORMAT(1X,'  WHEEL ',I3,' MULTIPLICATION FACTOR = ',
     1              F9.2)
1610  CONTINUE
      WRITE(IO1,1620) RAIL
1620  FORMAT(/1X,'RAIL SECTION PROPERTIES FOR ',A5)
      WRITE(IO1,1630) YI
1630  FORMAT(1X,'VERTICAL BENDING INERTIA FOR ENTIRE RAIL',
     1  1X,' = ',F7.3,' IN**4')
      WRITE(IO1,1640) ZI
1640  FORMAT(1X,'LATERAL BENDING INERTIA FOR ENTIRE RAIL',
     1  2X,' = ',F7.3,' IN**4')
      WRITE(IO1,1650) HIZ
1650  FORMAT(1X,'LATERAL BENDING INERTIA FOR HEAD ONLY',
     1  4X,' = ',F7.3,' IN**4')
      WRITE(IO1,1660) BIZ
1660  FORMAT(1X,'LATERAL BENDING INERTIA FOR BASE ONLY',
     1  4X,' = ',F7.3,' IN**4')
      WRITE(IO1,1670) HIY
1670  FORMAT(1X,'VERTICAL BENDING INERTIA FOR HEAD ONLY',
     1  3X,' = ',F7.3,' IN**4')
      WRITE(IO1,1680) AREA
1680  FORMAT(1X,'TOTAL RAIL CROSS SECTIONAL AREA',10X,' = ',F7.3,
     1  ' IN**2')
      WRITE(IO1,1690) HAREA
1690  FORMAT(1X,'RAIL HEAD CROSS SECTIONAL AREA',11X,' = ',
     1  F7.3,' IN**2')
      WRITE(IO1,1700) HGT
1700  FORMAT(1X,'TOTAL RAIL HEIGHT',24X,' = ',F7.3,' INCHES')
      WRITE(IO1,1710) ZNA
1710  FORMAT(1X,'NEUTRAL AXIS LOCATION',20X,' = ',F7.3,' INCHES')
      WRITE(IO1,1720) GDT
1720  FORMAT(1X,'DISTANCE FROM RAILBASE TO SHEAR CENTER',3X,
     1  ' = ',F7.3,' INCHES ')
      WRITE(IO1,1730) HDT
1730  FORMAT(1X,'DISTANCE FROM LOAD POINT TO SHEAR CENTER  = ',
     1  F7.3,' INCHES')
      WRITE(IO1,1740) TWB
1740  FORMAT(1X,'AVERAGE THICKNESS OF RAIL WEB',12X,' = ',F7.3,
     1  ' INCHES')
      WRITE(IO1,1750) HWB
1750  FORMAT(1X,'HEIGHT OF RAIL WEB',23X,' = ',F7.3,' INCHES')
      WRITE(IO1,1760) ZBR
1760  FORMAT(1X,'DISTANCE FROM RAILBASE TO CENTROID OF HEAD= ',
     1  F7.3,' INCHES')
```

```
      WRITE(IO1,1770) HWD
1770  FORMAT(1X,'WIDTH OF RAIL HEAD',23X,' = ',F7.3,' INCHES')
      WRITE(IO1,1780) FDT
1780  FORMAT(1X,'DISTANCE FROM LOAD POINT TO SHEAR CENTER  = ',F7.3,
     1  ' INCHES')
      WRITE(IO1,1790)
1790  FORMAT(/1X,'OTHER RAIL PARAMETERS:')
      WRITE(IO1,1800)
1800  FORMAT(/1X,'FOUNDATION MODULI FOR STRESS ANALYSIS:')
      WRITE(IO1,1810) FK0
1810  FORMAT(1X,'VERTICAL FOUNDATION MODULUS',14X,' = ',F6.1,' PSI')
      WRITE(IO1,1820) FK1
1820  FORMAT(1X,'LATERAL FOUNDATION MODULUS ',14X,' = ',F6.1,' PSI')
      WRITE(IO1,1830) FK2
1830  FORMAT(1X,'TORSIONAL FOUNDATION MODULUS ',12X,' = ',E10.3,
     1  ' LB-IN/RAD-IN')
      WRITE(IO1,1840)
1840  FORMAT(/1X,'BIN WIDTHS FOR HISTOGRAMS:')
      WRITE(IO1,1850) BL
1850  FORMAT(1X,'W/R HISTOGRAM BIN WIDTH',18X,' = ',F7.3,' KIPS')
      WRITE(IO1,1860) BR
1860  FORMAT(1X,'STRESS RANGE BIN WIDTH ',18X,' = ',F7.3,' KSI')
      WRITE(IO1,1870) BM
1870  FORMAT(1X,'MEAN STRESS BIN WIDTH  ',18X,' = ',F7.3,' KSI')
      WRITE(IO1,1880)
1880  FORMAT(/1X,'CRACK PROPAGATION PROPERTIES:')
      WRITE(IO1,1890) C
1890  FORMAT(1X,'CRACK GROWTH RATE CONSTANT',15X,' = ',E10.3,
     1  ' KSI-IN**1.5/CYCLE')
      WRITE(IO1,1900) P
1900  FORMAT(1X,'CRACK GROWTH RATE EXPONENT',15X,' = ',F7.3)
      WRITE(IO1,1910) Q
1910  FORMAT(1X,'R-EFFECT EXPONENT',24X,' = ',F7.3)
      WRITE(IO1,1920) TK1
1920  FORMAT(1X,'KTH PARAMETER IN DA/DN EQUATION',10X,' = ',
     1  F7.3,' KSI-IN**0.5')
      WRITE(IO1,1930) CPHA
1930  FORMAT(1X,'STAGE 1 TO STAGE 2',23X,' = ',F6.2,' %HA')
      IF(IAAA.EQ.11) GO TO 1180
      IF(IAAA.EQ.15) GO TO 2050
      IF(IFILE.EQ.1) GO TO 3110
      GO TO 20
C
C     "CALC" OPTION
C
2000  WRITE(6,2010)
2010  FORMAT(1X,'ENTER 1=OUTPUT TO DATAFILE, 0=OUTPUT TO TERMINAL:')
      READ(5,300) NFLAG
      IF(NFLAG.EQ.1) GO TO 2020
      IF(NFLAG.EQ.0) GO TO 2030
      WRITE(5,70)
      GO TO 2000
2020  IO2=18
      GO TO 2040
2030  IO2=5
2040  IO1=6
      IAAA=15
      GO TO 1420
C
2050  CONTINUE
```

```
      LG(1)=NAX(1)/2
      X(1)=0.
      X(2)=DC(1)
      J=2
      IF(NAX(1).NE.6) GO TO 2060
      X(3)=X(2)+DC(1)
      J=3
2060  DO 2160 N=2,NCARS
                  LG(N)=(NAX(N-1)+NAX(N))/2
                  X(J+1)=0.
                  X(J+2)=DC(N-1)
                  K=(2*NAX(N-1)+NAX(N)-10)/2
                  GO TO (2070,2080,2090,2100) K
2070              X1=0.5*(DA(N-1)-DB(N-1)-DC(N-1))
                  X2=0.5*(DA(N)-DB(N)-DC(N))
                  GO TO 2110
2080              X1=0.5*(DA(N-1)-DB(N-1)-DC(N-1))
                  X2=0.5*(DA(N)-DB(N))-DC(N)
                  GO TO 2110
2090              X1=0.5*(DA(N-1)-DB(N-1))-DC(N-1)
                  X2=0.5*(DA(N)-DB(N)-DC(N))
                  GO TO 2110
2100              X1=0.5*(DA(N-1)-DB(N-1))-DC(N-1)
                  X2=0.5*(DA(N)-DB(N))-DC(N)
2110              GO TO (2120,2130,2140,2150) K
2120              X(J+3)=X(J+2)+X1+X2
                  X(J+4)=X(J+3)+DC(N)
                  J=J+4
                  GO TO 2160
2130              X(J+3)=X(J+2)+X1+X2
                  X(J+4)=X(J+3)+DC(N)
                  X(J+5)=X(J+4)+DC(N)
                  J=J+5
                  GO TO 2160
2140              X(J+3)=X(J+2)+DC(N-1)
                  X(J+4)=X(J+3)+X1+X2
                  X(J+5)=X(J+4)+DC(N)
                  J=J+5
                  GO TO 2160
2150              X(J+3)=X(J+2)+DC(N-1)
                  X(J+4)=X(J+3)+X1+X2
                  X(J+5)=X(J+4)+DC(N)
                  X(J+6)=X(J+5)+DC(N)
                  J=J+6
2160  CONTINUE
      LGRPS=NCARS+1
      LG(LGRPS)=NAX(NCARS)/2
      X(J+1)=0.
      X(J+2)=DC(NCARS)
      IF(NAX(NCARS).NE.6) GO TO 2170
      X(J+3)=X(J+2)+DC(NCARS)
2170  CONTINUE
      GO TO 3110
C
C     "STOP" OPTION
C
3100  JFLAG=1
3110  RETURN
      END
C
```

```
      SUBROUTINE TRKCVE(ARG,SUM)
C
C     DEFINE THE TRACK CURVATURE EQUATION BY LAGRANGIAN INTERPOLATION
C
      DIMENSION X(17),Y(17)
      DATA X/2.9,3.1,3.4,3.7,4.6,5.8,7.5,8.0,8.4,9.5,10.0,11.0,11.5
     1 ,12.0,12.5,13.0,13.5/
      DATA Y/0.182,0.212,0.222,0.242,0.302,0.364,0.406,0.409,0.416
     1 ,0.445,0.451,0.465,0.472,0.475,0.478,0.481,0.485/
      SUM=0.0
      DO 20 I=1,17
            PROD=Y(I)
            DO 10 J=1,17
                  IF(I.EQ.J)GO TO 10
                  PROD=PROD*(ARG-X(J))/(X(I)-X(J))
10          CONTINUE
20          SUM=SUM+PROD
      RETURN
      END
```

```
C*
C*    SUBROUTINE TO STORE VEHICLE PARAMETERS
C*
      SUBROUTINE CARLIB(CTYP,EL,WGT,WRLD,DIMA,DIMB,DIMC,NAXLES,IFLAG)
      CHARACTER CT(43)*5
      CHARACTER CTYP*5
      DIMENSION WE(43),WL(43),PE(43),PL(43)
      DIMENSION AA(43),BB(43),CC(43),NA(43)
      DATA (CT(I),I=1,43) /'BOXUP','BOXNP','BOXNW','BOXTC','BOXPS',
     1              'BOXFG','STOCK','GOND1','GOND2','GONDB','CVRG1','CVRG2',
     1              'COILG','OHOP1','OHOP2','OHOP3','CHOP1','CHOP2','CHOP3',
     1              'TANK1','CABS1','CABS2','CABS3','CABS4','FLAT1','BKFT1',
     1              'BKFL2','PIGB1','LOCO1','LOCO2','LOCO3','LOCO4','LOCO5',
     1              'HOPR1','CABS5','DODX1','DODX2','125T','APLXE','APLXM',
     1              'ARROW','CBQDD','AMTK'/
      DATA WE/53.6,60.7,96.1,119.,100.,93.0,44.9,74.8,59.5,71.8,
     1   78.1,82.7,67.6,69.4,59.6,50.2,64.8,58.5,62.2,77.6,55.4,55.0,
     1   48.0,56.6,79.5,61.5,87.6,76.2,250.,230.,242.,356.,390.,
     1   58.,60.,92.7,94.7,65.0,45.0,60.0,125.0,110.2,108.0/
      DATA WL/231.,220.,269.,219.,263.,219.,177.,260.,214.,220.,
     1   220.,220.,263.,263.,263.,220.,263.,263.,263.,314.,57.4,57.0,
     1   50.0,58.6,263.,220.,263.,200.,250.,230.,242.,356.,390.,
     1   258.,60.,394.5,394.5,315.0,242.0,264.0,155.0,132.4,120.0/
      DATA AA/535.,654.,819.,1130.,818.,777.,547.,835.,849.,842.,
     1   599.,686.,692.,620.,585.,373.,711.,458.,661.,790.,499.,501.,
     1   501.,485.,778.,617.,958.,1060.,710.,536.,722.,790.,848.,
     1   620.,485.,867.,867.,620.,888.,1544.,1020.,1020.,1020./
      DATA BB/377.4,491.4,555.0,772.0,555.4,554.8,372.4,672.4,685.4,
     1   659.0,436.4,524.0,486.0,469.4,434.4,209.4,540.6,307.4,504.0,
     1   490.0,278.0,278.8,233.0,278.2,536.0,486.0,736.0,802.0,408.,
     1   264.0,434.0,561.9,621.5,469.4,278.2,552.0,552.0,469.4,608.,
     1   608.,714.,714.,714./
      DATA CC/66.,68.,70.,68.,70.,68.,66.,70.,68.,68.,68.,68.,70.,
     1   70.,70.,68.,70.,70.,70.,70.,68.,68.,66.,66.,70.,68.,70.,70.,
     1   108.,96.,168.,81.5,81.5,70.,66.,66.,66.,70.,70.,70.,102.,
     1   102.,102./
      DATA NA/4,4,4,4,4,4,4,4,4,4,4,4,4,4,4,4,4,4,4,4,4,4,4,4,4,4,4,
     1   4,4,4,4,4,4,6,6,4,4,6,6,4,4,4,4,4,4/
      DATA NN/43/
C
C     WE        = WHEEL LOAD OF EMPTY CARS
C     WL        = WHEEL LOAD OF FULLY LOADED CARS
C     AA,BB,CC  = CAR DIMENSIONS
C     NA        = NUMBER OF AXLES
C     NN        = NUMBER OF VEHICLES STORED IN LIBRARY
C
      IFLAG=1
      DO 30 N=1,NN
            IF(CTYP.NE.CT(N)) GO TO 30
            WGT=((WL(N)-WE(N))*EL)+WE(N)
20          DIMA=AA(N)
            DIMB=BB(N)
            DIMC=CC(N)
            NAXLES=NA(N)
            WRLD=WGT/(2.*FLOAT(NAXLES))
            IFLAG=0
            GO TO 40
30    CONTINUE
40    RETURN
      END
```

```
C*
C*    SUBROUTINE STORING RAIL SECTION PROPERTIES
C*
      SUBROUTINE RAILIB(RAIL,YI,ZI,HIY,HIZ,BIZ,AREA,HAREA,HGT,ZNA,
     1                  GDT,HDT,TWB,HWB,ZBR,HWD,FDT,C,D,E,IFLAG)
      CHARACTER RT(10)*5
      CHARACTER RAIL*5
      DIMENSION YY(10),YH(10),ZZ(10),ZH(10),ZB(10),AR(10),HA(10)
      DIMENSION H(10),ZN(10),ZC(10),HD(10),TW(10),HW(10),WD(10),ZR(10)
      DATA (RT(I),I=1,10) /'70ASC','85ASC','100RE','115RE','132RE',
     1                     '136RE','140RE','155PS','127DY','90ASC'/
      DATA YY/19.7,30.07,49.0,65.6,88.2,94.9,96.8,129.,81.57,34.39/
      DATA ZZ/4.86,6.95,9.35,10.40,14.20,14.50,14.70,20.00,15.18,7.24/
      DATA YH/0.329,0.558,0.714,0.729,0.837,1.17,1.38,1.38,0.79,0.64/
      DATA ZH/1.24,1.75,2.12,2.13,2.84,3.03,3.14,3.14,2.71,2.06/
      DATA ZB/3.53,5.11,7.13,7.99,11.10,11.20,11.10,16.60,12.20,6.43/
      DATA AR/6.81,8.33,9.95,11.26,12.95,13.35,13.80,15.2,12.5,8.83/
      DATA HA/2.81,3.49,3.80,3.91,4.42,4.86,5.00,5.09,4.26,3.77/
      DATA H/4.625,5.188,6.000,6.625,7.125,7.3125,7.3125,8.0,7.0,5.38/
      DATA ZN/2.22,2.47,2.75,2.98,3.20,3.35,3.37,3.51,3.14,2.55/
      DATA ZC/1.26,1.37,1.51,1.55,1.63,1.69,1.74,1.51,1.47,1.38/
      DATA HD/3.71,4.14,4.84,5.39,5.86,5.95,5.91,6.57,5.80,4.28/
      DATA TW/.5156,.5625,.5625,.625,.6560,.6875,.75,.75,.66,.56/
      DATA HW/2.469,2.75,3.281,3.812,4.188,4.156,4.062,4.656,4.16,2.86/
      DATA ZR/4.01,4.46,5.23,5.80,6.30,6.39,6.35,7.04,6.21,4.62/
      DATA WD/2.4375,2.5625,2.6875,2.7188,3.0,2.9375,3.0,3.0,3.0,2.63/
      DATA MM/10/
C
C     MM = NUMBER OF RAIL SECTIONS STORED IN LIBRARY (9)
C     YY = VERTICAL BENDING INERTIA
C     ZZ = LATERAL BENDING INERTIA
C     YH = VERTICAL BENDING INERTIA OF RAIL HEAD ONLY
C     ZH = LATERAL BENDING INERTIA OF RAIL HEAD ONLY
C     ZB = LATERAL BENDING INERTIA OF RAIL BASE ONLY
C     AR = TOTAL RAIL CROSS SECTIONAL AREA
C     HA = RAILHEAD CROSS SECTIONAL AREA
C     H  = TOTAL HEIGHT OF RAIL
C     ZN = DISTANCE BETWEEN RAILBASE AND NEUTRAL AXIS
C     ZC = DISTANCE FROM RAIL BASE TO CENTER OF SHEAR
C     HD = DISTANCE BETWEEN CENTROIDS OF HEAD AND BASE
C     TW = THICKNESS OF RAIL WEB
C     HW = TOTAL HEIGHT OF RAIL WEB
C     ZR = DISTANCE FROM RAIL BASE TO CENTROID OF HEAD
C     WD = WIDTH OF RAIL HEAD
C
      IFLAG=1
      DO 10 M=1,MM
            IF(RAIL.NE.RT(M)) GO TO 10
            YI=YY(M)
            ZI=ZZ(M)
            HIY=YH(M)
            HIZ=ZH(M)
            BIZ=ZB(M)
            AREA=AR(M)
            HAREA=HA(M)
            HGT=H(M)
            ZNA=ZN(M)
            GDT=ZC(M)
            HDT=HD(M)
            TWB=TW(M)
```

```
                HWB=HW(M)
                ZBR=ZR(M)
                HWD=WD(M)
                FDT=HGT-GDT
C
C       ADDITIONAL PROPERTIES FOR TIMOSHENKO AND LANGER STRESS ANALYSIS
C
C       E  = YOUNG'S MODULUS
C       G  = SHEAR MODULUS
C       D  = WARPING CONSTANT OF RAIL
C       C  = TORSION CONSTANT OF RAIL
C
                E=30.E+6
                G=11.5E+6
                D=HIZ*BIZ*E/(HIZ+BIZ)
                C1=G*(AREA**4)
                C2=40.*(YI+ZI+AREA*(ZNA-GDT)*(ZNA-GDT))
                C=C1/C2
C
                IFLAG=0
                GO TO 20
10      CONTINUE
C
20      RETURN
        END
```

```
C*
C*    WHEEL/RAIL LOAD SPECTRUM SUBROUTINE FOR
C*    DETAIL FRACTURE CRACK GROWTH PROGRAM
C*
      SUBROUTINE LOAD
      COMMON/BLCK2/ NFW,IFLAT(20),FWRL(20),FWMF(20),MFLAG
      COMMON/BLCK3/ SIG(4),RBOA,ELOC,TRKC,RLOVT,RLOVA,RAIL
      COMMON/BLCK4/ BL,BR,BM
      COMMON/BLCK6/ GTONS,NAXLES,LGRPS
      COMMON/BLCK7/ WRL(600),RLOV(600),X(600),LG(131)
      COMMON/BLCK0/ IO2,DMY1,NFLAG
      DIMENSION PP(600),ZCTR(100,2),IZCTR(100)
C
C     COMPUTE TOTAL WHEEL LOAD
C     (INCLUDE DYNAMIC FACTOR)
C
      DO 20 N=1,NAXLES
            CALL GAUSS(Z)
            IF(WRL(N).LT.27..AND.Z.LT.0.0) SIGX=SIG(1)
            IF(WRL(N).LT.27..AND.Z.GE.0.0) SIGX=SIG(2)
            IF(WRL(N).GE.27..AND.Z.LT.0.0) SIGX=SIG(3)
            IF(WRL(N).GE.27..AND.Z.GE.0.0) SIGX=SIG(4)
            SAV=WRL(N)
            WRL(N)=(1.+SIGX*Z)*WRL(N)
            IF(WRL(N).LT.0.0) THEN
              WRL(N)=0.01*SAV
              WRITE(6,10)
10            FORMAT(1X,'NEGATIVE WHEEL LOAD')
            END IF
20    CONTINUE
C
C     ASSIGN FLAT WHEEL LOAD
C
30    IF(NFW.EQ.0.) GO TO 60
      DO 40 I=1,NFW
            IF(MFLAG.EQ.1) WRL(IFLAT(I))=FWRL(I)
            IF(MFLAG.EQ.2) WRL(IFLAT(I))=WRL(IFLAT(I))*FWMF(I)
40    CONTINUE
C
C     PP = WHEEL LOAD
C
60    DO 70 N=1,NAXLES
            PP(N)=WRL(N)
70    CONTINUE
C
C     SORTING PP INTO DESCENDING ORDER
C
80    IFLAG=0
      DO 90 I=2,NAXLES
            IF(PP(I).LE.PP(I-1)) GO TO 90
            Z=PP(I)
            PP(I)=PP(I-1)
            PP(I-1)=Z
            IFLAG=1
90    CONTINUE
      IF(IFLAG.NE.0) GO TO 80
C
      IXTRA=INT((PP(1)-30.75)/2.0)+1
      MAXJ=IXTRA+5
C
```

```
C     FILL IN ARRAY WITH BIN CENTERS AND BINWIDTHS
C
C
C     INITIALIZE ARRAY ENTRIES TO ZERO
C
      DO 100 I=1,MAXJ
            DO 100 J=1,3
                  ZCTR(I,J)=0.0
100   CONTINUE
      DO 110 I=1,MAXJ
            IZCTR(I)=0.0
110   CONTINUE
      ZCTR(1,1)=5.0
      ZCTR(1,2)=10.00
      ZCTR(2,1)=13.75
      ZCTR(2,2)=7.5
      ZCTR(3,1)=20.0
      ZCTR(3,2)=5.0
      ZCTR(4,1)=25.0
      ZCTR(4,2)=5.0
      ZCTR(5,1)=29.125
      ZCTR(5,2)=3.25
      DO 120 I=6,MAXJ
            ZCTR(I,2)=2.00
            ZCTR(I,1)=(ZCTR(I-1,1)+(ZCTR(I-1,2)/2.))+(ZCTR(I,2)/2.)
120   CONTINUE
C
C     SORT WHEEL LOADS INTO BINS
C
      DO 150 N=1,NAXLES
            DO 130 M=1,MAXJ
                  TOP=ZCTR(M,1)+(ZCTR(M,2)/2.00)
                  BOT=ZCTR(M,1)-(ZCTR(M,2)/2.00)
                  IF(PP(N).GT.BOT.AND.PP(N).LE.TOP)THEN
                    IZCTR(M)=IZCTR(M)+1
                    GO TO 150
                  END IF
130         CONTINUE
            WRITE(6,140)N
140         FORMAT(1X,'MISSED LOAD #',I3)
150   CONTINUE
C
C     N    = LINE NUMBER
C     PP(N) = BIN CENTER
C     KK(N) = BIN COUNT
C     K    = CUMULATIVE COUNT
C
      WRITE(IO2,200)
200   FORMAT(//1X,'WHEEL LOAD SPECTRUM')
      WRITE(IO2,210)
210   FORMAT(/10X,'WHL LOAD',5X,'COUNT',1X,'CUMUL',1X,'FREQUENCY')
C
      K=0
      DO 220 N=1,MAXJ
            K=K+IZCTR(N)
            ICNT=IZCTR(N)
            FREQ=ICNT/FLOAT(NAXLES)
220   WRITE(IO2,230) N,ZCTR(N,1),ICNT,K,FREQ
230   FORMAT(1X,I5,1X,E12.5,2X,I5,3X,I4,2X,F8.6)
C
```

```
      RETURN
      END
C*
C*    SUBROUTINE TO GENERATE GAUSSIAN DISTRIBUTION
C*
      SUBROUTINE GAUSS(Z)
      SUM=0.0
      NSAMP=4
      SIG=1./SQRT(12.)
      XMU=0.5
      DO 10 I=1,NSAMP
            R=RAN(X)
            SUM=SUM+R
10    CONTINUE
      XN=FLOAT(NSAMP)
      XBAR=SUM/XN
      Z=(XBAR-XMU)*SQRT(XN)/SIG
      RETURN
      END
```

```
C
      FUNCTION RAN(X)
      I=I+1
      IF(I.EQ.1) X=1.
      X=7.**9*X
      Y=10.**6.
      Z=AMOD(X,Y)
      RAN=Z/Y
      X=RAN
      RETURN
      END
```

```
C*
C*      SUBROUTINE TO CALCULATE STRESS COMPONENTS FOR
C*      DETAIL FRACTURE CRACK GROWTH
C*
        SUBROUTINE STRESS(ZZ,YY,RS,THERM,SMAXM)
        COMMON/BLCK1/ SR(3000),NR(3000),MAXR,SM(3000),NM(3000)
        COMMON/BLCK3/ SIG(4),RBOA,ELOC,TRKC,RLOVT,RLOVA,RAIL
        COMMON/BLCK4/ BL,BR,BM
        COMMON/BLCK5/ C,P,Q,TK1,CPHA,XRS,ITH,ETHERM
        COMMON/BLCK6/ GTONS,NAXLES,LGRPS
        COMMON/BLCK7/ WRL(600),RLOV(600),X(600),LG(131)
        COMMON/BLCK8/ DA(130),DB(130),DC(130)
        COMMON/BLCK0/ IO2,DMY1,NFLAG
        COMMON/RAIL1/ CWARP,D,E,FK0,FK1,FK2
        COMMON/RAIL2/ FDT,GDT,HDT
        COMMON/RAIL3/ YI,ZI,HIZ,BIZ,HIY,AREA,HAREA
        COMMON/RAIL4/ HGT,ZNA,ZBR,TWB,HWB,HWD
        COMMON/RAIL5/ BETA1,BETA2,BHOWV,BHOWL
        CHARACTER*5 RAIL
        REAL KHOWV,KHOWL
        DIMENSION SMIN(3000),SMAX(3000),SXX(400)
        DIMENSION PP(6),PX(6),HX(6),EDIST(6),XX(6)
        DIMENSION XST(400),BMIN(20),BMAX(20)
        DATA PI/3.141592/
C
        J=0
        K=0
        DX=2.
        MX=325
        X0=-100.
C
        KHOWV=TWB*E/HWB
        KHOWL=KHOWV**3/E/E
        BHOWV=(KHOWV/(4.*E*HIY))**0.25
        BHOWL=(KHOWL/(4.*E*HIZ))**0.25
C
C       FOUNDATION MODULI
C       FK0 - VERTICAL
C       FK1 - LATERAL
C       FK2 - TORSIONAL
C
        BETA1=(FK0/(4.*E*YI))**0.25
        BETA2=(FK1/(4.*E*ZI))**0.25
        XPMAX=0.75*PI/BETA1
C
C       LGRPS     = NO. OF LOAD GROUPS
C       NN        = NO. OF APPLIED WHEEL/RAIL LOADS PER LOAD GROUP
C       NC        = NO. OF CYCLES PER LOAD GROUP
C
        DO 10 I=1,MX
10              XST(I)=X0+FLOAT(I-1)*DX
C
        DO 80 L=1,LGRPS
                NN=LG(L)
                DO 20 I=1,15
                        BMIN(I)=0.0
                        BMAX(I)=0.0
20              CONTINUE
                DO 30 I=1,NN
                        XX(I)=X(I+J)
```

```
                    PP(I)=WRL(I+J)
                    PX(I)=1000.*WRL(I+J)
                    HX(I)=RLOV(I+J)*PX(I)
                    III=I+J
                    EDIST(I)=ELOC
30              CONTINUE
                XMAX=XX(NN)+XPMAX
                NX=INT((XMAX-X0)/DX)
C
                CALL TIMO(PX,HX,EDIST,XST,NX,XX,NN,ZZ,YY,SXX)
C
C               CYCLE COUNTING PROCEDURE
C
                NC=1
                BMIN(1)=0.0
                LAST=0
                DO 50 I=1,NX
                    IF(I.EQ.1.OR.I.EQ.2) GO TO 50
                    IF(SXX(i-1).GT.SXX(i).AND.SXX(i-1)
     1          .GT.SXX(i-2))GO TO 40
                    IF(SXX(i-1).LT.SXX(i).AND.SXX(i-1)
     1          .LT.SXX(i-2))BMIN(NC)=SXX(I-1)
                    IF(XST(I).GT.XX(NN)) LAST=1
                    GO TO 50
40                  BMAX(NC)=SXX(I-1)
                    IF(LAST.EQ.1) GO TO 60
                    NC=NC+1
50              CONTINUE
                IF(LAST.EQ.1.AND.BMAX(NC).EQ.0.) BMAX(NC)=SXX(NX)
C
60              DO 70 I=1,NC
                    SMIN(K+I)=BMIN(I)/1000.
                    SMAX(K+I)=BMAX(I)/1000.
70              CONTINUE
                J=J+NN
                K=K+NC
80      CONTINUE
        MM=K
C       MM=TOTAL NUMBER OF MIN/MAX PAIRS
        WRITE(IO2,90)
90      FORMAT(/1X,'TABLE OF MIN/MAX PAIRS WITH STRESS RANGES
     1   AND MEANS')
        WRITE(IO2,100)
100     FORMAT(1X,'(INCLUDING ADDITIONAL MEAN STRESS COMPONENTS)')
        WRITE(IO2,110) MM
110     FORMAT(1X,'(TOTAL NUMBER OF MIN/MAX PAIRS',5X,'= ',I6,1H))
        WRITE(IO2,120)
120     FORMAT(/10X,4HSMIN,10X,4HSMAX,10X,2HSR,12X,2HSM,15X,1HR)
        SMA=RS+THERM
        DO 160 I=1,MM
            SSMIN=SMIN(I)+SMA
            SSMAX=SMAX(I)+SMA
            IF(SSMIN.LT.0.0.AND.SSMAX.LT.0.0) THEN
              RRATIO=0.0
              SR(I)=0.0
              SM(I)=0.0
              GO TO 140
            END IF
            RRATIO=(SMIN(I)+SMA)/(SMAX(I)+SMA)
            IF(RRATIO.LE.0.0) GO TO 130
```

```
                SR(I)=SMAX(I)-SMIN(I)
                SM(I)=0.5*(SMAX(I)+SMIN(I))+SMA
                GO TO 140
130             RRATIO=0.0
                SM(I)=0.5*(SMAX(I)+SMA)
                SR(I)=SMAX(I)+SMA
140             WRITE(IO2,150) I,SMIN(I),SMAX(I),SR(I),SM(I),RRATIO
150             FORMAT(1X,I5,1X,4(E12.5,2X),F7.2)
160     CONTINUE
C
C       SORTS STRESS RANGES INTO DESCENDING ORDER
C
170     IFLAG=0
        DO 180 I=2,MM
                IF(SR(I).LE.SR(I-1)) GO TO 180
                AA=SR(I)
                SR(I)=SR(I-1)
                SR(I-1)=AA
                AA=SM(I)
                SM(I)=SM(I-1)
                SM(I-1)=AA
                IFLAG=1
180     CONTINUE
        IF(IFLAG.NE.0) GO TO 170
        NN=INT(SR(1)/BR)
        AA=BR*FLOAT(NN)
        NN=0
        J=1
        K=0
190     NN=NN+1
        IF(NN.GT.MM) GO TO 220
        TEMP=SR(NN)
200     IF(TEMP.LE.AA) GO TO 210
        K=K+1
        IF(NN.NE.MM) GO TO 190
        SR(J)=AA+0.5*BR
        NR(J)=K
        GO TO 190
210     SR(J)=AA+0.5*BR
        NR(J)=K
        AA=AA-BR
        IF(K.EQ.0) GO TO 200
        J=J+1
        K=0
        GO TO 200
220     MAXR=J
C
C       MAXR=NO. OF STRESS RANGES
        II=2
        III=0
        J=1
        DO 400 L=1,MAXR
                III=III+NR(L)
                IF(III.LT.II) GO TO 290
C
C               SORTS MEAN STRESSES (WITHIN STRESS RANGE BIN)
C               INTO DESCENDING ORDER
C
230             IFLAG=0
                DO 240 I=II,III
```

```
                    IF(SM(I).LE.SM(I-1)) GO TO 240
                    AA=SM(I)
                    SM(I)=SM(I-1)
                    SM(I-1)=AA
                    IFLAG=1
240             CONTINUE
                IF(IFLAG.NE.0) GO TO 230
                NN=INT(SM(II-1)/BM)
                AA=BM*FLOAT(NN)
250             NN=II-2
                K=0
260             NN=NN+1
                IF(NN.GT.III) GO TO 300
                TEMP=SM(NN)
270             IF(TEMP.LE.AA) GO TO 280
                K=K+1
                IF(NN.NE.III) GO TO 260
                SM(J)=AA+0.5*BM
                NM(J)=K
                GO TO 260
280             SM(J)=AA+0.5*BM
                NM(J)=K
                AA=AA-BM
                IF(K.EQ.0) GO TO 270
                J=J+1
                K=0
                GO TO 270
290             NN=INT(SM(III)/BM)
                SM(J)=FLOAT(NN)
                SM(J)=BM*(SM(J)-0.5)
                NM(J)=1
300             II=III+2
                J=J+1
400     CONTINUE
C
C       LARGEST STRESS IN SPECTRUM (USED IN DEFGRO SUBROUTINE)
C
        SMAXM=SM(1)+0.5*SR(1)
C
        WRITE(IO2,410)
410     FORMAT(//1X,'STRESS SPECTRUM HISTOGRAM'/)
        WRITE(IO2,420) MAXR
420     FORMAT(1X,'NUMBER OF STRESS RANGES = ',I5)
C
        NN=0
        II=0
        J=0
        K=0
        DO 470 L=1,MAXR
                MCOUNT=0
                WRITE(IO2,430)
430             FORMAT(/12X,'RANGE (KSI)',6X,'COUNT')
                WRITE(IO2,440) L,SR(L),NR(L)
440             FORMAT(1X,I5,5X,E12.5,5X,I5)
                J=J+NR(L)
                WRITE(IO2,450)
450             FORMAT(/12X,'MEAN  (KSI)',6X,'COUNT')
460             NN=NN+1
                MCOUNT=MCOUNT+1
                WRITE(IO2,440) MCOUNT,SM(NN),NM(NN)
```

```
                K=K+NM(NN)
                II=II+1
                IF(K.LT.J) GO TO 460
470     CONTINUE
        WRITE(IO2,480)
480     FORMAT(/1X,'END OF STRESS SPECTRUM HISTOGRAM'/)
        WRITE(IO2,490) K,II
490     FORMAT(1X,'TOTAL COUNTS  = ',I5,
     1  /1X,'TOTAL BLOCKS  = ',I5)
        WRITE(IO2,500) SMAXM
500     FORMAT(/1X,'SMAX',10X,'= ',E12.5,' KSI')
C
        RETURN
        END
C*
C*      DEFECT GROWTH ANALYSIS SUBROUTINE FOR DETAIL
C*      FRACTURE CRACK GROWTH PROGRAM
C*
        SUBROUTINE DEFGRO
        COMMON/BLCK1/ SR(3000),NR(3000),MAXR,SM(3000),NM(3000)
        COMMON/BLCK2/ NFW,IFLAT(20),FWRL(20),FWMF(20),MFLAG
        COMMON/BLCK3/ SIG(4),RBOA,ELOC,TRKC,RLOVT,RLOVA,RAIL
        COMMON/BLCK4/ BL,BR,BM
        COMMON/BLCK5/ C,P,Q,TK1,CPHA,XRS,ITH,ETHERM
        COMMON/BLCK6/ GTONS,NAXLES,LGRPS
        COMMON/BLCK7/ WRL(600),RLOV(600),X(600),LG(131)
        COMMON/BLCK8/ DA(130),DB(130),DC(130)
        COMMON/BLCK9/ COEF(3,3)
        COMMON/BLCK0/ IO2,DMY1,NFLAG
        COMMON/RAIL1/ CWARP,D,E,FK0,FK1,FK2
        COMMON/RAIL2/ FDT,GDT,HDT
        COMMON/RAIL3/ YI,ZI,HIZ,BIZ,HIY,AREA,HAREA
        COMMON/RAIL4/ HGT,ZNA,ZBR,TWB,HWB,HWD
        COMMON/CRAX1/ NCRX,PHA(20)
        CHARACTER*5 RAIL
        DIMENSION DMGT(20),CMGT(20),SUM(20),DMGTC(20),DMGTP(20),
     1    AC(20),AP(20)
        DATA PI/3.141593/
C
        CPHAG=CPHA+.00001
        CPHAL=CPHA-.00001
C
C       COMPUTATION OF RADIUS FOR A GIVEN CRACK SIZE
C
        DO 20 I=1,NCRX
                IF(PHA(I).GT.CPHAG) GO TO 10
                AAP=PHA(I)*HAREA/PI
                AP(I)=SQRT(AAP)
10              AAC=4.*HAREA*PHA(I)/PI
                AC(I)=SQRT(AAC)
20      CONTINUE
        IMAX=NCRX-1
C
        DO 220 I=1,IMAX
                ASIZE=PHA(I)
                ASIZEA=PHA(I+1)
                IF(ASIZE.LT.CPHAL) THEN
                  NUM=1
                  AA1=AP(I)
                  AA2=AP(I+1)
```

```
                GO TO 50
              END IF
40            AA1=AC(I)
              AA2=AC(I+1)
C
50            WRITE(IO2,60) ASIZE,PHA(I+1)
60            FORMAT(/1X,30('*'),/1X,'INCREMENTAL LIFE CALCULATION',
     1               /1X,'INITIAL CRACK SIZE = ',F5.2,' %HA',/1X,'
     1               FINAL CRACK SIZE   = ',F5.2,' %HA',/1X,30('*'))
C
C             CALL SUBROUTINE TO COMPUTE CRACK GEOMETRY INTEGRAL
C             GTHN  =  CRACK GEOMETRY INTEGRAL
C
              IF(TRKC.EQ.0.0) THEN
                RLOVI=RLOVT
              ELSE
                RLOVI=RLOVA
              END IF
              CALL GNUM(RLOVI,GTHN,ASIZE,ASIZEA,RBOA,AA1,AA2,P,NUM)
              SUM(I)=0.0
              CMGT(I)=0.0
C
C             CRACK CENTER LOCATION
C             DEPTH = DISTANCE FROM TOP OF RAIL TO CRACK CENTER
C             YLOC  = DISTANCE FROM VERTICAL CENTERLINE TO CRACK CENTER
C
              DEPTH=FX2(ASIZE)
              IF(NUM.EQ.0) GO TO 70
              IF(AA1.GT.DEPTH) GO TO 230
70            YLOC=FX3(ASIZE)
              YMAX=(HWD/2.)-YLOC
              IF(NUM.EQ.0) GO TO 80
              IF(AA1.GT.YMAX) GO TO 230
C
80            WRITE(IO2,90) DEPTH,YLOC
90            FORMAT(/1X,'CRACK CENTER LOCATION',/1X,'DEPTH = ',F6.2
     1               ,' INCHES',/1X,'YLOC  = ',F6.2,' INCHES')
C
C             ADDITIONAL MEAN STRESS COMPONENTS
C             RS      = RESIDUAL STRESS
C             THERM       = THERMAL STRESS
C
              RS=FX1(ASIZE)
              RS=RS*XRS
              IF(ITH.EQ.0) THERM=FX4(ASIZE)
              IF(ITH.EQ.1) THERM=ETHERM
C
              WRITE(IO2,100) RS,THERM
100           FORMAT(/1X,'ADDITIONAL MEAN STRESS COMPONENTS',
     1               /1X,'RESIDUAL STRESS = ',E12.5,' KSI',
     1               /1X,'THERMAL STRESS  = ',E12.5,' KSI')
              IF(ASIZE.LT.CPHAL.AND.NUM.EQ.1) THEN
                ZZ=DEPTH
                YY=YLOC
              ELSE
                ZZ=0.0
                YY=HWD/2.
              END IF
C
```

```
                CALL STRESS(ZZ,YY,RS,THERM,SMAX)
C
                NN=0
                J=0
                K=0
C
C               COMPUTE STRESS SPECTRUM SUM
C
                DO 170 L=1,MAXR
                        ASIZEM=(ASIZEA+ASIZE)/2.
                        J=J+NR(L)
130                     NN=NN+1
                        K=K+NM(NN)
                        CC=0.0
                        IF(PHA(I).GT.CPHAL.OR.NUM.EQ.0) GO TO 140
C
C                       CALL SUBROUTINES TO COMPUTE MAGNIFICATION
C                       FACTORS FOR PENNY CRACK MODEL
C
                        CALL FMG(ASIZEM,RLOVI,FMAGG,1)
                        CALL FM1(ASIZEM,FMAG1,1)
                        CALL FMS(RBOA,FMAGS)
                        CC=SM(NN)+0.5*SR(L)
                        IF(CC.LE.0.) GO TO 160
                        CC1=CC-(RS+THERM)*(1.-1./FMAGG)
                        CC1=(CC1**Q)*NM(NN)
                        GA=FMAGS*FMAG1*2./SQRT(PI)
                        GO TO 150
C
C                       CALL SUBROUTINES TO COMPUTE MAGNIFICATION
C                       FACTORS FOR CORNER CRACK MODEL
C
140                     CALL FMG(ASIZEM,RLOVI,FMAGG,0)
                        CALL FM1(ASIZEM,FMAG1,0)
                        CC=SM(NN)+0.5*SR(L)
                        IF(CC.LE.0.) GO TO 160
                        CC1=CC-(RS+THERM)*(1.-1./FMAGG)
                        CC1=(CC1**Q)*NM(NN)
                        GA=FMAG1*2./SQRT(PI)
150                     DK=GA*SQRT(AA1)*((RS+THERM)*(1.-FMAGG)+(SM(NN)
   1                    +.5*SR(L))*FMAGG)
                        IF(DK.LT.TK1) GO TO 160
                        SUM(I)=SUM(I)+CC1*(ABS(SR(L)))**(P-Q)
160                     IF(K.NE.J) GO TO 130
170             CONTINUE
C
                WRITE(IO2,180) SUM(I)
180             FORMAT(/1X,'PALMGREN-MINER DAMAGE SUM = ',E12.5)
                IF(SUM(I).NE.0.0) GO TO 190
                DMGT(I)=0.0
                GO TO 220
190             DMGT(I)=1.E-6*GTONS*GTHN/(C*SUM(I))
                IF(ASIZE.LT.CPHAL) THEN
                  IF(NUM.EQ.1)THEN
                    DMGTP(I)=DMGT(I)
                    NUM=0
                    GO TO 40
                  END IF
                  DMGTC(I)=DMGT(I)
                  DMGT(I)=(1.-(ASIZEM/CPHA))*DMGTP(I)+
```

```
     1                  DMGTC(I)*(ASIZEM/CPHA)
                    END IF
                    WRITE(6,200) ASIZEM,DMGTP(I),DMGTC(I),DMGT(I)
200                 FORMAT(1X,'%HA =',F6.4,5X,'PC=',E11.5,5X,'CC=',
     1                  E11.5,5X,'CL=',E11.5)
C
                    WRITE(IO2,210) DMGT(I)
210                 FORMAT(/1X,'INCREMENTAL LIFE = ',E11.5,' MGT')
C
220     CONTINUE
C
230     CMGT(1)=DMGT(1)
        DO 240 I=2,IMAX
240                 CMGT(I)=CMGT(I-1)+DMGT(I)
C
        IF(NFLAG.NE.0) WRITE(IO2,250)
        WRITE(6,250)
250     FORMAT(//1X,'DEFECT GROWTH/LIFE DATA')
        IF(NFLAG.NE.0) WRITE(IO2,260)
        WRITE(6,260)
260     FORMAT(/1X,'INITIAL',8X,'FINAL',10X,'INCREMENTAL',
     1   4X,'CUMULATIVE',/1X,'CRACK SIZE',5X,'CRACK SIZE',
     1   5X,'LIVES',10X,'LIVES')
        IF(NFLAG.NE.0) WRITE(IO2,270)
        WRITE(6,270)
270     FORMAT(5X,'(%HA)',10X,'(%HA)',8X,'(MGT)',8X,'(MGT)'/)
C
        DO 310 I=1,IMAX
                    A1=PHA(I)
                    A2=PHA(I+1)
                    IF(DMGT(I).NE.0.0) GO TO 290
                    IF(NFLAG.NE.0) WRITE(IO2,280) A1,A2
                    WRITE(6,280) A1,A2
280                 FORMAT(2(6X,F5.2),6X,'INFINITE LIFE',3X,
     1                  'INFINITE LIFE')
                    GO TO 310
290                 IF(NFLAG.NE.0) WRITE(IO2,300) A1,A2,DMGT(I),
     1              CMGT(I),SUM(I)
                    WRITE(6,300) A1,A2,DMGT(I),CMGT(I),SUM(I)
300                 FORMAT(2(5X,F6.3),3(6X,E12.5))
310     CONTINUE
C
        RETURN
        END
C*
C*      FUNCTION TO CALCULATE RESIDUAL STRESS WITH CRACK SIZE
C*
        FUNCTION FX1(X)
        COMMON/BLCK9/ COEF(3,3)
        FX1=COEF(1,1)+X*(COEF(1,2)+X*COEF(1,3))
        RETURN
        END
C*
C*      FUNCTION TO CALCULATE DEPTH WITH CRACK SIZE
C*
        FUNCTION FX2(X)
        COMMON/BLCK9/ COEF(3,3)
        FX2=COEF(2,1)+X*(COEF(2,2)+X*COEF(2,3))
        RETURN
        END
```

```
C*
C*      FUNCTION TO CALCULATE YLOC WITH CRACK SIZE
C*
        FUNCTION FX3(X)
        COMMON/BLCK9/ COEF(3,3)
        FX3=COEF(3,1)+X*(COEF(3,2)+X*COEF(3,3))
        RETURN
        END
C*
C*      FUNCTION TO CALCULATE THERMAL STRESS WITH CRACK SIZE
C*      (RAIL 1 ONLY)
C*
        FUNCTION FX4(X)
        DIMENSION CKS(5),THS(5)
        DATA CKS/.119,.137,.241,.474,.804/
        DATA THS/7.0,3.9,0.4,0.4,4.3/
        DO 10 I=1,4
        IF(X.GE.CKS(I).AND.X.LT.CKS(I+1))THEN
          FX4=THS(I+1)-(((CKS(I+1)-X)/(CKS(I+1)-CKS(I)))*(THS(I+1)
     1       -THS(I)))
          GO TO 20
        END IF
10      CONTINUE
        FX4=0.0
20      RETURN
        END
C*
C*      FUNCTION TO CALCULATE FREE SURFACE CORRECTION
C*      FACTOR USING LAGRANGIAN INTERPOLATION
C*
        FUNCTION CMK(ARG)
        DIMENSION X(5),Y(5)
        DATA X/0.5,0.6,0.7,0.8,0.9/
        DATA Y/1.01,1.03,1.06,1.10,1.20/
        NPTS=5
        CMK=0.0
        DO 20 I=1,NPTS
                PROD=Y(I)
                DO 10 J=1,NPTS
                        IF(I.EQ.J) GO TO 10
                        PROD=PROD*(ARG-X(J))/(X(I)-X(J))
10              CONTINUE
20      CMK=CMK+PROD
        RETURN
        END
```

```
c
c       SUBROUTINE TO IMPLEMENT 'SIMPLIFIED' TIMOSHENKO AND LANGER
C       STRESS ANALYSIS PROGRAM FOR CRACK GROWTH ANALYSIS
C       LATEST VERSION - APRIL 1988
c       (ASSUMES GAUGE SIDE STRESS POINT)
c
        SUBROUTINE TIMO(P1,P2,EDIST,X,NX,XP,NP,DEPTH,YLOC,SXX)
        real k1,k2,kt
        real iyy,izz,iyyh,izzh,izzb
        real lambda,mom1
        dimension p1(6),p2(6),xp(6),edist(6)
        dimension x(400),sxx(400)
        common/rail1/ c,d,e,k1,k2,kt
        common/rail2/ f,g,h
        common/rail3/ iyy,izz,izzh,izzb,iyyh
        common/rail4/ htot,zc,zh,tweb,hweb
        common/rail5/ beta1,beta2,bhow1,bhow2
c
c       INPUT PARAMETERS
c
c       c       = torsion constant of rail
c       d       = Timoshenko's or warping constant of rail
c       e       = modulus of elasticity
c
c       iyy     = vertical bending inertia for entire rail
c       izz     = lateral bending inertia for entire rail
c       iyyh    = vertical bending inertia for rail head only
c       izzh    = lateral bending inertia for rail head only
c       izzb    = lateral bending inertia for rail base only
c
c       htot    = total height of rail
c       h       = distance between centroids of head and base
c       f       = distance from top of rail to shear center
c       zc      = distance from bottom of rail to centroid of entire rail
c       zh      = distance from bottom of rail to centroid of head
c       zb      = distance from bottom of rail to top of base
c       tweb    = average thickness of web
c       hweb    = height of web
c
c       k1      = vertical foundation modulus
c       k2      = lateral foundation modulus
c       kt      = torsional foundation modulus
c
c       np      = number of applied loads (maximum of 6)
c       p1(i)   = vertical load at location i
c       p2(i)   = lateral load at location i
c       edist(i) = offset distance for vertical load
c
c       yloc    = distance from z centroidal axis to stress point
c       depth   = distance from top of rail to stress point
c
c       xi      = initial value of x
c       dx      = increment of x
c       nx      = number of values for x
c
        cz1=htot-zc-depth
        cz2=htot-zh-depth
        dcrit=htot-hweb-zb
        h1=h*izzb/(izzh+izzb)
        fx1=4.*d*h*h
```

```
      lambda=sqrt(kt/fx1)
      a=sqrt(c/fx1+lambda)
      b=sqrt(c/fx1-lambda)
      crit=c*c/fx1
c
      do 500 i=1,nx
            xmz=0.0
            xmy=0.0
            xmhz=0.0
            xmhy=0.0
            dftot=0.0
c
c     LONGITUDINAL BENDING STRESS COMPONENTS
c     sxz       = vertical
c     sxy       = lateral
c     sxw       = warping
c     showz     = vertical head on web
c     showy     = lateral head on web
c     sxx       = total longitudinal bending stress
c
            sxz=0.0
            sxy=0.0
            sxw=0.0
            showz=0.0
            showy=0.0
            sxx(i)=0.0
c
            do 450 j=1,np
                  ax=abs(x(i)-xp(j))
                  mom1=p2(j)*f-p1(j)*edist(j)
                  coef=mom1/(fx1*a*b)
                  arg1=beta1*ax
                  arg2=beta2*ax
                  arh1=bhow1*ax
                  arh2=bhow2*ax
                  arga=a*ax
                  argb=b*ax
                  fz2=gx1(arg1)
                  fy2=gx1(arg2)
                  fh12=gx1(arh1)
                  fh22=gx1(arh2)
                  xmz=xmz+p1(j)*fz2/(4.*beta1)
                  xmy=xmy+p2(j)*fy2/(4.*beta2)
                  xmhz=xmhz+p1(j)*fh12/(4.*bhow1)
                  xmhy=xmhy+p2(j)*fh22/(4.*bhow2)
                  if(kt.le.critk) df2=coef*exp(-arga)*((a-b)
     1            *exp(argb)-(a+b)*exp(-argb))/2.
                  if(kt.gt.critk) df2=coef*exp(-arga)*(-b*
     1            cos(argb)+a*sin(argb))
                  dftot=dftot+df2
450         continue
c
            sxz=-xmz*cz1/iyy
            sxy=-xmy*yloc/izz
            sxw=e*h1*dftot*yloc
            if(depth.gt.dcrit) go to 480
            showz=-xmhz*cz2/iyyh
            showy=-xmhy*yloc/izzh
480         sxx(i)=sxz+sxy+sxw+showz+showy
500   continue
```

```
c
      return
      end
c
c     subroutine to evaluate Hetenyi equation
c
      function gx1(arg)
      expa=0.
      if(arg.lt.50.) expa=exp(-arg)
      gx1=expa*(cos(arg)-sin(arg))
      return
      end
```

```
C
C     COMPUTATION OF CRACK GEOMETRY INTEGRAL
C     (TRANSITION AT 50%, 136RE RAIL)
C
      SUBROUTINE GNUM(RLOVT,GTHN,ASIZE,ASIZEA,RBOA,AA1,AA2,P,NUM)
      DATA PI/3.141593/
C
C     APPLIED TRAPEZOID RULE TO INTEGRAL
C
C     FMS = SHAPE MAGNIFICATION FACTOR
C     FM1 = FINITE-SECTION MAGNIFICATION FACTOR
C
C
C     PENNY CRACK MODEL
C
      IF(NUM.EQ.1) THEN
        CALL FMS(RBOA,FMAGS1)
        CALL FM1(ASIZE,FMAG11,NUM)
        CALL FMS(RBOA,FMAGS2)
        CALL FM1(ASIZEA,FMAG12,NUM)
        TFMAG1=2.*FMAGS1*FMAG11/SQRT(PI)
        TFMAG2=2.*FMAGS2*FMAG12/SQRT(PI)
        GTHN=(AA2-AA1)*.5*(1./(TFMAG2*SQRT(AA2))**P+1./(TFMAG1*
     1  SQRT(AA1))**P)
        GO TO 20
      END IF
C
C     CORNER CRACK MODEL
C
      CALL FM1(ASIZE,FMAG11,NUM)
      CALL FM1(ASIZEA,FMAG12,NUM)
      TFMAG1=2.*FMAG11/SQRT(PI)
      TFMAG2=2.*FMAG12/SQRT(PI)
      GTHN=(AA2-AA1)*.5*(1./(TFMAG2*SQRT(AA2))**P+1./(TFMAG1*
     1          SQRT(AA1))**P)
20    RETURN
      END
```

```
C
C     COMPUTATION OF THE SHAPE MAGNIFICATION FACTOR
C
      SUBROUTINE FMS(RBOA,FMAGS)
      DIMENSION FACTS(6),BOA(6)
      DATA BOA/.4,.5,.6,.7,.8,.9/
      DATA FACTS/.907,.944,.969,.984,.994,.999/
      DO 10 I=1,6
              IF(BOA(I).EQ.RBOA)THEN
                FMAGS=FACTS(I)
                GO TO 20
              END IF
              IF(I.GE.6)THEN
                WRITE(6,5)
5               FORMAT(1X,'B/A RATIO TOO HIGH, NOT ENOUGH DATA')
                GO TO 20
              END IF
              IF(BOA(I).LT.RBOA.AND.BOA(I+1).GT.RBOA)THEN
                FMAGS=FACTS(I+1)-(FACTS(I+1)-FACTS(I))*(BOA(I+1)-
     1                RBOA)/(BOA(I+1)-BOA(I))
                GO TO 20
              END IF
10    CONTINUE
20    RETURN
      END
```

```
C
C     COMPUTATION OF THE FINITE-SECTION MAGNIFICATION FACTOR
C     (TRANSITION AT 50%, 136RE RAIL)
C
      SUBROUTINE FM1(ASIZE,FMAG1,NUM)
      DIMENSION FACT1P(6),PHA(9),FACT1C(9)
      DATA PHA/.05,.1,.2,.3,.4,.5,.6,.7,.8/
      DATA FACT1P/1.025,1.072,1.236,1.513,1.946,1.26/
      DATA FACT1C/1.226,1.275,1.45,1.746,2.212,1.475,1.589,1.728,1.895/
      IF(NUM.EQ.1) THEN
        DO 10 I=1,6
                IF(PHA(I).EQ.ASIZE) THEN
                  FMAG1=FACT1P(I)
                  GO TO 40
                END IF
                IF(I.GE.6) THEN
                  WRITE(6,5)
5                 FORMAT(1X,'%HA TOO LARGE FOR PENNY CRACK,',
     1                  ' NOT ENOUGH DATA IN 1')
                END IF
                IF(PHA(I).LT.ASIZE.AND.PHA(I+1).GT.ASIZE) THEN
                  FMAG1=FACT1P(I+1)-(FACT1P(I+1)-FACT1P(I))*
     1                  (PHA(I+1)- ASIZE)/(PHA(I+1)-PHA(I))
                  GO TO 40
                END IF
10      CONTINUE
      END IF
      DO 30 I=1,9
              IF(PHA(I).EQ.ASIZE) THEN
                FMAG1=FACT1C(I)
                GO TO 40
              END IF
              IF(I.GE.9) THEN
                WRITE(6,20)
20              FORMAT(1X,'%HA TOO LARGE, NOT ENOUGH DATA IN 1')
                GO TO 40
              END IF
              IF(PHA(I).LT.ASIZE.AND.PHA(I+1).GT.ASIZE) THEN
                FMAG1=FACT1C(I+1)-(FACT1C(I+1)-FACT1C(I))*
     1                (PHA(I+1)- ASIZE)/(PHA(I+1)-PHA(I))
                GO TO 40
              END IF
30    CONTINUE
40    RETURN
      END
```

```
C
C     COMPUTATION OF NONUNIFORM STRESS MAGNIFICATION FACTOR
C     (TRANSITION AT 50%, 136RE RAIL)
C
      SUBROUTINE FMG(ASIZE,RLOVT,FMAGG,NUM)
      DIMENSION FACTGP(6,6),FACTGC(6,9),PHA(9),RLOV(6),TEMPP(6),
     1          TEMPC(9)
      DATA PHA/.05,.1,.2,.3,.4,.5,.6,.7,.8/
      DATA RLOV/.05,.1,.2,.3,.4,.5/
      DATA FACTGP/1.0,1.001,1.002,1.004,1.006,1.007,1.001,1.002,1.005,
     1     1.008,1.012,1.016,1.002,1.004,1.011,1.02,1.029,1.039,
     1     1.003,1.006,1.018,1.033,1.049,1.066,1.004,1.008,1.025,
     1     1.046,1.069,1.092,1.005,1.011,1.031,1.056,1.084,1.112/
      DATA FACTGC/.988,.978,.962,.949,.939,.931,.984,.969,.947,.929,
     1     .915,.904,.977,.957,.925,.901,.882,.867,.972,.948,
     1     .909,.88,.858,.839,.967,.94,.896,.863,.838,.817,
     1     .964,.933,.884,.848,.821,.799,.96,.927,.874,.835,
     1     .806,.783,.957,.921,.865,.824,.792,.769,.954,.916,
     1     .856,.813,.78,.756/
C
C     COMPUTE A SET OF DATA FOR A GIVEN L/V RATIO BY INTERPOLATION
C
      DO 40 I=1,6
            IF(RLOV(I).EQ.RLOVT) THEN
              DO 10 J=1,6
                    TEMPP(J)=FACTGP(I,J)
10            CONTINUE
              DO 15 J=1,9
                    TEMPC(J)=FACTGC(I,J)
15            CONTINUE
              GO TO 50
            END IF
            IF(I.GE.6) THEN
              WRITE(6,20)
20            FORMAT(1X,'L/V RATIO TOO HIGH, NOT ENOUGH DATA')
              GO TO 70
            END IF
            IF(RLOV(I).LT.RLOVT.AND.RLOV(I+1).GT.RLOVT) THEN
              DO 30 J=1,6
                    TEMPP(J)=FACTGP(I+1,J)-(FACTGP(I+1,J)-
     1                     FACTGP(I,J))*(RLOV(I+1)-RLOVT)/
     1                     (RLOV(I+1)-RLOV(I))
30            CONTINUE
              DO 35 J=1,9
                    TEMPC(J)=FACTGC(I+1,J)-(FACTGC(I+1,J)-
     1                     FACTGC(I,J))*(RLOV(I+1)-RLOVT)/
     1                     (RLOV(I+1)-RLOV(I))
35            CONTINUE
              GO TO 50
            END IF
40    CONTINUE
C
C     DETERMINE THE TRANSITION MAGNIFICATION FACTOR FOR A GIVEN
C     CRACK SIZE BY INTERPOLATION
C
50    IF(NUM.EQ.1)THEN
        DO 60 J=1,6
              IF(PHA(J).EQ.ASIZE) THEN
                FMAGG=TEMPP(J)
                GO TO 70
```

```
                END IF
                IF(I.GE.6) THEN
                  WRITE(6,55)
55                FORMAT(1X,'%HA TOO HIGH FOR PENNY CRACK, NOT ',
     1            'ENOUGH DATA')
                  GO TO 70
                END IF
                IF(PHA(J).LT.ASIZE.AND.PHA(J+1).GT.ASIZE) THEN
                  FMAGG=TEMPP(J+1)-(TEMPP(J+1)-TEMPP(J))*(PHA(J+1)-
     1            ASIZE)/(PHA(J+1)-PHA(J))
                  GO TO 70
                END IF
60      CONTINUE
        END IF
        DO 65 J=1,9
                IF(PHA(J).EQ.ASIZE) THEN
                  FMAGG=TEMPC(J)
                  GO TO 70
                END IF
                IF(J.GE.9) THEN
                  WRITE(6,62)
62                FORMAT(1X,'%HA TOO LARGE, NOT ENOUGH DATA IN G')
                  GO TO 70
                END IF
                IF(PHA(J).LT.ASIZE.AND.PHA(J+1).GT.ASIZE) THEN
                  FMAGG=TEMPC(J+1)-(TEMPC(J+1)-TEMPC(J))*(PHA(J+1)-
     1            ASIZE)/(PHA(J+1)-PHA(J))
                  GO TO 70
                END IF
65      CONTINUE
70      RETURN
        END
```

REFERENCES

[1] D.D. Davis, M.W. Joerms, O. Orringer, and R.K. Steele, "The Economic Consequences of Rail Integrity," *Proc. Third International Heavy Haul Railway Conference*, Vancouver, BC, Canada (1986).

[2] O. Orringer and M.W. Bush, "Applying Modern Fracture Mechanics to Improve the Control of Rail Fatigue Defects in Track," *American Railway Engineering Association Bulletin 689, Vol. 84*, 19-53 (1983).

[3] O. Orringer, J.M. Morris, and R.K. Steele, "Applied Research on Rail Fatigue and Fracture in the United States," *Theoretical and Applied Fracture Mechanics 1*, 23-49 (1984).

[4] O. Orringer, J.M. Morris, and D.Y. Jeong, "Detail Fracture Growth in Rails: Test Results," *Theoretical and Applied Fracture Mechanics 5*, 63-95 (1986).

[5] A. Kish, G. Samavedam, and D. Jeong, "The Neutral Temperature Variation of Continuous Welded Rails," *American Railway Engineering Association Bulletin 712, Vol. 88*, 257-279 (1987).

[6] J.R. Carden, "Derailment December 21, 1983 - Burlington Northern Railroad Company - Trinidad, Colorado," memo to FRA Regional Director of Railroad Safety, Denver, CO (1984).

[7] S.T. Rolfe and J.M. Barsom, *Fracture Control and Fatigue in Structures*, Prentice-Hall, Inc., Englewood Cliffs, NJ (1977).

[8] M.F. Kanninen and C.H. Popelar, *Advanced Fracture Mechanics*, Oxford University Press, New York (1985).

[9] G.C. Sih, *Handbook of Stress Intensity Factors*, Institute of Fracture and Solid Mechanics, Lehigh University, Bethlehem, PA (1973).

[10] D.P. Rooke and D.J. Cartwright, *Compendium of Stress Intensity Factors*, HM Stationery Office, United Kingdom (1976).

[11] Y. Murakami (ed.), *Stress Intensity Factors Handbook*, Pergamon Press, Oxford, England (1987).

[12] I.N. Sneddon, "The Distribution of Stress in the Neighbourhood of a Crack in an Elastic Solid," *Proc. Royal Society, Series A*, 187-229 (1946).

[13] D. Broek, *Elementary Engineering Fracture Mechanics*, Noordhoff International Publishing Co., Leyden, the Netherlands (1974).

[14] Anon., "Standard Method of Test for Plane-Strain Fracture Toughness of Metallic Materials," Standard E-399-72, American Society for Testing and Materials, Philadelphia, PA (1972).

[15] P.M. Besuner, "Fracture Mechanics Analysis of Rails with Shell-Initiated Transverse Cracks," in: D.H. Stone and G.G. Knupp (eds.), *Rail Steels - Developments, Processing, and Use, ASTM STP 644*, 303-329 (1978).

[16] J.M. Barsom and E.J. Imhoff, Jr., "Fatigue and Fracture of Carbon-Steel Rails," in: D.H. Stone and G.G. Knupp (eds.), *Rail Steels - Developments, Processing, and Use, ASTM STP 644*, 387-413 (1978).

[17] W. Elber, "Equivalent Constant-Amplitude Concept for Crack Growth Under Spectrum Loading," *Fatigue Crack Growth Under Spectrum Loads, ASTM STP 595*, 236-250 (1976).

[18] G.J. Fowler and A.S. Tetelman, "The Effect of Grain Boundary Ferrite on Fatigue Crack Propagation in Pearlitic Rail Steels," in: D.H. Stone and G.G. Knupp (eds.), *Rail Steels - Developments, Processing, and Use, ASTM STP 644*, 363-386 (1978).

[19] C.E. Fedderson and D. Broek, "Fatigue Crack Propagation in Rail Steels," in: D.H. Stone and G.G. Knupp (eds.), *Rail Steels - Developments, Processing, and Use, ASTM STP 644*, 414-429 (1978).

[20] R. Rungta, R.C. Rice, and R.D. Buchheit, "Post-Service Rail Defect Analysis," Battelle Columbus Laboratories, Columbus, OH, interim report, Contract No. DOT-TSC-1708 (1982).

[21] J.J. Scutti, R.M. Pelloux, and R. Fuquen-Moleno, "Fatigue Behavior of a Rail Steel," *Fatigue & Fracture of Engineering Materials & Structures 7*, 121-135 (1984).

[22] R.C. Shah and A.S. Kobayashi, "Stress Intensity Factor for an Elliptical Crack Under Arbitrary Normal Loading," *Engineering Fracture Mechanics 3*, 71-96 (1971).

[23] S.M. Selby (ed.), *Standard Mathematical Tables*, the Chemical Rubber Co., Cleveland, OH, 15th ed. (1967).

[24] S. Timoshenko and J.N. Goodier, *Theory of Elasticity*, McGraw-Hill, New York, 2nd ed. (1951).

[25] R.C. Shah and A.S. Kobayashi, "Stress Intensity Factor for an Elliptical Crack Approaching the Surface of a Semi-Infinite Solid," *International Journal of Fracture 9*, 133-146 (1973).

[26] O. Orringer, "Rapid Estimation of Spectrum Crack Growth Life Based on the Palmgren-Miner Rule," *Computers & Structures 19*, 149-153 (1984).

[27] J. Schijve, "Effect of Load Sequences on Crack Propagation Under Random and Program Loading," *Journal of Engineering Fracture Mechanics 5*, 269-280 (1973).

[28] J.B. Chang and C.M. Hudson (eds.), *Methods and Models for Predicting Fatigue Crack Growth Under Random Loading, ASTM STP 748*, American Society for Testing and Materials, Philadelphia, PA (1981).

[29] B.G. Journet and R.M. Pelloux, "A Direct Method for Laboratory Spectrum Crack Growth Testing," *Theoretical and Applied Fracture Mechanics 7*, 19-22 (1987).

[30] B.G. Journet and R.M. Pelloux, "A Methodology for Studying Fatigue Crack Propagation Under Spectrum Loading - Application to Rail Steels," *Theoretical and Applied Fracture Mechanics 8*, 117-123 (1987).

[31] A.N. Talbot et al., "Fifth Progress Report of the Special Committee on Stresses in Track," *Proc. American Railway Engineering Association 31*, 69-336 (1930).

[32] S. Timoshenko and B.F. Langer, "Stresses in Railroad Track," *ASME Transactions 54*, 277-293 (1932).

[33] M. Hétenyi, *Beams on Elastic Foundation*, University of Michigan Press, Ann Arbor, MI (1983).

[34] Anon., *Manual for Railway Engineering (Fixed Properties)*, American Railway Engineering Association, Chicago, IL, Vol. 1 (1976).

[35] A.B. Perlman, B.R. Lewin, and L.R. Toney, "Rail Section Properties," Tufts University, Medford, MA (1982) unpublished.

[36] D.K. Heron and A. Flassig, "Rail Overturning Test Data," Association of American Railroads, Track/Train Dynamics Report (1976).

[37] D.P. McConnell and A.B. Perlman, "An Investigation of the Structural Limitations of Railroad Track," DOT Transportation Systems Center and Tufts University (1979) unpublished.

[38] T.G. Johns, S.G. Sampath, J.C. Bell, and K.B. Davies, "Engineering Analysis of Stresses in Railroad Rails," Battelle Columbus Laboratories, Columbus, OH, Report No. FRA/ORD-81/51 (1981).

[39] A.M. Zarembski, "Effect of Rail Section and Traffic on Rail Fatigue Life," *American Railway Engineering Association Bulletin 673, Vol. 80*, 514-527 (1979).

[40] O. Orringer, "Analysis of Pre-Production Operational Test Data for New Truck Bolster for Metroliner," Aeroelastic and Structures Research Laboratory, MIT, Cambridge, MA, ASRL TR 185-5 (1977).

[41] M.R. Johnson, "Summarization and Comparison of Freight Car Truck Load Data," *ASME Transactions, Journal of Engineering for Industry 100*, 60-66 (1978).

[42] D.R. Ahlbeck, M.R. Johnson, H.D. Harrison, and J.M. Tuten, "Measurements of Wheel/Rail Loads on Class 5 Track," Battelle Columbus Laboratories, Columbus, OH, and IIT Research Institute, Chicago, IL, FRA/ORD-80/19 (1980).

[43] O. Orringer and R.P. Owings, "Results from Operational Tests of Hollow and Solid M-2 Axles," DOT Transportation Systems Center, Cambridge, MA, and Ensco, Inc., Springfield, VA, PM-76-C-14-1 (1982).

[44] J.M. Tuten and H.D. Harrison, "Design, Validation, and Application of a Monitoring Device for Measuring Dynamic Wheel/Rail Loads," *Proc. ASME Winter Annual Meeting*, Paper No. 84-WA/RT-10 (1984).

[45] H.G. Moody, Office of Research and Development (RRS-31), Federal Railroad Administration, Washington, DC, private communication (1985).

[46] F.B. Blader, "Analytic Studies of the Relationship Between Track Geometry Variations and Derailment Potential at Low Speeds," the Analytic Sciences Corporation, Reading, MA (1983).

[47] H. Weinstock, "Vehicle Track Interaction Studies for Development of Track Performance Specifications," *Proc. British Rail / Association of American Railroads Vehicle Track Interaction Symposium*, Princeton, NJ (1984).

[48] H. Weinstock, Structures & Dynamics Division, U.S. DOT Transportation Stystems Center, Cambridge, MA, private communication (1987).

[49] L.E. Daniels, Transportation Test Center, Association of American Railroads, Pueblo, CO, private communication (1985).

[50] D.R. Ahlbeck and J.A. Hadden, "Measurement and Prediction of Impact Loads from Worn Railroad Wheel and Rail Surface Profiles," *Proc. ASME Winter Annual Meeting*, Paper No. 84-WA/RT-4 (1984).

[51] D.Y. Jeong, O. Orringer, A.B. Perlman, and R.C. Rice, "Beam Theory Predictions of Shell Nucleation Life," *Proc. International Symposium on Contact Mechanics and Wear of Rail /Wheel Systems II*, University of Rhode Island, Kingston, RI (1987) addendum.

[52] J. Orkisz, A.B. Perlman, and A. Harris, "Formulation of a Method of Evaluation of Residual Stresses in Railroad Rails," Tufts University, Medford, MA (1988).

[53] P. Tong and J.N. Rossettos, *Finite Element Method: Basic Technique and Implementation*, MIT Press, Cambridge, MA (1977).

[54] J. Orkisz, A.B. Perlman, A. Harris, and O. Orringer, "Recent Progress in the Development of a Rail Residual Stress Calculation Method," *Proc. International Symposium on Contact Mechanics and Wear of Rail /Wheel Systems II*, University of Rhode Island, Kingston, RI, 147-161 (1987).

[55] J. Orkisz and M. Pazdanowski, "Obliczanie Aktualnych Naprężen Resztkowych MRS w Ciałach Pryszmatycznych Poddanych Ociazeniom Cyklicznie Zmiennym [Quantifying Existing Residual Stresses by the Finite Difference Method in Prismatic Bodies Under Given Cyclic Fatigue Loads]," *VIII Konferencia Metody Komputerowe w Mechanice Konstrukcji [Eighth Conference on Compter Methods in Structural Mechanics]*, Jadwisin, Poland (1987).

[56] R. Hill, *The Mathematical Theory of Plasticity*, Oxford University Press, London, England (1950).

[57] J. Orkisz and A. Harris, "Analysis of Residual Stresses in Railroad Rails at Shakedown: A Hybrid Approach," to appear in *Theoretical and Applied Fracture Mechanics.*

[58] R.C. Rice, R. Rungta, and P.M. Scott, "Post-Service Rail Defect Analyses," Battelle Columbus Laboratories, Columbus, OH, 4th technical report, Contract No. DOT-TSC-1708 (1984).

[59] R.C. Rice, S.G. Sampath, and H.C. Meacham, "Task 6: Residual Stress Determination in Curved Rail," Battelle Columbus Laboratories, Columbus, OH, final report, Contract No. DOT-TSC-1663 (1983).

[60] R.K. Steele and R.P. Reiff, "Rail: Its Behavior in Relationship to Total System Wear," *Proc. Second International Heavy Haul Railway Conference*, Colorado Springs, CO, Paper No. 82-HH-24 (1982).

[61] B.J. Dabell, S.J. Hill, and P. Watson, "An Evaluation of the Fatigue Performance of Conventional British Rail Steels," in: D.H. Stone and G.G. Knupp (eds.), *Rail Steels - Developments, Processing, and Use, ASTM STP 644*, 430-448 (1978).

[62] V. Bhargava, G.T. Hahn, G. Ham, S. Kulkarni, and C.A. Rubin, "Influence of Kinematic Hardening on Rolling Contact Deformation," *Proc. International Symposium on Contact Mechanics and Wear of Rail/Wheel Systems II*, University of Rhode Island, Kingston, RI, 133-146 (1987).

[63] T.N. Farris, L.M. Keer, and R.K. Steele, "The Effect of Service Loading on Shell Growth in Rails," *J. Mechanics and Physics of Solids 35*, 677-700 (1987).

[64] Z. Świderski, Centralny Ośrodek Badań i Rozwoju Techniki Kolenictwa [Research Institute of the Polish State Railways], Warsaw, Poland, private communication (1988).

[65] R.R. John et al., "Task Force Report - Rail Failure Evaluation," DOT Transportation Systems Center, Cambridge, MA (1984).

[66] O. Orringer and P. Tong, "Investigation of Catastrophic Failure of a Premium-Alloy Railroad Rail," *Fracture Problems in the Transportation Industry* (P. Tong and O. Orringer, eds.), American Society of Civil Engineers, New York, NY, 62-79 (1985).

[67] M. Gence et al., "Possibilities of Improving the Service Characteristics of Rails by Metallurgical Means, Report No. 1, Factors Influencing the Fracture Resistance of Rails in the Unused Condition," D-156 Committee, Office de Recherches et d'Essayons, International Union of Railways, Utrecht, the Netherlands (1984).

[68] S.J. Wineman and F.A. McClintock, "Rail Web Fracture in the Presence of Residual Stresses," *Theoretical and Applied Fracture Mechanics 8*, 87-99 (1987).

[69] C.H. Cundiff and R.C. Rice, "Determination of Residual Stresses in Carbon and Alloy Roller Straightened Rail," Battelle Columbus Laboratories, Columbus, OH, final report, Contract No. DTRS-57-83-C-00076 (1987).

[70] O. Orringer and R.K. Steele, "Structural Integrity of Rail in Railroad Track in the United States," *Fracture Mechanics: Nineteenth Symposium, ASTM STP 969* (T.A. Cruse, ed.), American Society for Testing and Materials, Philadelphia, PA, 260-278 (1987).

[71] O. Orringer, "Rail Testing: Strategies for Safe and Economical Rail Quality Assurance," *Proc. TRB Symposium on Rail: Replacement Strategies and Maintenance Management*, Transportation Research Board, Washington, DC (1988).

[72] M.A. Miner, "Cumulative Damage in Fatigue," *J. Applied Mechanics 12*, A159-A164 (1945).

[73] C.L. Combes (ed.), Car and Locomotive Cyclopedia of American Practice, Simmons-Boardman Publishing Corporation, New York, second edition (1970).